NASA CONTRACTOR REPORT 165886

ANALYSIS OF REMOTE SENSING DATA COLLECTED FOR DETECTION AND MAPPING OF OIL SPILLS

INTERA Environmental Consultants Ltd.
Ottawa, Ontario, Canada

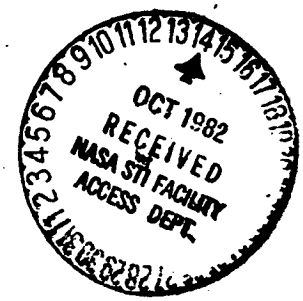

Contract NAS1-16178
May 1982

National Aeronautics and Space Administration
Langley Research Center
Hampton, Virginia 23665

NASA CONTRACTOR REPORT 165886

ANALYSIS OF REMOTE SENSING DATA COLLECTED FOR DETECTION AND MAPPING OF OIL SPILLS

REDUCTION AND ANALYSIS OF MULTI-SENSOR AIRBORNE DATA OF THE NASA WALLOPS OIL SPILL EXERCISE OF NOVEMBER 1978

INTERA Environmental Consultants Ltd.
Ottawa, Ontario, Canada

Contract NAS1-16178
May 1982

National Aeronautics and Space Administration

Langley Research Center
Hampton, Virginia 23665

PREFACE

The work described herein has been sponsored by the National Aeronautics and Space Administration (NASA) under the title: Analysis of Remote Sensing Data Collected for Detection and Mapping of Oil Spills, and contract reference number NAS1-16178. The technical authority for the contract was Mr William Croswell of NASA Langley Research Center, and subsequently, Dr Harold Maurer of NASA Wallops Flight Center.

Much of the original data was supplied by the Canada Centre for Remote Sensing (CCRS) of the Department of Energy, Mines and Resources (EMR). In addition, CCRS made available several image analysis devices and computing facilities for use in this project. The author would like to thank Dr R.A. Neville of CCRS for initiating and extensively supporting this project through consultations, provision of technical data and information, and reviewing the completed work. Several CCRS staff members have provided their special expertise: Drs R.A. O'Neil, R.K. Hawkins and B. Guindon.

NASA, which gave the necessary financial support, also assisted through the welcome contributions of Drs H.E. Maurer, and J.D. Oberholtzer, and of R. Swift of EG&G and W. Oderman of CSC. The author is particularly thankful for the motivation and guidance received from W. Croswell, who acted as the scientific authority for most of the term of this project.

The author is indebted to several colleagues at INTERA for their help in this project: G.J. Wessels for computer programming and technical assistance; Drs R.T. Lowry and D.R. Inkster for constructive discussion; and D. Kemp for preparation of figures.

T.T. Alfoldi

TABLE OF CONTENTS

LIST OF TABLES

LIST OF FIGURES

LIST OF PLATES[1]

[1]Plates are contained in an envelope following page 225.

1. INTRODUCTION

Use of commercial products or names of manufacturers in this report does not constitute official endorsement of such products or manufacturers, either expressed or implied, by the National Aeronautics and Space Administration.

1.1 BACKGROUND

To test the effectiveness of the oil dispersant, Corexit 9527, JBF Scientific Corp. (JBF) conducted a controlled oil spill experiment on behalf of the American Petroleum Institute. Several oil spills were carried out at Dump Site 106 off the New Jersey coast, in the first ten days of November 1978. It was recognized that this was an excellent opportunity to test various remote sensing devices for their ability to detect, identify and map oil slicks in a marine environment. Therefore, several remote sensing groups joined in a co-ordinated effort of airborne overflights of the oil spills. The Canada Centre for Remote Sensing (CCRS) participated with two aircraft, a DC-3 and a Convair 580 (CV-580); the latter in co-operation with the Environmental Research Institute of Michigan (ERIM). The United States Coast Guard used a C-130 aircraft, and the National Aeronautics and Space Administration (NASA), a C-54 to acquire oil spill data; JBF monitored the oil spill site from a Skymaster II.

Following a practice session on 1 November 1978, using a spill of Rhodamine WT dye, an oil spill was emplaced, on 2 and 3 November, by the ship R/V Annandale, operated by the Marine Science Consortium Inc. Buoys, dye markers and surface current cards were positioned in the vicinity of the oil slicks by the vessel Geo. B. Kelez, from the National Oceanographic and Atmospheric Administration (NOAA). A helicopter was used to apply dispersant to the oil, 110 minutes after the beginning of the spills.

1.2 PURPOSE

Since the time of the oil spills in November 1978, many researchers in the participating agencies have been working on reducing and analysing the vast amount of data collected. It was recognized that the multiple overflights with numerous types of sensors afforded a unique opportunity to compare the relative merits and limitations of these sensors. Therefore, NASA awarded a contract to Intera Environmental Consultants Ltd. (INTERA) to analyse certain data sets, with the purpose of:

1. correcting and calibrating the recorded data from some of the more promising sensors;
2. calculating oil/water contrasts;
3. geometrically rectifying and subsequently overlaying the data (or images) from certain sensors.

These goals were possible, within the confines of remotely sensed data, availability of supporting data, and data-set/time coincidence.

The physical basis for the remote detection of oil on water is referred to herein; however, a more direct and extensive treatment is available in the literature listed in the references. Because this report deals principally with the data recorded on the two CCRS aircraft, the reader is directed especially to the Report of the Arctic Marine Oilspill Program Remote Sensing Project (O'Neil et al., 1980a), which is regularly drawn upon here.

2. MISSION DESCRIPTION

2.1 SENSOR COMPLEMENT

Most of this analysis was conducted on a subset of the data gathered by the two CCRS aircraft on 2 and 3 November 1981, with additional and coincident data recorded by the NASA aircraft. The CCRS DC-3 (registration: C-GRSA) carried the following sensor complement:

* 2 Vinten 70-mm Cameras (Vinten)
  Multiple Detector Electro-Optical Imaging Scanner (MEIS)
  Optical Multi-channel Analyser (OMA)
  Miller Pieau Photometer (MPPH)
* Laser Fluorosensor Mk III (LFS)
  Low Light Level Television (LLLTV)
* Multispectral Scanner (MSS)
  Closed Circuit Television (CCTV)

while the CCRS CV-580 (registration: C-GRSC) was configured with:

  Closed Circuit Television (CCTV)
* Microwave Scatterometer (MS)
* ERIM Synthetic Aperture Radar (SAR)
* Dual-channel (ultraviolet and infrared) Line Scanner (DCLS)
* Wild Heerbrugg RC-10, 23-cm Camera (RC-10)
  Side-looking 35-mm Camera (35-mm).

In addition, each of these aircraft employed an airborne data acquisition system (ADAS), controlled by a mini-computer, for recording sensor, navigation and ancillary data. The data analyses required under this contract involved the sensors above that are marked with an asterisk.

The specifications for the instruments are given in Appendix A. For purposes of sensor cross-comparison, some of the data recorded by the Scanning Microwave Radiometer (SMR) and the Airborne Oceanographic Lidar (AOL), carried by the NASA aircraft, plus colour photography from the JBF overflights, were provided for this exercise by NASA Wallops Flight Center.

2.2 SORTIES

2.2.1 2 November

An oil spill took place between 16:53 and 16:55 GMT on 2 November 1978, at 40°08.4'N, 73°32'W. Murban crude oil (Abu Dahbi; 1666 litres) was emplaced by the Annandale, under clear skies and a surface wind of 6 to 7 knots at 240°. The oil formed an emulsion (O'Neil et al., 1980a) within a short time of the spill. An oil dispersant was applied to the oil slick between 18:50 and 19:15 GMT. The DC-3 made 25 passes over the oil between 17:14 and 18;24 GMT, from which three data sets (Passes 9, 21 and 24) were chosen for rigorous analysis.

The CV-580 made six passes over the spill, at 250 m altitude, between 16:56 and 17:14 GMT, recording data with the DCLS and the MS. A seventh pass was made at 17:39 GMT at 5.5 km altitude, with the DCLS operating. Thereafter, seven flight lines were flown with the SAR at 5.5 km altitude, between 17:53 and 19:17 GMT. Two of the lower-altitude passes (Passes 3 and 6) were analysed for the DCLS and MS data, as was Pass 2 (also labelled "C") of the SAR coverage. Detailed descriptions of all of the remotely sensed data utilized in this study are tabled in Appendix B.

2.2.2 3 November

On 3 November 1978, another controlled spill took place at 40°09.5'N, 73°35'W, between 15:14 and 15:18 GMT. The Annandale placed 1666 litres of La Rosa crude oil (Venezuela) on the ocean, under clear skies and a 10-knot wind at 060°. The heavier and darker La Rosa did not form an emulsion. The oil dispersant was added to the oil between 16:55 and 17:10 GMT. The CCRS DC-3 made a total of 29 passes between 15:41 and 18:20 GMT, of which four data sets (Passes 9, 14, 19 and 22) have been used in this study.

On the CV-580, the DCLS, RC-10 and MS were used during five passes over the spill, at an altitude of 250 m, between 15:17 and 15:31 GMT. One additional pass, at an altitude of 5.5 km, was made with the DCLS and the RC-10 in operation, at 15:44 GMT. From 15:56 to 17:32 GMT, nine more passes recorded SAR imagery over the slick. Pass 4B, made with the DCLS and MS, have been used in this study, and also Pass 5 (also labelled "F") with the SAR.

3. DATA REDUCTION AND ANALYSIS

The large and diverse array of sensors tested over the Wallops oil spill of 1978 was chosen to capture and record much of the known phenomena in the electromagnetic spectrum, by which oil could be detected on the sea surface. The sensors carried by the two CCRS aircraft on that occasion are listed in Appendix A, along with the technical specifications of the instruments chosen for rigorous analysis in this study.

Digital data reduction and analysis were conducted on the CCRS Image Analysis System (CIAS), a dedicated, interactive system, based on a PDP-11/70 computer, and also on the CCRS time-sharing PDP-10 computer. Some electro/optical/mechanical devices were used with analogue data formats, such as a reflecting projector and a zoom transfer scope.

3.1 MSS (REFLECTIVE BANDS)

3.1.1 Sensor and Data

The airborne MSS is an 11-channel, optical/mechanical line-scan spectrometer, which records emitted or reflected radiation. It has a 2.5-mrad, instantaneous field of view (IFOV), and on the oil spill mission of November 1978, was used at a scanning rate of 50 Hz. Calibrated reference sources within the instrument permit the absolute calibration of the recorded radiation. Only bands 2, 3, 4, 6, 8, 9, 10 and 11 were actively recorded for this mission, and sensor noise problems prevented the use of the data from band 9. S-bend correction was not applied during MSS data recording. High-density data tapes (HDDTs) of the MSS recording were converted to computer-compatible

tapes (CCTs). Each CCT, representing one MSS flight line, contained 716 pixels across track (representing the 85.9° field of view) and approximately 1000 lines along track, for all of the eight active bands. Radiometric resolution was 8 bits (0 to 255) per pixel, per band.

3.1.2 Radiometric Corrections and Calibration

To permit the comparison of oil/water contrasts among several flight lines and on different dates, it is necessary to reduce the recorded MSS data to absolute radiance units. To further eliminate the variability of the signal, which is due to non-target effects such as atmospheric path length, it is desirable to deal with upwelling radiance at the water surface.

The true spectral radiance N_λ , can be derived for any one spectral band, from the recorded digital signal S, by means of:

$$N_\lambda = \frac{S-D}{g \cdot R_\lambda} \tag{3.1}$$

where D is the dark offset, g is the gain setting, and R is the spectral responsivity.

The radiance recorded at the sensor can be broken into two main components:

$$N_\lambda = N_\lambda^t + N_\lambda^a \tag{3.2}$$

the target radiance N_λ^t , and the radiance that is scattered by the atmosphere into the field of view of the detector, N_λ^a . This latter term is called atmospheric "path radiance", and in general, increases as the path length from detector to target increases, but is also

dependent on the sun/detector look angle. The presence of the atmospheric path radiance complicates the interpretation of the final results, and distorts (reduces) the contrasts. Because N_λ^a varies with path length (hence, look angle and altitude), and with sun/detector angle (hence, flight direction), N_λ^a will be different for each flight line, but generally will remain constant for the relatively short (approximately 10 sec) interval of interest.

Path radiance was calculated for each flight line, and as a function of sensor look angle by subtracting the upwelling water radiance N_λ^w at the water surface (Personal Communication, Neville, 1981). N_λ^w was first derived for each of 2 and 3 November by performing a linear regression of average nadir radiances, against altitudes (which varied from approximately 500 ft to 3000 ft ASL), and extrapolating the regression line to the sea surface. The resulting water radiances for the active MSS bands are shown in Figure 3.1.A and 3.1.B for 2 and 3 November respectively. The dotted lines define the $\pm$ one standard deviation envelope. The single point in the UV is derived from the DCLS data.

Assuming that N_λ^w remains constant over the time interval of the flights for one day, and is constant over the look angles that cover the oil slick, the atmospheric path radiance term can be calculated by subtracting the N_λ^w constants from the average total radiance found over open water.

$$N_\lambda^a = \bar{N}_\lambda - N_\lambda^w \qquad (3.3)$$

The atmospheric path radiances at nadir for the seven MSS flight lines, which were thus calculated, are displayed graphically in Figure 3.1.C. Decreasing backscatter at the longer wavelengths may be observed on this graph, as well as the increased backscatter with increased path length. Note on this Figure (3.1.C) that flight 3/09 was flown at 2 X to 3.5 X greater altitude than the other six lines.

Path radiance as a function of look angle is described in Figures 3.1.D through 3.1.J, for the seven MSS data sets. The minimum N_λ^a for one band of one flight line is consistently near nadir, and increases with look angle (or atmospheric path length). The asymmetry of each of these seven graph sets is due to non-uniform sky illumination conditions, and varying detector/atmospheric-scatterer/sun angle. The last of these effects can be eliminated by flying directly into or out of the sun's azimuth; however, other flight logistics did not permit this.

It should also be noted that the above illumination geometry considerations also affect the earlier assumption that the water is of uniform radiance over the range of look angles viewed by the sensor. It is not possible, with the existing data set, to identify and separate the water radiance non-uniformity across the flight track. It is recognized, therefore, that oil/water contrast calculations should be done with both oil and water values extracted from similar look angle positions. The procedure described above is expected to produce first-order accuracies in radiance and contrast calculations, while non-uniformity of water radiance results in second-order contributions.

Another complicating factor is the presence of sun glitter in the scene. Wave facets with sufficient slope will reflect sunlight directly into the field of view of the detector. This results in increased radiance being recorded for specific pixels so influenced. Sun glitter often leads to saturation of individual pixels. Because the presence of oil reduces the wave slopes of the capillary waves, there generally will be less sun glitter on the oil slick than on the water; the effect is to reduce the total radiance from the oil as compared to the water.

The effects of sun glitter were reduced by a number of measures. First, the flight lines were chosen so that the angle between scanner look angle on either limit of the scan and the sun would be greater than approximately 60°. Second, the glitter-dominated pixels were screened out by replacing these pixels (which fell above a threshold intensity) with the corresponding pixel in the preceding scan line. Third, the calculation of mean water radiances was accomplished by constructing a histogram of a large number of water pixels, and then truncating the histogram limits to eliminate outlying values.

3.1.3 Geometric Correction

To present a geometrically accurate image of the oil spill scene from the MSS digital data, it is necessary to remove the geometric distortions introduced by the relative movements of the scanning system and the aircraft with respect to the earth's surface. One of the more serious distortions is caused by the scanning process of the MSS, which is at a constant angular rate. The effect of this on a (near-)flat target, such as the sea surface, is to produce the common "S-bend" curvature in the cross-track direction.

The provision for S-bend correction is in the MSS hardware, and is usually done in real time during data acquisition. This correction hardware was not activated during the Wallops oil spill mission. Consequently, S-bend distortions may be observed in some of the MSS scenes. Because the oil slick head is typically at near-nadir position on all MSS recordings, the oil slick head is least distorted, while the tail of the slick may be observed to "bend" on some scenes where the tail is located at large look angles (i.e., 3 November, Lines 19 and 22 [Plates F and G]).

The other significant distortion is that of non-square pixels. This effect is due to the fact that the aircraft ground speed was too high for the 50 Hz MSS scan rate and aircraft altitude for most flight lines, and therefore, could not produce contiguous imagery. Thus, the sample interval in the along-track direction L, and the cross-track direction p, produced a pixel aspect ratio F, not equal to one:

$$F = L/p \neq 1 \qquad (3.4)$$

For the seven MSS flight lines analysed, the value F ranges between 0.460 (oversampling) and 1.71 (undersampling) at nadir. Aspect ratio correction of the MSS (and DCLS) data was necessary to permit the overlay and comparison of other sensors' data. To avoid losing any data, the oversampled scenes were not line-decimated to correct for aspect ratio distortion; instead, the pixels were repeated in the cross-track direction by the factor F.

Using the same rationale for undersampled scenes, lines were repeated at a rate of F, to produce "square" imagery. The resulting corrected imagery displayed square pixels (or more correctly, equal sample intervals in orthogonal directions) between 0.848 m and 1.36 m on a side (see Table 3.1.A).

3.1.4 False-colour MSS Images

Most of the multi-sensor comparisons in this study involve the MSS. To provide a convenient, visual mode for these comparisons, photographic representations of the MSS scenes were prepared. Plates A through G depict the seven MSS images in false-colour assignment of three of the bands: MSS 3 = blue; MSS 4 = green; and MSS TIR (with an inverted radiance scale) = red. This particular combination was found to provide enhanced detail within the oil slick. The geometric characteristics of these scenes are described in Table 3.1.A.

Table 3.1.A. Geometry of MSS and DCLS false-colour images (aspect ratio correction applied)

Date/Line (November 1978)	Aspect Ratio Correction (F)	Square Pixel Size (metres)	Plate Number	Scale of Photo
MSS				
2/09	1.711	0.848	A	1:2856
2/21	1.166	1.26	B	1:4244
2/24	0.9160	1.28	C	1:4311
3/09	0.4597	1.36	D	1:4581
3/14	1.235	0.965	E	1:3251
3/19	1.123	1.07	F	1:3604
3/22	1.482	0.88	G	1:2964
DCLS				
2/03	3.675	0.360	H	1:1212
2/06	3.692	0.384	I	1:1294
3/4B	2.098	0.407	J	1:1371

The choice of scale and coverage is a compromise between facilitating profile and image overlays from other sensors and providing sufficient spatial detail of the oil slicks.

Selective contrast stretching was applied to each of the three bands of each MSS scene to further highlight detail in the oil slick. For additional enhancement of subtle radiometric detail, background noise reduction of speckle was necessary. Instead of applying the typical low-pass spatial filter, which would have resulted in degraded spatial resolution, a "saw-tooth" radiometric look-up table was used on each band. This process re-valued those water pixels with abnormally low or high intensities to brightness values in the range typified by neighbouring pixels.

3.1.5 Oil/Water Contrast

The relationship between oil thickness and oil reflectivity in the visible wavelengths, especially as it is exemplified in the Wallops oil spill data of 1978, was described by Neville et al. (1979), and by O'Neil, et al. (1980a). Their observations of the decreasing thickness of oil being imaged by decreasing wavelength bands is confirmed here, as well as the increased brightness of the emulsified Murban crude over the non-emulsified and more absorptive La Rosa crude.

The spectral radiance of the thickest part of the oil is described in the graphs of Figures 3.1.K and 3.1.L, for Murban and La Rosa crude respectively. The relative brightness and oil/water contrast of these two oils becomes more apparent in Figure 3.1.M, where the function:

$$K = \frac{N_\lambda^o - N_\lambda^w}{N_\lambda^o + N_\lambda^w} \qquad (3.5)$$

is applied to the absolute spectral radiances of the oil head (N^O) and the water (N^W_λ) at sea level. The non-emulsified, darker La Rosa oil appears darker (in the thickest oil regions) than the water in the 440-to-600-nm region, producing negative contrast. Outside of this wavelength region (at both shorter and longer wavelengths), the oil/water contrast (K) is positive. O'Neil, et al. (1980a) suggest that the cause of this phenomenon is the increased absorptivity of oil in the shorter wavelengths, which reduces the (upwelling) volume radiance of water beneath the oil. In the case of the emulsified Murban oil, the increased volume scattering of the oil/water emulsion dramatically increases the radiance in the shorter wavelengths. The thin regions of oil appear brighter than the surrounding water, due to the greater surface reflectance of oil throughout the UV to near-IR spectral region.

The pattern of contrast increase with longer wavelength is shown consistently from flight line to flight line, and even from one day to the next (Figure 3.1.M). The positive offset of the contrasts derived from the Murban oil, with respect to the La Rosa, may be explained by the above-described relationship of oil state versus radiance. The changing value of contrast (from negative to positive) across the reflective wavelengths suggests a means of spectrally "fingerprinting" an oil slick feature in a marine environment. In addition, the spectral function of contrast may provide a useful mechanism for identifying an emulsified oil.

3.1.6 Time History of Contrast

A study of the time dimension of oil/water contrast in Figures 3.1.N and 3.1.O reveals yet another useful phenomenon of radiance contrast which could be used for the detection and identification of surface oil slicks. For both oil types, there appears a simultaneous trend of increasing contrast with time at the oil head, at wavelengths greater than (approximately) 600 nm, with

decreasing contrast at wavelengths below 600 nm. Since these changes in contrast occur during a period when the sun elevation is decreasing, the cause of this temporal feature of oil/water contrast is more likely due to volume scattering effects, rather than surface reflection. The wavelength distinction between increasing and decreasing contrast may be the influence of the greater atmospheric path length as the solar elevation decreases. With longer atmospheric path, the illumination on the target decreases faster for the shorter wavelengths, which are more efficiently scattered out of the illumination path.

It still remains, then, to explain increasing contrast at long wavelengths, while the target is experiencing reducing illumination. Since the radiance of oil and of water (N^O; N^W) is decreasing, as is the sum of these two variables, the only manner in which the contrast (K) may increase is for N^W to decrease proportionately faster than N^O. This is quite likely, because oil is a more efficient backscattering target than water at longer (reflective) wavelengths.

Once the time history of oil/water contrast is better defined, it may become yet another dimension in which to detect and identify oil types. A temporal-spectral signature could be used to confirm the presence of oil on water, and if sufficiently refined, some basic categorization of oil types may be possible.

Since the oil/water contrast must eventually decrease, even at longer (reflective) wavelengths, it may be possible to use the maximum contrast achieved and its corresponding time point (or the shape of the contrast-time curve) to estimate the original spill time. This may be very useful information for oil spill legislation enforcement.

3.1.7 Spatial Variation of Contrast

The study of oil/water radiance contrast as it is distributed spatially is made particularly difficult by the lack of an easily defined reference frame, and by the intrusion of temporal effects. Some basic observations are still possible for the seven MSS data sets of the Wallops oil spill of 1978, presented herein (Figures 3.1.P through 3.1.V):

1. The oil/water contrast shows a general decrease at all wavelengths (400 to 950 nm), progressing away from the oil head for the Murban crude; the La Rosa crude maintains a reasonably constant contrast for the several-hundred-metre span analysed.

2. For both oils, the oil/water contrast becomes more uniform among the MSS bands, away from the oil head.

3. Some of the contrast perturbations shown at the slick edges may be indicative of thin-film interference effects.

3.1.8 Chromaticity Analysis

The study of the relative, rather than absolute, brightness of a target in the reflective bands permits the quantitative characterization of target "colour" in a simple manner. This technique has many applications, one of which, in a closely related discipline, offers the measurement of suspended sediment concentration by the chromaticity transformation of Landsat satellite data (Munday et al., 1979).

The chromaticity transform involves the radiance normalization of three MSS bands by:

$$x = N_i/(N_i + N_j + N_k) \tag{3.6}$$

and

$$y = N_j/(N_i + N_j + N_k) \tag{3.7}$$

where N_i, N_j and N_k are the (full-band) radiance values in three of the MSS bands. Here, bands 3, 6 and 8 were used in one combination, and 4, 6 and 8 in another combination. Only three MSS bands were used so that the resulting two dimensional chromaticity transform (x, y) could be presented easily. Note that the transform takes up one degree of freedom:

$$z = N_k/(N_i + N_j + N_k) = 1 - (x + y) \tag{3.8}$$

The choice of bands was made to span the available spectrum of MSS sensitivity, while choosing bands reasonably clear of noise.

Radiance data (at the sea surface), from varying distances from the oil head for each of the seven MSS lines, were transformed into chromaticity space for each of the two three-band combinations. The chromaticity plots are shown in Figures 3.1.W through 3.1.CC. In the chromaticity space described in these figures, the "colour" information apparent is that of colour hue and colour saturation. There is no brightness dimension. The point "E" at co-ordinates (x, y) = (0.333, 0.333) is the achromatic (non-coloured) point. Hue is defined by the angular variation about E, while saturation is represented as the radial distance from E.

On each of the chromaticity plots, the data point closest to E represents the oil head, with increasing distance from the oil head resulting in chromaticity co-ordinates farther and farther from E. The data point farthest from E on each graph represents transformed water radiances taken from that MSS flight line.

The obvious, yet surprising, observation to be made on each of the seven chromaticity plots is that the oil and water data are consistently colinear with E, and assume the same angular position about E. In chromaticity terms, that means that increasing the oil thickness results in:

1. no hue variation (thin oil, thick oil and water are the same "colour");
2. desaturation of colour (the thicker the oil, the more grey it appears).

It is perhaps even more intriguing that the MSS data from multiple flight lines, and even from different days, align themselves at the same angle (hue) about E. Whereas a comparison of absolute radiances or contrasts of the various MSS lines shows substantial differences, the chromaticity transform has removed these variations, and has reduced the data to a single dimension.

3.2 DCLS-UV

3.2.1 Sensor and Data

The DCLS is an optical/mechanical device for recording reflected or emitted energy. It is typically configured with an ultraviolet and a thermal infrared detector, which is a particularly useful combination for oil spill detection. The DCLS sweeps a 77.3° scan angle at a rate of 60 Hz. The IFOV for the UV detector is 5.5 mrad, and the spectral sensitivity is between 0.30 and 0.37 um. Additional technical specifications are given in Appendix A.

Three data sets (flight lines) were identified for analysis in this project: 2 November, Lines 3 and 6, and 3 November, Line 4B. These data sets are described in Appendix B. The DCLS-UV digital data were transcribed from HDDTs to CCTs. The imagery of 2/03 and 2/06 were S-bend corrected at this stage of conversion. Scene 3/4B was not S-bend corrected, due to data degradation in the original recording. As a result of the S-bend correction, the 2 November scenes contain 1024 pixels across track, while the 3 November scene contains the original 716 pixels. Radiometric resolution is 8 bits (0 to 255) per pixel.

3.2.2. Radiometric Corrections and Calibration

The same procedure was used for generating absolute radiances of the DCLS-UV data, as for the MSS visible bands (Equation 3.1). Since appropriate multi-altitude UV data were not available from the DCLS, the method of atmospheric path correction, as described for the MSS (Section 3.1.1), was not possible. Instead, the trends and constraints of several wavelength-dependent functions were extrapolated to the UV, to provide an iterative estimate of N. The functions used to derive these estimates were:

1. the McCluney single scattering model (McCluney, 1974);
2. spectral irradiance of sunlight outside of, and below, the atmosphere (Valley, 1965);
3. path radiance at nadir (Figure 3.1.C);
4. oil/water contrast (Figure 3.1.M);
5. oil radiance (Figures 3.1.K and 3.1.L).

Since this methodology was not as rigorous as that applied to the MSS data, oil and water UV radiances were extracted from near-nadir locations whenever possible. In addition, the interpretations of the UV data (to follow) are more cautious.

Sun glitter, which also influences DCLS-UV data, was treated as well. A low-pass video filter to smooth the speckled UV data, then histogram truncation to further eliminate data extremes were used. The resulting path radiance at nadir derived for 2 and 3 November, using the above techniques, extends the spectral curves of path radiance (from MSS data) in Figure 3.1.C into the UV.

3.2.3 Geometric Corrections

As was the case with the MSS, the need for visual presentation of UV scenes with geometric fidelity, as well as for allowing the overlay of data from other sensors, necessitates the geometric rectification of the DCLS digital data. As mentioned in section 3.2.1, S-bend correction was possible, through software, for the two flight lines (3 and 6) of 2 November, but not of the 3 November line (4B).

Aspect ratio correction was applied to each of the three DCLS data sets. As may be observed in the DCLS geometry data in Table 3.1.A, the correction factors were sizable and varied, due to the high degree of undersampling in the along-track direction.

3.2.4 False-Colour Composites

A false-colour representation of the UV and TIR DCLS data was constructed to provide convenient display of subtle oil slick features. The colour combination, which applies to all three of the DCLS scenes (Plates H, I and J), is: red = TIR, green = UV, and blue = UV (with an inverted radiance scale). The scenes in these three plates have been contrast-stretched, and the "saw tooth" transformation applied to

reduce noise. In addition, a low-pass video filter was used for smoothing speckle, because the larger image scale of the DCLS (over that of the MSS) could afford the loss in spatial resolution. The geometric characteristics of these scenes are listed in Table 3.1.A.

3.2.5 Oil/Water Contrast

The oil and water radiances derived from the UV band of the DCLS are listed in Table 3.2.A and included in the Figures 3.1.A, B, K and L. Although these radiances have been corrected for path radiance and sun glitter, the observations made by Neville et al. (1979) and O'Neil et al. (1980a) on UV radiances at the sensor still apply. The UV band gives excellent demarcation of the thinnest part of the slick, better than in any of the higher-wavelength visible bands. The outer (thinner) oil appears brighter in the UV than the thicker oil head. The darker, thick parts of the slick are still somewhat brighter than the clear water areas. This phenomenon occurs with both oil types, despite the emulsified state of one oil and not of the other.

The explanation offered is that while the presence of any thickness of oil increases the surface reflection component of the upwelling light, a thin oil layer allows the upward passage of the volume reflection of the water below. Conversely, a thick oil layer would absorb this volume reflection from the water.

These characteristics of UV absorption and reflectivity may be observed when transformed to oil/water radiance contrast. Figure 3.1.M shows the average oil head contrast with water in the UV, indicatin· that contrast is higher at both lower and higher wavelengths than the depressed contrast point around 500 nm. This makes the characteristic contrast fluctuation of oil as a function of wavelength an even more important identification feature of oil targets.

Table 3.2.A. DCLS-UV contrast of oil/water -- spot locations

Date/Line	Location In Slick *	UV Radiance ($W/m^2/\mu m/sr$)	Oil/Water Contrast (O-W)/(O+W)
2/03	H	0.769	0.261
	2	0.769	0.261
	3	0.877	0.321
	4	0.970	0.365
	E	0.778	0.266
	Water	0.451	
2/06	H	0.850	0.264
	2	0.898	0.290
	3	0.994	0.336
	4	1.108	0.383
	E	0.873	0.277
	Water	0.494	
3/4B	H	0.458	0.187
	2	0.463	0.192
	3	0.468	0.197
	4	0.473	0.202
	E	0.528	0.254
	Water	0.314	

* For coded locations in slick, see Figures 3.3.A through J. Codes H to E refer to progressively farther locations away from the oil head (= H), within the oil.

Oil/water contrast for discrete locations within each slick is also listed in Table 3.2.A. Positive contrast values are achieved throughout the slick for both the emulsified and non-emulsified oil. As might be expected, the brighter, outer edges of the slick show higher contrast with water than the darker, thick oil at the head. The better depiction of oil by the DCLS-UV imagery over the low-wavelength MSS bands can also be attributed partly to the higher signal-to-noise (S/N) ratio of the UV detector.

3.3 THERMAL INFRARED (MSS AND DCLS)

The measurement of emitted radiance in the thermal infrared (TIR) portion of the electromagnetic spectrum (4 to 20 μm) is a particularly useful mechanism for identifying oil targets in a marine environment. Besides providing an independent dimension of oil/water discrimination, it is one of the few spectral bands in which passive sensors can be used in darkness.

The complex mechanisms affecting the relative radiances of oil and water in the TIR band are well described in O'Neil et al. (1980a). The physical temperature and the emittance of the targets will define their relative radiation emission magnitudes. The emittance factor is influenced by such variables as thin film interference (constructive and destructive), surface reflectance, and bulk oil emissivity. These variables change in their impact on oil emittance, depending on the thickness of the oil layer.

3.3.1 Sensors and Data

Data from both the MSS and the DCLS thermal channels are presented here. Both instruments were operated with similar sensor characteristics of spectral band width, responsivity, spatial resolution and noise equivalent temperature (see Appendix A). In

Appendix B, the data sets from these two instruments are listed: seven flight lines for the MSS (three on 2 November; four on 3 November) and three flight lines for the DCLS (two on 2 November; one on 3 November). As was the case with the shorter wavelength data from these scanners, the digital TIR data were formatted onto CCTs, and contained an 8-bit radiance range per pixel.

3.3.2. Data Reduction and Calibration

The geometric corrections applied to the TIR data were identical to those applied to the shorter-wavelength bands. In the case of the MSS, this meant aspect ratio correction and no S-bend correction. For the DCLS data, aspect ratio correction was applied to each of the three scenes, and S-bend correction also for 2 November, Lines 3 and 6, but not for 3 November, Line 4B. Fortunately, this last scene contains the oil slick on nadir; also, the slick is oriented with its longitudinal axis parallel to the flight track, minimizing any distortions due to S-bend curvature.

Calibration of the TIR radiometry to absolute units of radiance, apparent temperature and physical temperature was conducted by multiple application of the Planck equation to the radiances recorded by the sensors. In this method (conversation with R. Neville, CCRS, July 1981) mean radiance and temperature were calculated for a small area of water near the oil slick, using an emissivity of water = 0.988 (mean value of emissivity for range 8.5 to 12.5 nm reported by Wolfe [1965]). Then, assuming that the physical temperature of the water near the edge of the slick will be equivalent to that of the thinnest oil just inside the slick boundary, the emissivity of the oil was calculated. A further assumption of equal oil emissivity throughout the oil slick was used to calculate the adjusted physical temperature of the oil. Coherent radiation interference effects (for thin oil films) were not considered here.

The results are presented in three formats. First, the false-colour photographic representations maintain and enhance the spatial and radiometric detail of the TIR radiation distribution (Plates A through G: MSS; Plates H through J: DCLS), albeit without a convenient reference to precise calibration. These (photographic) images have been selectively contrast-stretched and noise-filtered.

Second, the entire oil slick (head), as imaged in the TIR, is shown in Figures 3.3.A through G for the MSS, and in Figures 3.3.H through J for the DCLS. In these TIR images, the whole range of TIR radiance has been "sliced" into four sub-ranges, with each sub-range boundary identified in units of absolute radiance, apparent temperature and physical temperature. These sub-range limits are valid for the oil only; the mean radiance and temperature for water are defined in a different manner, due to the different emissivity of water. A nearest-neighbour theme filter, which considers both spatial and radiometric characteristics of a pixel "neighbourhood", was applied to smooth the thematic representation of TIR régimes within the oil.

Third, TIR data were extracted from discrete locations within the oil slick and in the open water. These "spot" locations are actually representative of the mean of a very small neighbourhood (3 by 3 pixels), to reduce speckle effects. The locations were chosen to give a good cross-section of oil thicknesses, and are identified by alphanumeric code on the grey maps of Figures 3.3.A through J. The radiometric values corresponding to the spot locations in the oil (H = oil head, 2, 3, 4; E = oil edge) were contrasted with that of the water (W), using the formula of Equation (3.5) and the resulting values of contrast plotted in Figure 3.3.K.

3.3.3 Data Analysis

There is a consistent trend of temperature variation in the TIR grey maps of Figures 3.3.A through J. Only the oil head is discriminated from the water by the TIR. In the thermal images of both the Merban and La Rosa crude oils, the brightest (warmest) areas are those in the centre of the oil head. The coldest regions are in an intermediate position in the oil head. The surrounding water is at a temperature between the two extremes of oil temperatures. There is a sharply increasing temperature gradient in the oil head, from the coldest to the warmest regions; at those locations in the gradient where the temperature of the oil is equivalent to that of the water, the grey maps show the same shade of grey for both oil and water. There is a more gradual temperature increase from the coldest oil regions to the edge of the oil head.

The relative emphasis of several physical processes for differential thicknesses provides the explanation for the increased and decreased temperature of the oil, with respect to the water (Neville et al., 1979; O'Neil et al., 1980a). The warmer region is predominantly influenced by the solar heating of optically thick oil, while for the cooler region, the lower emittance of the oil film is the more prominent influence.

The positive and negative contrast of oil and water is clearly shown for all MSS and DCLS TIR scenes in Figure 3.3.K. In this figure, the positive contrast at the brightest parts of the oil head (indicated by "H") is consistent from flight line to flight line, from Merban crude to La Rosa crude, and from sensor to sensor. Negative contrast with water is shown by other areas in the oil head, progressing to no constrast (equal brightness with water) at the edge of the oil slick.

The different ranges of contrasts shown by the MSS data and the DCLS data are probably due to system variability, rather than the environment. Therefore, the data sets from the two sensors should not be strictly compared. The locations in the oil head identified as "2, 3 and 4" are not intended to be (spatially) matched from one flight line to another; therefore, their respective contrasts are only roughly comparable.

Increasing flight line numbers on any one day for the sensor used, was analogous to increasing time. It became noticeable, then, that oil/water contrast was increasing over time. This is a definite trend for the brightest areas (H) in the oil head. There is also a suggestion of increasing negative contrast for the darker areas (2, 3, 4) in the oil slick. The explanation for the increasing contrast at the oil slick locations (H) can be derived from the observation that the water radiation is reasonably constant over the time interval of the observations, and that these optically thick patches of oil are subject to solar heating and, subsequently, thermal inertia. The time history of TIR oil/water contrast will be influenced primarily by oil thickness, solar elevation angle, and the original temperatures of the oil and water targets.

3.4 LASER FLUOROSENSOR

Fluorescence occurs when radiation-stimulated molecules drop from an excited state to the ground state and, in the process, emit an ultraviolet or visible light photon. It is practical to use fluorescence to detect and identify targets such as marine oil slicks, because few molecules found in the marine environment fluoresce strongly under 337 nm excitation, and those which do may exhibit a unique fluorescence spectrum. In a practical sense, fluorescence can be expected to discriminate oil from other marine substances and among major oil type groups (i.e., light, heavy, etc.) (O'Neil et al., 1980a). The use of fluorescence time decay analysis can further refine a fluorescence spectral fingerprint of an oil, since the decay rate of fluorescence radiation is again a characteristic identifier of oil type.

The irradiation of seawater at a specific wavelength will result in a small fraction of the backscattered light at a different, but predictable, wavelength; this is Raman scattering. The heavier oils will absorb much of the incident radiation, thus permitting a distinctive water Raman scattering suppression to: 1) identify heavier from lighter oils, and 2) measure the oil layer thickness. Because other substances will also produce this Raman suppression, the positive identification of an oil target will necessitate the use of its own fluorescence radiation spectrum (O'Neil et al., 1980a).

3.4.1 Sensor Description

The CCRS LSF operates by means of a pulsed nitrogen gas laser which emits UV radiation at 337-nm wavelength. The receiver is range-gated so that it will selectively identify only the short period of time during which the induced fluorescence is expected. Sixteen spectral channels in the UV and visible wavelengths identify the spectral nature of the return fluorescence radiation. The first channel is intended to detect water Raman scattering at 381 nm. The next 14 channels cover the visible range from 400 nm to 660 nm, at 20-nm intervals. The sixteenth channel is located at 685 nm, which is the mean wavelength of chlorophyll fluorescence emission. In addition to the sixteen spectral intensities being recorded, a variety of navigation and fluorosensor housekeeping data is also preserved, to permit precise track recovery, intercomparision of fluorosensor and other sensors' data, and absolute calibration of target fluorescent return. Technical specifications for the fluorosensor are listed in Appendix A, and further details are described in the paper by O'Neil et al. (1980b).

3.4.2 Data Analysis

Of the seven MSS data sets from the CCRS DC-3 that are analyzed herein (see Appendix B), six provide laser fluorosensor transects of the oil spill. The fluorescence return intensity for these

six flight lines is shown for all 16 spectral channels (corrected for altitude, receiver gain and laser power) in Figures 3.4.A through F. The abscissa in each of these graphs indicates the fluorosensor sample number; the sampling rate in all cases is 100 Hz.

It should be noted that the receiver gain on 3 November (Figures 3.4.D, E, F) was set higher than on 2 November. The result of this is that system noise is more appparent on the 3 November flight lines. The purpose of the higher gain setting, however, was to enhance the detectability of the La Rosa crude oil (3 November) with its lower fluorescence conversion efficiency (Buja-Bijunas et al., 1979; O'Neil et al., 1980b).

Except for the case of 2 November, Line 24 (Figure 3.4.C), where the ground trace of the fluorosensor did not cross the oil head, the Murban crude shows stronger fluorescence than the La Rosa, in all 15 visible spectral channels. The Raman scattering suppression in the 380-nm channel is more prominent on 3 November flight lines, also because of the higher receiver gain on that date, but probably also due to partial filling of the suppression feature by the higher Murban fluorescence on 2 November (O'Neil, 1980a, b).

The water Raman scattering suppression identifies a larger oil slick than does the spectral signature derived from the 15 visible wavelength channels. This is probably due to the effective two-way attenuation, by the oil layer, of the incoming fluorescence excitation radiation and of the upwelling Raman-scattered radiation. For the thicker oil régimes, the oil will reflect and absorb most of the incident (excitation) radiation, effectively preventing this radiation from penetrating through to the water; thus, water Raman scattering is practically eliminated. With thin oil layers, where penetration of the oil by incident radiation is significant, the upwelling water Raman

scattered radiation is still attenuated by reflection from two interfaces (water/oil and oil/air) and by absorption in the oil volume. Thus, water Raman scattering is effectively suppressed by oil films of 0.05 μm thickness or greater (Hoge and Swift, 1980).

Whereas the measurement of water Raman suppression can detect the presence of some surface substance, the fluorescence spectrum, as defined by the 16 spectral channels, can lead to an identification of that substance. The analysis method used for the identification of oil was the correlation technique described by Dagg (1979) and by Buja-Bijunas et al. (1979). The normalized fluorescence intensity in the 16 spectral channels is compared between the airborne fluorescence data and a standard spectrum, acquired in the laboratory (Buja-Bijunas et al., 1979; O'Neil et al., 1980b), using the correlation function:

$$P = \frac{N\Sigma X_i Y_i - \Sigma X_i \Sigma Y_i}{\left[N\Sigma X_i^2 - (\Sigma X_i)^2\right]^{1/2}\left[N\Sigma Y_i^2 - (\Sigma Y_i)^2\right]^{1/2}} \qquad (3.9)$$

where X_i and Y_i are the fluorescence intensities in the "ith" of 16 spectral channels, as measured in flight and the laboratory respectively. The laboratory reference spectra for Murban and La Rosa crude oils are shown in Figure 3.4.G.

After passing the appropriate reference spectrum across the flight data, the resulting correlations are plotted in Figure 3.4.H, along with the original 500-nm fluorescence channel. A good "match" between the flight and laboratory spectra is indicative of oil having been identified. This correlation process is dependent on the normalized fluorescent intensities (shape of the spectral reflectance curve) in the N channels where N equals 16, instead of the radiation magnitude (curve amplitude); therefore, the weaker fluorescence is also successfully "fingerprinted". Thus, the oil of lower fluorescence efficiency can be well identified, as can thin oil films.

An example of the first case may be observed in Figure 3.4.M, wherein the 500-nm spectral channel does not provide any distinction between oil and water, yet the correlation plot gives a clear statement of the identification of the La Rosa oil. For the second case, Figure 3.4.I shows that the correlation analysis produces a more extended oil slick than does the single (500 nm) spectral channel. O'Neil et al. (1980b) also point out that strongly fluorescing anomalies may be identified as oil targets, using the normal spectral channels, whereas correlation analysis can eliminate these false targets.

A further clarification of the identification of an oil target is provided by a stretching function, applied to the normal (RHO) correlation:

$$PHI = 10^{RHO} \qquad (3.10)$$

which enhances strong positive correlation. In Figures 3.4.N through S, PHI correlations show more distinctive oil targets than their RHO counterparts.

The spectral sensitivity of the correlation technique was tested on two data sets: 2 November, Line 9 (Murban); and 3 November, Line 14 (La Rosa). The Murban crude oil fluorescence spectrum, obtained in flight, was correlated with the laboratory spectrum of La Rosa crude; the La Rosa airborne spectrum was correlated with the Murban laboratory spectrum. The results of the former correlation are shown in Figure 3.4.T, and of the latter, in Figure 3.4.U. These cross-correlations indicate that there is sufficient confusion between the two spectra, and that the shapes of the fluorescence spectra cannot be used alone to differentiate between these two oil types, under these conditions. Discrimination would be successful, however, if the absolute amplitude of the fluorescent radiation were taken into account (since the two oils have fluorescence conversion efficiencies which

vary by a factor of 10). O'Neil et al. (1980b) conclude, from similar cross-correlation tests with these two oils, Rhodamine WT dye, and oils from other groups, that this fluorescence data and analysis process is a viable means of identifying oils from the major oil groups and of removing false targets.

3.5 MICROWAVE SCATTEROMETER

The appearance of an oil slick on the sea surface, as represented on a radar image, is manifested by the reduction of the radar cross-section, σ_o, of the ocean. Thus, an oil slick will be recorded as a darker and smoother region than the typical sea clutter in a microwave radar image. The reduction in microwave backscatter is due to the damping of ocean capillary waves which, under normal conditions, act as strong reflectors of the similar-wavelength microwaves. The damping effect of the capillary waves by the oil layer on the water surface is described by van Kuilenberg (1975) as the interference by the oil membrane of the air-water interface and mechanical damping by the oil layer.

3.5.1 Sensor

The CCRS Ryan scatterometer, which was used on the Wallops oil spill mission, operates at 13.3 GHz (Ku band; 2.25 cm). It is not an imaging radar, but uses a continuously radiating 60° fan beam (fore and aft) to characterize the radar reflectivity of targets below the aircraft. The fan beam has a cross-track spread of 3°, and is sampled in the along-track direction by means of the Doppler effect (frequency change) on the backscattered radiation. Either vertical (V) or horizontal (H) polarization may be transmitted, and both H and V polarizations can be received simultaneously. Thus, this instrument is able to characterize the reflective microwave signature of targets by

their influence in the look-angle domain, and with respect to signal polarization, although it is limited to a single radar frequency. Technical specifications for the scatterometer are listed in Appendix A, and in Gray et al. (1979).

3.5.2 Data Acquired

Of the 10 scatterometer data sets acquired over the Wallops oil spills, only three were found to be sufficiently on target. These three, fortunately, covered both (H and V) transmit polarizations and experienced uniform sea-surface windspeeds of 4 to 5 m/s (7 to 10 knots). Altitudes ranged between 232 and 274 m (760 to 900 ft), resulting in nominal scatterometer nadir footprints of 19 by 13 m (along-track by across-track). At 60° look angle, the across-track dimension of the footprint is twice that at nadir. The three flight lines processed were the same as those analysed for the DCLS (see Appendix B): 2 November, Lines 3 and 6; and 3 November, Line 4B.

Data degradation from aircraft motion is a possible influence on the results presented here; however, their magnitude is uncertain, due to the unavailability of the inertial navigation data for 2 November 1978. Pitch variations will cause mis-calibration of the backscatter data, when applying antenna pattern gain correction, especially at the extremes of the incidence angle range. As well, aircraft drift will produce spatial de-correlation of the ground footprints of the scatterometer, because the illuminating fan beam traverses the target at an angle to the aircraft motion (Gray et al., 1979).

3.5.3 Data Analysis

The original scatterometer data were first digitized onto CCTs to facilitate subsequent manipulation by computer. The data were then calibrated to absolute radar cross-section by applying the

internal calibration signal and antenna pattern of the scatterometer (Gray et al., 1979). To provide a convenient display of target/background contrast, the next step involved the subtraction of average sea backscatter. The resulting time histories of normalized backscatter for six of the look angles are displayed in Figures 3.5.A through L. The oil feature is shown consistently to be a depression of the radar backscatter of the ocean. The backscatter depression increases with greater look angle (to a maximum of approximately 10 dB, at 55°, then decreases, but does not appear to be influenced by polarization mode. A ship within the scatterometer coverage swath produces a bright return. This may be seen in Figures 3.5.A, B, C and D. Flight Line 4B on 3 November contains a complex radar backscatter signature of ship and oil (Figures 3.5.I, J, K and L).

In Figures 3.5.M through R, a quasi-image of backscatter intensity is constructed on time and look-angle axes. Backscatter intensity is coded as grey level, to present a convenient observation of targets in an ocean-clutter background. A thorough discussion of these scatterometer data sets is given by Hawkins et al. (1979), and also in O'Neil et al. (1980a).

3.6 SYNTHETIC APERTURE RADAR

Like the microwave scatterometer, SAR depends on suppression of capillary waves by an oil film to detect the presence of an oil slick. The suppression leads to a reduction in the radar cross-section of the ocean (sea clutter). Of course, non-oil targets that also suppress capillary waves will not be separable from true oil slicks, using only SAR data. The main advantages of SAR for detecting oil slicks lie in its ability to image the sea surface in day or night, and under most weather conditions. Also, this sensor offers high spatial and radiometric resolution, and wide-swath coverage.

3.6.1 Sensor and Data

The ERIM SAR was flown on the CCRS CV-580 in the Wallops oil spill mission of November 1978. It is a four-channel SAR, operating in both X (9.350 GHz) and L (1.315 GHz) bands, with either horizontal (H) or vertical (V) transmit polarization, and both like- and cross-receive polarization modes. During this mission, the SAR operated with HH and HV (transmit/receive polarizations. The 5.7 km slant range produced a nominal swath width of 8 km, resulting in a variation of incidence angles for the oil of 40° to 42° (Pass 2 on November 2) and 40° to 47° (Pass 5 on November 3) (H. Maurer, NASA, personal communication, 26 January 1982).

Early evaluation of the four-channel data (Hawkins et al., 1979) indicated that the X-band HH-polarization (X-HH) images were superior to the other polarization and band combinations. Thus, ERIM processed the signal film on their optical correlator/image dissector, and converted the imagery to digital format. Two scenes were so digitized: Pass 2, Line C, 2 November; and Pass 5, Line F, 3 November. Each digitized scene of one SAR channel (X-HH) contained 2560 lines of 2560 pixels, on an 8-bit (0 to 255) linear radiometric scale. Initial study of the photographic records of these scenes by Hawkins et al. (1979) identifies the pertinent environmental and sensor features.

3.6.2 Radiometric Corrections

To present a SAR image that shows backscatter intensity variations which are indicative of target reflectivity, it is necessary to 1) remove the contribution of the antenna power pattern, and 2) correct for the slant range R^3 attenuation law. The CCRS radar preprocessing software (Teillet et al., 1979) was used to correct the original SAR data provided by ERIM through NASA Wallops. ERIM was also the source (letter, dated May 1981, from W. Croswell, NASA Langley) of the vertical plane, antenna power pattern. The antenna pattern was converted to weighting factors at 1° angular increments about the principal axis of the antenna, prior to application to the SAR images.

Following the radiometric correction of the original data, the transformed data set was converted to the commonly used dB scale by means of:

$$dB = 10 \log (I_2/I_1) \qquad (3.11)$$

where I_1, and I_2 are radar backscatter intensities. The dB scale provides a relative calibration of intensities for either SAR image.

3.6.3 Geometric Correction

The original digital SAR image provided by NASA contained a pixel matrix in the slant-range/azimuth plane, with a sampling interval of 1.5 m in both slant-range and azimuth directions. To facilitate inter-sensor comparisons of data, this image geometry had to be rectified to fit a plane, parallel to the Earth's surface.

Once again, the CCRS radar-preprocessing software (Teillet et al., 1979) was employed to transform the slant-range image into a ground-range image. The geometric transformation also provided the mechanism for pixel averaging and resulted in (transformed) pixels that were larger than the original pixels, and which had equal (azimuth- and ground-range) dimensions.

3.6.4 Data Analysis

Once the SAR image data had been radiometrically and geometrically corrected, further data reduction was performed to facilitate analysis. The backscatter intensity range was divided into four subsets for 2 November, Pass 2, and three subsets for 3 November, Pass 5, to permit a simple, visual distinction of the oil slick from its open ocean background, and of the brightness features within the oil slick. Figure 3.6.A shows the 2 November, Pass 2, SAR X-HH image of the slick in this manner, with minimum loss of spatial detail. In Figure 3.6.B, the same scene has been intensively smoothed, using several passes of a nearest-neighbour theme filter. This process provides a reduced mapping scale, with its attendant loss of spatial resolution; however, it also generates a great reduction in radar "speckle" effects, which is a masking noise for visual analysis of gross features.

These two figures (3.6.A and B) represent the Murban oil spill of 2 November, and show an oil slick with the anticipated backscatter depression, relative to normal sea clutter. As well, there are several brightness régimes within the oil slick. The lowest backscatter intensity is found in a swath, corresponding to the longitudinal axis of the slick, with a width equal to one-third to one-half of the width of the whole slick. This is probably because at the slick edges, capillary wave suppression by the oil film is incomplete, whereas further into the slick, the travelling capillary waves have experienced the cumulative effect of amplitude suppression over a longer period of time. Also, it is likely that the oil film is less continuous at the edges, permitting surface wind enhancement of the capillary waves at breaks in the oil film. There are also bright (backscatter) features within the oil slick; this phenomenon is discussed in Section 4.4.

The SAR image of 3 November, Pass 5 is shown in a similar manner in Figures 3.6.C and 3.6.D (smoothed). This image is more troublesome to analyse, due to the extra complication of the appearance of a helicopter, in the process of applying the oil dispersant. This "artifact" is the apparent discontinuity of the oil slick, located about two-thirds from the bottom of the scene. Considering only the other areas of this oil slick, away from the helicopter location, the same pattern of backscatter intensity distribution takes place, as was observed for the Murban crude slick of 2 November. Again, the greatest backscatter depression is found along the longitudinal axis of the oil slick, ringed by increasing backscatter intensity away from this axis, until the brightness of the surrounding sea clutter is reached.

To better demonstrate the finer detail of the spatial variability of the backscatter intensity, a profile transect of each of the two SAR scenes is displayed in Figure 3.6.E (Murban) and 3.6.F (La Rosa). The high (spatial) frequency of backscatter intensity variations, which is sea clutter, is evident in the open water. The smoother, darker oil slick is in obvious contrast to the water on these profiles. The two-dimensional version of the backscatter profile is given in Figure 3.6.G for the 2 November scene, and in Figure 3.6.H for the 3 November scene. The vertical axis in each of these two graphs is a dB scale of radar backscatter, inverted, to better expose the oil slick feature. The oil (shaded area on graphs) areas exhibit their two characteristics: depressed radar backscatter intensity and lower intensity-variance.

To quantify variables that may permit the (automatic) detection of oil in a marine environment by means of radar, each of the oil and water features was identified on the X-HH SAR digital images, and statistics were collected in the form of radar backscatter histograms. In Figures 3.6.I and 3.6.J, the oil data histogram is shown on a backscatter (dB) scale, overlaid with the outline of the water data

histogram. Obvious in these histograms are the differences in both the histogram mean, which defines the mean backscatter intensity for oil and water, and the standard deviation of the histogram, which gives a description of the magnitude of the variations found within the oil or water feature. The data for 2 and 3 November are in close agreement; that is, the oil slicks show a suppression of the sea clutter by approximately 3-dB, and the oil regions are "smoother" by about a 2-dB reduction in the standard deviation of the backscatter.

The mechanism by which these two characteristics of oil and seawater may be employed in an oil target identification algorithm is shown, in simplified form, in Figure 3.6.K. It is suggested that a decision rule or threshold, which would identify a slick feature on radar imagery, should simultaneously use both criteria of backscatter mean and variance depression, to reduce the frequency of occurrence of false targets. The relationship of return signal strength and its variance, independent of target characteristics, must, however, be taken into account.

4. SENSOR COMPARISONS

One of the principal objectives of this project is the intercomparison of oil spill imagery. By overlaying or correlating the data from two different sensors, a better understanding of the features recorded by each may be realized. In addition, the successful measure of some oil parameter (e.g., thickness) by one sensor can be correlated to the recorded radiation of another sensor.

These intercomparisons are very difficult for a number of reasons. Precise geometric rectification is essential to relate an image element from one sensor to that of another. The great variance of sensor-operation geometry complicates the process of accurate multi-sensor overlay. Whenever the sensors being compared are carried on different aircraft, the time skew of the resulting images adds distortions that are irrevocable. In many of the sensor comparisons, there exists some temporal difference. The data sets have been chosen to minimize this time-distortion. In the case of SAR/MS/SMR comparison, the imaging time differences among the data sets identified for this project were too large (30 to 115 minutes) to allow any useful data comparisons. For the sensor comparisons described below, the temporal variations are smaller, but still contribute to correlation noise.

4.1 MSS/FLUOROSENSOR COMPARISON

To compare the data from the MSS and the LFS, the footprint of the LFS was identified on the Vinten photography (conversation with R. Neville, CCRS, June 1981), and from there, transferred to the MSS imagery. The data comparison is made in three ways:

1. LFS (PHI) correlation profiles have been constructed to match the scale and timing of the MSS scenes on Plates A, B, C, E, F and G. The LFS profiles are on overlays in Figures 4.1.A, C, E, F, H and J respectively.

2. The LFS correlation profiles can also be compared to radiance profiles for MSS Bands 4 and TIR, in Figures 4.1.B, D, G, I and K. These MSS profiles are in a similar graphical form to the LFS profiles, and thus, facilitate inter-comparison.

3. MSS TIR apparent temperatures and Band 4 radiances are individually compared to LFS (PHI) correlations in scattergram plots, shown in Figures 4.1.L through W. Any relationships between these data types are exposed most easily in this format.

Due to its operating characteristics and interaction with the oil and water targets, the LFS has been identified (O'Neil et al., 1980a) as the prime sensor for oil spill detection in Canadian waters; however, the performance of this sensor at the Wallops oil spill exercise, as shown in Figures 4.1.A through W, is less than anticipated. One of the reasons for this reduced level of expected performance is that the flights were conducted during near-peak illumination levels at midday, in consideration of many of the other (passive) sensors. The LFS would show better S/N characteristics if flown at night, or at least dawn or dusk. The fluorescence "noise" is due in part to the fluorescence evoked by natural (solar) excitation, but mostly due to system (sensor) noise.

It may be observed from these data sets that the LFS detects thicker oil better (i.e., with greater correlation accuracy) than thinner oil. Thus, the fluoroscence spectrum of the oil is more precisely defined by the increased radiance received from a larger volume (depth) of oil, which also masks more efficiently the interfering fluorescence spectrum of the underlying water.

MSS Band 4 "sees" more of the oil slick area than does the LFS. The MSS TIR band shows oil/water contrast about as well or perhaps slightly better than the LFS. The relative oil detection capability of the LFS over these MSS bands would probably improve significantly under lower (natural) illumination conditions.

The scattergram plots (Figures 4.1.L through 4.1.W) show a detectable relationship between MSS (Band 4 and TIR) response and fluorescence correlation for some of the flight lines. A strong correlation is not observable because:
1) the fluorescence and MSS data are not linearly related, and
2) there is a suspicion of a negative temporal offset of the LFS data with respect to the MSS data (less than 1 sec), which has not been explained, but which could substantially de-correlate the data sets, since the strong fluorescence feature is 1 second or less in size.

4.2 MSS/AOL COMPARISON

The Airborne Oceanographic Lidar (AOL) operated by NASA Wallops staff, is a scanning laser radar system, used with nitrogen gas to provide an output wavelength of 337.1 nm. The incoming spectral radiation, from 350 to 800 nm wavelengths, is received by 40 detectors. Background ambient radiation is removed by monitoring non-laser-induced radiation, and subtracting it from target fluoroscence radiation. Further system description details are contained in Hoge and Swift (1980).

The AOL data reduction uses the measurement of water Raman scattering suppression by the oil to arrive at an estimate of oil thickness. In the case of the Wallops oil spill exercise, the range of oil film thickness effectively measured was from 0.05 to 5 μm (Hoge and Swift, 1980).

Oil thickness data, derived from the AOL measurements, were provided for this project by NASA Wallops Flight Center. Oil thickness profile transects, as well as two-dimensional contour plots were made available. The oil thickness resolution of the original contour plots was 0.5 μm, and ranged between 1 and 4 μm oil thickness. The contour locations are based on (resampled) 1 m pixels, and the swath of AOL coverage (on the water surface) was 30 m.

With the intent of comparing AOL oil thickness values with MSS data, the AOL contour plots were scaled to match the MSS scenes used herein. With the aid of the JBF photography (also supplied by NASA Wallops), the AOL oil thickness plots were located and oriented with respect to the oil slick in the MSS scenes. Of necessity, due to the small size of the resulting AOL contour plots, the contour interval was reduced to 1 μm.

AOL Pass 12 is shown in Figure 4.2.A, and was recorded 4.3 minutes after MSS Line 14 on 3 November (Plate E). AOL Pass 15 in Figure 4.2.B was 1.1 minutes ahead of MSS Line 19 on 3 November (Plate F). Figure 4.2.C shows AOL Pass 18, acquired 1.8 minutes after MSS Pass 22 on 3 November (Plate G).

Quantitative assessments of the relationship between AOL-derived oil thickness and radiance in MSS Bands 4 and TIR are given in the scattergram plots of Figures 4.2.D through I. These scattergrams are not conclusive, due to de-correlation from MSS-derived noise, AOL-derived noise and the additional noise of data mismatch. The fact that oil thickness versus MSS radiance is a double-valued function is a further disturbance to an "elegant" relationship. It may be observed, however, that the (approximately) 4-μm range of oil thickness, as derived from AOL data, corresponds to a radiance range of 2. $W/m^2/\mu m/sr$ in MSS Band 4, and 0.3 $W/m^2/\mu m/sr$ in the TIR band.

An evaluation of the graphical overlay of the AOL oil contours on the MSS photographic images shows, on each of the three comparisons provided, that some gross features of radiance and oil thickness do match. It may be noted, for instance, that the 1 μm oil contour from the AOL has reasonably good agreement with the oil slick edge as observed in the TIR. Also, the thickest oil defined by the AOL occurs more or less consistently within the "warmest" regions, as mapped by the TIR band. Finer detail correspondence, however, is elusive.

4.3 SCANNING MICROWAVE RADIOMETER

During the Wallops controlled oil spill exercise, the NASA Langley Research Center operated a dual-channel (22 and 31 GHz) imaging microwave radiometer from the NASA C-54 aircraft. This radiometer was developed and tested by the Naval Research Laboratory, Washington, D.C.

This radiometer measures microwave brightness temperature, which is then converted to oil thickness estimation (Croswell et al., 1981). Two frequencies were used to eliminate ambiguities arising from "alias" oil thickness measurements at a single microwave frequency (O'Neil et al., 1980a). The background sea temperature is measured at all incidence angles, then subtracted from the oil slick image data, to eliminate bias, polarization and incidence angle effects.

Oil thickness contours, derived from microwave radiometer images of the oil slick, were provided by NASA Wallops. The radiometer data is limited in its definition of the distribution of the oil slick, due to its (nominal) spatial resolution of 10 m; its oil thickness discrimination has a (lower) threshold of 100 μm. These limitations, in combination with the relatively small size of the spills of 2 and 3 November, somewhat restrict the applicability of this data set.

Three comparisons of radiometer-derived oil thickness with MSS imagery are presented: radiometer Pass 17 (Figure 4.3.A) registers with MSS Line 19 (Plate F); radiometer Pass 17 (Figure 4.3.B) registers with MSS Line 22 (Plate G); and radiometer Pass 18 (Figure 4.3.C) registers with MSS Line 22 (Plate G). The time variance between the radiometer and MSS coverages are, respectively: +8.5 min, -2.4 min, and +1.8 min.

There is general agreement in the depiction of the oil spill head by the radiometer and the MSS, as permitted by the 10x difference in spatial resolution. The outermost oil thickness contour (0.1 mm) defines a slightly smaller part of the oil head than does the MSS TIR band, which is estimated, however, to resolve oil thickness to a minimum level of 2 μm (O'Neil et al., 1980a).

The radiometer and the AOL were configured in these experiments in such a way as to have oil-thickness-resolving characteristics, exclusive in range. Thus, the AOL resolved oil thickness $\leq$ 10 μm while the radiometer resolved oil thickness 100 um (Croswell et al., 1981). Yet, the oil thickness contour plots from these two data sets are not mutually exclusive, but show substantial overlap. The reason for this is partly due to the relatively large footprint of the radiometer, which results in much averaging of radiance within a pixel. The non-linear relationship between emitted microwave radiance and oil thickness will subsequently lead to increased error in oil thickness estimation for those pixels with greater spatial heterogeneity of radiance.

It is apparent that the radiometer defines an oil thickness distribution with a fall-off for the oil head more gently sloping upwind than downwind. This is a particularly interesting feature of the oil being "pushed" by the wind and the radiometer is the only sensor showing this phenomenon.

The quantitative comparison of radiometer-derived oil thickness and MSS radiance in Bands 4 and TIR are given in Figures 4.3.D through I. The relationships here are somewhat more definitive than were the MSS/AOL comparisons. Although once again, the relationship is double-valued and suffers from several sources of de-correlation noise, it may be observed that:

1. maximum MSS 4 radiance corresponds to the minimum oil thickness (as defined by the radiometer);
2. maximum MSS TIR radiance corresponds to the maximum oil thickness;
3. minimum MSS TIR radiance occurs for an oil thickness of approximately 0.2 mm.

The range of oil thicknesses defined by the microwave radiometer extends from 0.1 to 0.5 mm, which corresponds to a radiance interval of approximately 2.0 ($W/m^2/\mu m/sr$) for the MSS Band 4, and 0.3 ($W/m^2/\mu m/sr$) or 2.3 K° for the MSS TIR.

4.4 MSS/SAR COMPARISON

The geometric rectification of the SAR images permitted their overlay with other data sets. The SAR X-HH image of 2 November, Line 2 was scaled to match the MSS scene of Line 21, because this SAR image was unencumbered with helicopter/dispersant interference. The SAR scene was recorded 5.6 minutes before the MSS pass. Two forms of data comparison were constructed: backscatter intensity contour map and profiles.

In Figure 4.4.A, the thematic map of backscatter intensity was contoured to show the best dB discrimination level between sea clutter and its suppression by the oil layer. The contour line in this figure represents (approximately) 18 dB, with the surrrounding sea clutter being greater that 18 dB. Inside the contour line, the oil slick is below 18 dB in backscatter intensity, except for small,

discrete areas (outlined) where also, the radar echo is above 18 dB. There is strong agreement in spatial coincidence of these "bright" areas inside the oil slick, on the SAR image, and the thickest areas in the oil head, as observed in the MSS image. The MSS image verifies a contiguous oil film at these anomalous locations, precluding the possibility of small areas of bright sea clutter in the oil head. It is not known whether these features are due to system or environmental phenomena.

The backscatter profiles on Figures 4.4.B and C indicate the degree of backscatter suppression on a (continuous) dB scale. One of the bright radar anomalies is shown to be as strong a radar reflection as is sea clutter. On these SAR profiles, the boundary between sea clutter and the suppression by the oil slick is obvious, and matches well the slick edge as best defined by the MSS (Band 3). The backscatter suppression, however, is equally strong in both thick and thin oil regions (excluding consideration of the bright anomalies). These two observations suggest that radar is best applied to search and detection of spills, rather than to thickness measurement or identification of type. The radar profile graphs also indicate that where the slick edge is not abrupt, but discontinuous, the backscatter suppression feature on radar is lost in the intervening sea clutter, despite the radar's fine spatial resolution. This would indicate that radar sensing would become less effective with increasing age of spill, presuming that, with time, the slick would become less cohesive.

4.5 DCLS/SCATTEROMETER COMPARISON

The DCLS and MS were both carried on the CV-580, facilitating the comparison of these two data sets. Most of the mismatch of scatterometer profiles on DCLS imagery can probably be attributed to angular differences between aircraft heading and ground track, or to uncertainty of this flight parameter.

Backscatter intensity profiles from the MS have been scaled and oriented with respect to DCLS imagery (Plates H, I and J) in Figures 4.5.A through F. Three representative look angles (shallow, medium and steep) for each of the fore and aft beams are displayed along with the ground-track reference line. These overlay profiles and the DCLS images indicate that the backscatter depression in the MS data is responsive to the whole oil slick, as defined by the DCLS-UV band. This is the case with each of these look angles, although the steeper look angles produce more intensive suppression of the scatterometer return.

Scattergram plots of MS backscatter intensity versus UV and TIR radiance are presented in Figures 4.5.G through R. The poor expression of any relationship between the MS and DCLS data is due in great part to the large scatterometer footprint (or conversely, the small oil slick size), which limitation is most aggravated for the larger look angles. The area of oil depicted by the TIR band is smaller than that in the UV, resulting in no appreciable correlation between MS and DCLS TIR data. In the UV/MS scattergrams, however, there is a consistently detectable trend of decreasing backscatter intensity with increasing UV radiance. This relationship, which is supported by theory but is quite subtle in these figures, is due in most part to the UV brightness difference between oil and water. Brightness variations within the oil slick itself have not contributed to the observed trend in these data sets. For a UV radiance range of (typically) 0.2 - 1.0 $W/m^2/\mu m/sr$, the corresponding MS backscatter intensity range (with sea-clutter background removed) is approximately -4 to +2 dB.

5. CONCLUSIONS

Each of the sensors used in this study has some capabilities and characteristic limitations for oil slick detection and measurement. When used in an orchestrated manner, however, multi-sensor coverage can exhibit a synergism, due to the independent verification of oil targets by complementary sensors. Additionally, the capabilities of one sensor can offset the limitations of another.

To date, the intercomparison of data from differing sensors is a difficult task, which is hampered further when the sensors are carried on different aircraft. Future tests of multi-sensor oil spill mapping must give substantial consideration for geometric and time referencing among sensors. Much additional experimentation and development is required before multi-sensor data can be routinely overlaid and analysed in combination, in real time, which would be an ideal monitoring scheme.

The following are the summary findings of this study with respect to the various modes of oil spill monitoring:

1. OIL DETECTION — All of the sensors investigated herein have some abilities for oil spill detection in a marine environment. The imaging sensors are, of course, more practical when the requirement is for search and detection, due to their greater areal coverage. High-resolution radar is probably the most effective for use over an open ocean, due to its independence from (natural) illumination conditions and from most adverse weather situations, and also because of its wide imaging swath. The optimum sensor for a particular situation will depend on the environmental conditions on site (haze, fog, sea state, etc.).

2. AREAL EXTENT AND DISTRIBUTION — All imaging sensors described in this study will provide a map of oil slick spatial distribution (within their respective capabilities for contrasting oil with water and for spatial resolution). The better instruments for this task would be a camera or scanner, recording in the UV or blue spectral band. The compromise between these two options is related to the higher geometric fidelity and spatial resolution of the camera system, versus the higher dynamic range and generally greater flexibility of digital scanner data.

3. OIL THICKNESS MEASUREMENT — The dual-channel (UV and TIR) line scanner provides a basic but effective distinction between thin and thick oil films. A (dual-frequency) microwave radiometer can generate a more refined thickness measurement, for oil films of thickness $\geq$100 μm. The most promising sensor for measuring thin films is the laser fluorosensor, with its ability to use water Raman scattering suppression by the overlying oil to measure thickness $\leq$10 μm.

4. OIL IDENTIFICATION — The laser fluorosensor is pre-eminent among remote sensing devices for oil identification. This ability extends to both the identification of oil apart from other marine phenomena, as well as the categorization of basic oil types. The basic reason for the aptitude of the LFS is due to its measurement of several independent variables, such as fluorescence conversion efficiency, fluorescence decay history and fluorescent radiation over numerous spectral bands.

6. RECOMMENDATIONS

1. It is recommended that studies be conducted of the time history of oil/water contrast, particularly for passive sensors. The study of oil and water radiances in the time domain is difficult logistically, and also due to the interfering influence of environmental variables. Nevertheless, the definition of radiance as a function of time is a potentially valuable tool for target indentification and the determination of the time of spilling.

2. The chromaticity technique for multi-spectral data analysis has been found useful for measuring suspended sediment concentration (Munday et al., 1979) due to its capability for (relative) atmospheric adjustment. This method should be investigated for its applicabiiity to oil slick targets, since atmospheric correction would not be possible, using the altitude/radiance regression technique used herein, for data sets which are limited to a small range of altitudes or acquired from satellite platforms.

3. One dimension for oil detection or oil/water contrast measurement, which is only basically addressed in this report, is that of spatial texture. This is an important variable for radar wavelengths, and should also be investigated for all high (spatial) resolution sensors — both imaging and profiling.

4. The laser fluorosensor is recognized as, probably, the most successful remote sensor for detecting and identifying marine oil slicks under a variety of conditions (O'Neil et al., 1980c). It should be tested under conditions more suitable for its performance than were the case during the Wallops exercise in November 1978. Flights should be conducted at dusk and/or dawn, when illumination conditions are adequate for aircraft navigation, yet minimum for generating naturally (solar) excited fluorescence. The fluorosensor should also be tested for the variety of oil target conditions that occur when the oil is in an ice-infested environment. This is of particular interest for Arctic waters, where many other sensors have significantly reduced abilities, due to false targets and noise introduced by ice in its varied forms.

5. It is recommended that thermal infrared sensors be tested for oil detection in an ice environment. TIR may be the most effective passive sensor to use in the Arctic, with the ability to "see" oil when it is in, on and, perhaps, under (thin) ice.

6. The spectral signature of oil and the influence of oil/ice mixtures within a resolution cell should be established for all existing satellite systems that may be used for spill location and measurement. This type of data should be collected and stored now, in preparation for an emergency situation in which lengthy investigations are impractical.

7. Airborne multi-spectral scanner data of oil in a marine/ice environment can be used to synthesize oil spill data for future satellite systems. This type of activity has been conducted already, for a variety of other environmental targets, to determine the effort that should be applied towards receiving, processing and analysing such data. It would be advisable to collect similar information for oil spill targets, to select among the multitude of satellite systems forthcoming, and thereby, apply resources to those of the greatest utility.

8. Whereas any single sensor may misinterpret "false" oil targets, the probability of this occurring is greatly reduced when different sensors are used simultaneously. Additional development and testing of multi-sensor overlay/comparison/correlation is recommended for cross-calibration of one sensor with another, and to take advantage of their independent oil detection abilities.

7. REFERENCES

Buja-Bijunas, L., R.A. O'Neil, V. Thomson, R.A. Neville, K. Dagg and D. Rayner. April 1979. Oil spill detection and identification using a laser fluorosensor. Proceedings of the Workshop of the NATO-CCMS Pilot Study on the Use of Remote Sensing for the Control of Marine Pollution, Washington, D.C.

Canada Centre for Remote Sensing. July 1977. Information bulletin -- airborne operation. Canada Centre for Remote Sensing, Ottawa.

Dagg, K. June, 1979. The fluorosensor processing system. Technical Memorandum No. DPD-TM-79-087. Canada Centre for Remote Sensing, Ottawa.

Edgerton, A.T., J.J. Bommurito, R.S. Schwantje and D.C. Meek. May 1975. Development of a prototype oil surveillance system; final report. U.S. Coast Guard, Department of Transportation, Washington, D.C. Report # CG-D-90-75.

Gray, A.L., R.K. Hawkins and C.E. Livingstone. September 1979. CCRS scatterometer operator and user's guide; technical memorandum no. DPD-TM-79-104, Canada Centre for Remote Sensing. Ottawa.

Hawkins, R.K. and A.L. Gray. Wallops Island oil spill: scatterometer results. Canada Centre for Remote Sensing. Unpublished report.

Hawkins, R.K., A.L. Gray, V. Thomson and R.A. Neville. April 1979. Observation of two test oil spills with a microwave scatterometer and a synthetic aperture radar (SAR). Proceedings of the Workshop of the NATO-CCMS Pilot Study on the Use of Remote Sensing for the Control of Marine Pollution, Washington, D.C.

Hoge, F.E. and R.N. Swift. October 1980. Oil film thickness measurement using airborne laser-induced water Raman backscatter. Applied Optics 19(19).

Jones, W.L., L.C. Schroeder and J.L. Mitchell. 1977. Aircraft measurements of the microwave scattering signature of the ocean. IEEE Transactions on Antennas and Propogation AP-25:52-61.

van Kuilenberg, J. 1975. Radar observations of controlled oilspills. Proceedings of the 9th International Symposium on Remote Sensing of Environment, Ann Arbor, Michigan.

McCluney, W.R. 1974. Ocean colour spectrum calculations. Applied Optics 13(10).

Munday, J.C., Jr., T.T. Alfoldi and C.L. Amos. June 1979. Bay of Fundy verification of a system for multidate landsat measurement of suspended sediment. Proceedings of the 5th William T. Pecora Memorial Symposium. Satellite Hydrology, American Water Resources Association, Sioux Falls, South Dakota.

Neville, R.A., V. Thomson, K. Dagg and R.A. O'Neil. April 1979. An analysis of multispectral line scanner imagery for two test oil spills. Proceedings of the Workshop of the NATO-CCMS Pilot Study on the Use of Remote Sensing for the Control of Marine Pollution, Washington, D.C.

O'Neil, R.A., R.A. Neville and V. Thomson. 1980a. Report on the Arctic marine oilspill program remote sensing project. Canada Centre for Remote Sensing, Ottawa. In press.

O'Neil, R.A., L. Buja-Bijunas and D.M. Rayner. 1980b. Field performance of a laser fluorosensor for the detection of oil spills. Applied Optics, 19(6).

O'Neil, R.A., R.A. Neville and V. Thomson. June 1980c. The recommended remote sensing system for the detection and tracking of oil spills in Canada. Proceedings of the Arctic Marine Oil Spill Program Technical Seminar, Edmonton, Alberta.

Skolnik, M.I. July 1969. A review of radar sea echo. U.S. Navy. Naval Research Lab, Washington, D.C. 20375. AD 693 452.

Teillet, P.M., G. Guindon, D.G. Goodenough, R. Lowry and S. Shlien. 1979. User's guide to the CCRS radar preprocessing package. Canada Centre for Remote Sensing, Ottawa.

Valley, S.L., Editor. 1965. Handbook of geophysics and space environments. ARCRL.

Wolfe, W.L. 1965. Handbook of military infrared technology. Office of Naval Research, Washington, D.C.

8. APPENDICES

8.1 APPENDIX A: CCRS SENSORS AND PLATFORMS USED IN THE WALLOPS OIL SPILL MISSION

DC-3 (C-GRSA) Complement:

Closed Circuit Television (CCTV)
* Laser Fluorosensor Mk III (LFS)
Low Light Level Television (LLLTV)
* Vinten 70-mm Cameras (Vinten)
* Multispectral Scanner (MSS)
Optical Multispectral Analyser (OMA)
Miller Pieau Photometer (MPPH)
Multiple Detector Electro-optical Imaging Scanner (MEIS)

CV-580 (C-GRSC) Complement:

Closed Circuit Television (CCTV)
* Wild Heerbrugg RC-10 23-cm Camera (RC-10)
* Dual-channel (UV/TIR) Line Scanner (DCLS)
* ERIM Synthetic Aperture Radar (SAR)
* Microwave Scatterometer (MS)
Side-looking 35-mm Cameras (35-mm)

Sensors used in this study are marked with an asterisk in the above list, and their technical specifications (from: CCRS, 1977; and O'Neil et al., 1980a) are given below.

AIRCRAFT C-CRSA

Type:	DC-3 (Dakota)
Description:	Transport-type aircraft, having two Pratt and Whitney reciprocating engines. Two pilots are mandatory, and an additional five or six sensor operators may be carried.
Performance:	Operational Ceiling — 3000 m Flight Duration — 5 hours Range -- 1200 km True Airspeed 220 to 280 km/hr Basic Weight -- 8871 kg Fuel Load (volume; weight) 3046 l: 2188 kg Total all up Weight -- 12 200 kg Fuel consumption — 245 kg/hr @ 260 km/hr Electric Power Available -- 7.2 kVA
Sensor Locations:	All sensors are located aft of the wing-root, and are completely accessible during flight.
Sensor Control:	Three double equipment racks have been provided to mount all sensor controls.
Support Systems:	14-channel Mincom tape recorder Closed circuit television and video tape recording system ADAS Navigation -- ADF, INS, VLF, provision for Doppler Radar altimeter Communication -- VHF, HF APU — Gas-operated for ground power and internal engine starting.

AIRCRAFT C-CRSC

Type:	CV-580 (known as the SAR-580 when equipped with SAR)
Description:	The CV-580 is a former passenger-transport aircraft, having two Allison 501-d13d propeller jet engines, producing 8000 hp. The aircraft crew consists of two pilots. It has positions for seven sensor operators.
Performance:	Operational Ceiling — 7000 m Flight Duration -- 5 hours (with full sensor and operator complement aboard) Range -- 2800 km True Airspeed — 280 to 550 km/hr. Basic Weight — 13 044 kg Zero Fuel Weight -- 20 408 kg Fuel Load (volume; weight) — 11 010 l; 8941 kg Total all up Weight -- 26 375 kg Fuel Consumption — 900 kg/hr @ 550 km/hr (5500 m) @ 370 km/hr (1500 m) Electric Power Available — 15 kVA
Sensor Location:	Aft part of the fuselage completely accessible during flight.
Support Systems:	14-channel Mincom Tape Recorder Closed-circuit colour television and video tape recording system ADAS Navigation -- ADF, INS, VLF, provision for Doppler APU — for ground power and internal engine starting

CCRS MK III LASER FLUOROSENSOR

Description: A pulsed UV, laser-activated, range-gated fluoresence detector. A medium-resolution spectrometer allows the fluorescent return to be categorized.

Transmitter:

Laser:	nitrogen gas
Wavelength:	337 nm
Pulse length:	3 ns FWHM
Pulse energy:	1 mJ/pulse
Beam divergence:	3 mrad x 1 mrad
Repetition rate:	100 Hz

Receiver:

Telescope:	f/3.1 Dall Kirkham
Clear aperture:	0.0232 m^2
Field of view:	3 mrad x 1 mrad
Intensifier on-gate period:	70 ns
Spectral range:	377 to 689 nm
Nominal spectral bandpass:	20 nm/channel
Noise equivalent energy:	4.8 x 10^{-17}J
Lidar altimeter range:	75 to 750 m
Lidar resolution:	1.5 m
Recording medium:	CCT (Kennedy 9800)
Real time analyser & display:	FDF-80
Weight:	267 kg
Power:	28 V DC, 20.5 A
	110 V 60 Hz, 9 A

VINTEN 70-mm CAMERA - TYPE 492 (MODIFIED)

Description: A 5-cm-by-5.5-cm format camera

AS FLOWN:

	UV	VISIBLE
Filter:	Wratten 18A	NAV
Lens:	7.5 cm f/2.0	3.8 cm f/2.8
Film:	2405 (B & W neg)	2445 (colour neg)
Film capacity	700 exposures	460 exposures
Position:	45° forward	Nadir
Shutter speed:	1/500 sec	1/500 sec

Cycle rate: 0.5 to 999 seconds — pulse mode

Weight: 29.5 kg (2 cameras)

Power: 28 V DC, 15 A (2 cameras)

MULTISPECTRAL SCANNER — DAEDALUS MODEL 1260

Description: A multi-channel, optical-mechanical line-scan spectrometer which records energy reflected or emitted from the Earth's surface.

CHANNEL	SPECTRAL RANGE (μm)	RESPONSIVITY counts x 10^3 ($W m^{-2} nm^{-1} sr^{-1}$) for gain 1	NOISE EQUIVALENT SPECTRAL RADIANCE NEN_λ ($W m^{-2} nm^{-1} sr^{-1} \times 10^{-3}$) for 50 scans/sec	
1	0.390 to 0.415	5.7	4.2	
2	0.415 to 0.450	7.0	1.6	
3	0.445 to 0.495	2.6	0.72	
4	0.500 to 0.550	1.5	0.52	
5	0.550 to 0.595	1.1	0.45	
6	0.590 to 0.645	1.1	0.42	
7	0.625 to 0.695	1.3	0.40	
8	0.680 to 0.780	1.9	0.23	
9	0.765 to 0.895	1.5	0.31	
10	0.865 to 1.035	1.4	0.34	
IR	8.5 to 12.5	210.0*	0.005	NOISE EQUIVALENT TEMPERATURE NET (°C) 0.04
w/filter	8.5 to 10.5		0.02	0.2

continued . . .

MULTISPECTRAL SCANNER. Concluded.

Digital range:	0 to 255 (8-bit)
Gains:	0.5, 1, 2, 4, 10
Spatial resolution:	2.5 mrad
Field of view:	85.9° (73.7° with S-bend correction)
Repetition rate:	12.5, 25, 50, 100 scans/sec
Recording medium:	instrumentation tape recorder (digital)
Weight:	129 kg
Power:	28 V DC, 50 A

*IR responsivity is continuously adjustable for coverage of selected temperature range; value given is for coverage of range 0 to 10°C.

WILD HEERBRUGG — RC-10

Description:	23-cm-by-23-cm format, aerial survey camera
Lens:	88-mm SAG II
Shutter speed:	1/100 to 1/1000 sec
Cycle rate:	1-per-1.8-sec maximum
Film supply:	individual feed and take-up cassettes with a separate vacuum platen
Film capacity:	280 exposures B & W, 225 exposures colour
Filter:	NAV 3.3
Film types:	2445 (colour neg) 2443 (false-colour IR)
Weight:	164 kg
Power:	28 V DC, 25 A

MICROWAVE SCATTEROMETER -- RYAN MODEL 720

Description:	Measures absolute radar backscatter cross-section as a function of look angle from nadir.
Transmitter frequency:	13.3 GHz (2.25 cm)
Transmitter power:	2 W
Antenna:	slotted-guide phased array
Antenna gain:	38 dB
Antenna beam width (broadside):	3°
Antenna beam width (fore-aft):	120°
Transmit polarization:	H or V
Receive polarization:	like and crossed
Ground speed range:	120 to 180 knots
Recording medium:	instrumentation tape recorder (analogue)
Accuracy:	Absolute HH 1. dB HV 3. dB VH 3. dB VV 3. dB Relative 0.5 dB
Resolution:	0.26 x (ground speed [ms^{-1}]) along track 0.052 x (altitude [m]) cross track
Sensitivity:	8 dB SNR for σ_oHH = -35 dB* at 600 m at 60° incidence angle.
Weight:	antenna — 16 kg electronics — 41 kg
Power:	110 V, 400 Hz, 2.8 A 110 V, 60 Hz, 0.3 A

* σ_oHH for sea clutter for wind speed of 2 m/sec (Jones, 1977)

DUAL-CHANNEL LINE SCANNER -- Daedalus Model 1230

Description: A dual-channel optical/mechanical linescanning radiometer that records energy reflected or emitted from the Earth's surface.

Channel:	UV	IR
Spectral region:	0.30 to 0.37 μm FWHM	8.5 to 12.5 μm or 8.5 to 10.5 μm with filter
Spatial resolution:	5.5 mrad	2.5 mrad
Responsivity:	2.56×10^4 $\frac{\text{counts}}{\text{W m}^{-2}\,\text{sr}^{-1}\,\text{nm}^{-1}}$ for gain setting = 100	21.0×10^4 $\frac{\text{counts}}{\text{W m}^{-2}\,\text{sr}^{-1}\,\text{nm}^{-1}}$ for selected temperature range 0 to 10°C
NEN_λ/NET:	1×10^{-4} W m^{-2} sr^{-1} nm^{-1} (at approx. 20°C: temperature dependent)	0.04°C 0.2°C with filter
Field of view:	77.3°	
Repetition rate:	60 scans per second	
Recording ium:	instrumentation tape recorder (analogue)	
Weight:	54.5 kg	
Power:	28 V DC, 20 A	

ERIM SYNTHETIC APERTURE RADAR

Description: The ERIM SAR provides simultaneous microwave imagery in the X and L Bands

	X Band	L Band
Frequency:	9.350 GHz (3.2 cm)	1.315 GHz (22.8 cm)
Transmitter peak power:	1 kW	5 kW
Antenna gain:	28 dB	16.5 dB
Along track beamwidth:	1.1°	7°
Depression angle:	0° to 90°	0° to 90°
Recorder swath width: (slant range)	5.6 km*	5.6 km
Maximum range:	24.1 km	24.1 km
Pulsewidth:	3 μsec	2 μsec
Resolution: range:	1.5 m	2.3 m
azimuth:	2.1 m	2.1 m
Sensitivity:** (SNR)	3 dB for VV = -40 dB	12 dB for VV = -40 dB
	-17 dB for HH = -60 dB	-15 dB for HH = -67 dB
Recording medium:	- film with subsequent optical processing - a single-channel real time processor is also available	
Weight:	- digital magnetic tape 1635 kg total (501 kg real time processor)	
Power:	4.8 kVA	

---

* 20 km with wide-swath antenna, X-HH mode only.

** for a depression angle of 8° and altitude of 600 m, and for normalized radar cross-sections for the subsection given in Edgerton (1975) and Skolnik (1969).

9.2 APPENDIX B: DATA USED

The following tables list the subsets of the sensors used and data collected by the two CCRS aircraft that were used in this analysis.

CONVAIR 580

NAVIGATION				SENSORS			
Altitude (feet)	Ground Speed (knots)	Track ---- Drift	Time On Target (GMT)	SAR Time On Target (GMT) Band/Pol./Depr.Angle	SCATTEROMETER Polarization Transmit/Receive	DCLS Time On Time Off	RC-10 Frame I.D.
November 2/Line 3							
760	155	006 +05	17:04:01		V/V V/H	17:03:47 17:04:16	3394 3395
November 2/Line 6							
810	167	010 +06	17:13:38		H/V	17:13:21 17:13:54	3398
November 2/Line C-2				18:06:49 X/HH/43°			
November 3/Line 4B							
900	149	072 0	15:30:20		H/V H/H	15:26:26 15:30:43	3524 3525
November 3/Line F-5				16:59:35 X/HH/43°			

NAVIGATION					SENSORS		
DATE LINE	ALTITUDE (feet)	GROUND SPEED (knots)	TRACK DRIFT	TIME ON TARGET (GMT)	MSS Time On Time Off	FLUOROSENSOR Time On Time Off	VINTEN Frame I.D.
Nov 2 Line 9	950 - 1060	141	030 -2	17:39:59	17:39:48 17:40:17	17:39:42 17:40:19	153/75206 154/75207
Nov 2 Line 21	1500- 1490	143	070 +1	18:11:18	18:11:02 18:11:29	18:10:57 18:11:26	230/75305 231/75307
Nov 2 Line 24	1640- 1660	124	006 +8	18:20:59	18:20:44 18:21:09	18:20:38 18:21:08	244/75323 245/75325
Nov 3 Line 9	3500	132	334 -1	16:56:03	16:55:43 16:56:24	---	304/75401
Nov 3 Line 14	1150- 1130	117	059 0	17:19:10	17:18:30 17:19:35	17:18:54 17:19:24	333/75439 334/75440
Nov 3 Line 19	1260- 1280-	117	011 -3	17:39:21	17:39:07 17:39:42	17:39:02 17:39:40	365/75480- 367/75483
Nov 3 Line 22	1020- 1070	127	019 -2	17:50:17	17:50:06 17:50:34	17:50:01 17:50:29	383/75504

FIGURES AND PLATES

FIGURES

PLATES

All plates are contained in an envelope inside the back cover of the report.

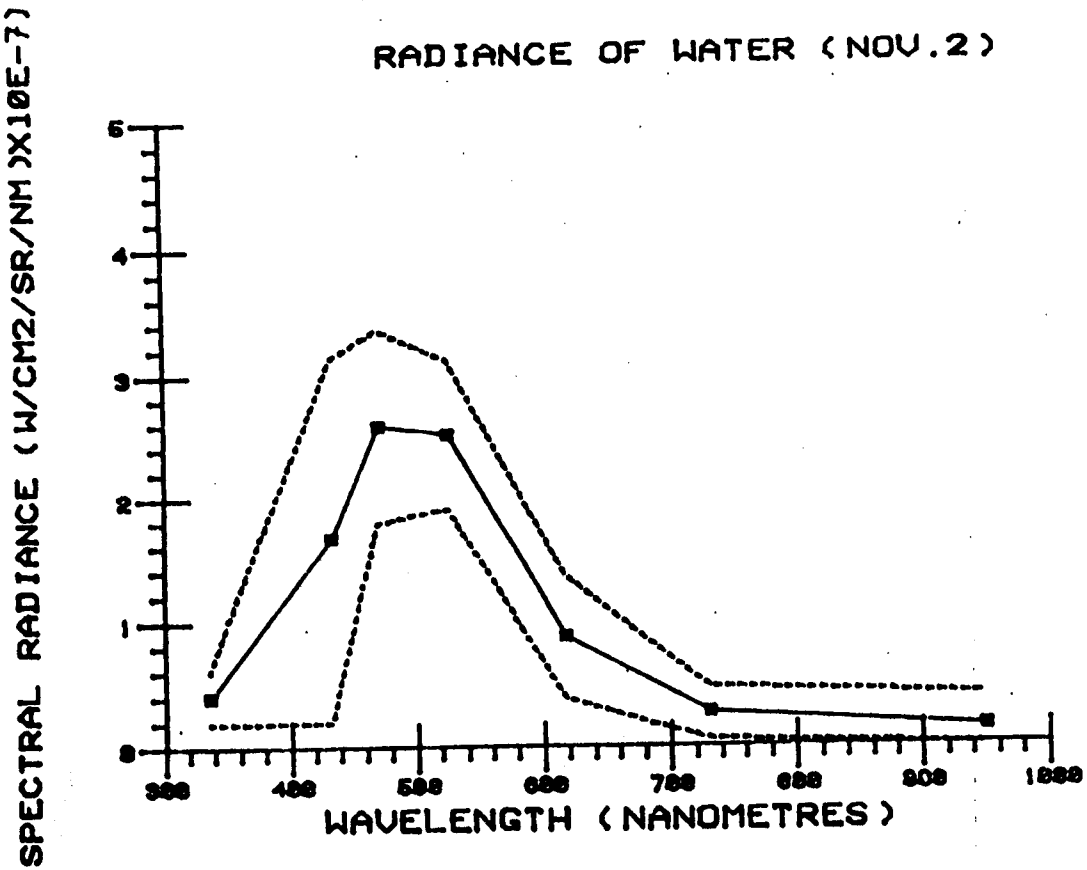

Figure 3.1.A. Volume and surface reflection of water; from the MSS and the DCLS. Dotted lines represent standard error envelope.

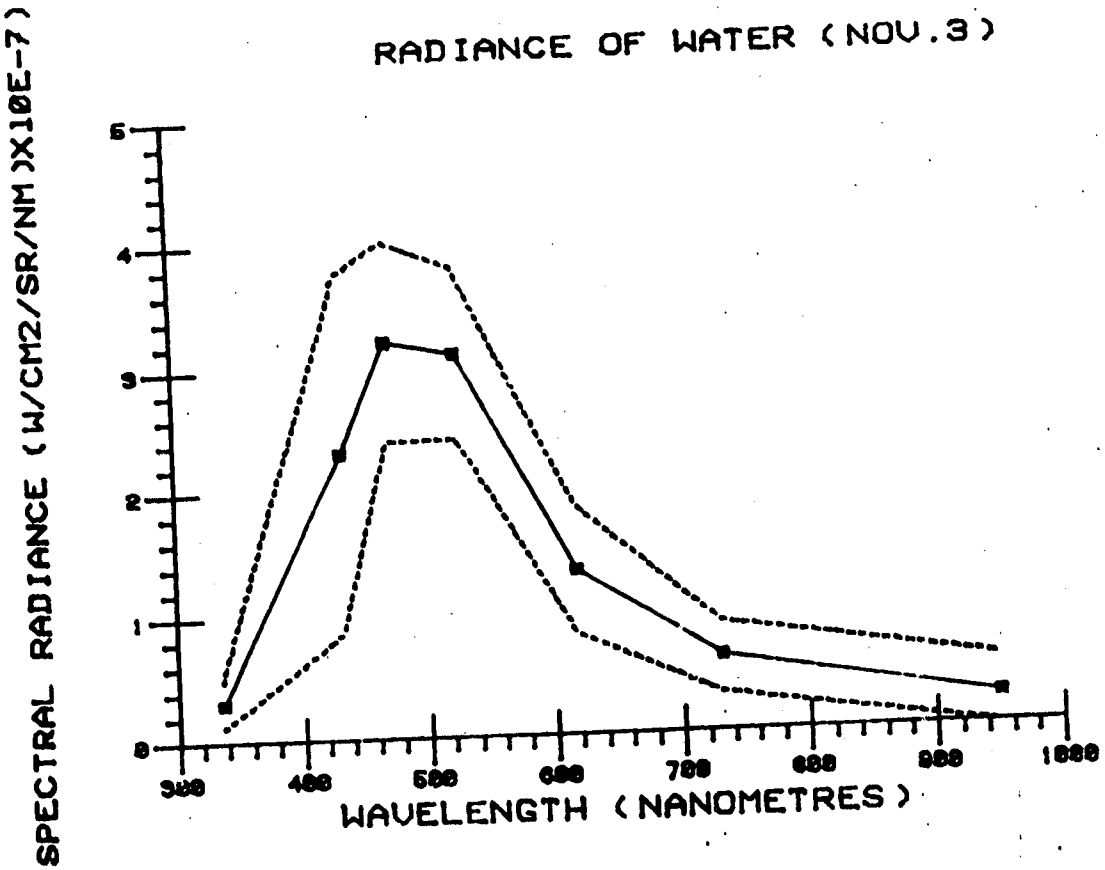

Figure 3.1.B. Volume and surface reflection of water; from the MSS and the DCLS. Dotted lines represent standard error envelope.

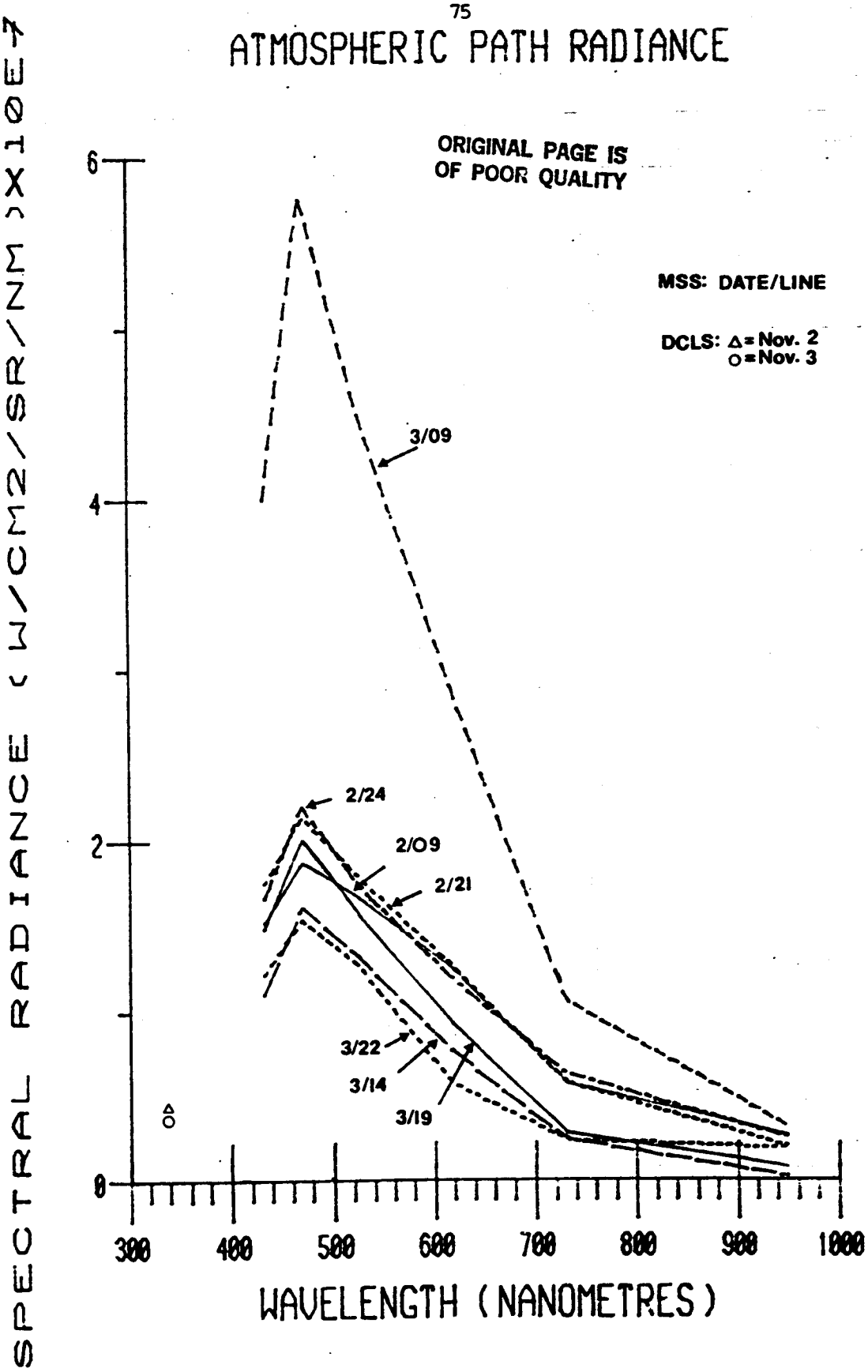

Figure 3.1.C. Atmospheric path radiance at nadir

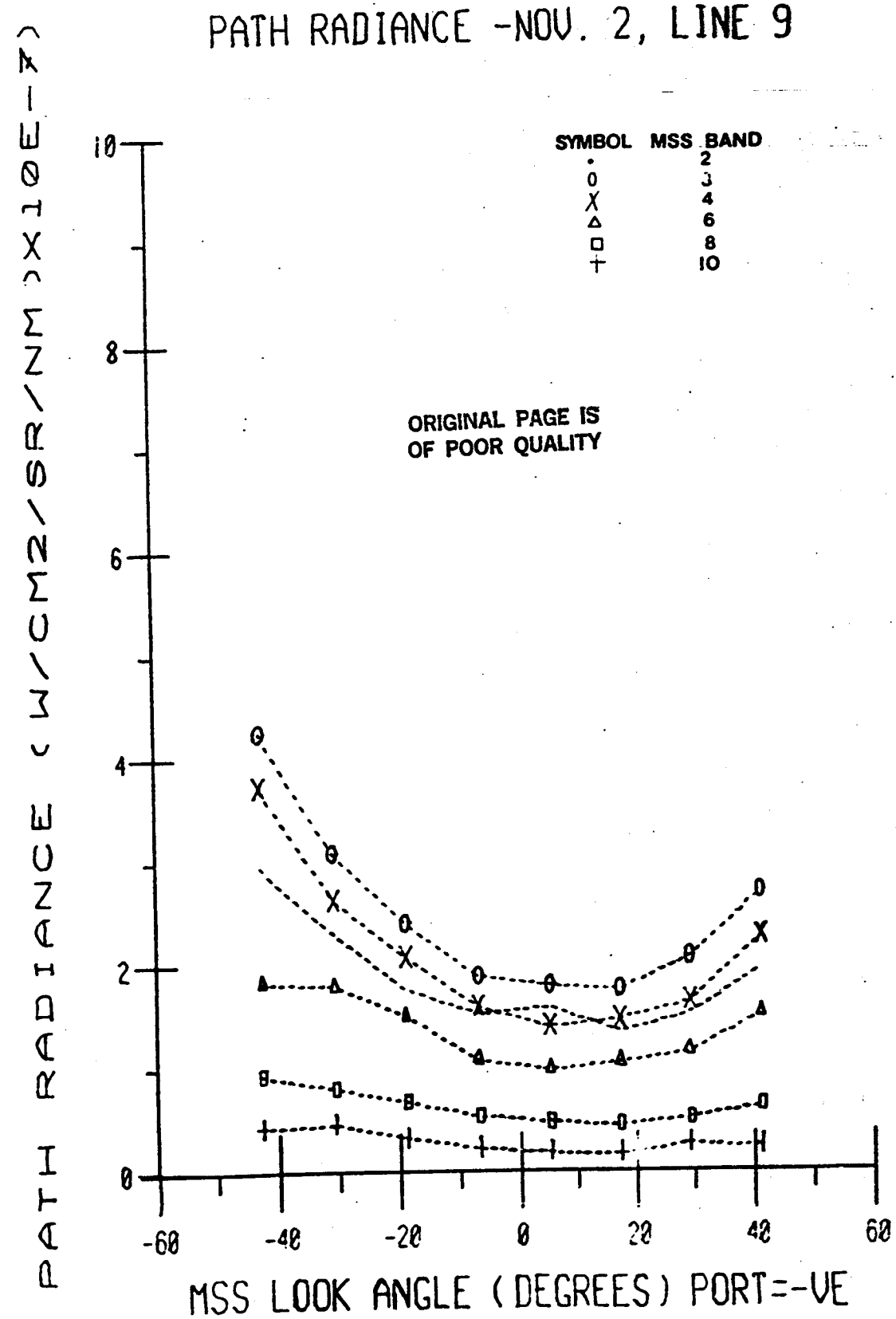

Figure 3.1.D. Path radiance for varying MSS look angle and spectral bands.

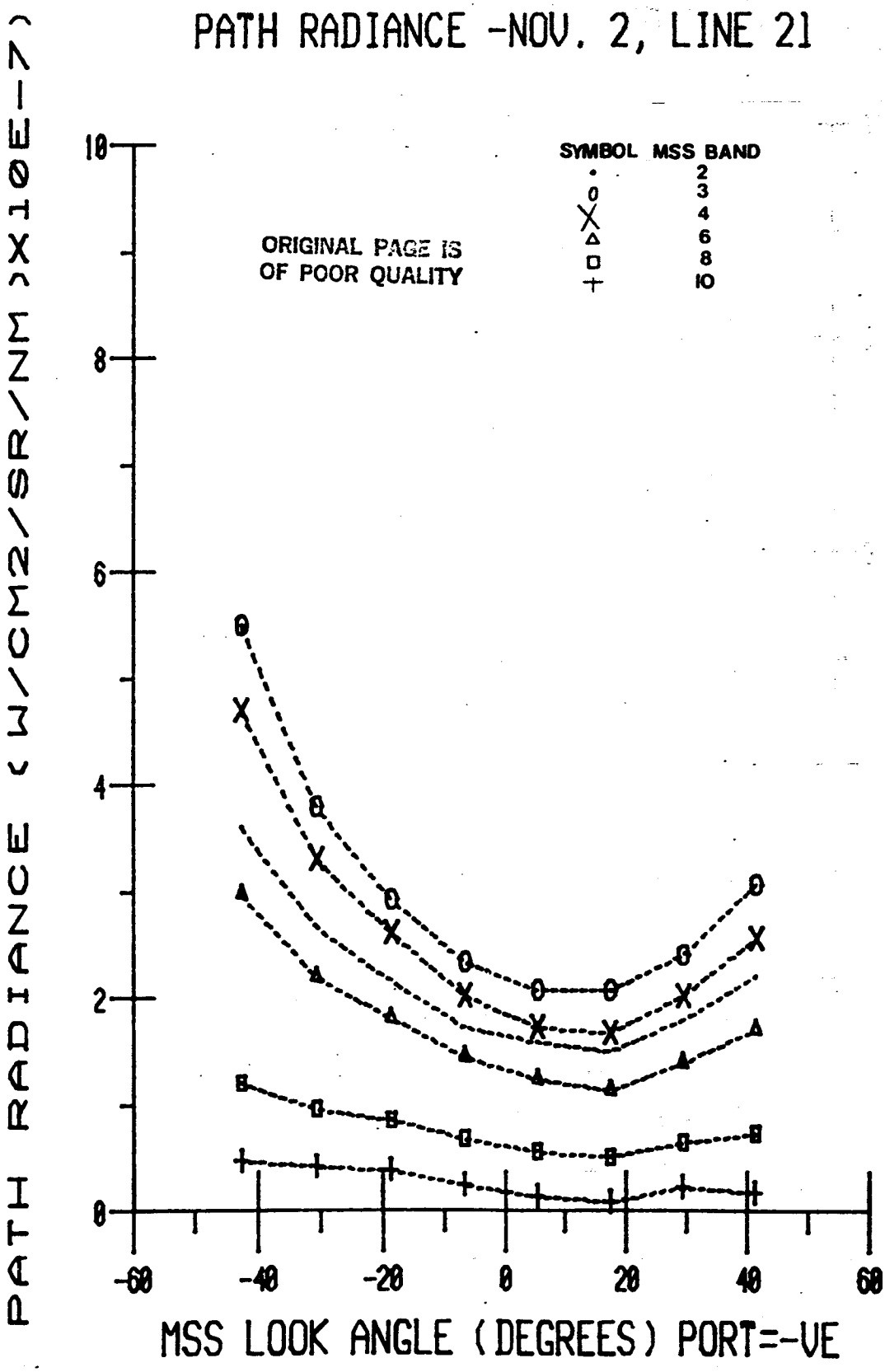

Figure 3.1.E. Path radiance for varying MSS look angle and spectral bands.

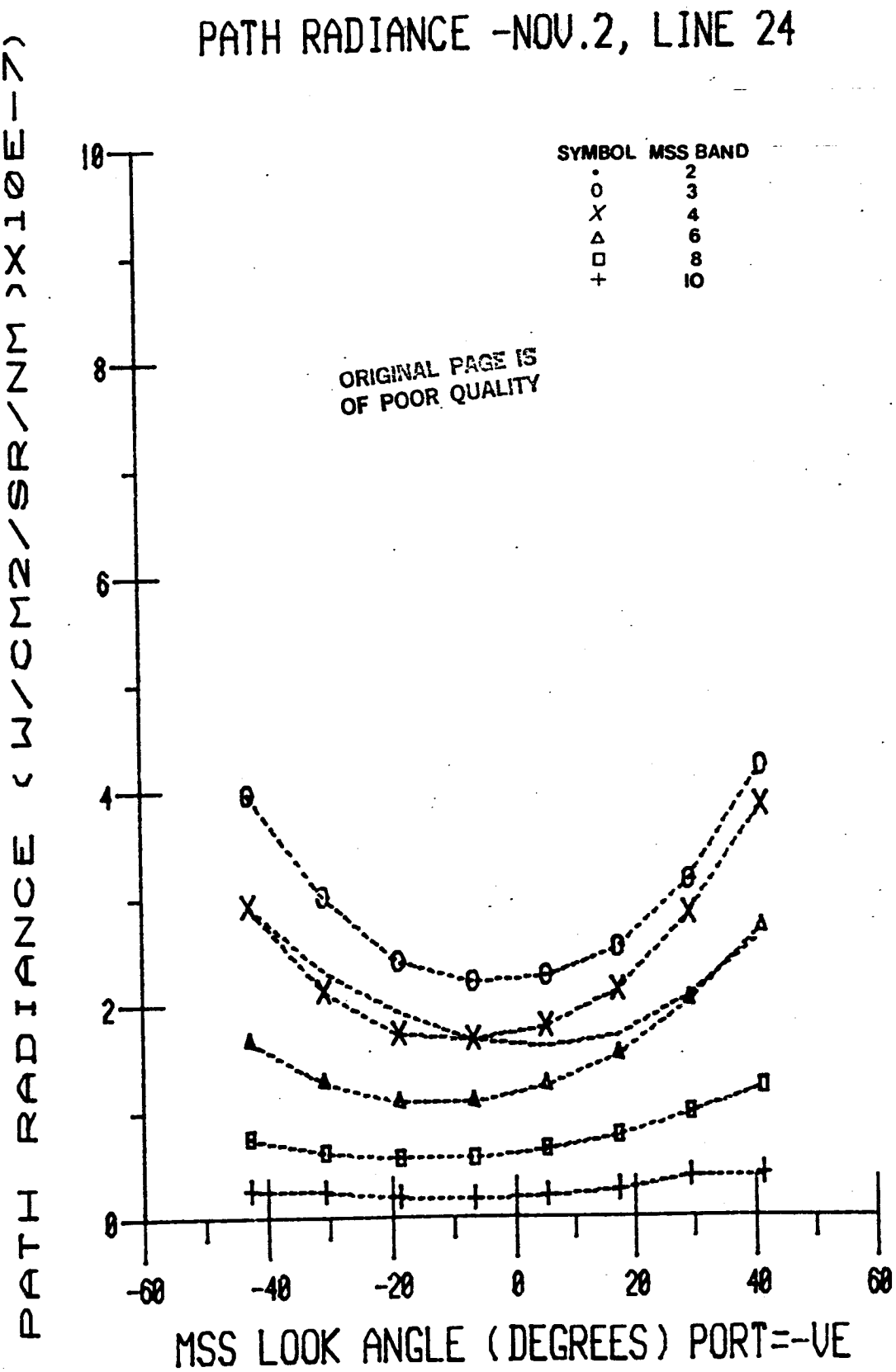

Figure 3.1.F. Path radiance for varying MSS look angle and spectral bands.

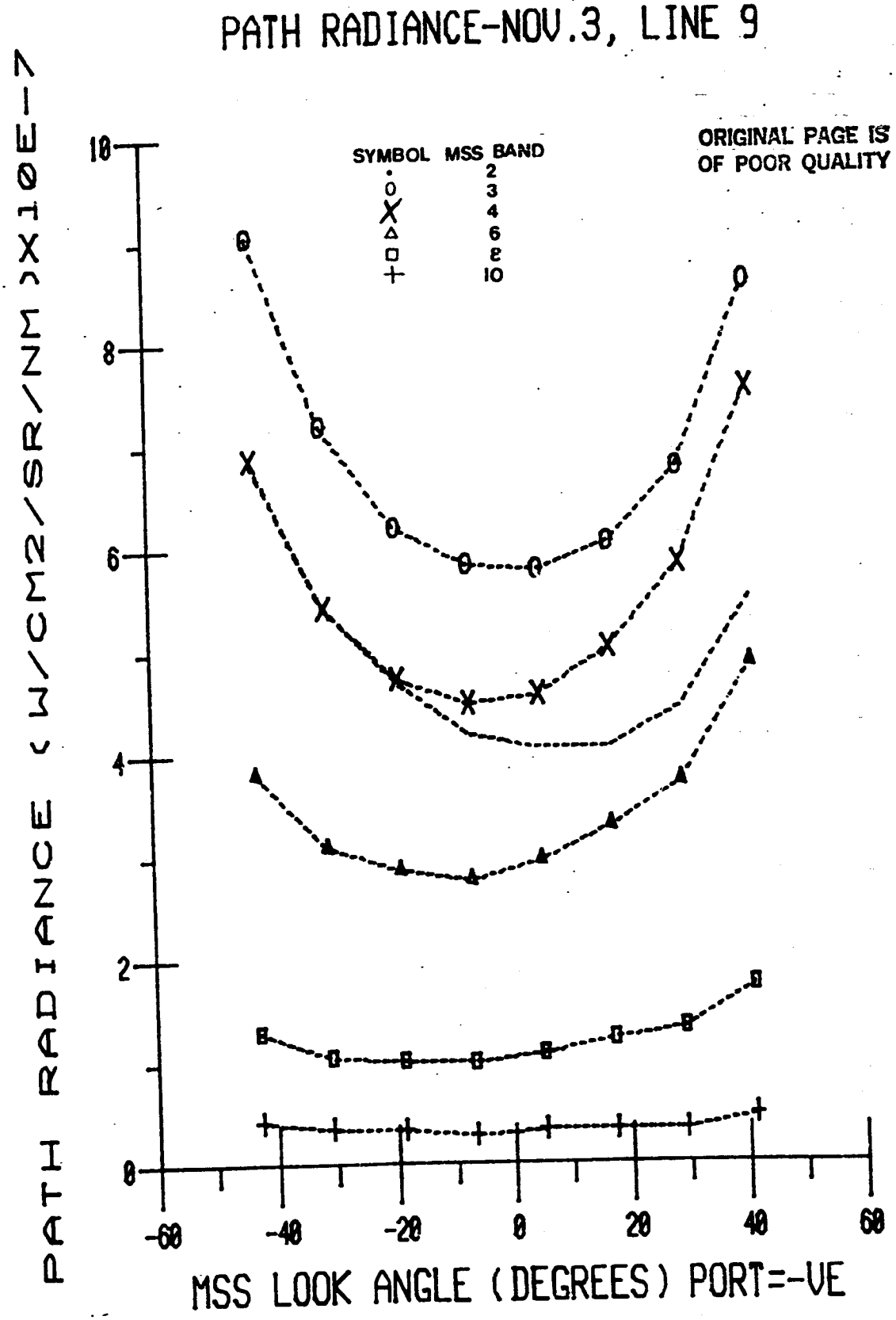

Figure 3.1.C. Path radiance for varying MSS look angle and spectral bands

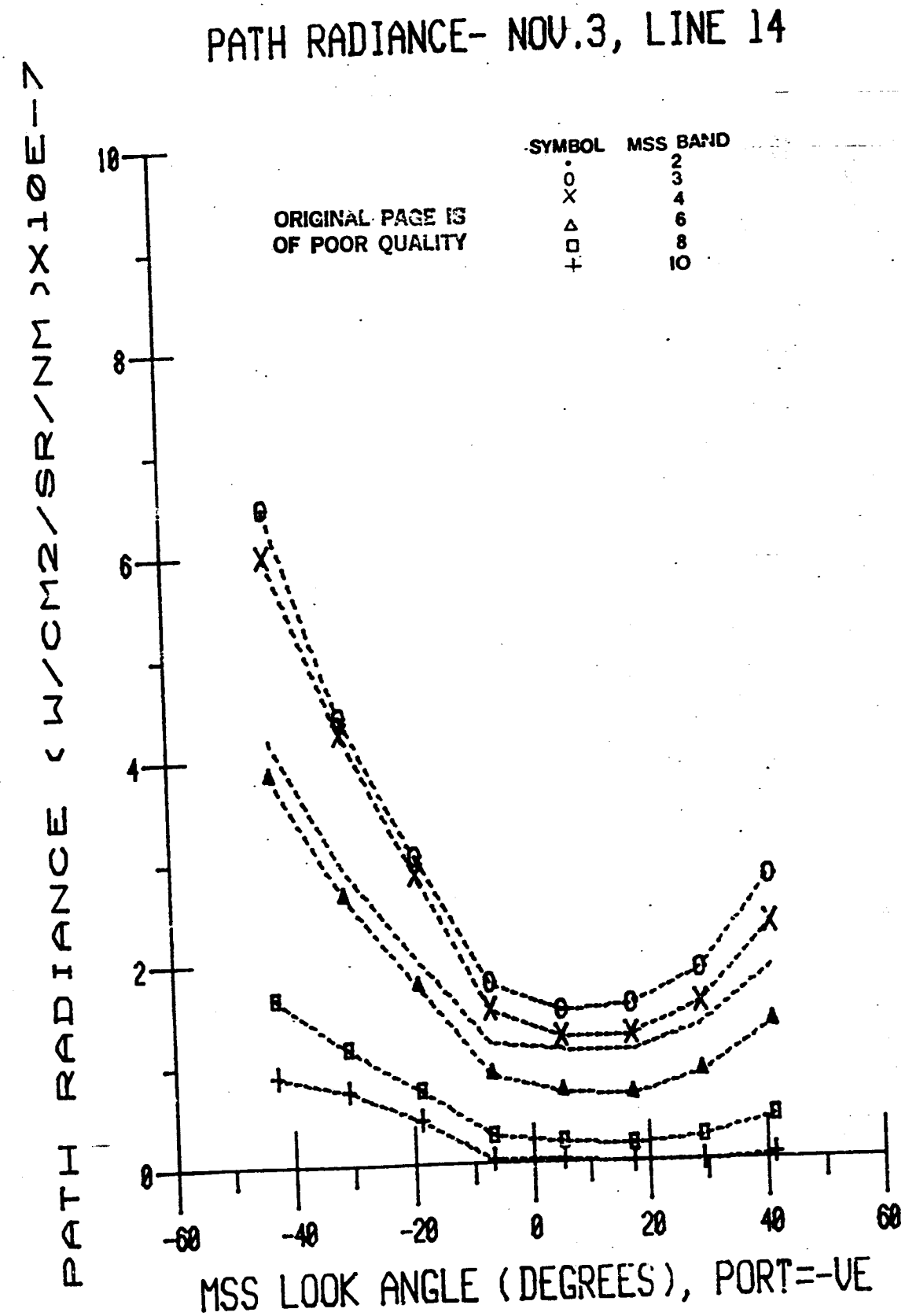

Figure 3.1.H. Path radiance for varying MSS look angle and spectral bands

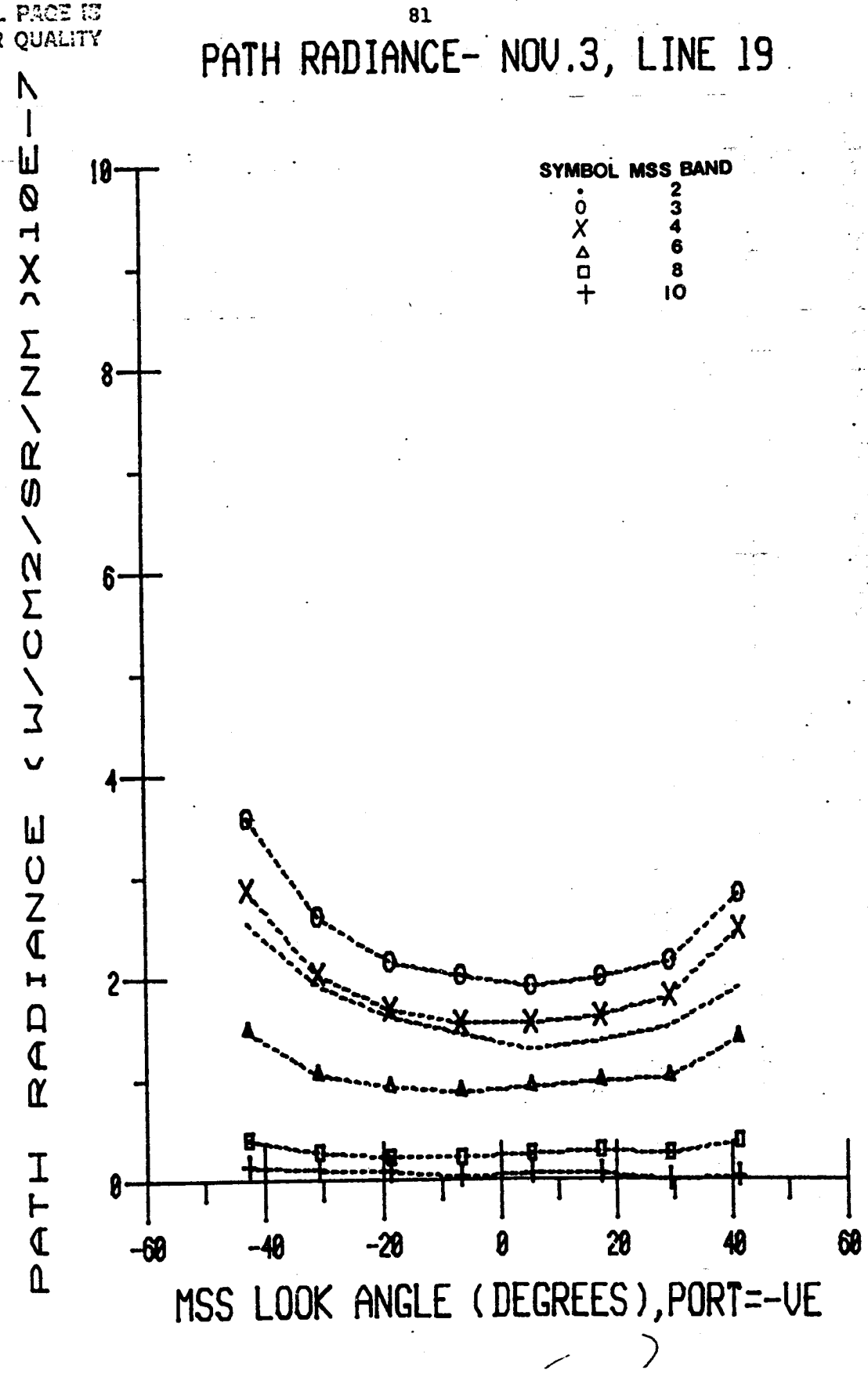

Figure 3.1.1. Path radiance for varying MSS look angle and spectral bands

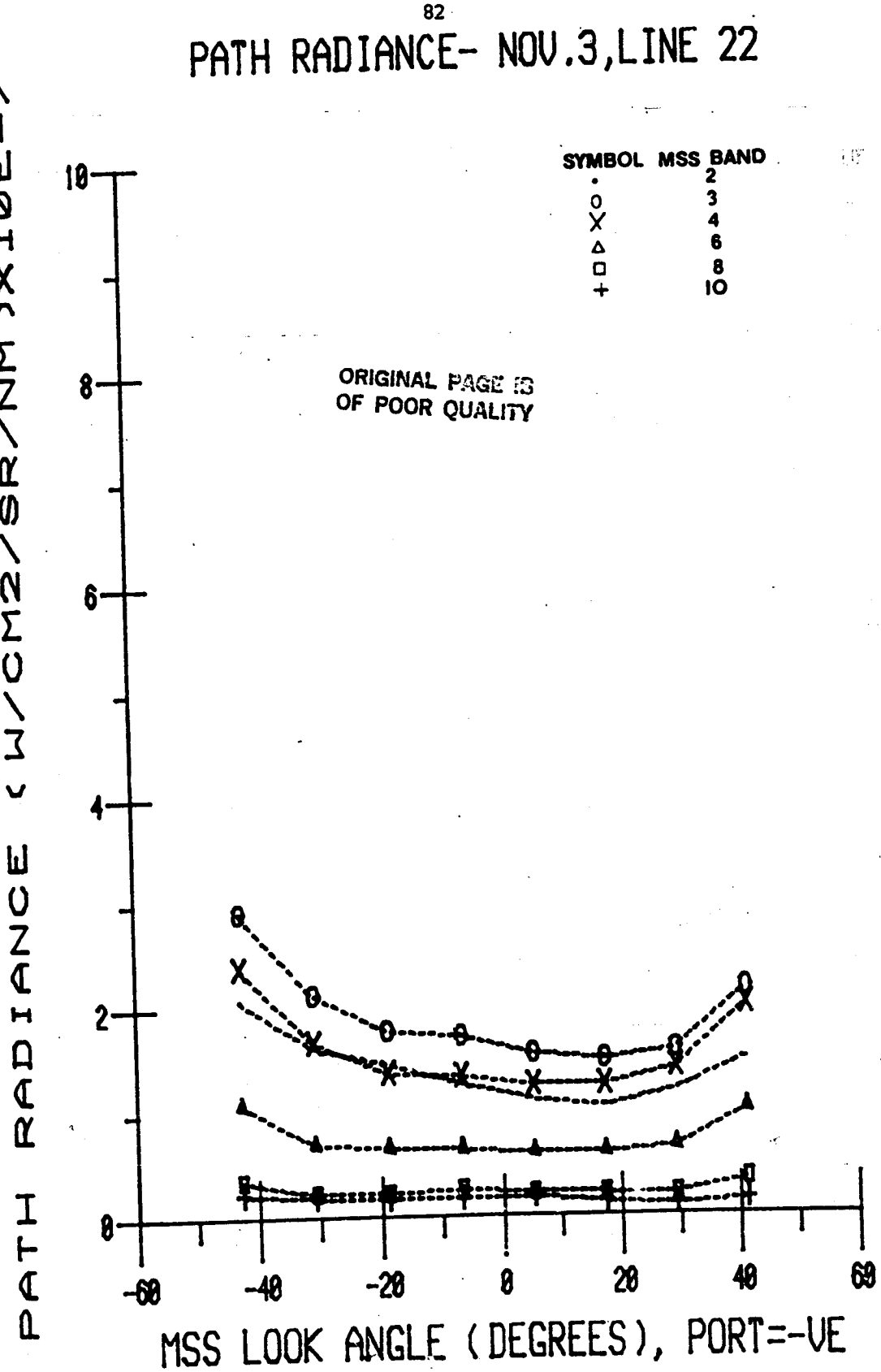

Figure 3.1.J. Path radiance for varying MSS look angle and spectral bands

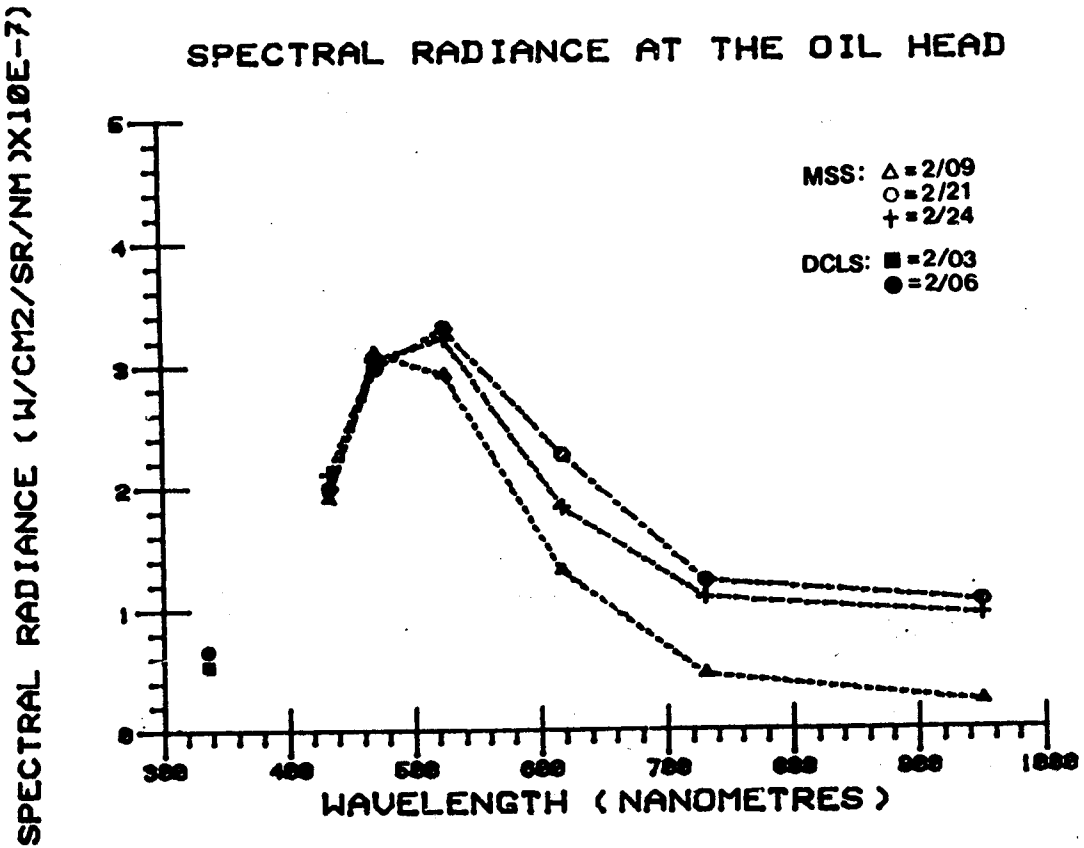

Figure 3.1.K. Upwelling radiance at the surface of the oil head. 2 November 1978; Murban crude oil.

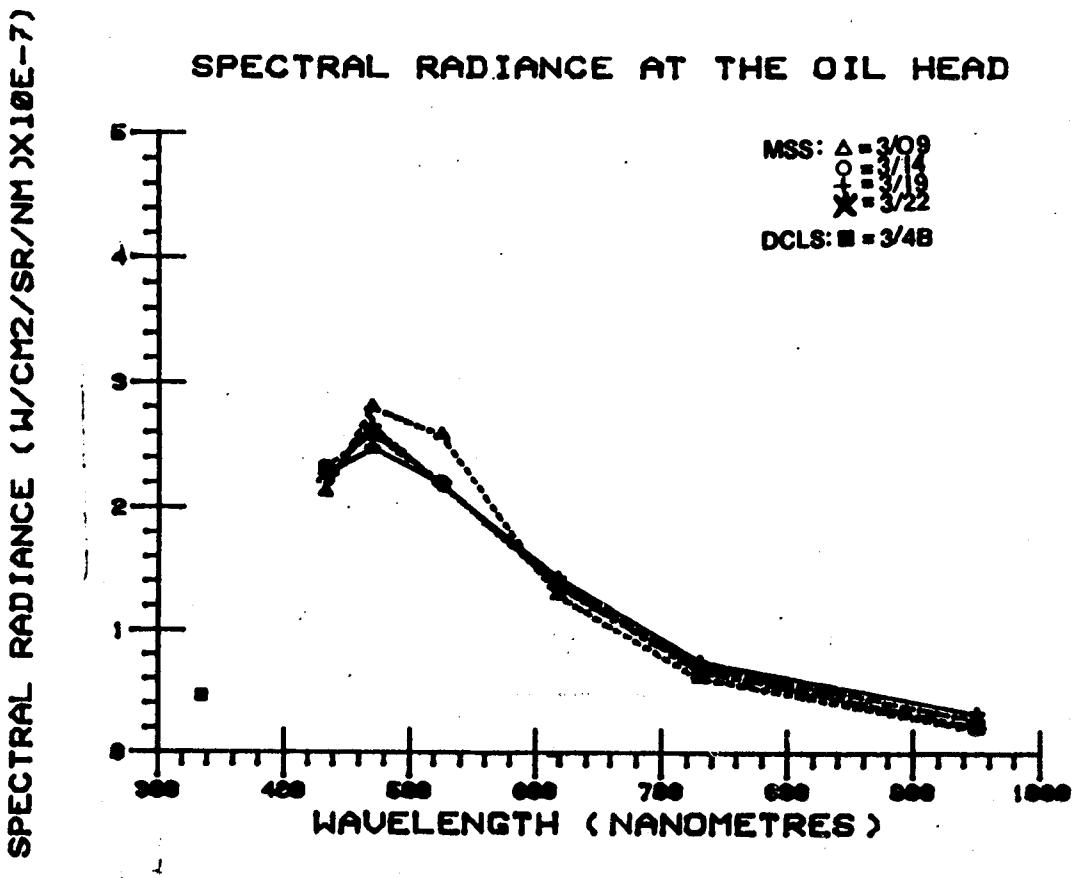

Figure 3.1.L. Upwelling radiance at the surface of the oil head. 3 November 1978; La Rosa crude oil

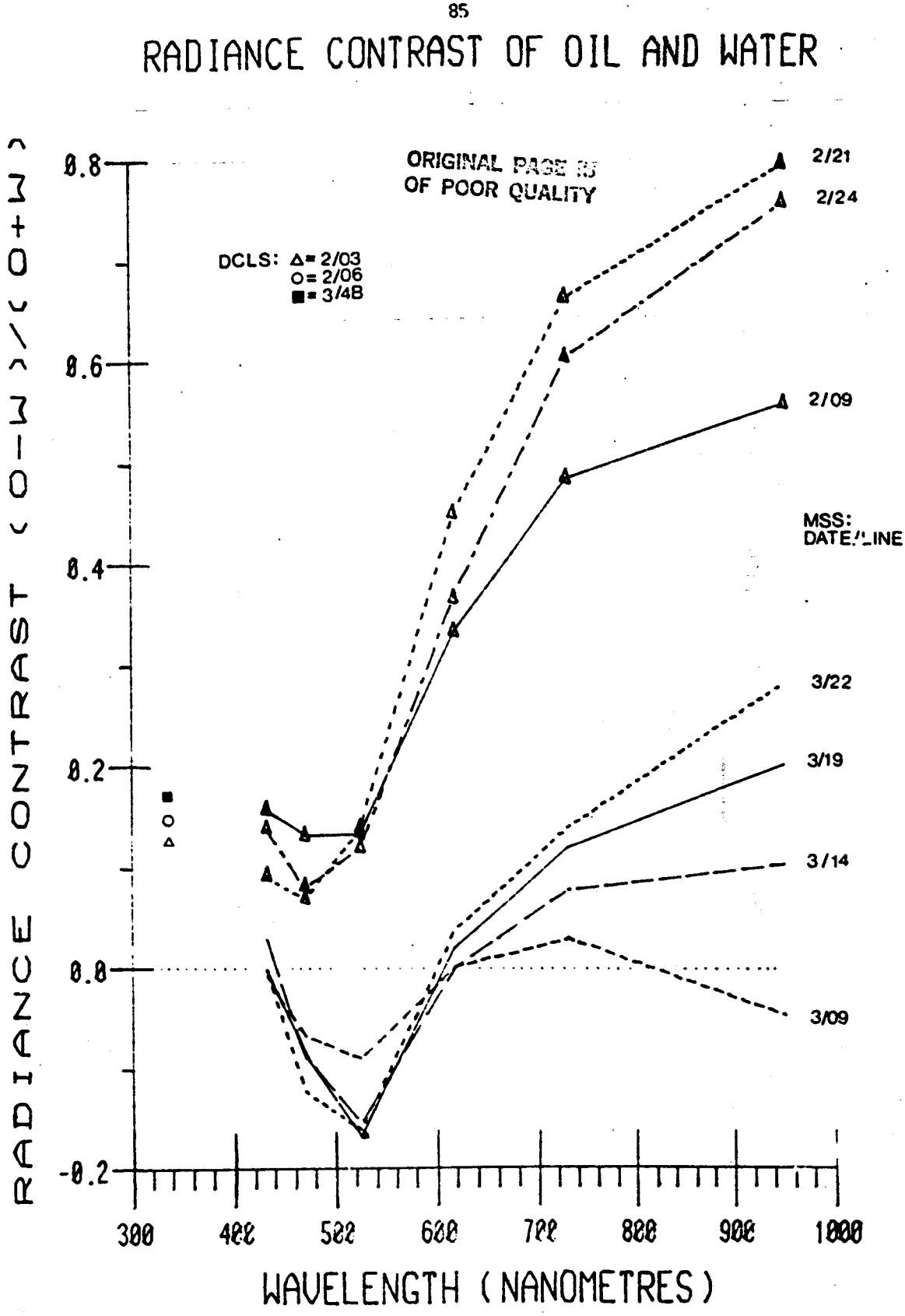

Figure 3.1.M Contrast of oil head radiance versus water radiance

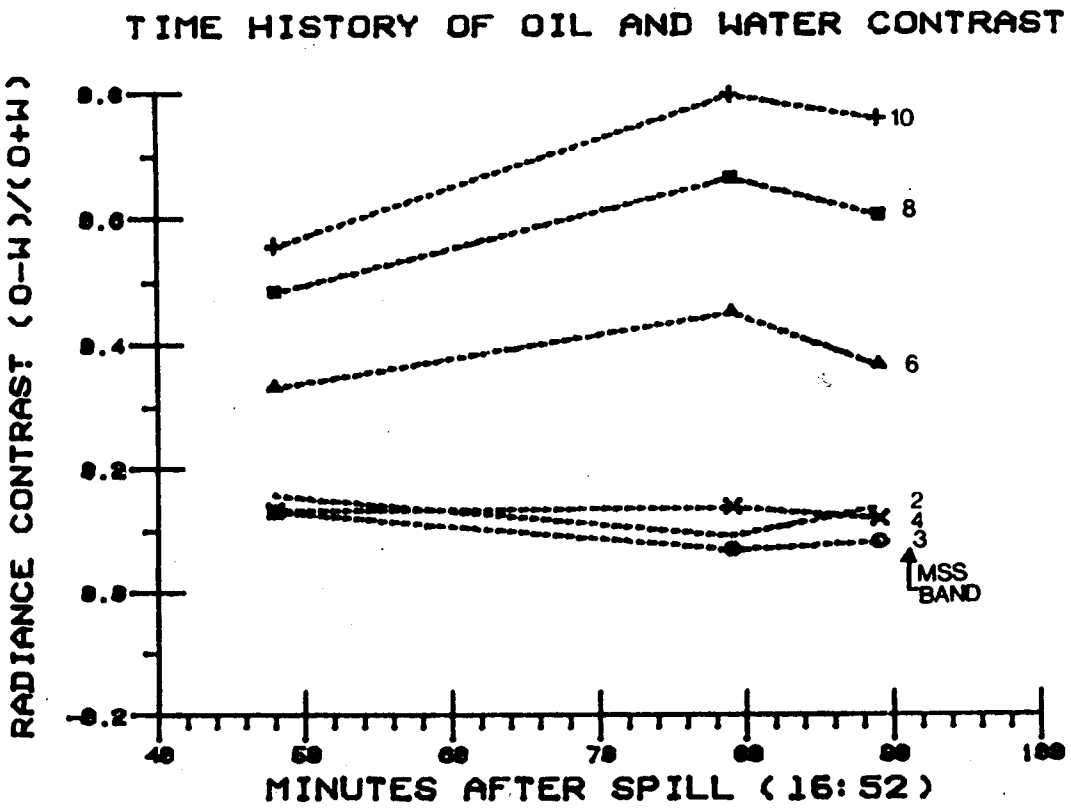

Figure 3.1.N. Murban crude oil; 2 November 1978

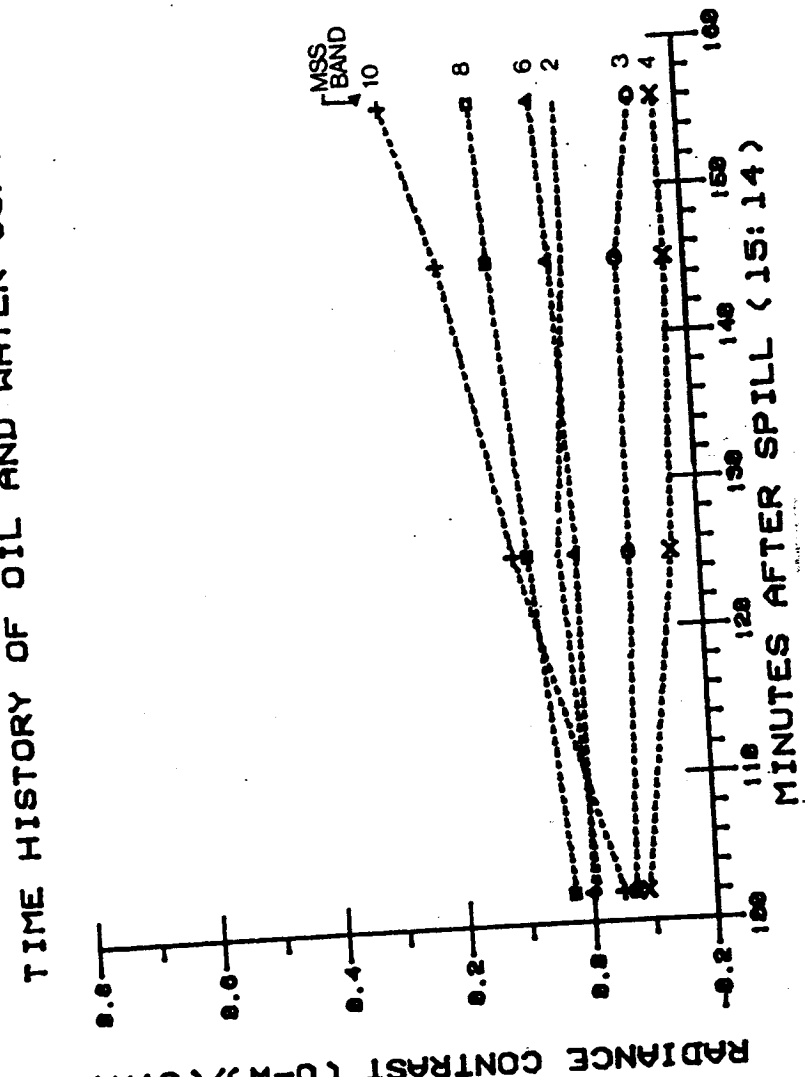

Figure 3.1.0. La Rosa crude oil; 3 November 1978

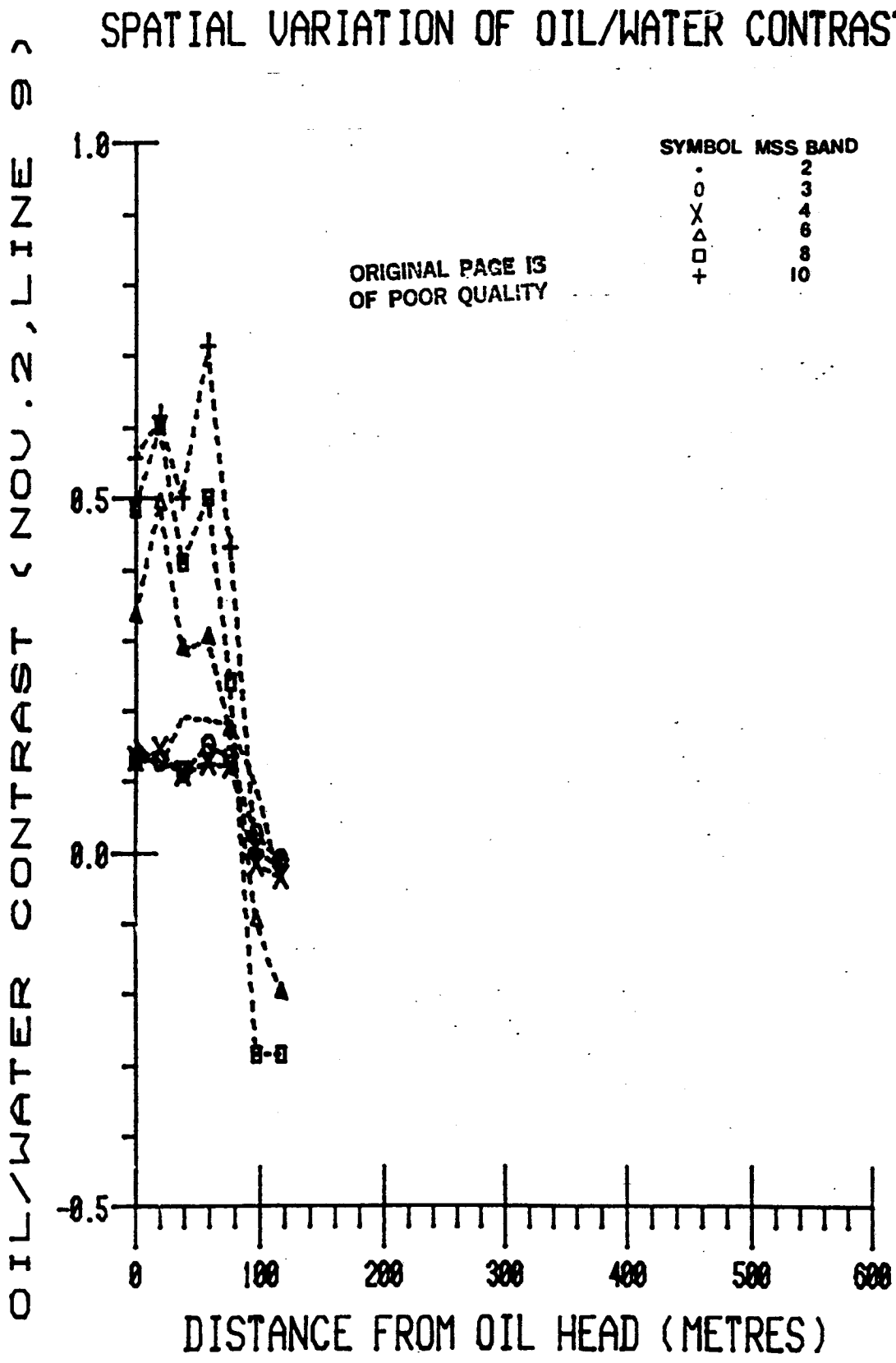

Figure 3.1.P. Spatial variation of oil/water contrast; 2 November, line 9

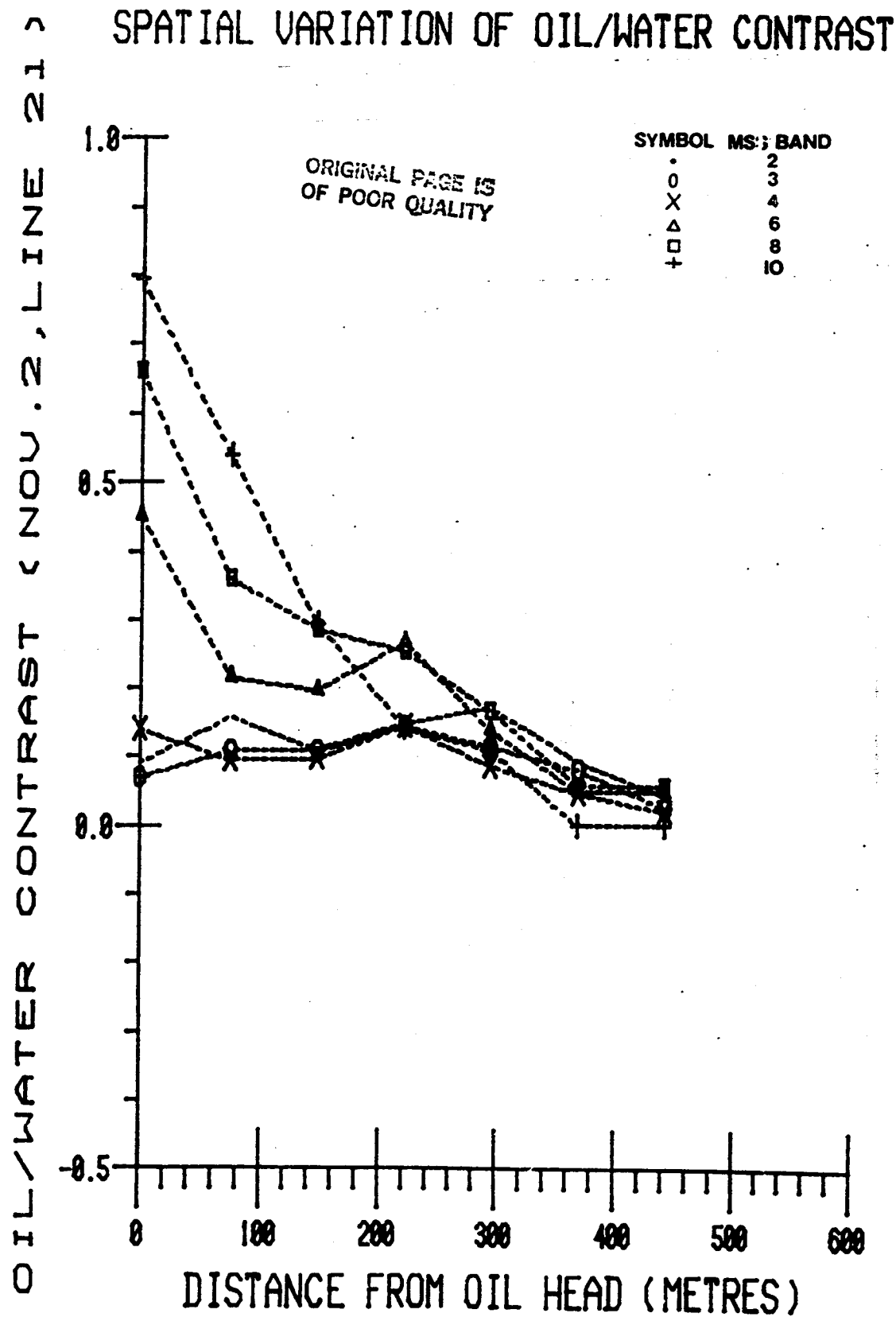

Figure 3.1.Q. Spatial variation of oil/water contrast; 2 November, line 21

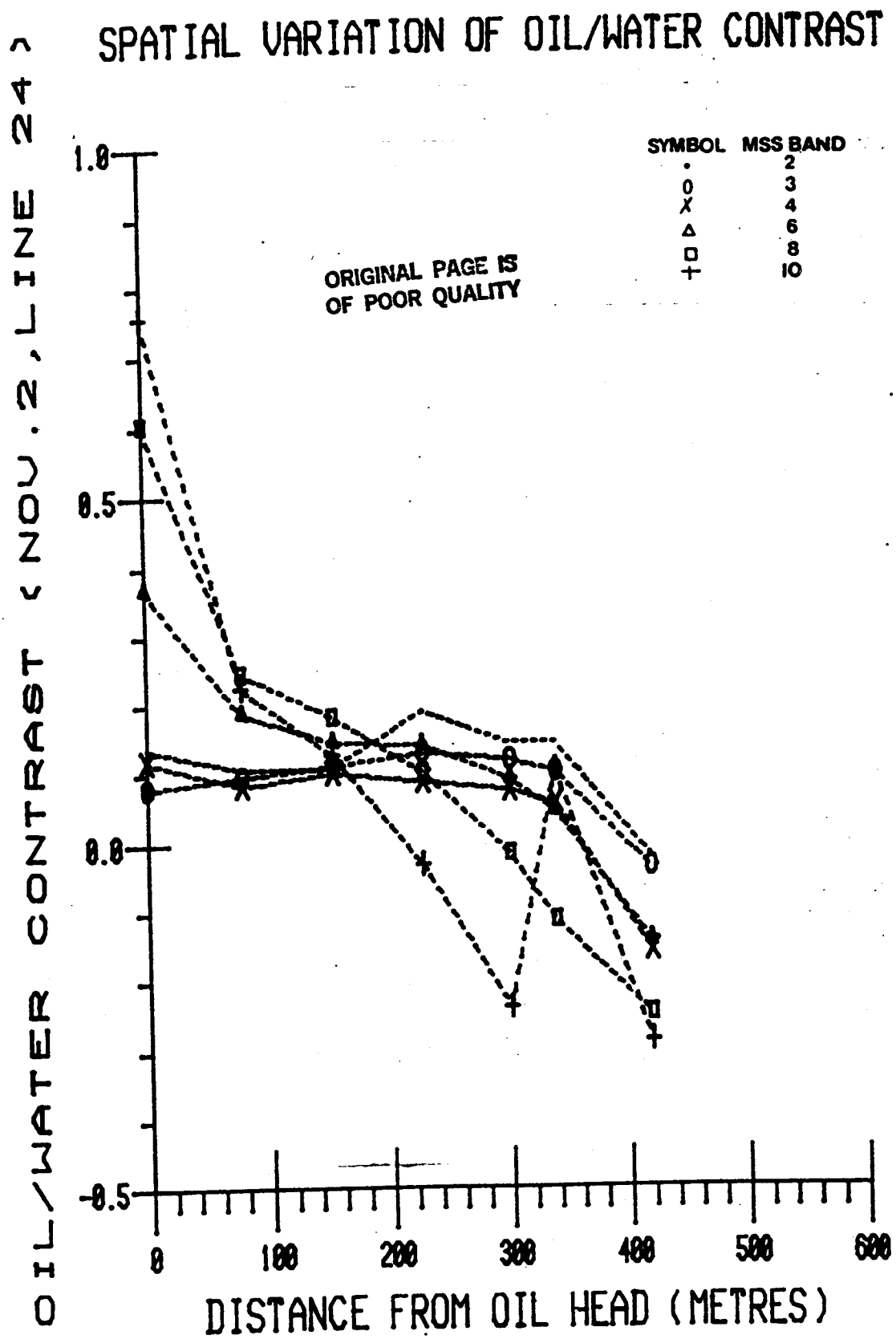

Figure 3.1.R. Spatial variation of oil/water contrast; 2 November, line 24

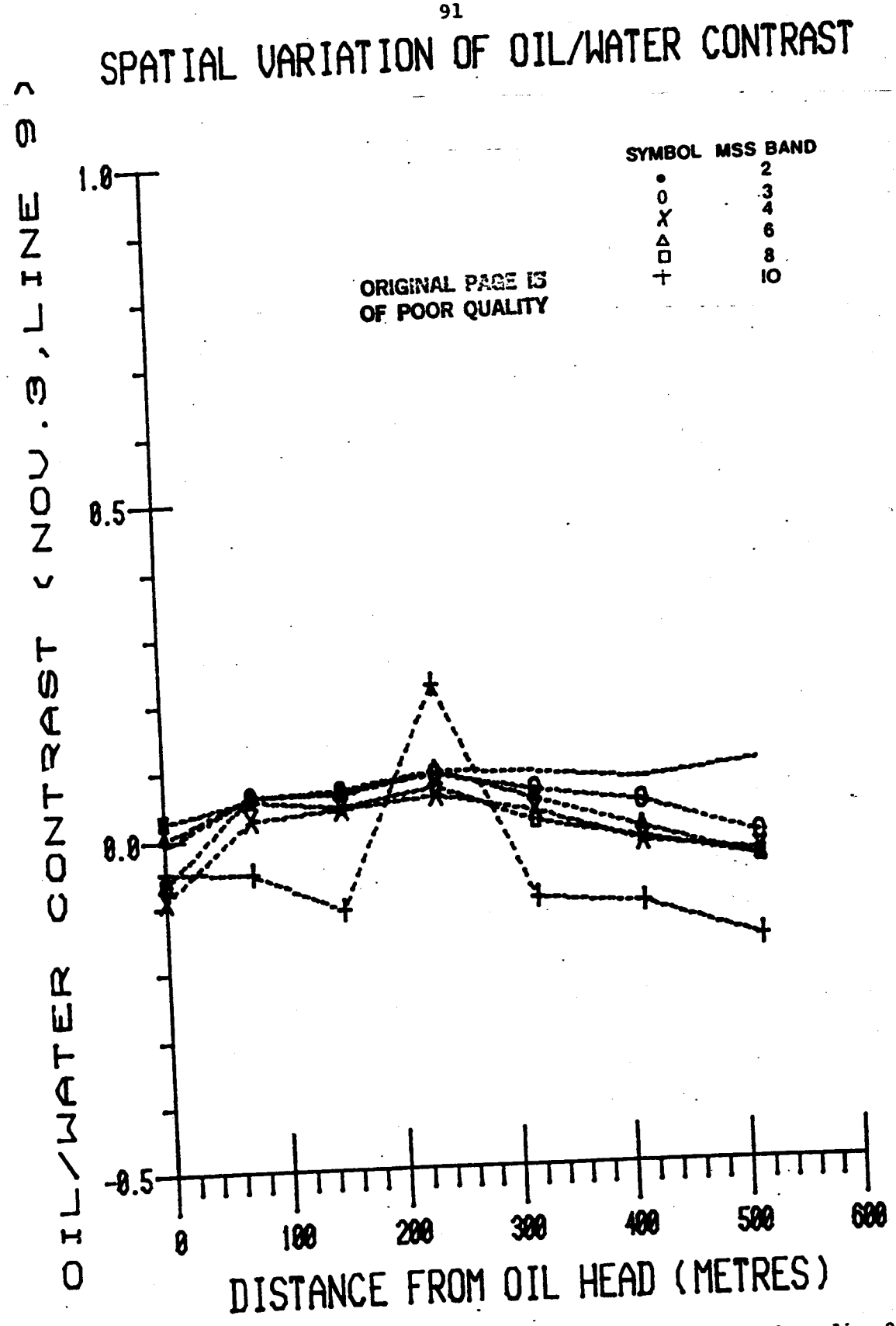

Figure 3.1.S. Spatial variation of oil/water contrast; 3 November, line 9

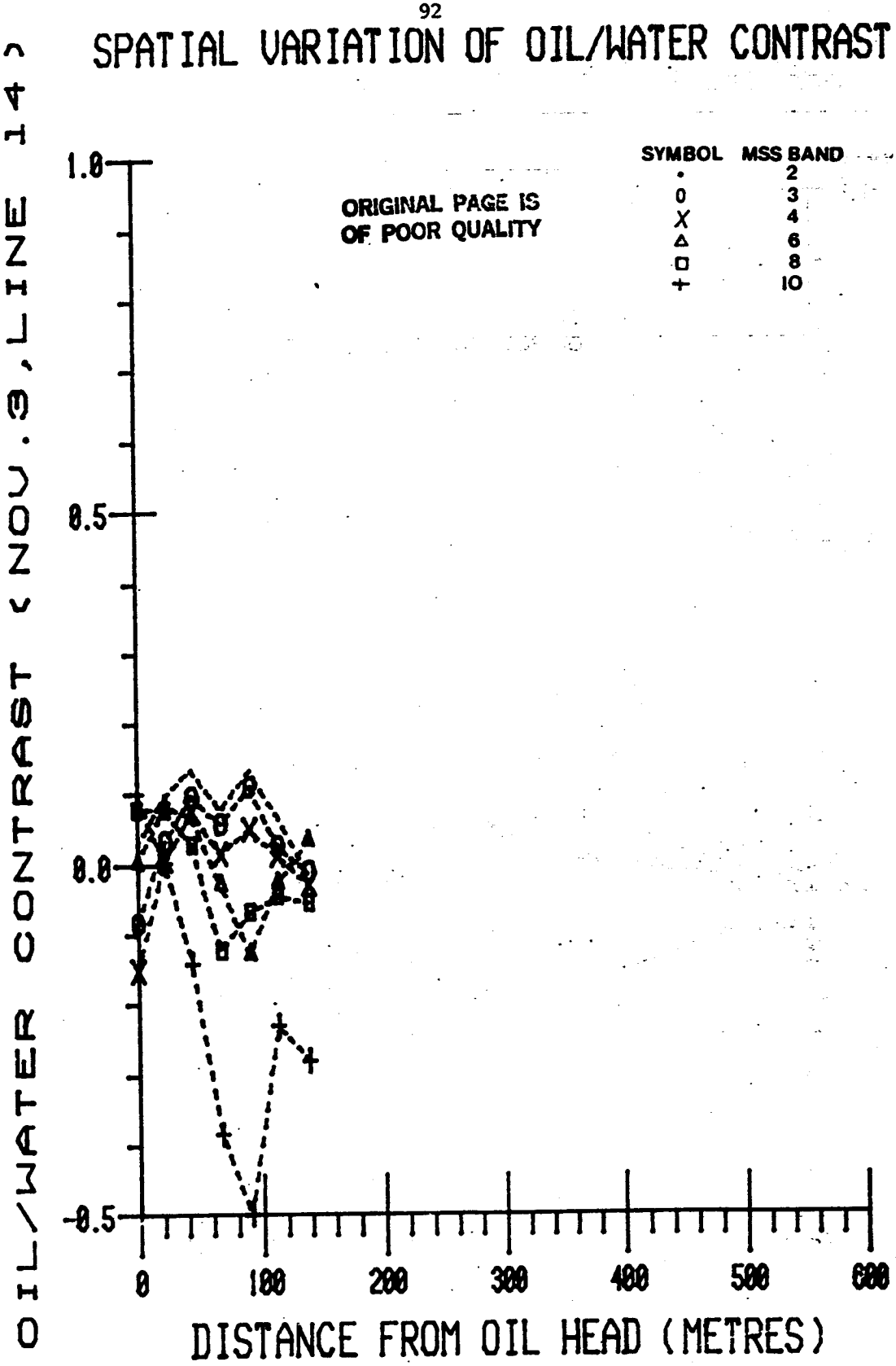

Figure 3.1.T. Spatial variation of oil/water contrast; 3 November, line 14

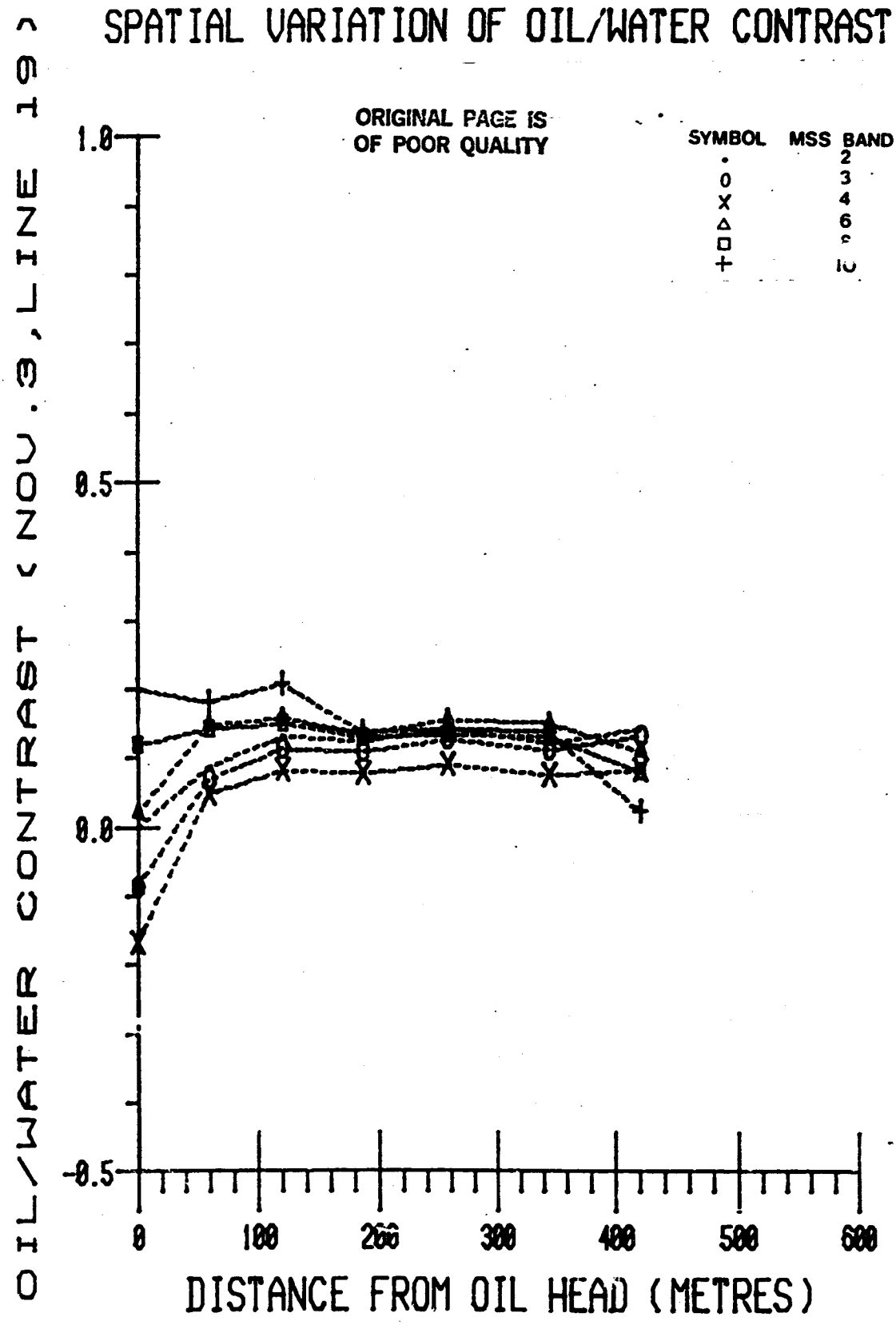

Figure 3.1.U. Spatial variation of oil/water contrast; 3 November, line 19

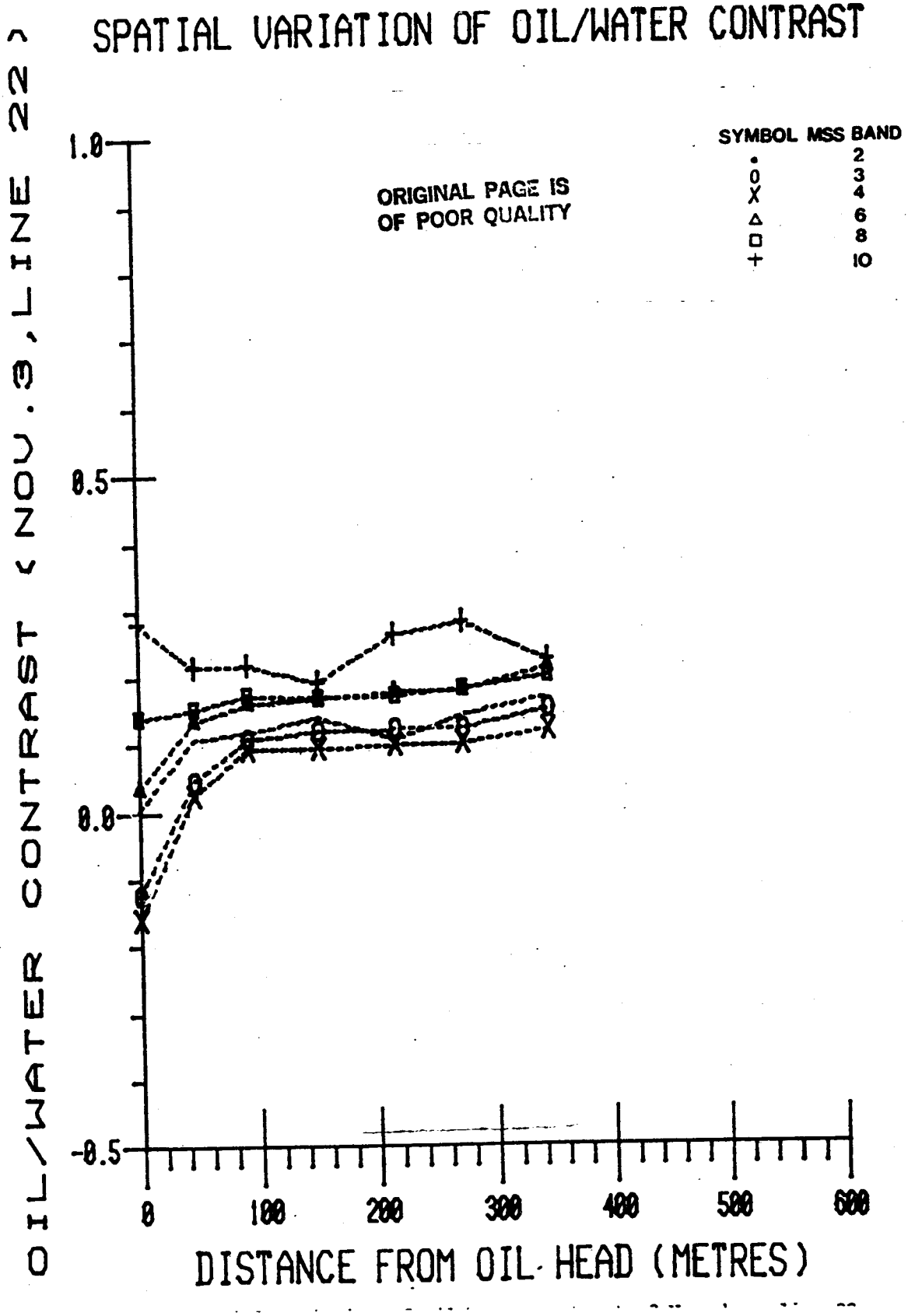
SPATIAL VARIATION OF OIL/WATER CONTRAST
ORIGINAL PAGE IS
OF POOR QUALITY
SYMBOL MSS BAND
• 2
0 3
X 4
△ 6
□ 8
+ 10
OIL/WATER CONTRAST (NOV.3,LINE 22)
1.0
0.5
0.0
-0.5
0
100
200
300
400
500
600
DISTANCE FROM OIL HEAD (METRES)

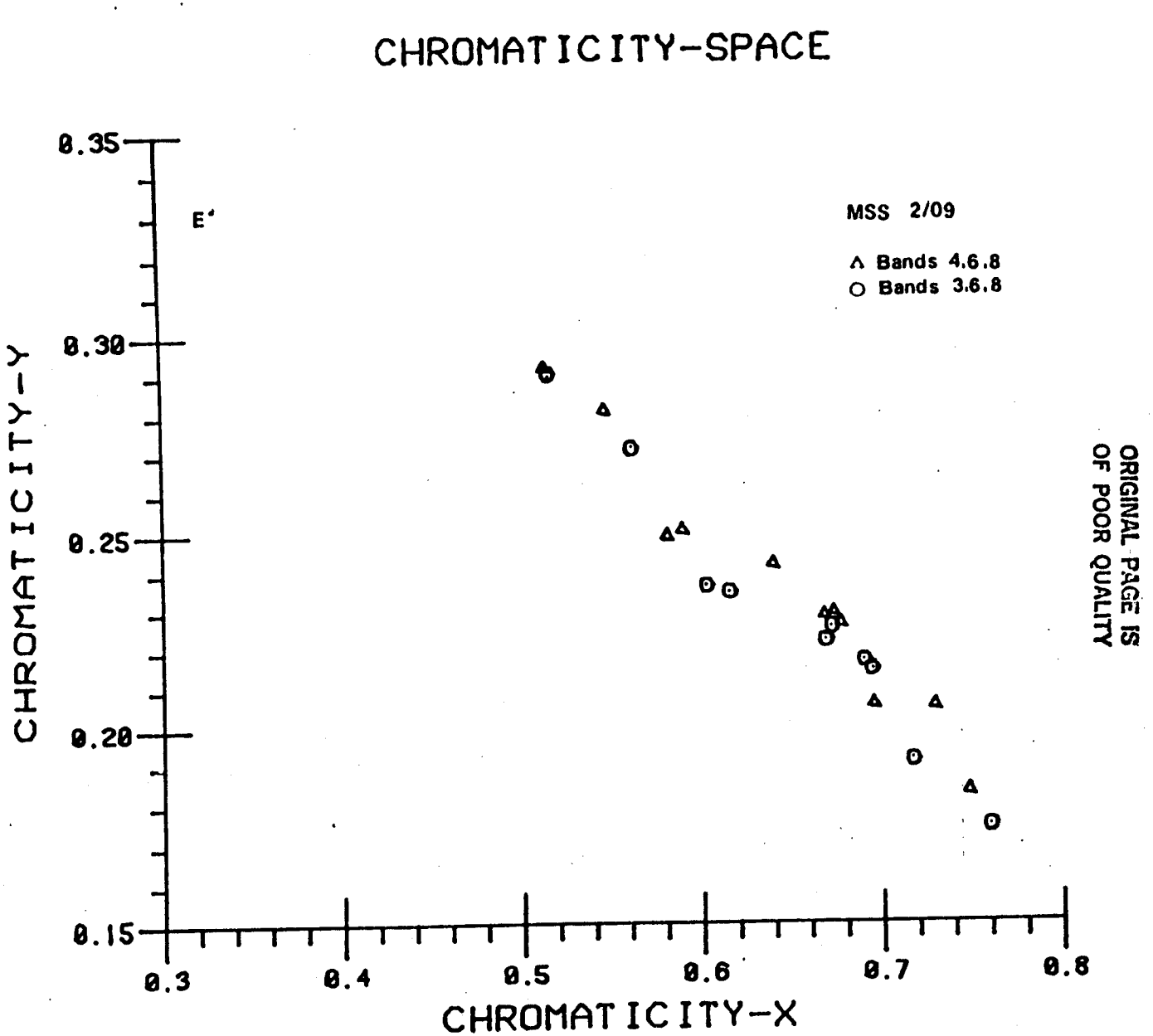

Figure 3.1.W. Oil/water chromaticities; 2 November, line 9

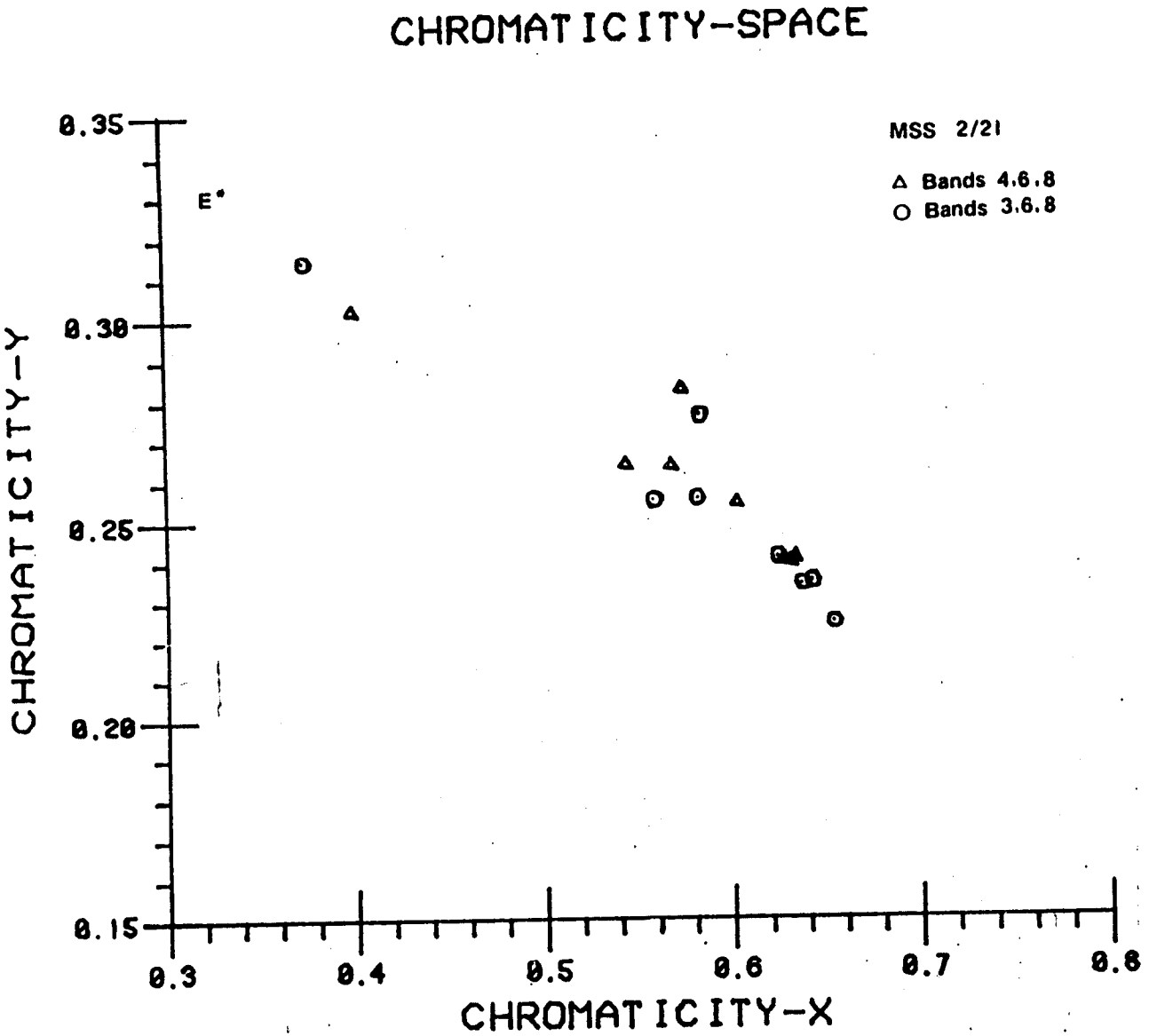

Figure 3.1.X. Oil/water chromaticities

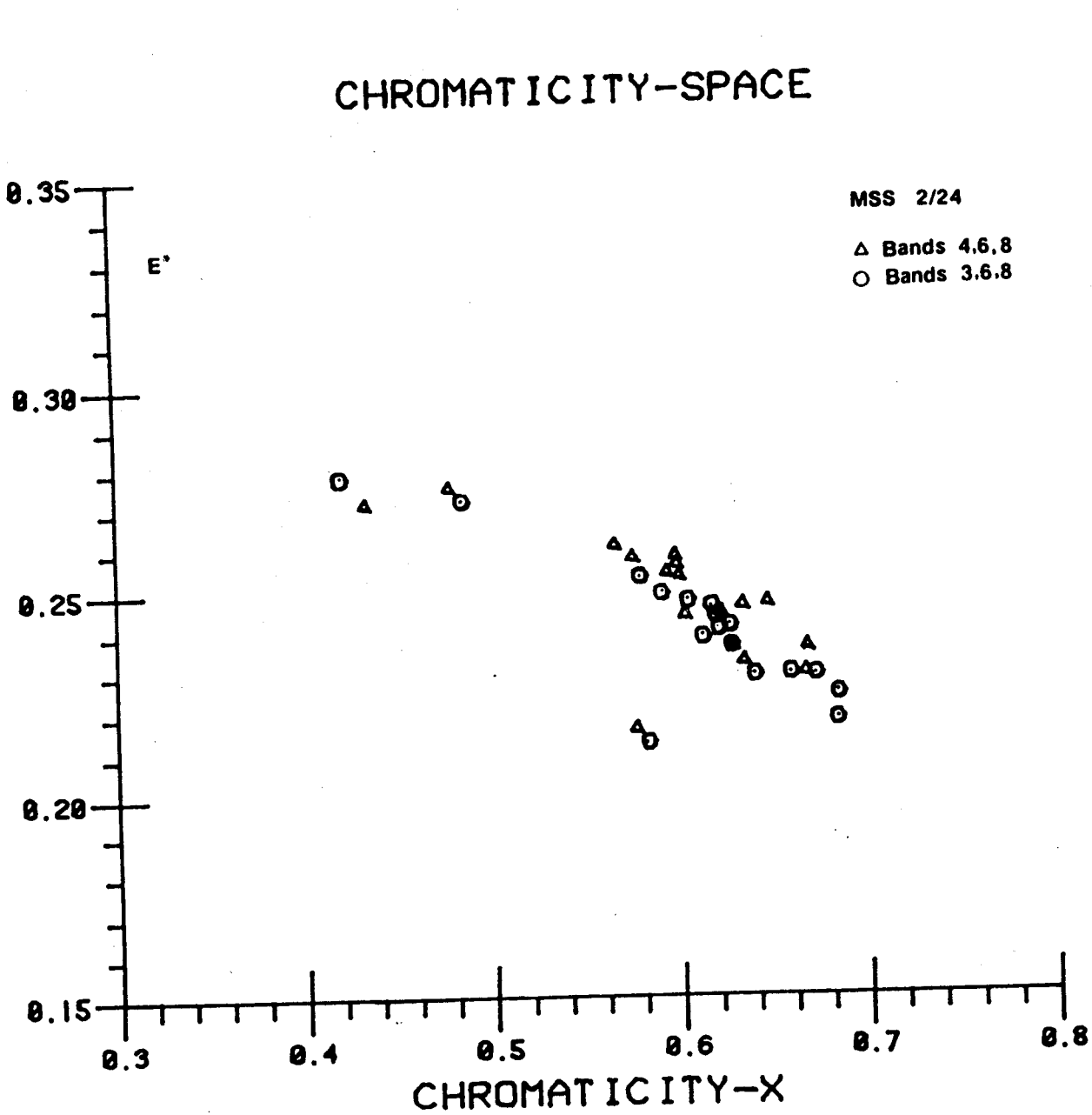

Figure 3.1.Y. Oil/water chromaticities

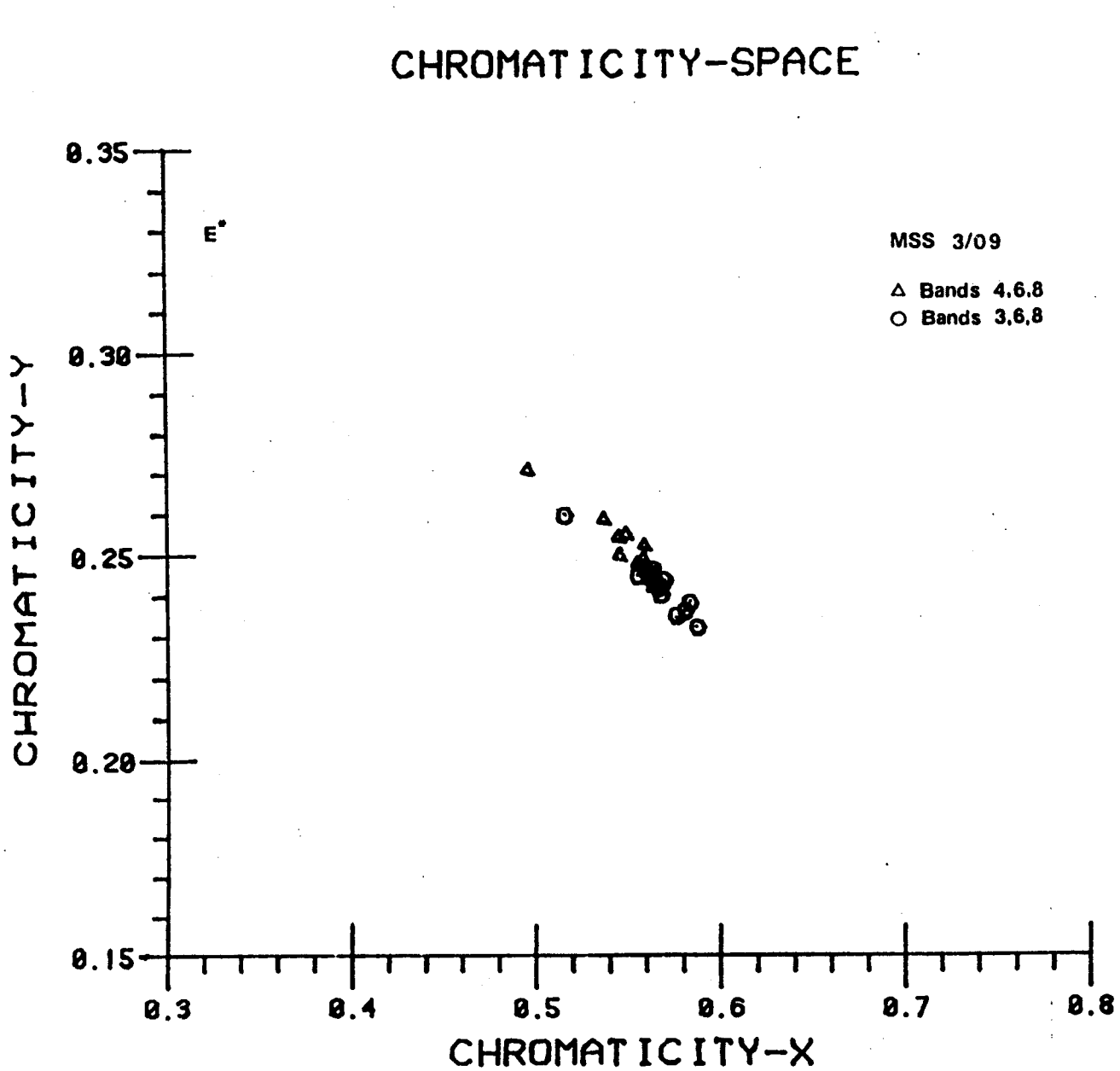

Figure 3.1.2. Oil/water chromaticities

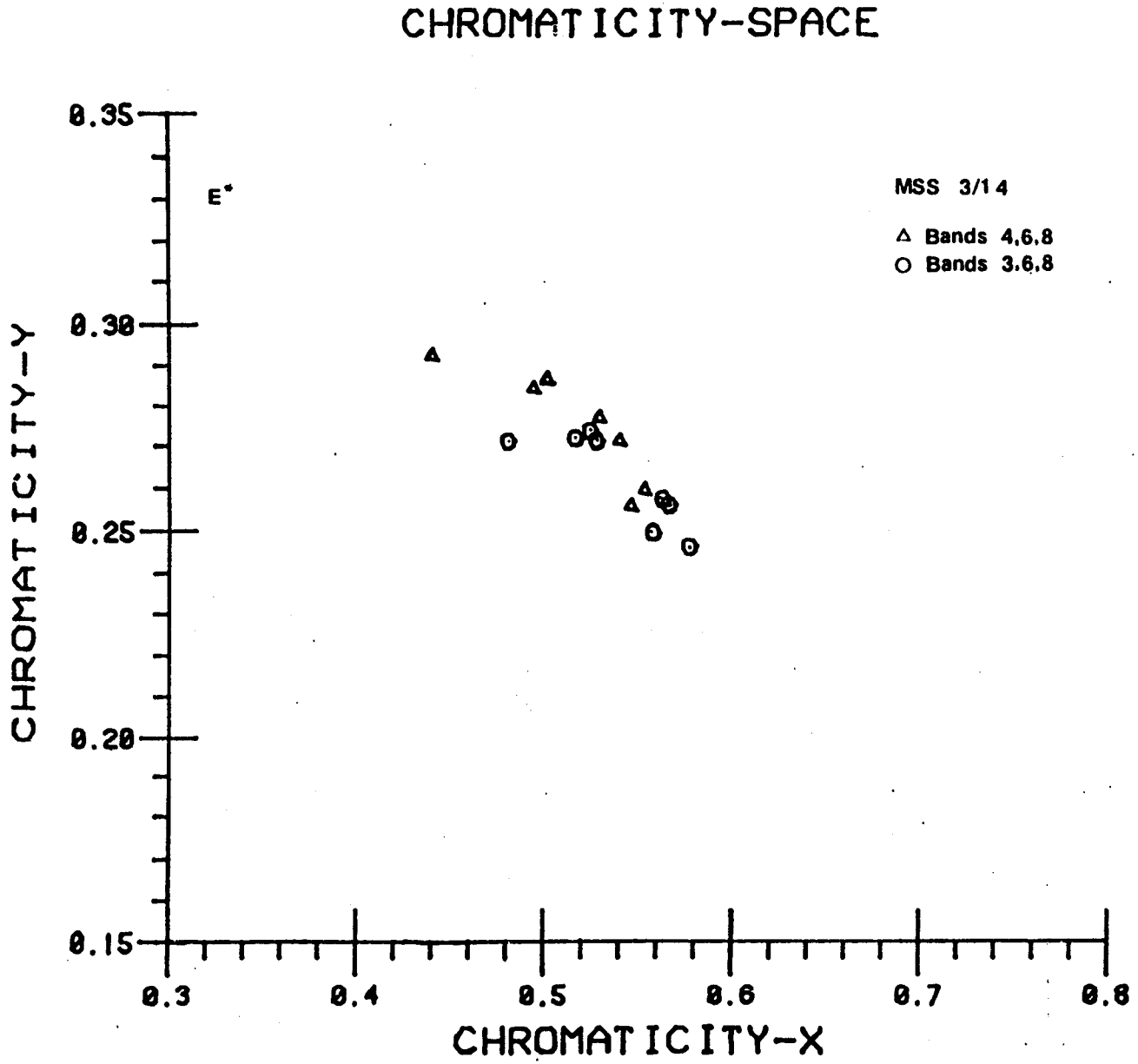

Figure 3.1.AA. Oil/water chromaticities

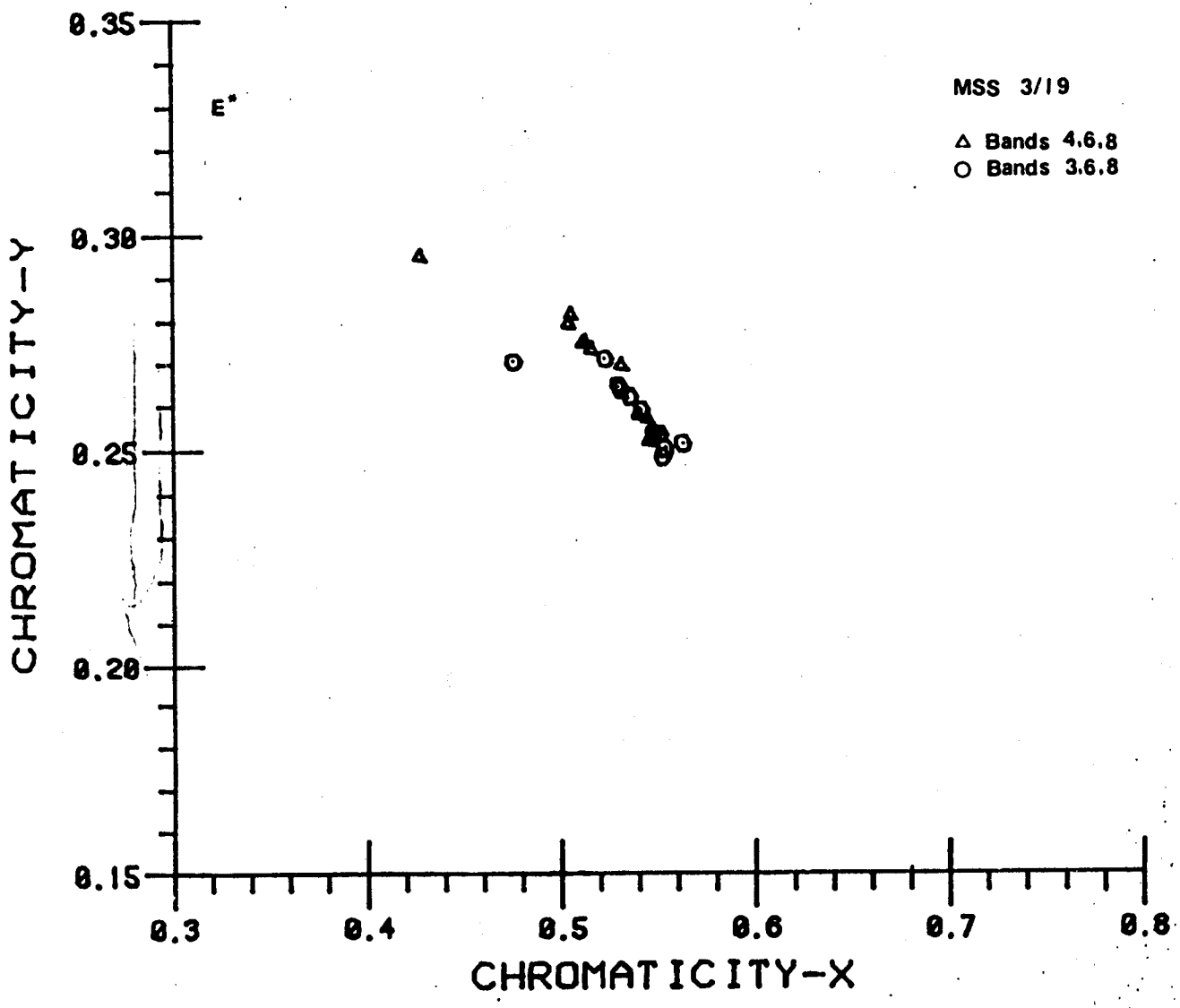

Figure 3.1.BB. Oil/water chromaticities

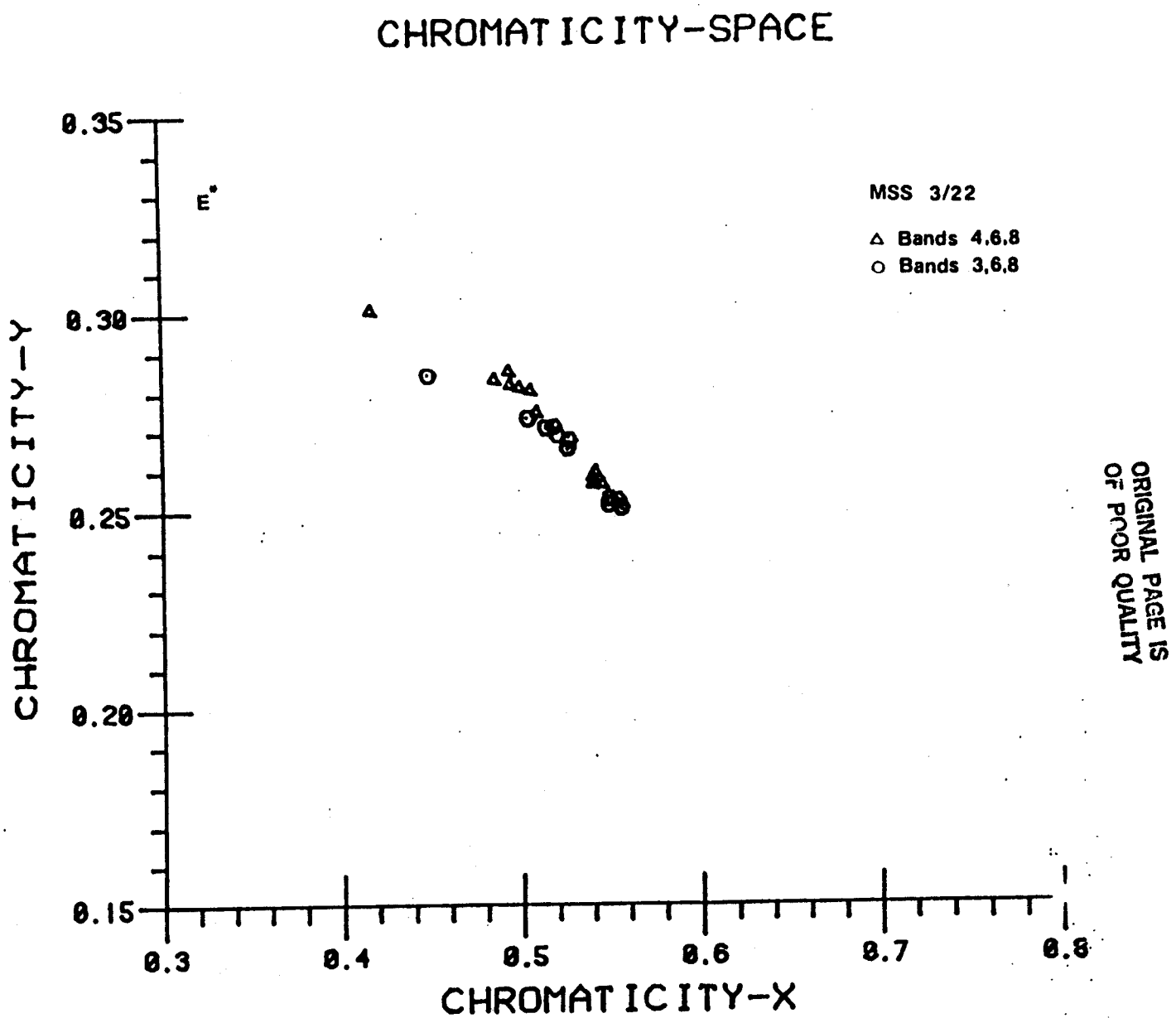

Figure 3.1.CC. Oil/water chromaticities

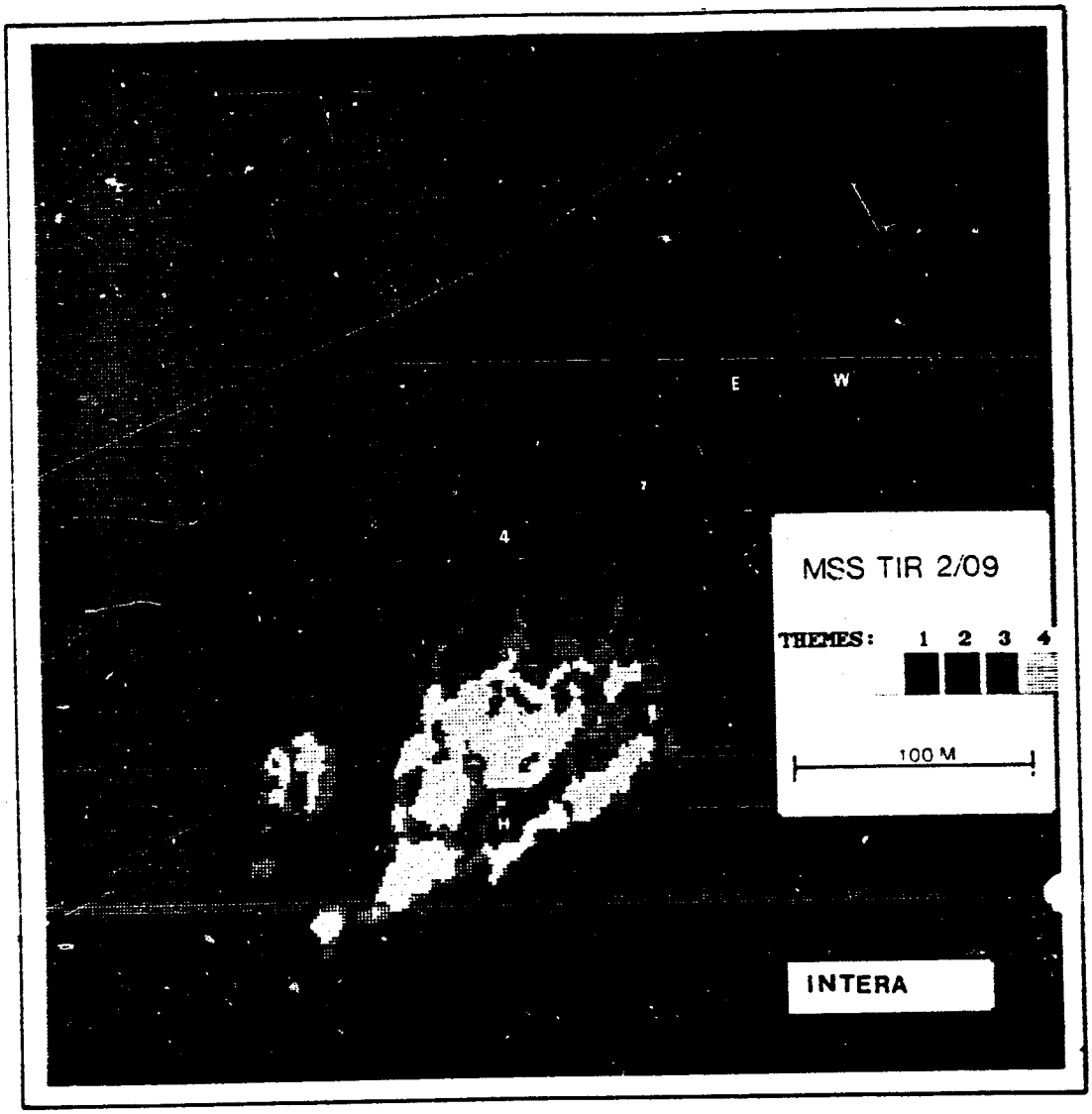

Figure 3.3.A. Thermal infrared record from the Multispectral Scanner; 2 November 1978; line 09. Data have been aspect-ratio corrected to present square pixels (no S-bend correction). Nearest neighbour theme filter applied, to smooth speckle. Radiometric calibration (for oil only):

Theme #	Radiance ($W\ m^{-2}\ \mu^{-1}\ sr^{-1}$)	Apparent Temp. (^{o} Kelvin)	Physical Temp. (^{o} Kelvin)
1	8.19	288.8	289.6
2	8.09	288.0	288.8
3	7.98	287.2	288.0
4	7.87	286.4	287.2
	7.76	285.6	286.4
Water	8.05	287.8	288.5

oil emissivity = 0.987

Alphanumeric characters show position of discrete data points in Figure 3.3.K.

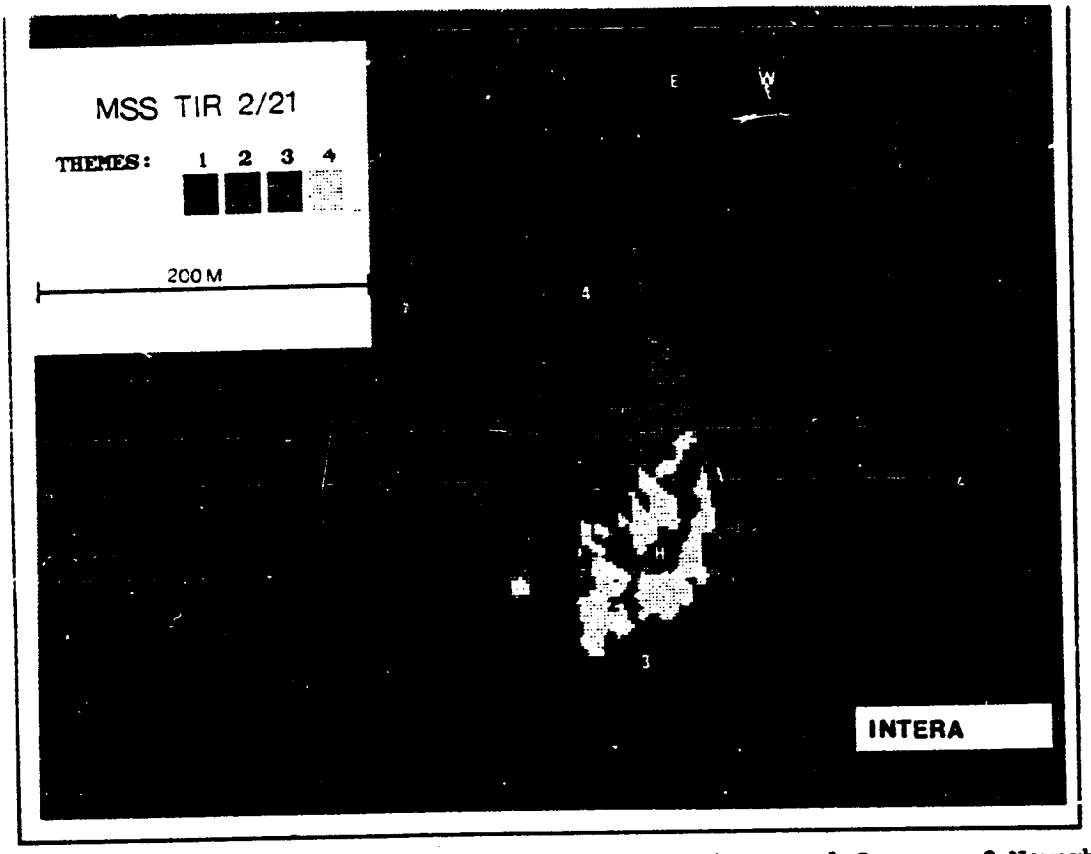

Figure 3.3.B. Thermal infrared record from the Multispectral Scanner; 2 November 1978; line 21. Data have been aspect-ratio corrected to present square pixels (no S-bend correction). Nearest neighbour theme filter applied, to smooth speckle. Radiometric calibration (for oil only):

Theme #	Radiance (W m^{-2} μ^{-1} sr^{-1})	Apparent Temp. (° Kelvin)	Physical Temp. (° Kelvin)
	7.95	287.0	287.8
1	7.87	286.4	287.2
2	7.78	285.8	286.5
3	7.70	285.1	285.9
4	7.62	284.5	285.3
Water	7.80	285.9	286.6
	oil emissivity = 0.987		

Alphanumeric characters show position of discrete data points in Figure 3.3.K.

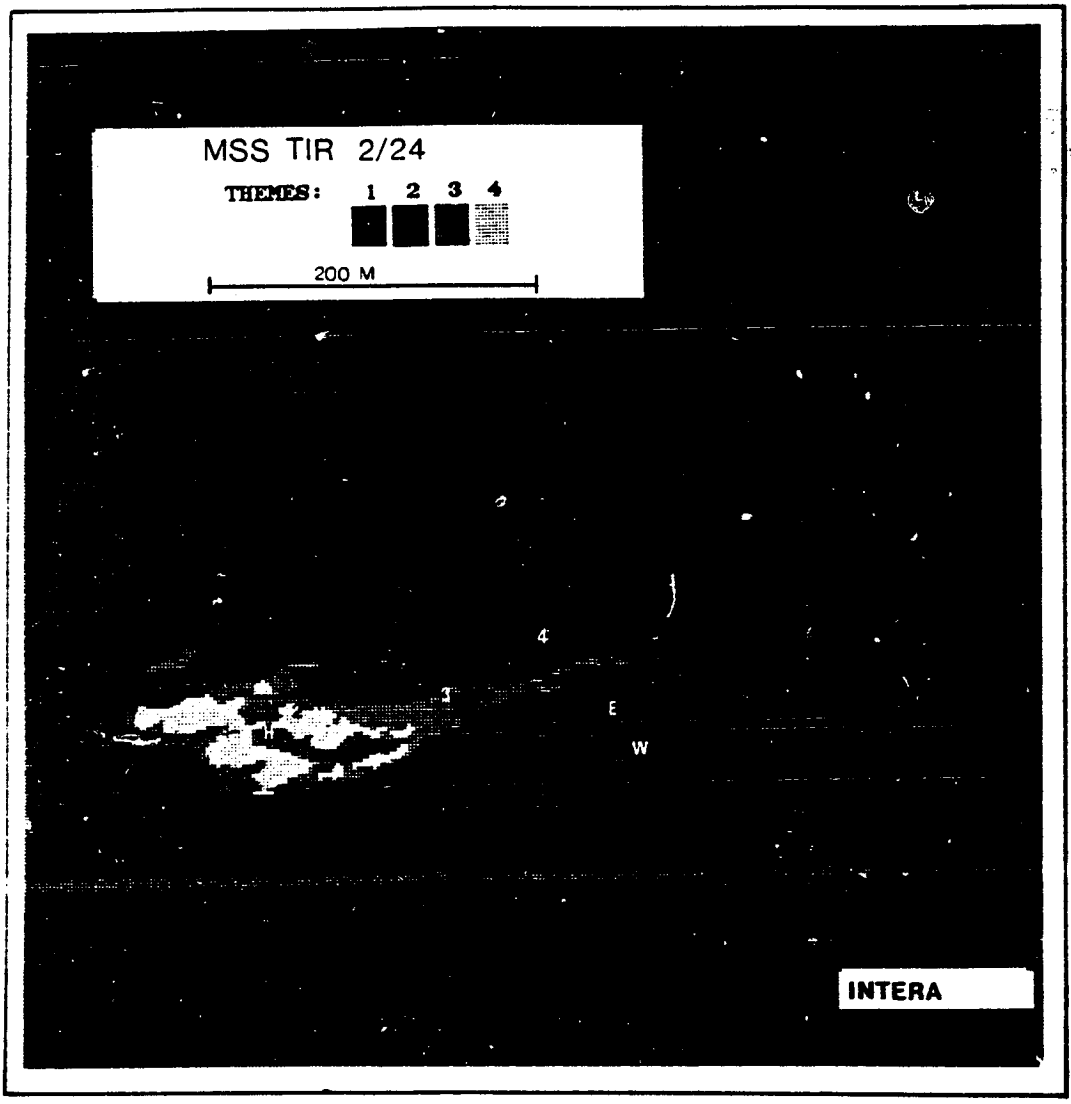

Figure 3.3.C. Thermal infrared record from the Multispectral Scanner; 2 November 1978; line 24. Data have been aspect-ratio corrected to present square pixels (no S-bend correction). Nearest neighbour theme filter applied, to smooth speckle. Radiometric calibration (for oil only):

Theme #	Radiance (W m^{-2} μ^{-1} sr^{-1})	Apparent Temp. (° Kelvin)	Physical Temp. (° Kelvin)
	8.17	288.6	289.5
1	7.81	286.0	286.8
2	7.96	287.1	287.9
3	8.02	287.6	288.4
4	8.01	287.5	238.3
Water	8.03	237.6	288.3
	oil emissivity = 0.986		

Alphanumeric characters show position of discrete data points in Figure 3.3.K.

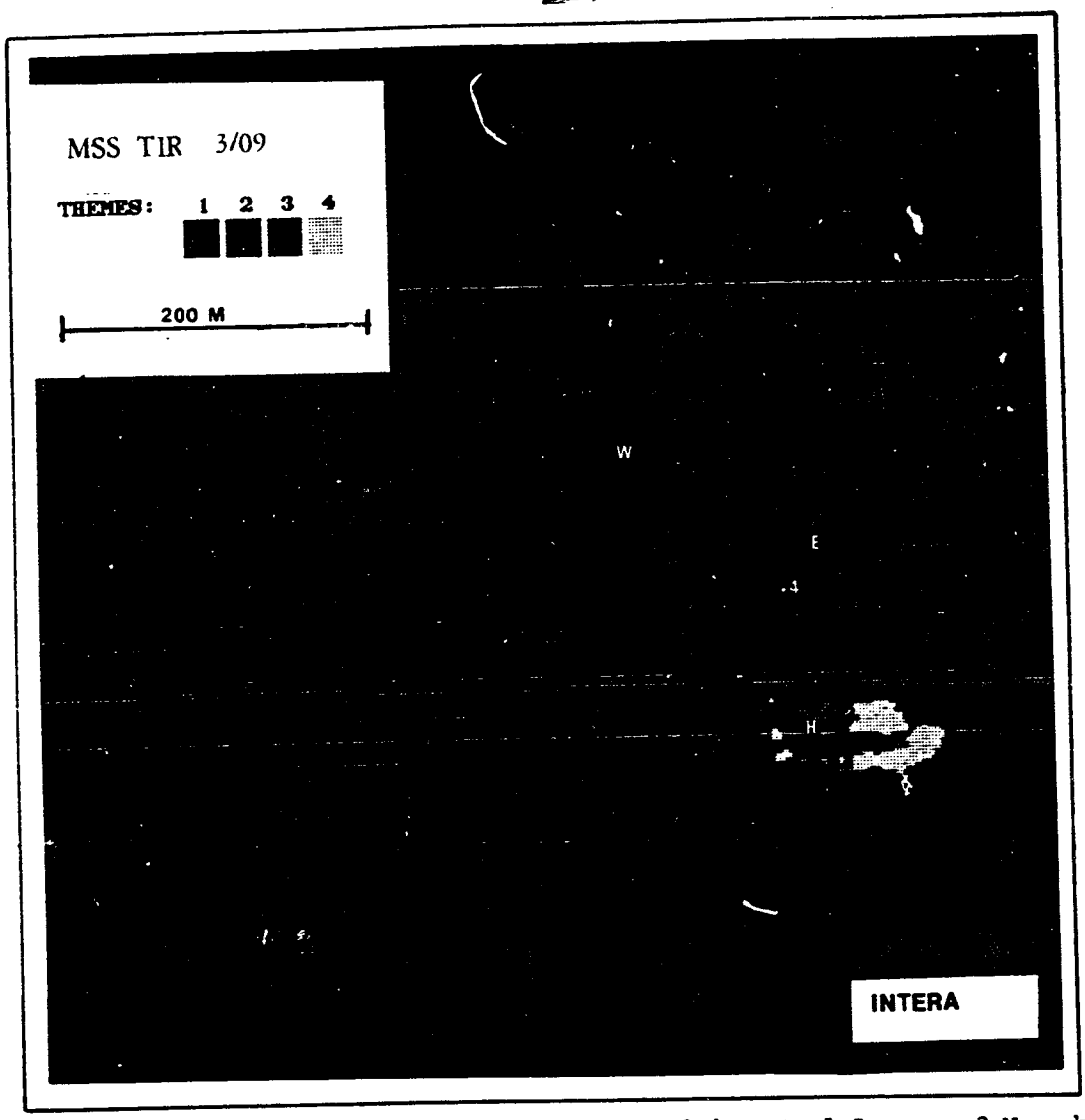

Figure 3.3.D. Thermal infrared record from the Multispectral Scanner; 3 November 1978; line 09. Data have been aspect-ratio corrected to present square pixels (no S-bend correction). Nearest neighbour theme filter applied, to smooth speckle. Radiometric calibration (for oil only):

Theme #	Radiance ($W\ m^{-2}\ \mu^{-1}\ sr^{-1}$)	Apparent Temp. (° Kelvin)	Physical Temp. (° Kelvin)
	8.05	287.8	288.7
1	7.98	287.2	288.1
2	7.90	286.6	287.5
3	7.82	286.0	286.9
4	7.74	285.5	286.3
Water	8.03	287.6	288.3

oil emissivity = 0.986

Alphanumeric characters show position of discrete data points in Figure 3.3.K.

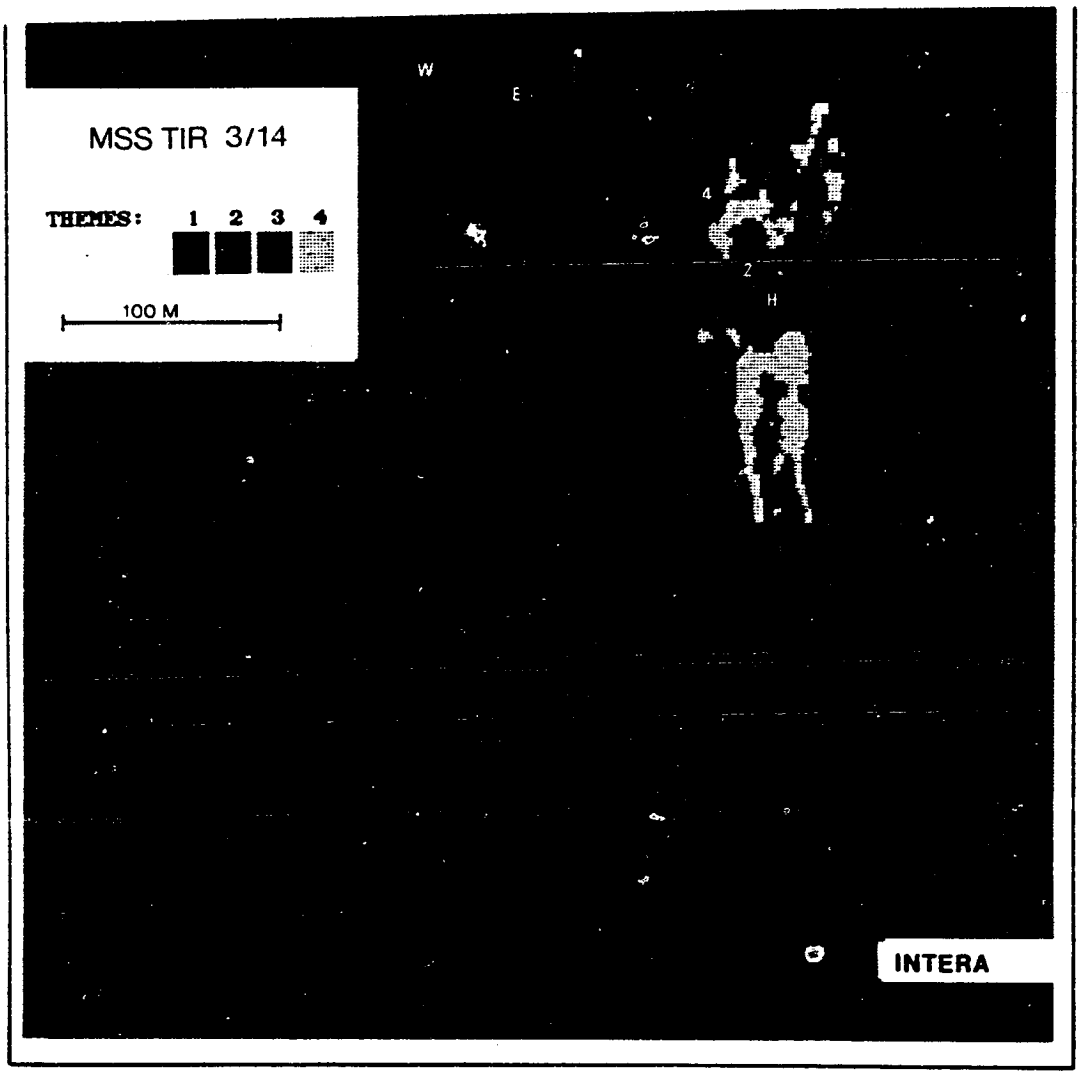

Figure 3.3.E. Thermal infrared record from the Multispectral Scanner; 3 November 1978; line 14. Data have been aspect-ratio corrected to present square pixels (no S-bend correction). Nearest neighbour theme filter applied, to smooth speckle. Radiometric calibration (for oil only):

Theme #	Radiance (W m^{-2} μ^{-1} sr^{-1})	Apparent Temp. (° Kelvin)	Physical Temp. (° Kelvin)
	8.17	288.7	289.5
1	8.03	287.6	288.4
2	7.89	286.6	287.4
3	7.75	285.5	286.3
4	7.61	284.5	285.2
Water	8.02	287.6	288.3
	oil emissivity = 0.987		

Alphanumeric characters show position of discrete data points in Figure 3.3.K.

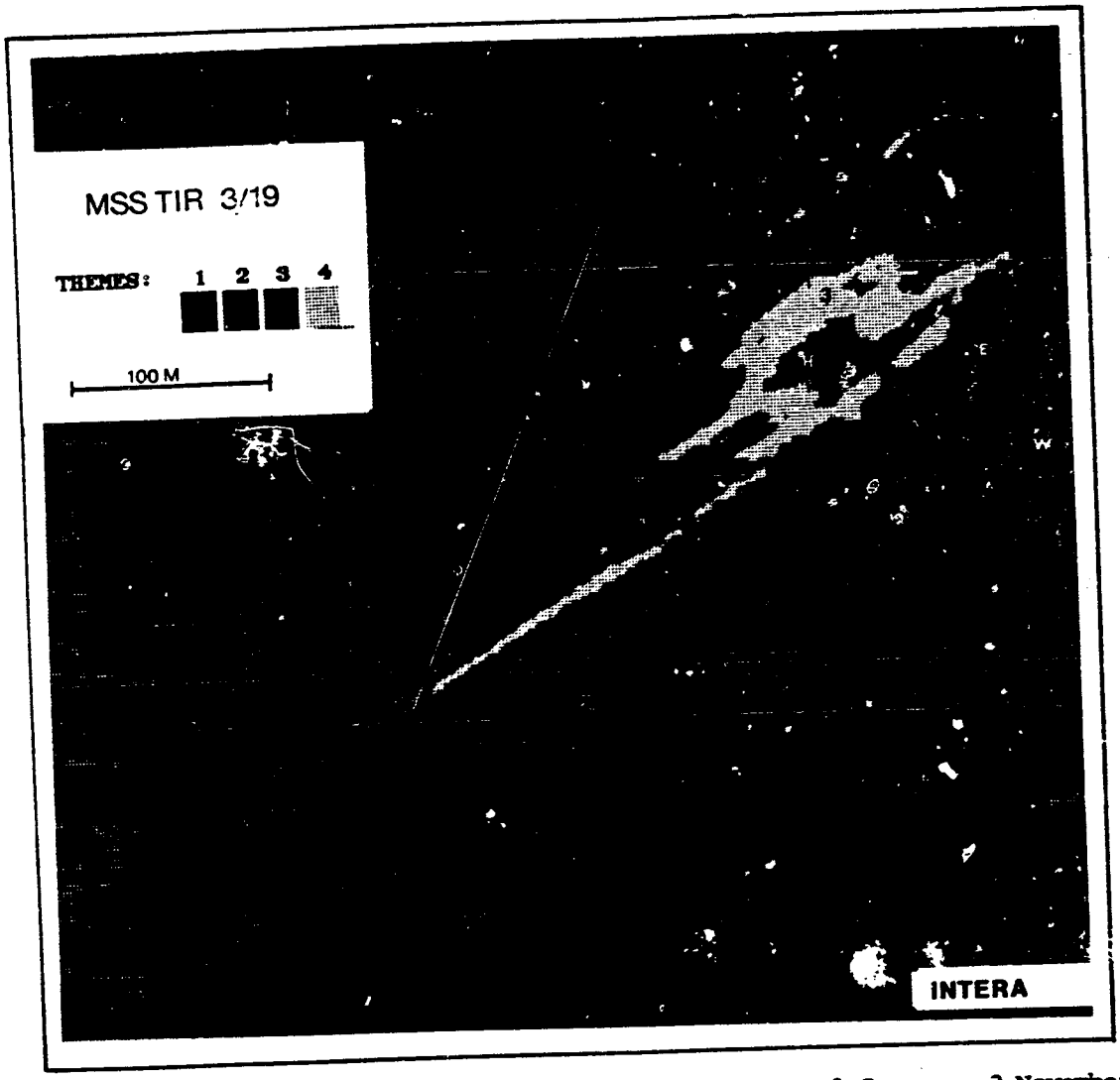

Figure 3.3.F. Thermal infrared record from the Multispectral Scanner; 3 November 1978; line 19. Data have been aspect-ratio corrected to present square pixels (no S-bend correction). Nearest neighbour theme filter applied, to smooth speckle. Radiometric calibration (for oil only):

Theme #	Radiance (W m^{-2} μr^{-1} sr^{-1})	Apparent Temp. (o Kelvin)	Physical Temp. (o Kelvin)
	8.35	289.9	291.0
1	8.19	288.8	289.8
2	8.03	287.6	288.6
3	7.87	286.4	287.4
4	7.72	285.3	286.2
Water	8.05	287.8	288.5

oil emissivity = 0.984

Alphanumeric characters show position of discrete data points in Figure 3.3.K.

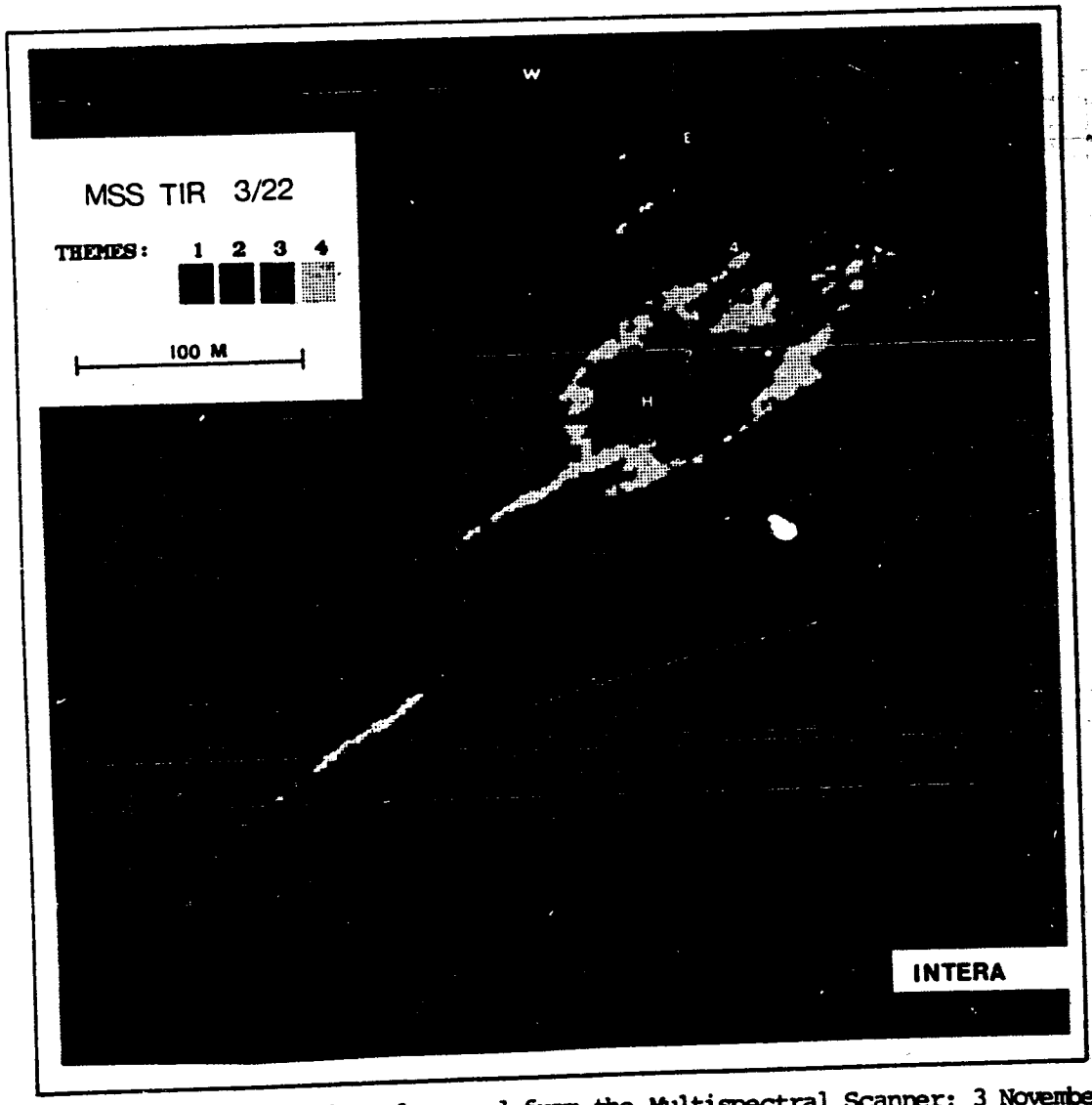

Figure 3.3.G. Thermal infrared record from the Multispectral Scanner; 3 November 1978; line 22. Data have been aspect-ratio corrected to present square pixels (no S-bend correction). Nearest neighbour theme filter applied, to smooth speckle. Radiometric calibration (for oil only):

Theme #	Radiance ($W\ m^{-2}\ \mu^{-1}\ sr^{-1}$)	Apparent Temp. (° Kelvin)	Physical Temp. (° Kelvin)
	8.34	289.9	290.7
1	8.22	289.0	289.8
2	8.10	288.1	288.9
3	7.98	287.2	288.0
4	7.86	286.3	287.1
Water	8.21	289.0	289.7

oil emissivity = 0.987

Alphanumeric characters show position of discrete data points in Figure 3.3.K

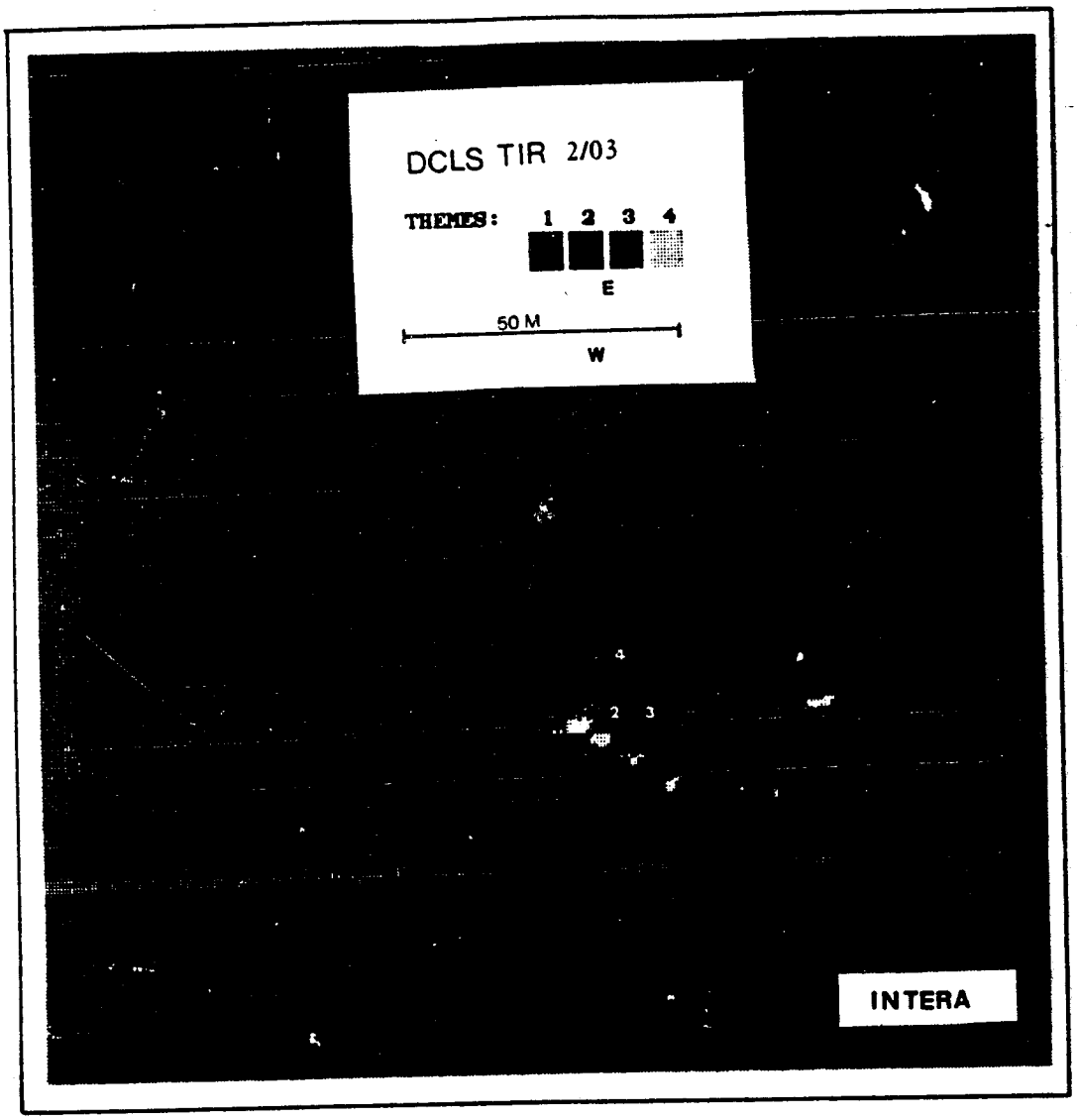

Figure 3.3.H. Thermal infrared record from the Dual-Channel Line Scanner; 2 November 1978; line 03. Data have been aspect-ratio and S-bend corrected, and a low-pass video filter applied to smooth speckle. Radiometric calibration (for oil only):

Theme #	Radiance ($W\ m^{-2}\ \mu^{-1}\ sr^{-1}$)	Apparent Temp. (° Kelvin)	Physical Temp. (° Kelvin)
	7.76	285.6	286.4
1	7.91	286.7	287.6
2	8.10	288.1	289.0
3	8.30	289.6	290.5
4	8.48	291.0	291.8
Water	8.22	289.0	289.7
	oil emissivity =	0.986	

Alphanumeric characters show position of discrete data points in Figure 3.3.K. and Table 3.2.A.

ORIGINAL PAGE
BLACK AND WHITE PHOTOGRAPH

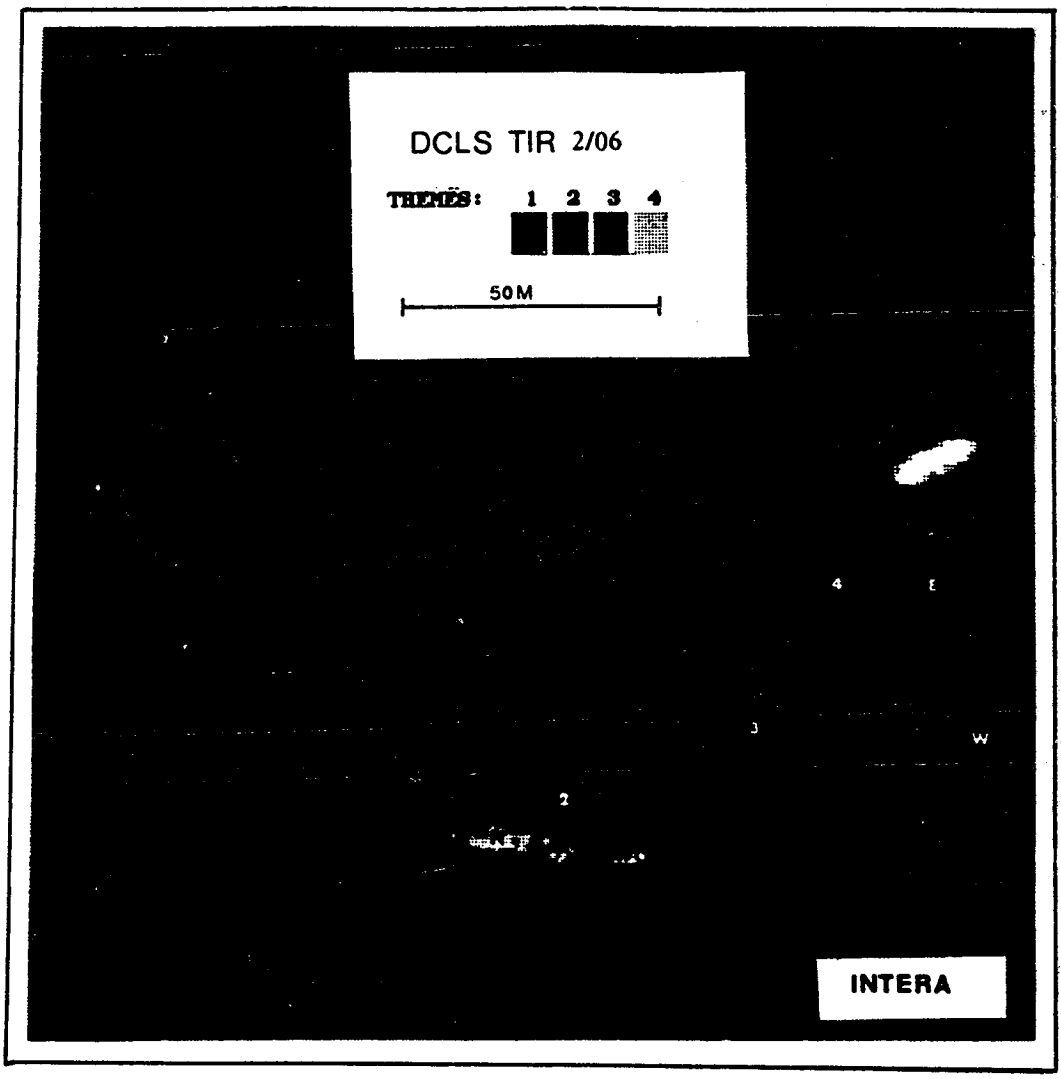

Figure 3.3.I. Thermal infrared record from the Dual-Channel Line Scanner; 2 November 1978; line 06. Data have been aspect-ratio and S-bend corrected, and a low-pass video filter applied to smooth speckle. Radiometric calibration (for oil only):

Theme #	Radiance ($W\ m^{-2}\ \mu^{-1}\ sr^{-1}$)	Apparent Temp. (° Kelvin)	Physical Temp. (° Kelvin)
1	7.72	285.3	286.1
2	7.92	286.8	287.6
3	8.12	288.3	289.1
4	8.33	289.8	290.6
Water	8.53	291.2	289.3
	8.16	288.6	289.3

oil emissivity = 0.987

Alphanumeric characters show position of discrete data points in Figure 3.3.K and Table 3.2.A.

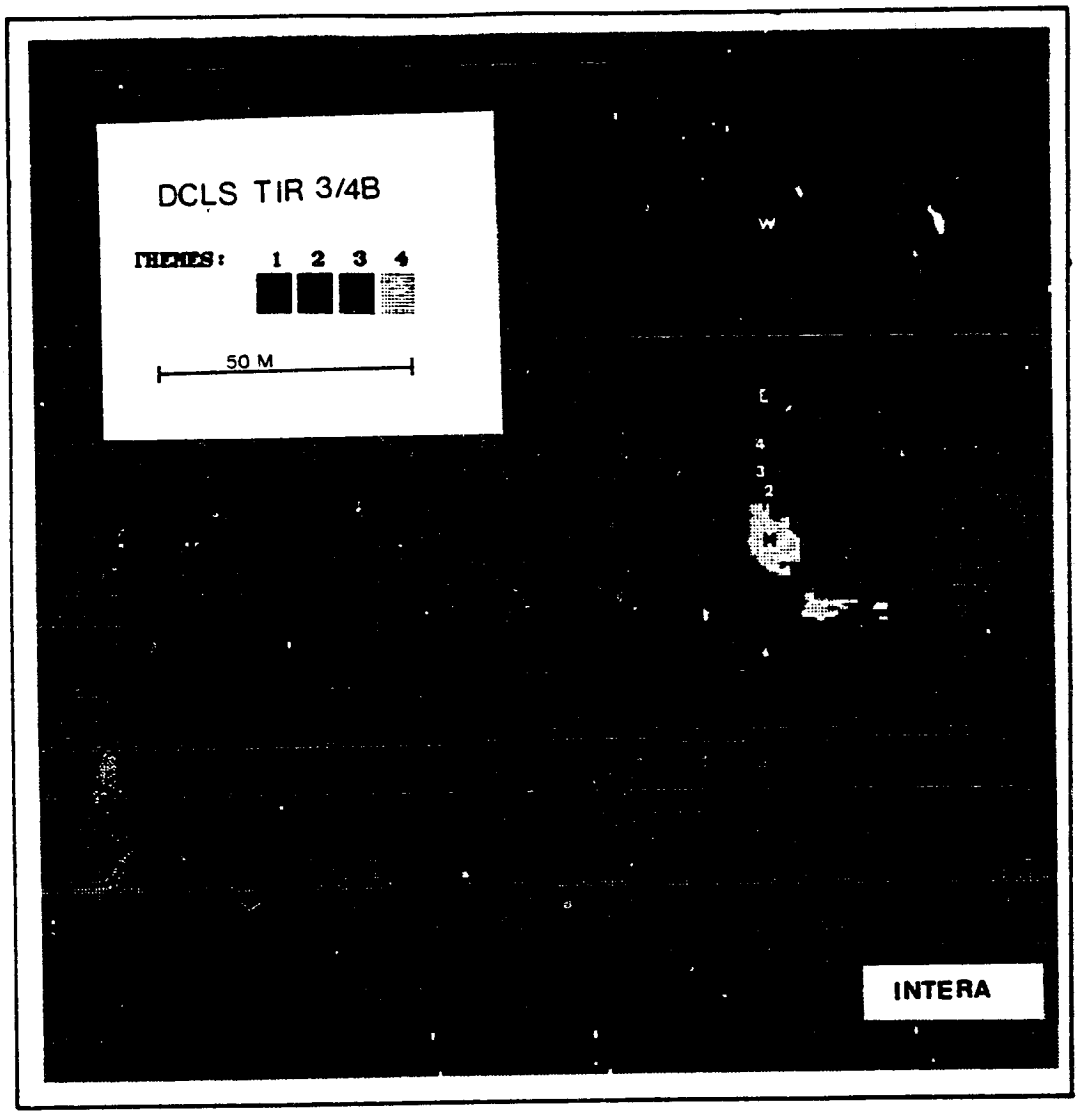

Figure 3.3.J. Thermal infrared record from the Dual-Channel Line Scanner; 3 November 1978; line 4B. Data has been aspect ratio corrected (no S-bend correction), and a low-pass video filter applied to smooth speckle. Radiometric calibration (for oil only):

Theme #	Radiance ($W\ m^{-2}\ \mu^{-1}\ sr^{-1}$)	Apparent Temp. (° Kelvin)	Physical Temp. (° Kelvin)
	7.69	285.1	285.8
1	7.96	287.1	287.9
2	8.13	288.4	289.2
3	8.59	291.7	292.5
4	8.88	293.8	294.6
Water	8.18	288.7	289.5

oil emissivity = 0.987

Alphanumeric characters show position of discrete data points in Figure 3.3.K and Table 3.2.A.

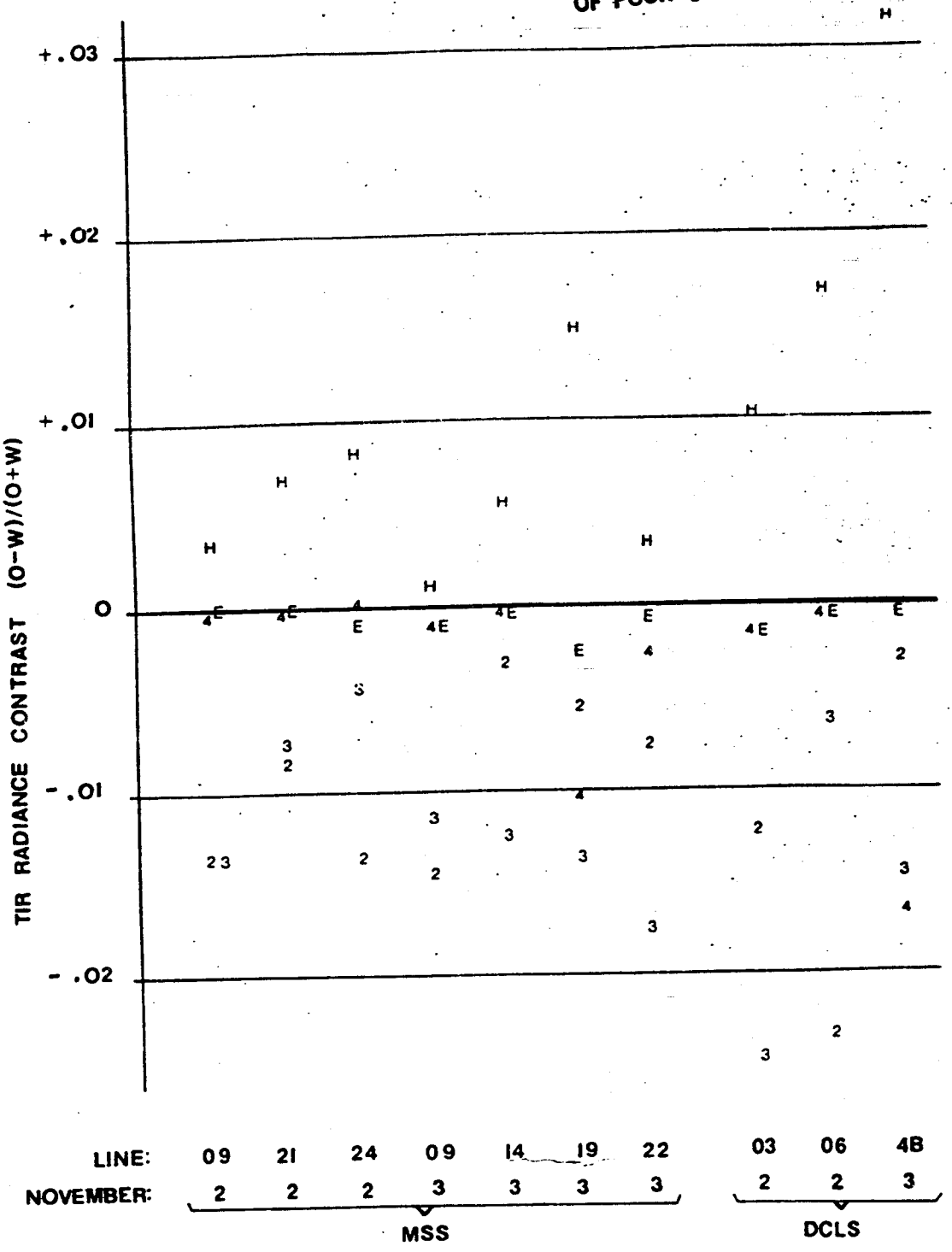

Figure 3.3.K. Thermal infrared radiance contrast of oil/water from the MSS and DCLS. Murban crude on 2 November, La Rosa crude on 3 November. Alphanumeric codes refer to spot locations identified on Figures 3.3.A through 7. Spatial progression is: H (= oil head), 2, 3, 4, E (= edge of slick).

ORIGINAL PAGE IS
OF POOR QUALITY

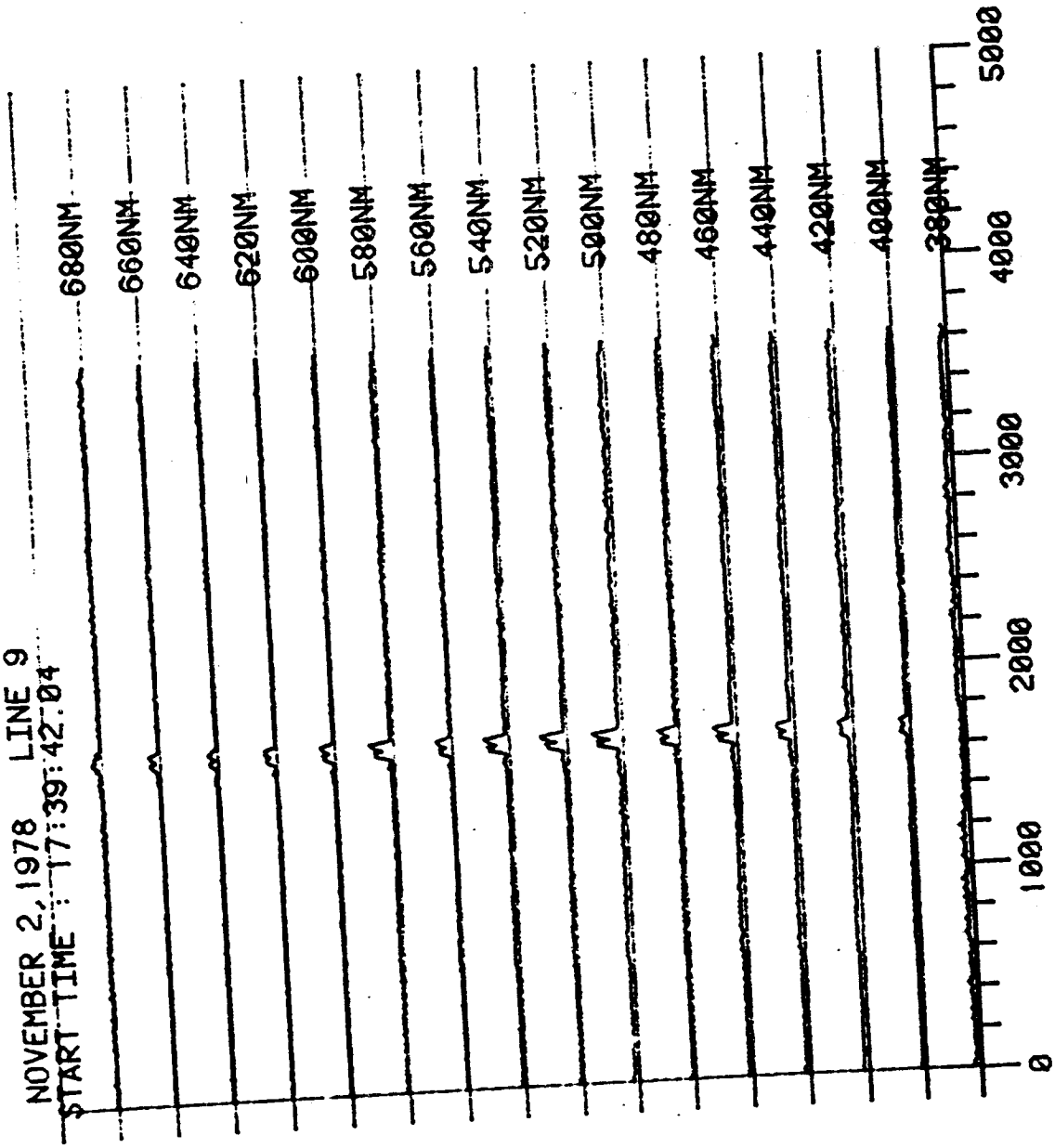

Figure 3.4.A. Fluorescence spectrum: history for Murban crude oil transect at sampling rate of 100 Hz

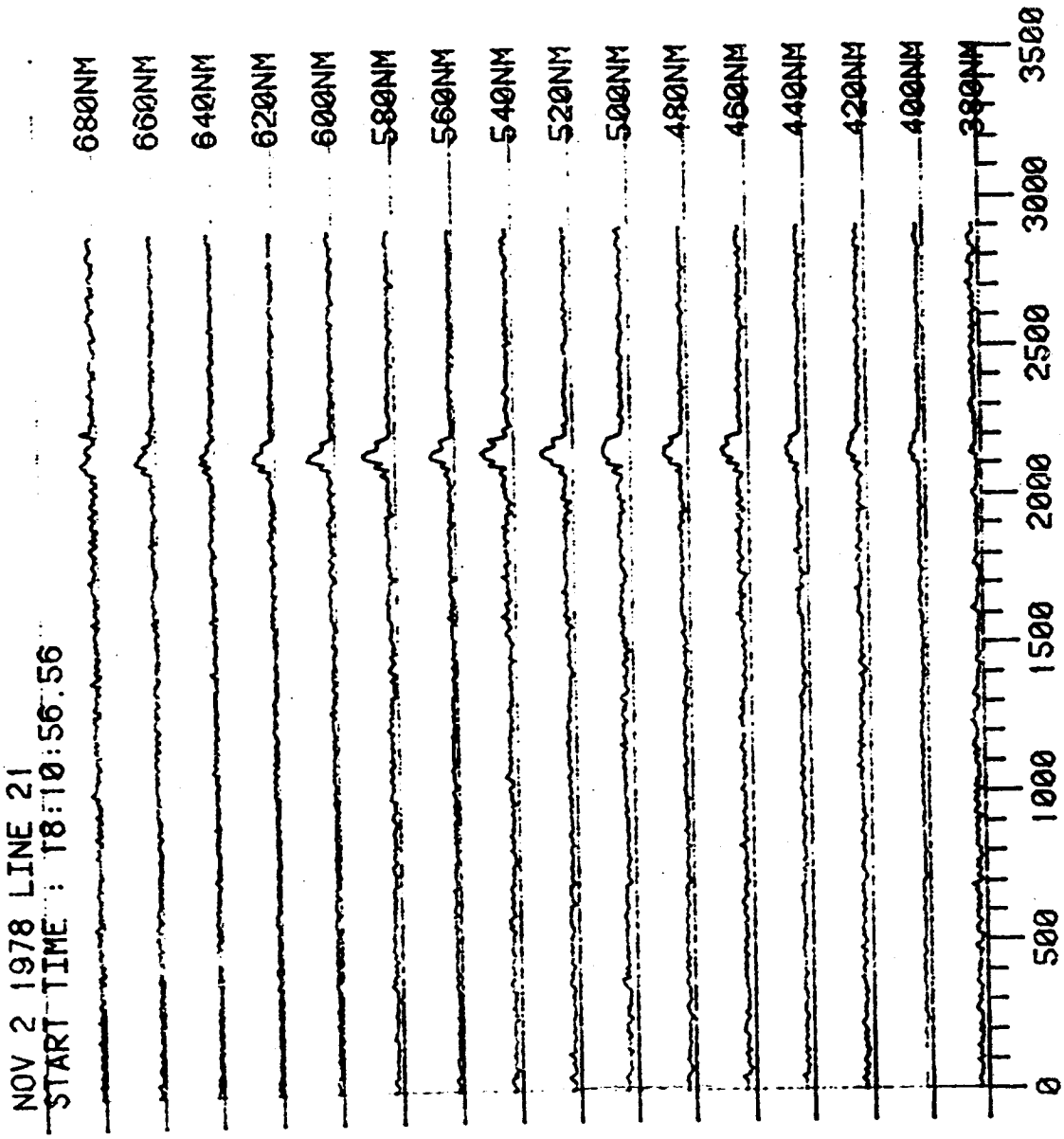

Figure 3.4.B. Fluorescence spectrum: history for Murban crude oil transect at sampling rate of 100 Hz

ORIGINAL PAGE IS
OF POOR QUALITY

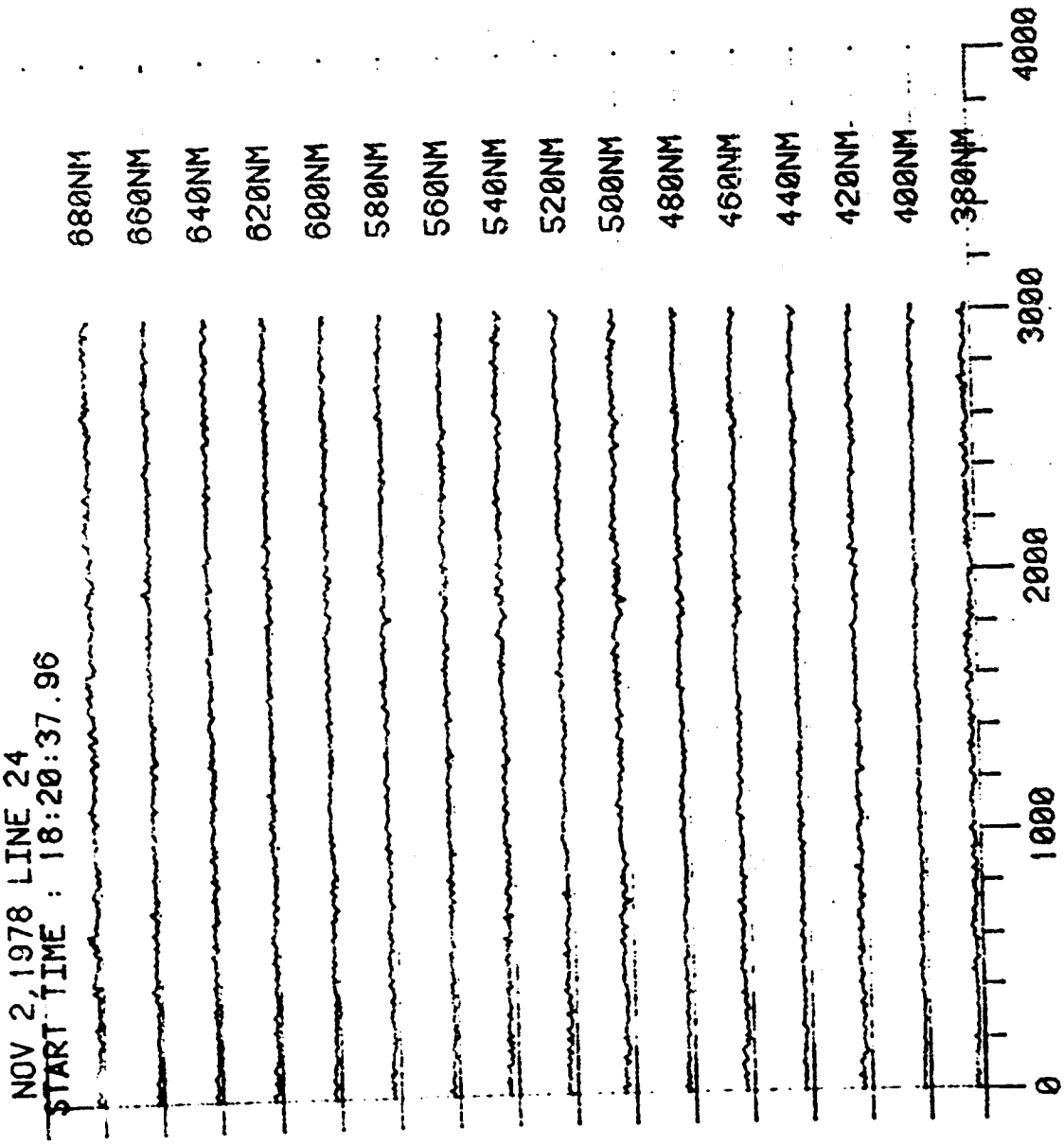

Figure 3.4.C. Fluorescence spectrum: history for Murban crude oil transect at sampling rate of 100 Hz

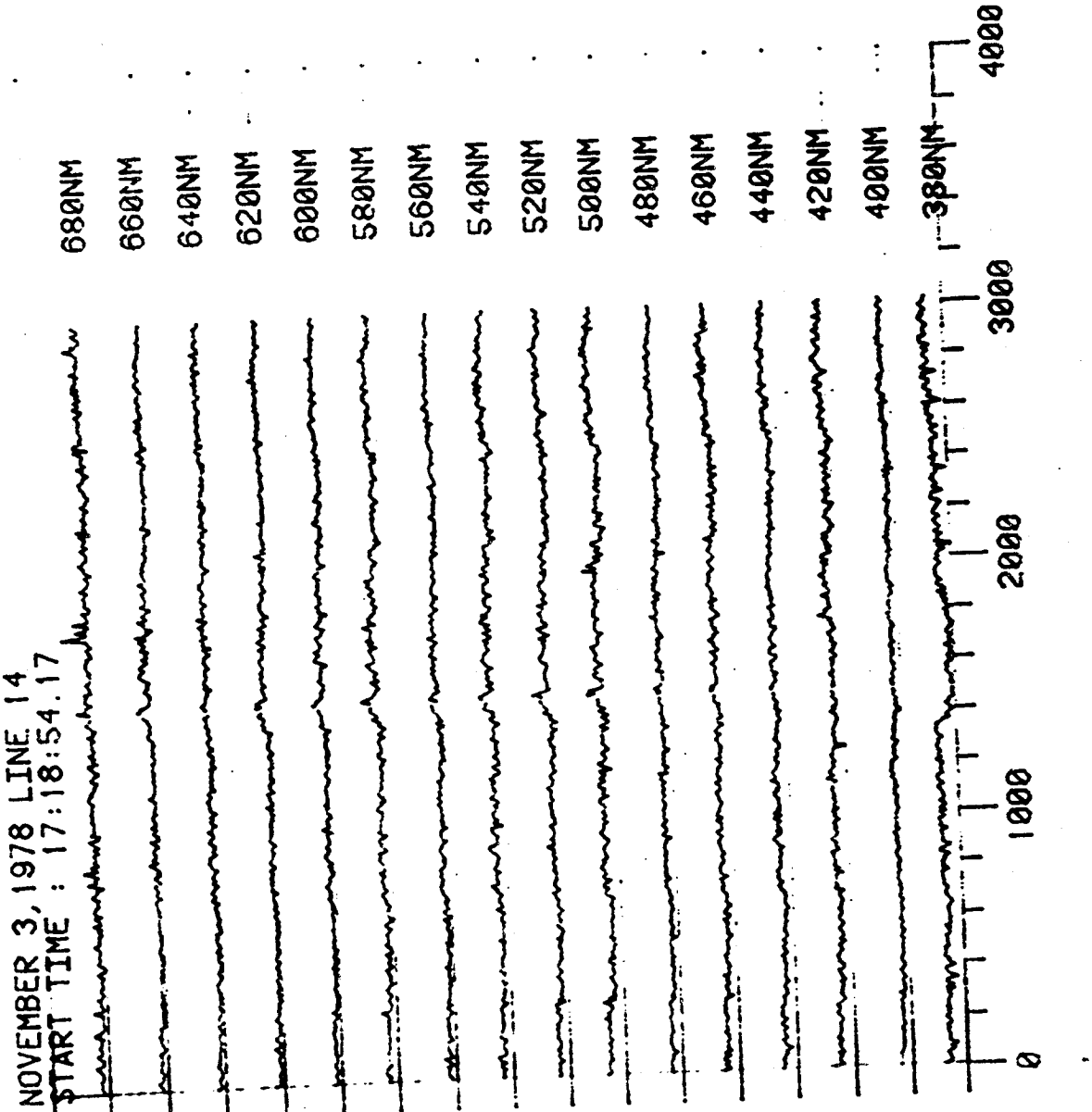

Figure 3.4.D. Fluorescence spectrum: history for La Rosa crude oil transect at sampling rate of 100 Hz

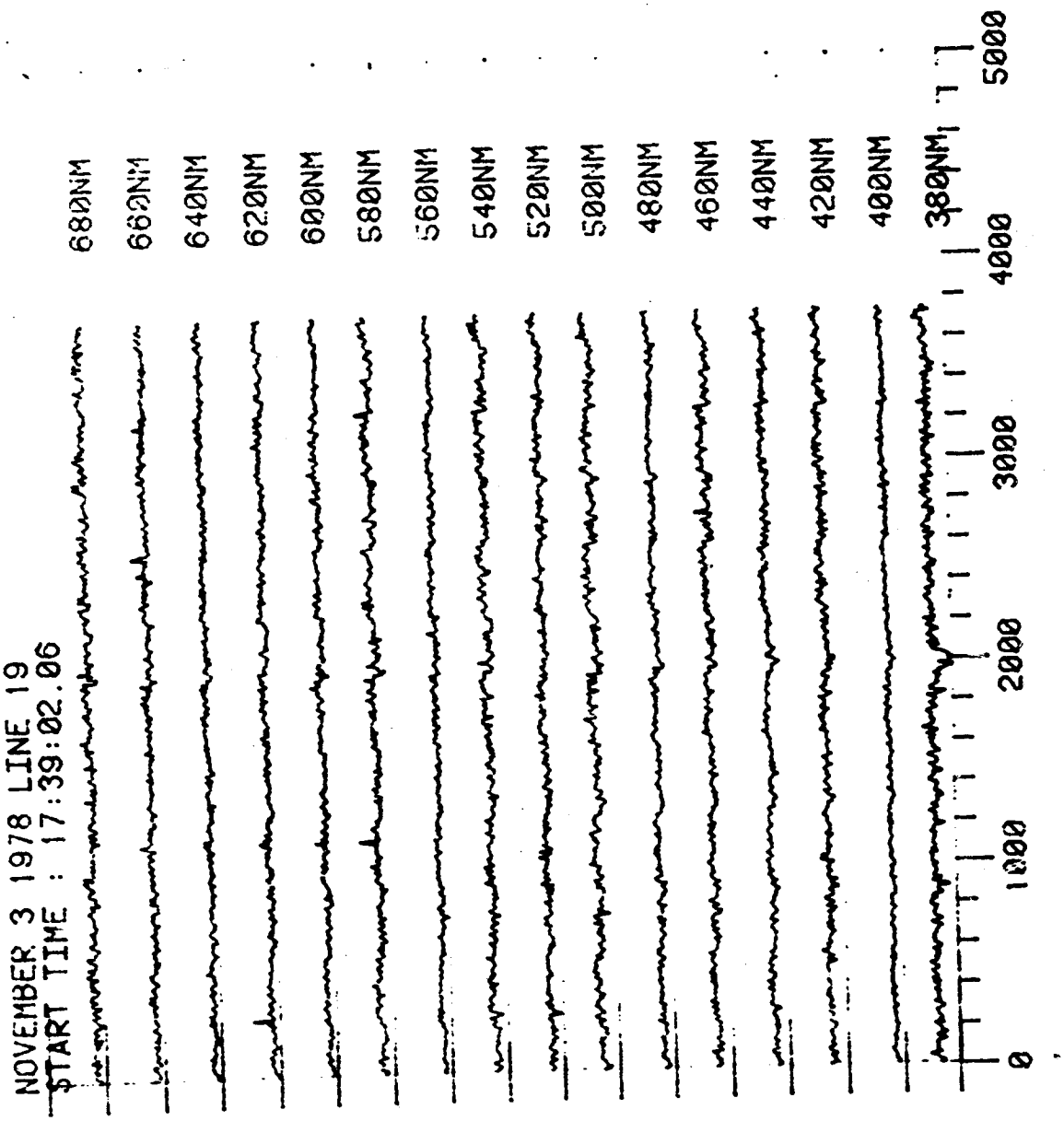

Figure 3.4.E. Fluorescence spectrum: history for La Rosa crude oil transect at sampling rate of 100 Hz

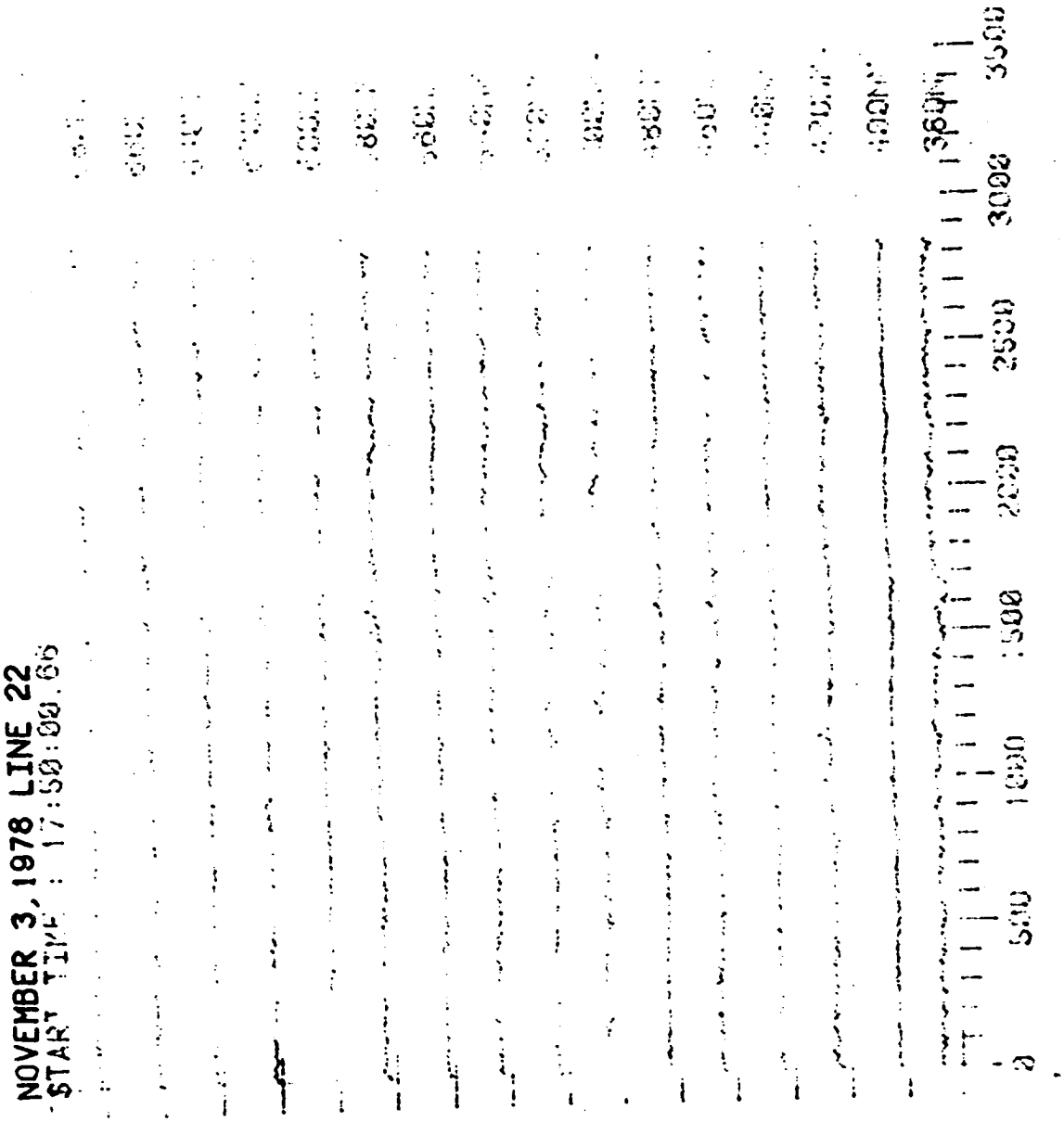

Figure 3.4.F. Fluorescence spectrum: history for La Rosa crude oil transect at sampling rate of 100 Hz

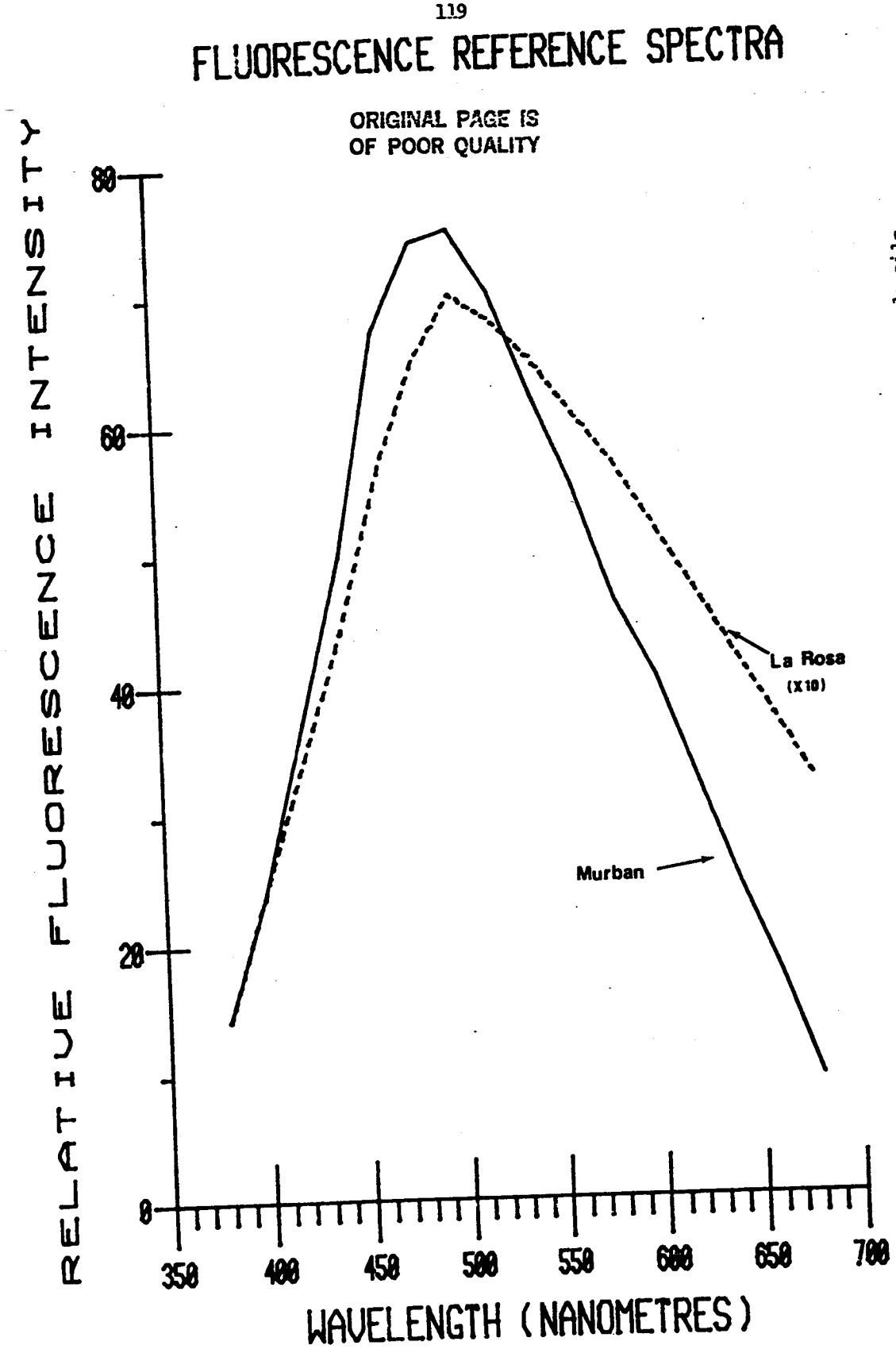

Figure 3.4.G. Laboratory-derived fluorescence emission spectra of Murban and La Rosa crude oils, for 337 nm excitation wavelength

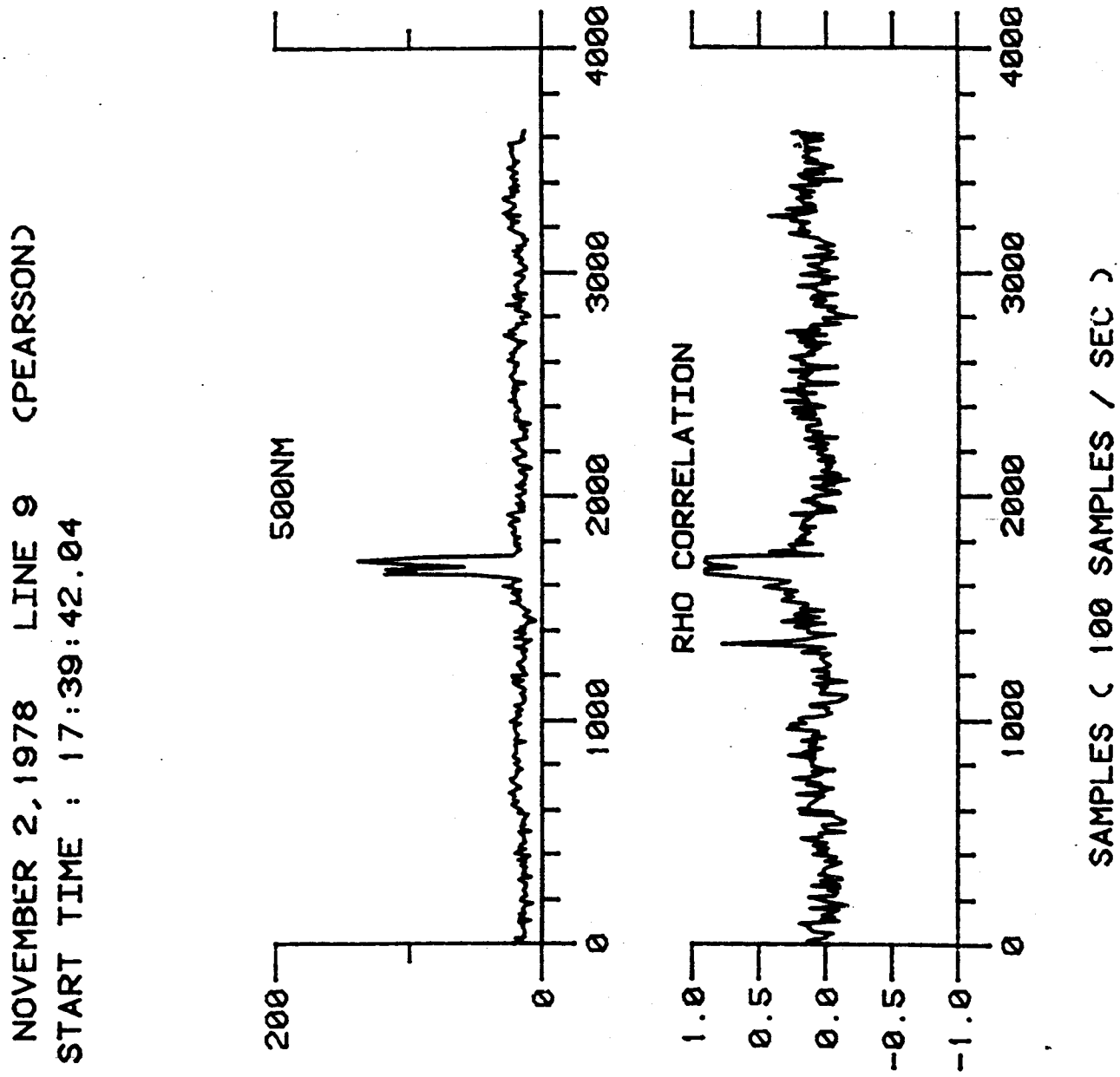

Figure 3.4.H. The 500 nm fluorescence emission for Murban crude, and the 16 channel correlation of airborne and laboratory fluorescence spectra

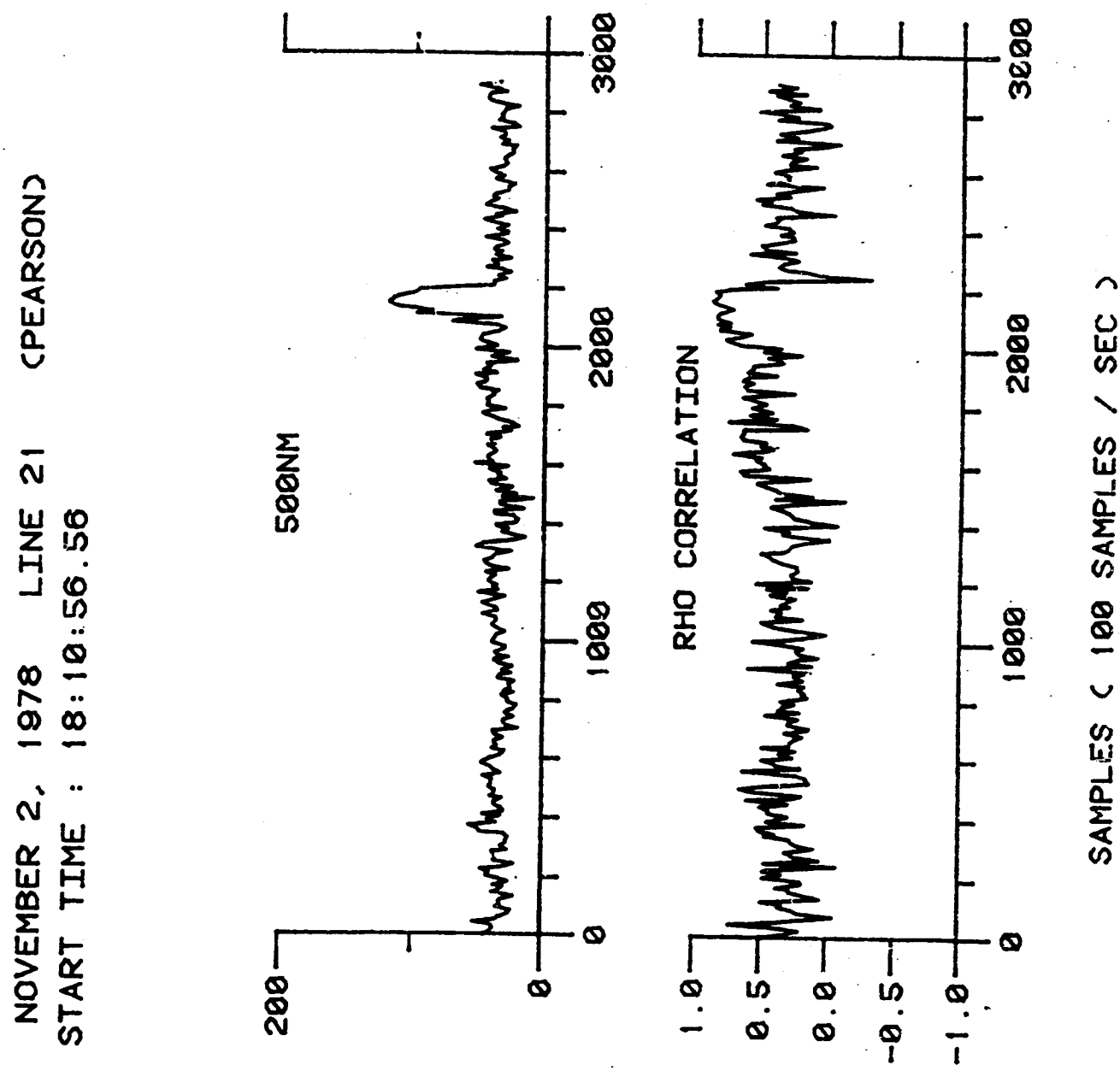

Figure 3.4.I. The 500 nm fluorescence emission for Murban crude, and the 16 channel correlation of airborne and laboratory fluorescence spectra

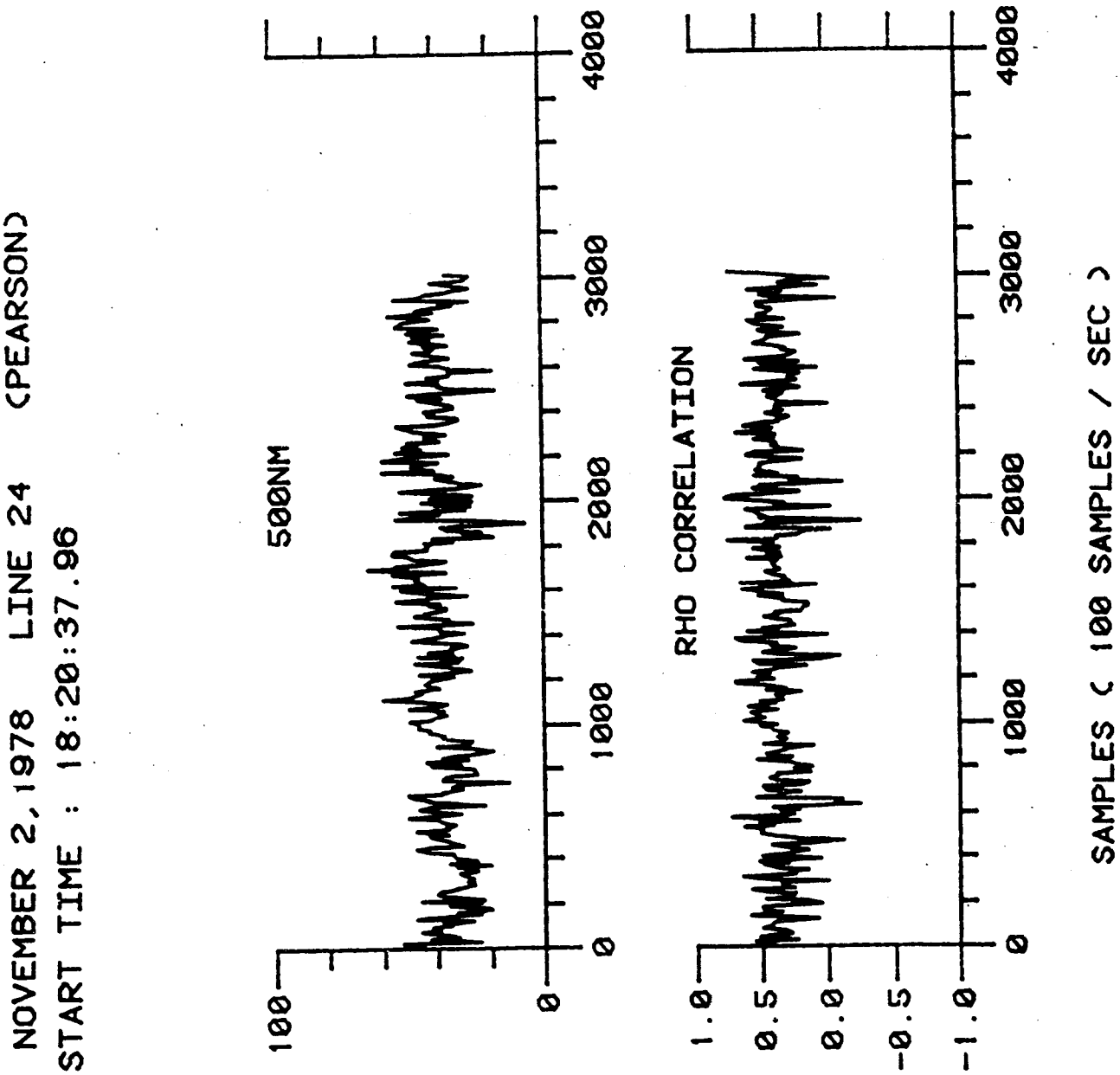

Figure 3.4.J. The 500 nm fluorescence emission for Murban crude, and the 16 channel correlation of airborne and laboratory fluorescence spectra

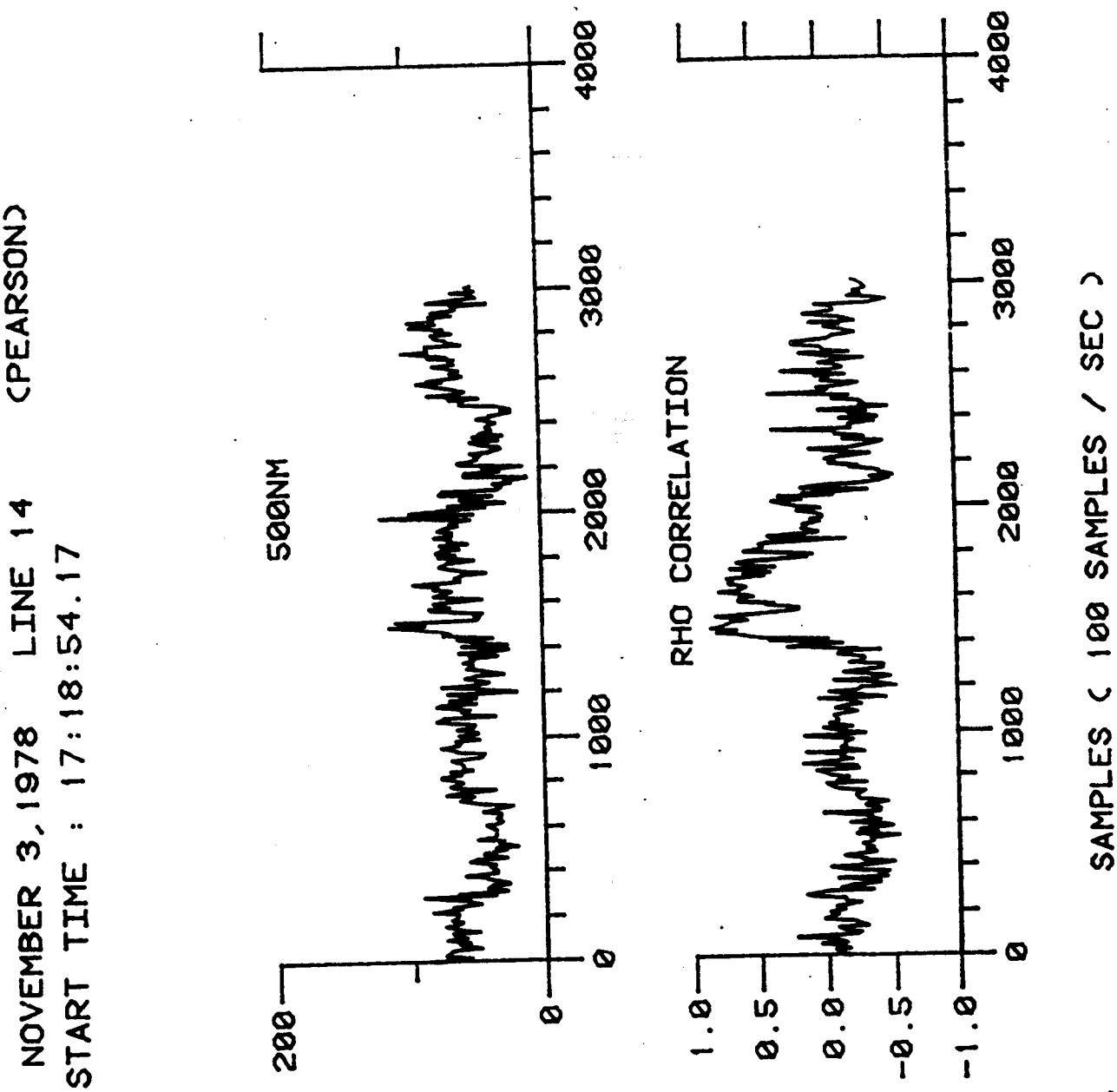

Figure 3.4.K. The 500-nm fluorescence emission for La Rosa crude, and the 16-channel correlation of airborne and laboratory fluorescence spectra.

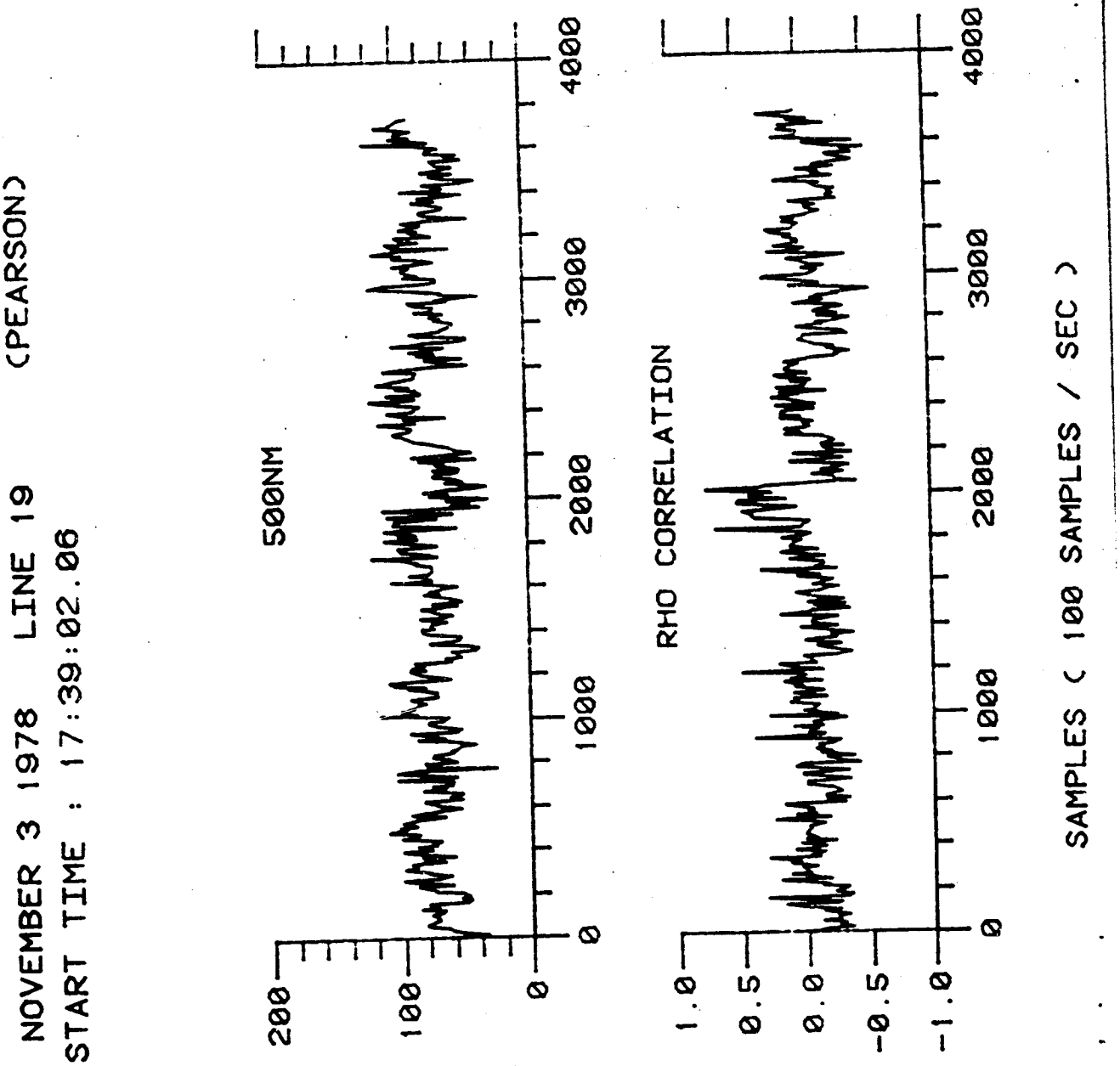

Figure 3.4. L. The 500-nm fluorescence emission for La Rosa crude, and the 16-channel correlation of airborne and laboratory fluorescence spectra.

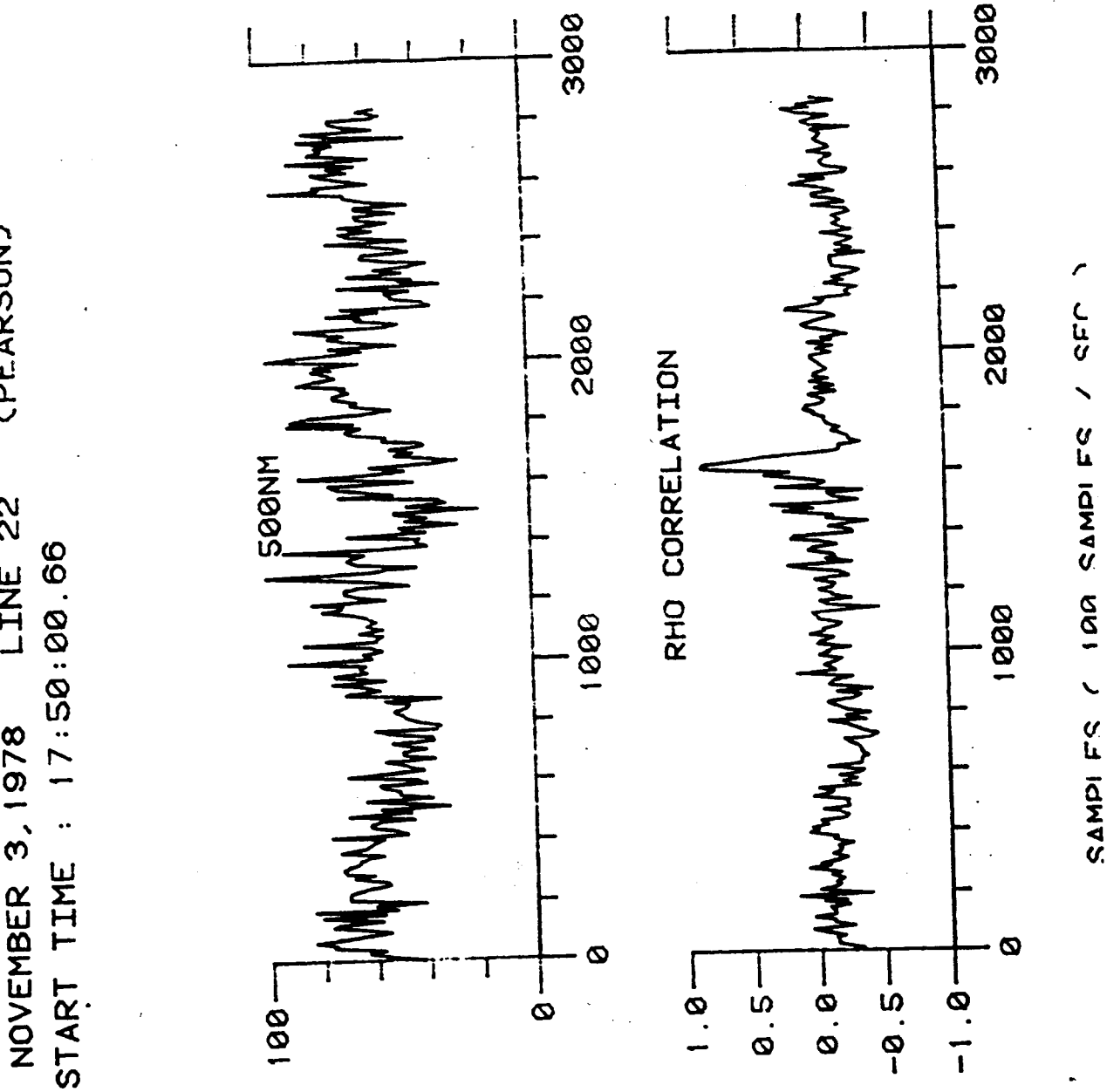

Figure 3.4.M. The 500-nm fluorescence emission for La Rosa crude, and the 16-channel correlation of airborne and laboratory fluorescence spectra.

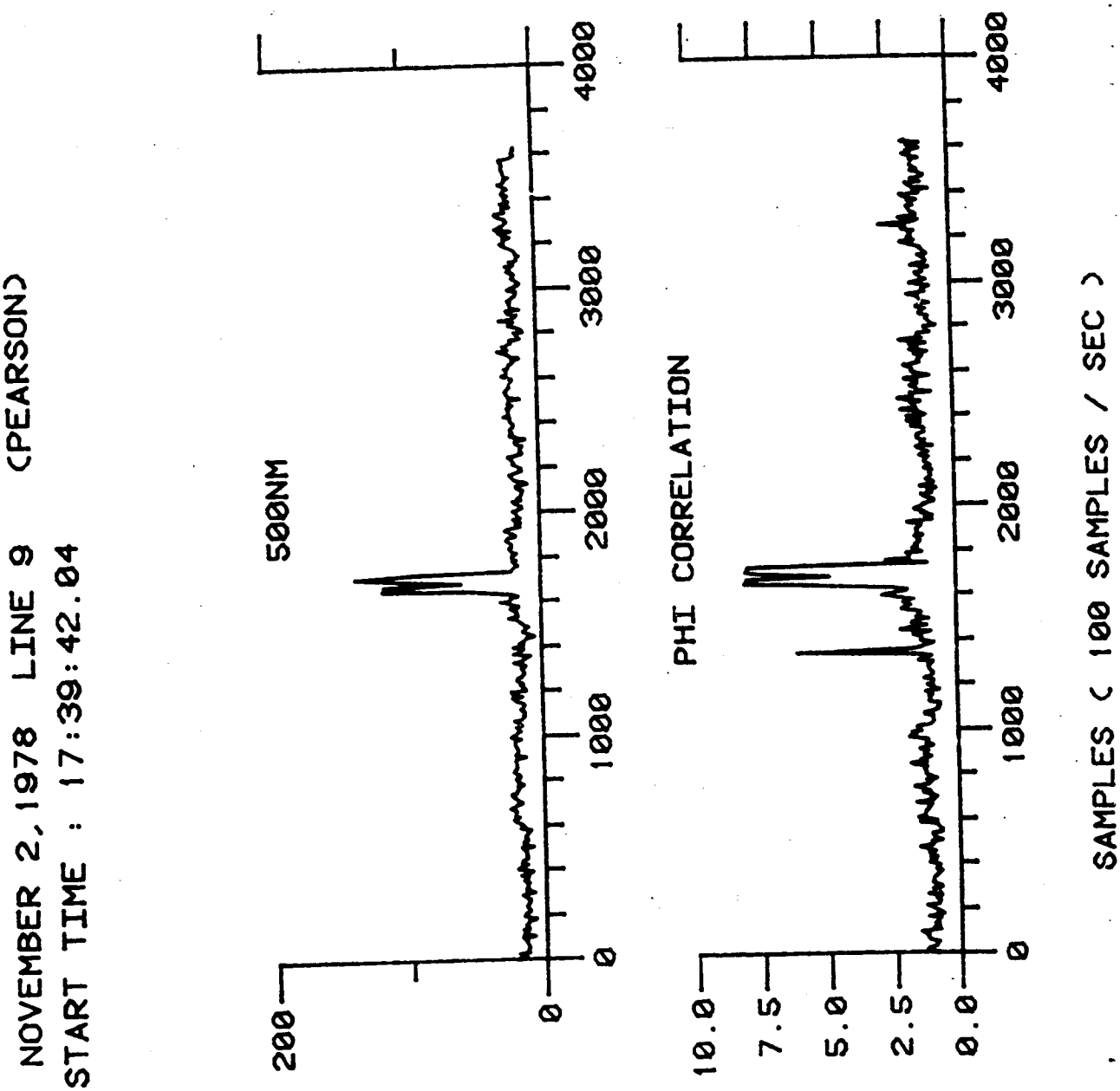

Figure 3.4.N. The 500 nm fluorescence emission for Murban crude, and the 16 channel (transformed) correlation of airborne and laboratory fluorescence spectra

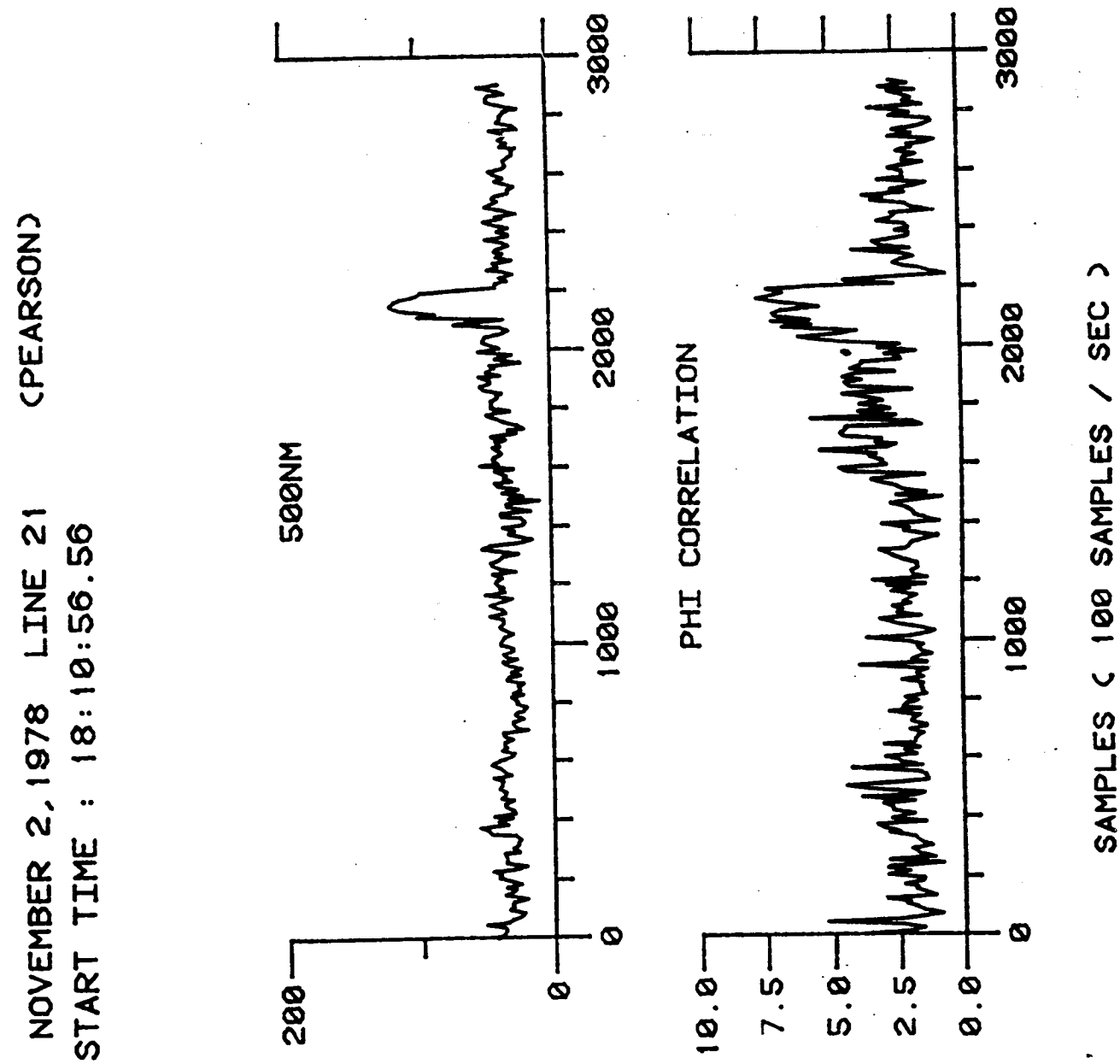

Figure 3.4.0. The 500 nm fluorescence emission for Murban crude, and the 16 channel (transformed) correlation of airborne and laboratory fluorescence spectra

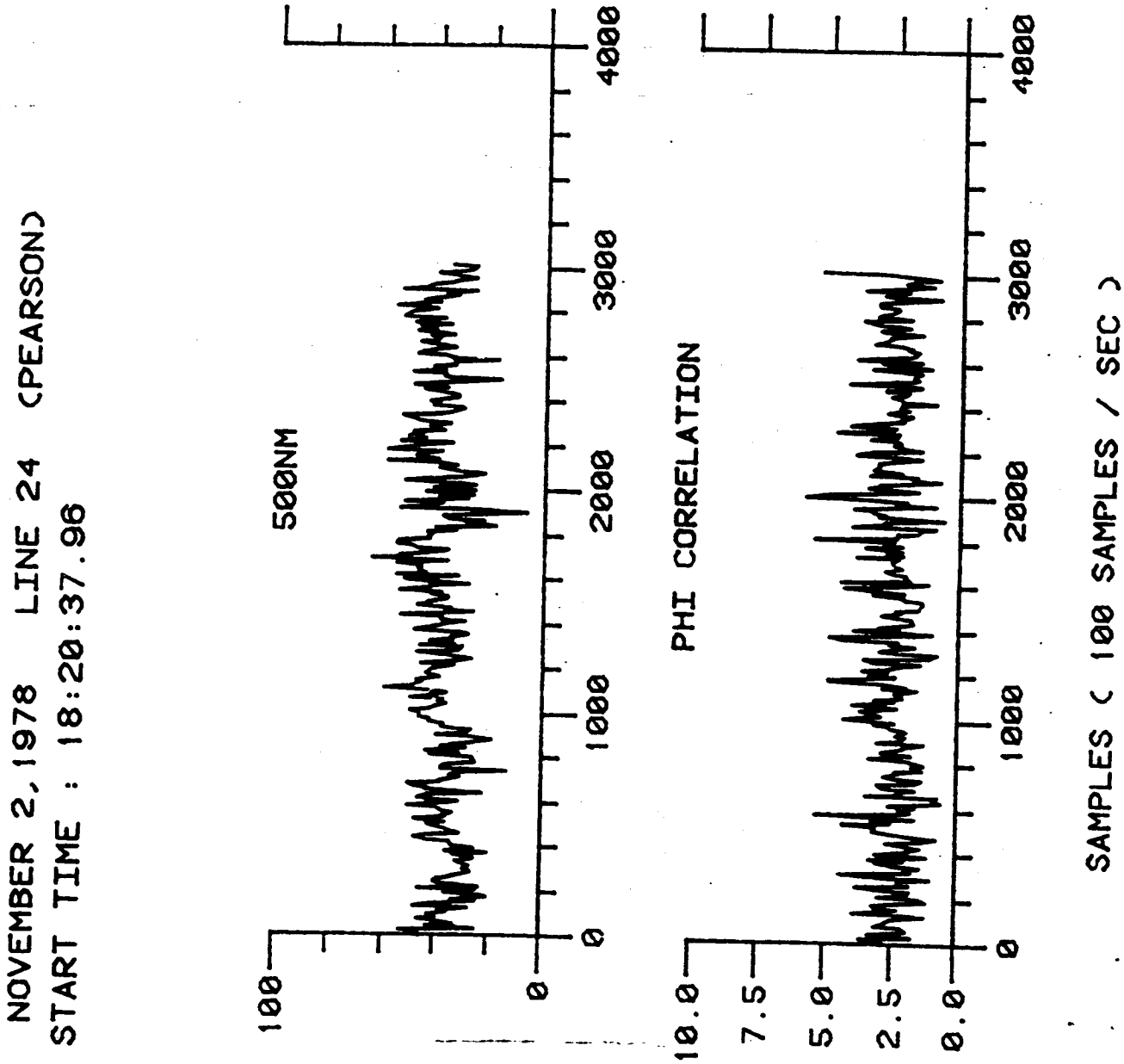

Figure 3.4.P. The 500 nm fluorescence emission for Murban crude, and the 16 channel (transformed) correlation of airborne and laboratory fluorescence spectra

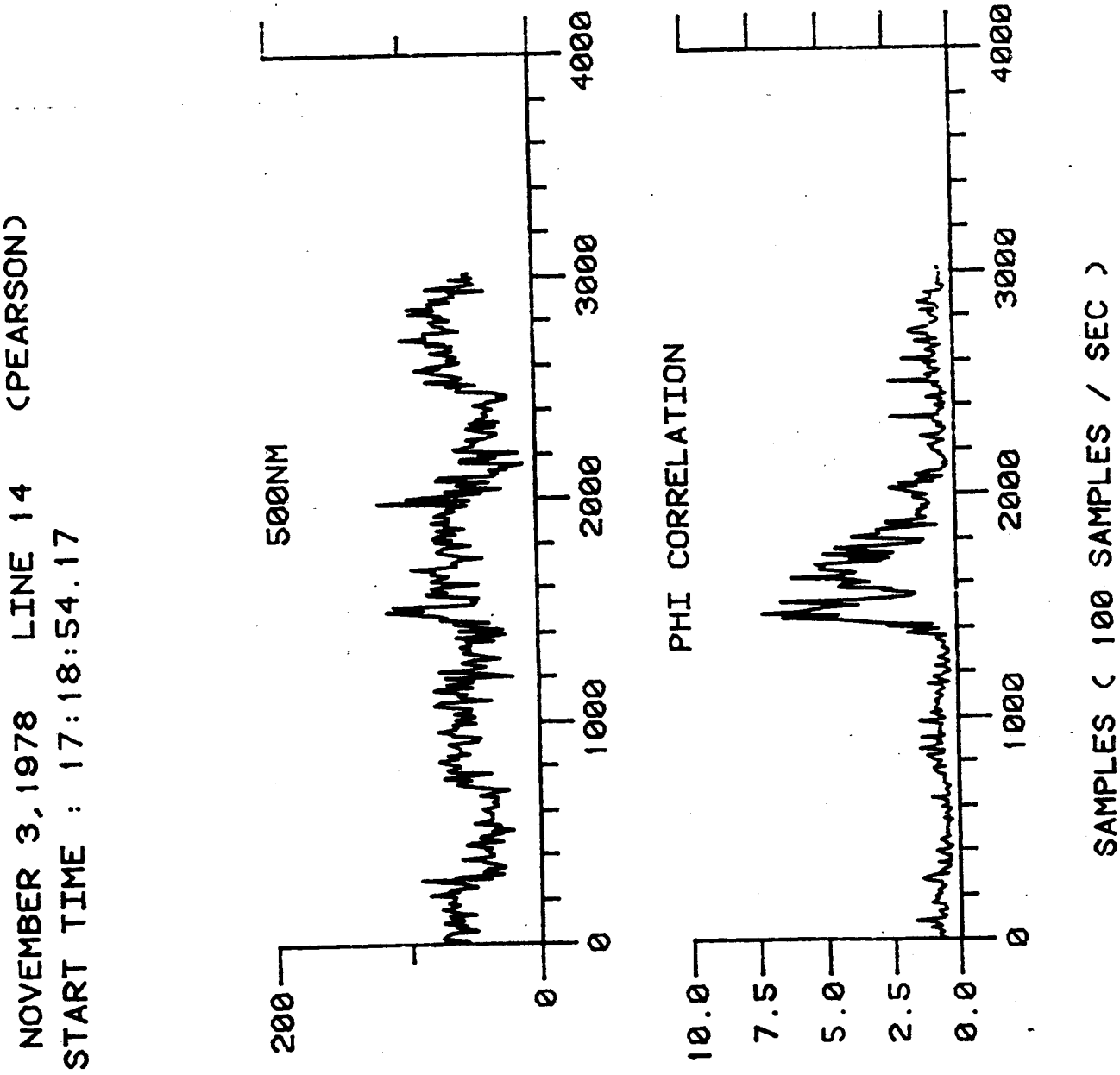

Figure 3.4.Q. The 500-nm fluorescence emission for La Rosa crude, and the 16-channel (transformed) correlation of airborne and laboratory fluorescence spectra.

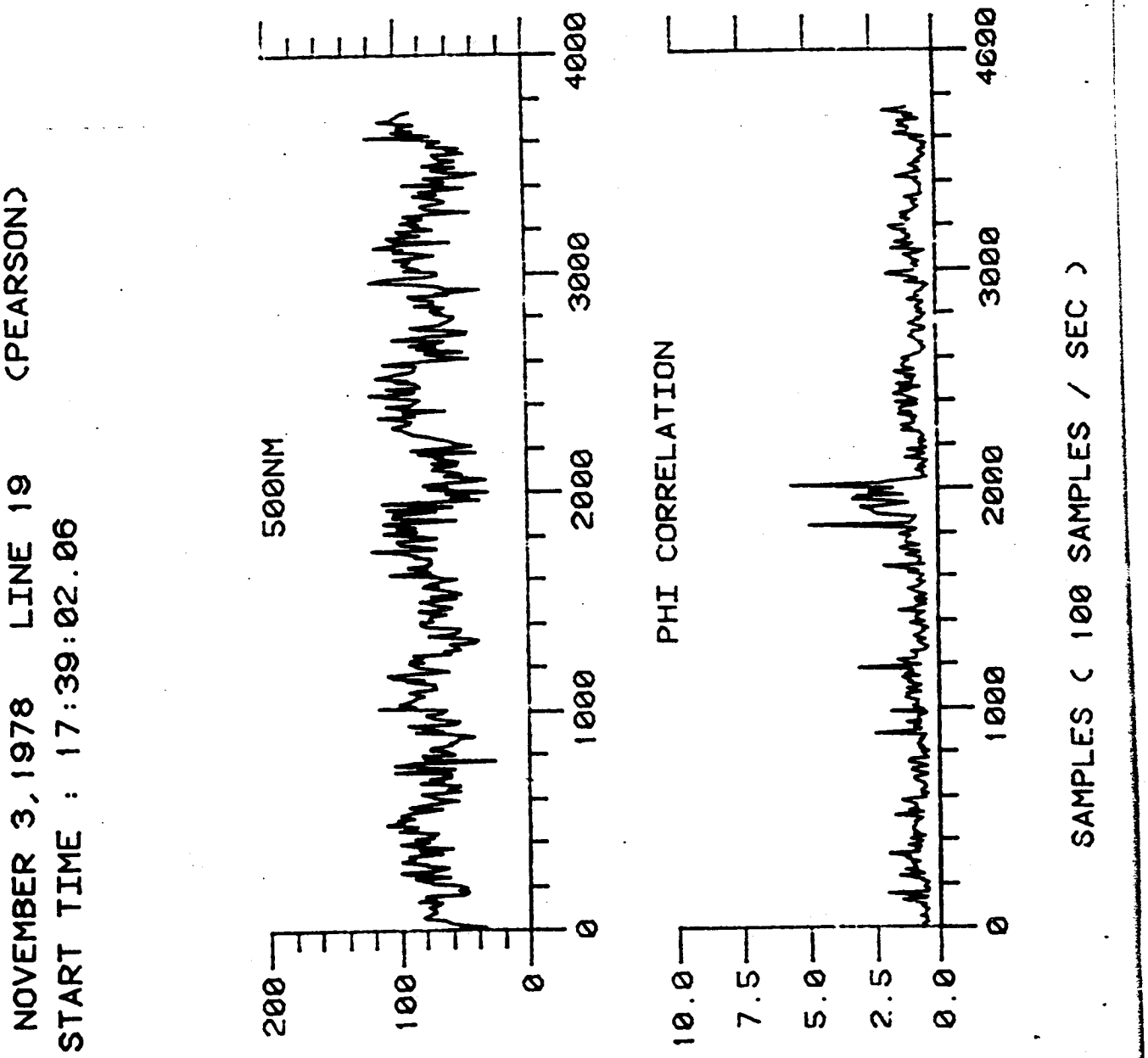

Figure 3.4.R. The 500-nm fluorescence emission for La Rosa crude, and the 16-channel (transformed) correlation of airborne and laboratory fluorescence spectra.

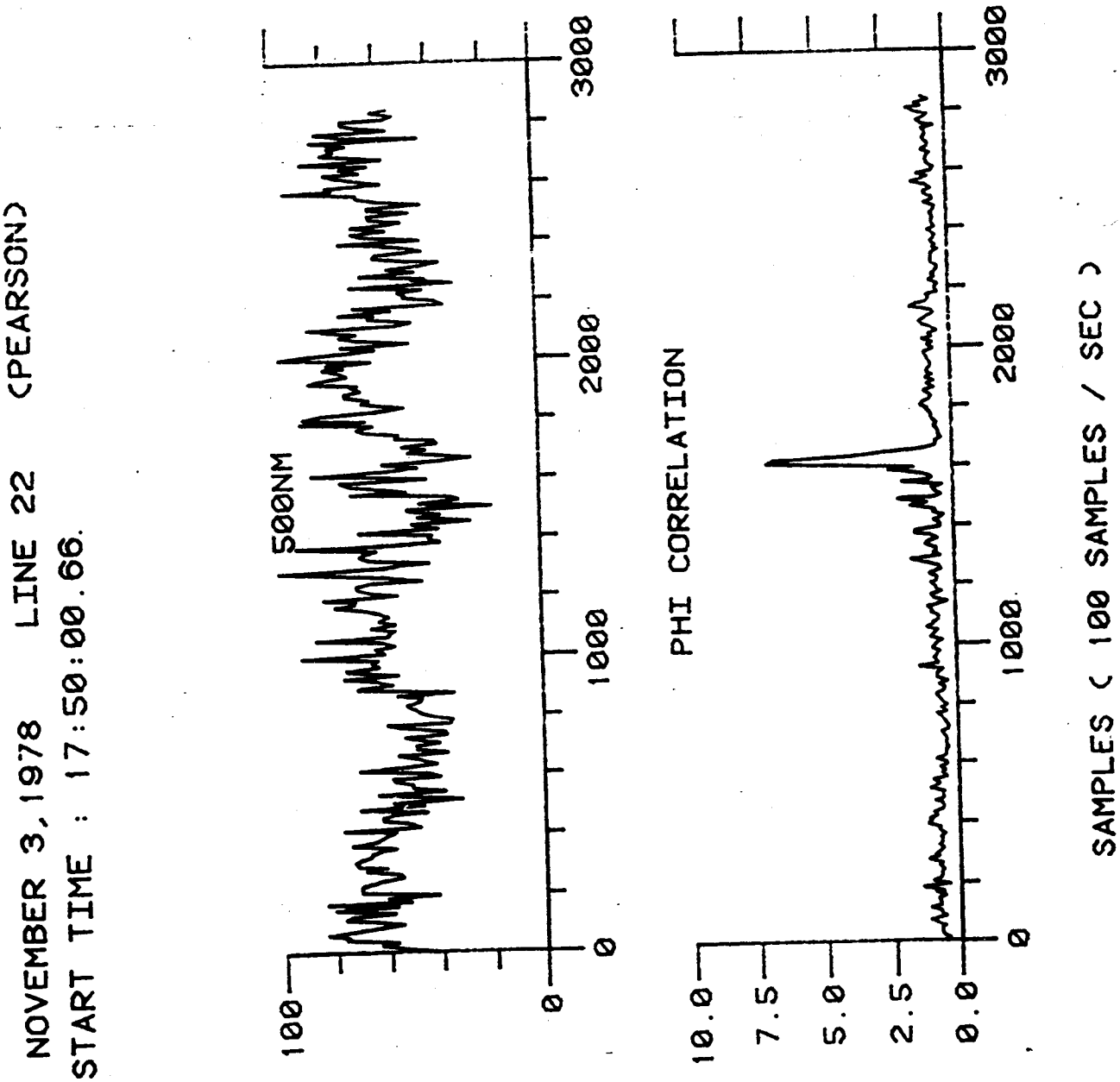

Figure 3.4.S. The 500-nm fluorescence emission for La Rosa crude, and the 16-channel (transformed) correlation of airborne and laboratory fluorescence spectra.

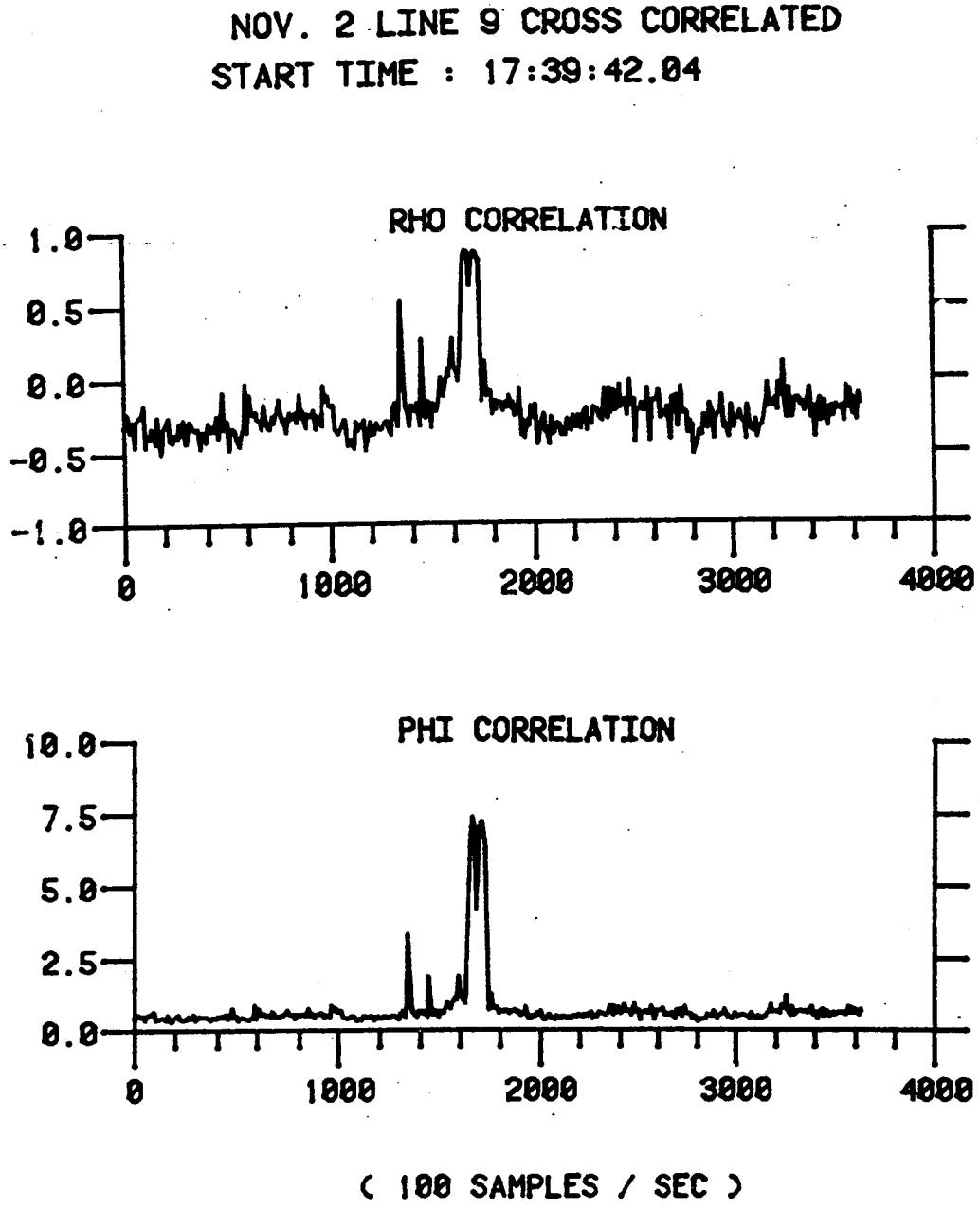

Figure 3.4.T. 16 channel correlation of airborne fluorescence spectrum of Murban crude oil with laboratory spectrum of La Rosa crude oil. RHO = log (PHI).

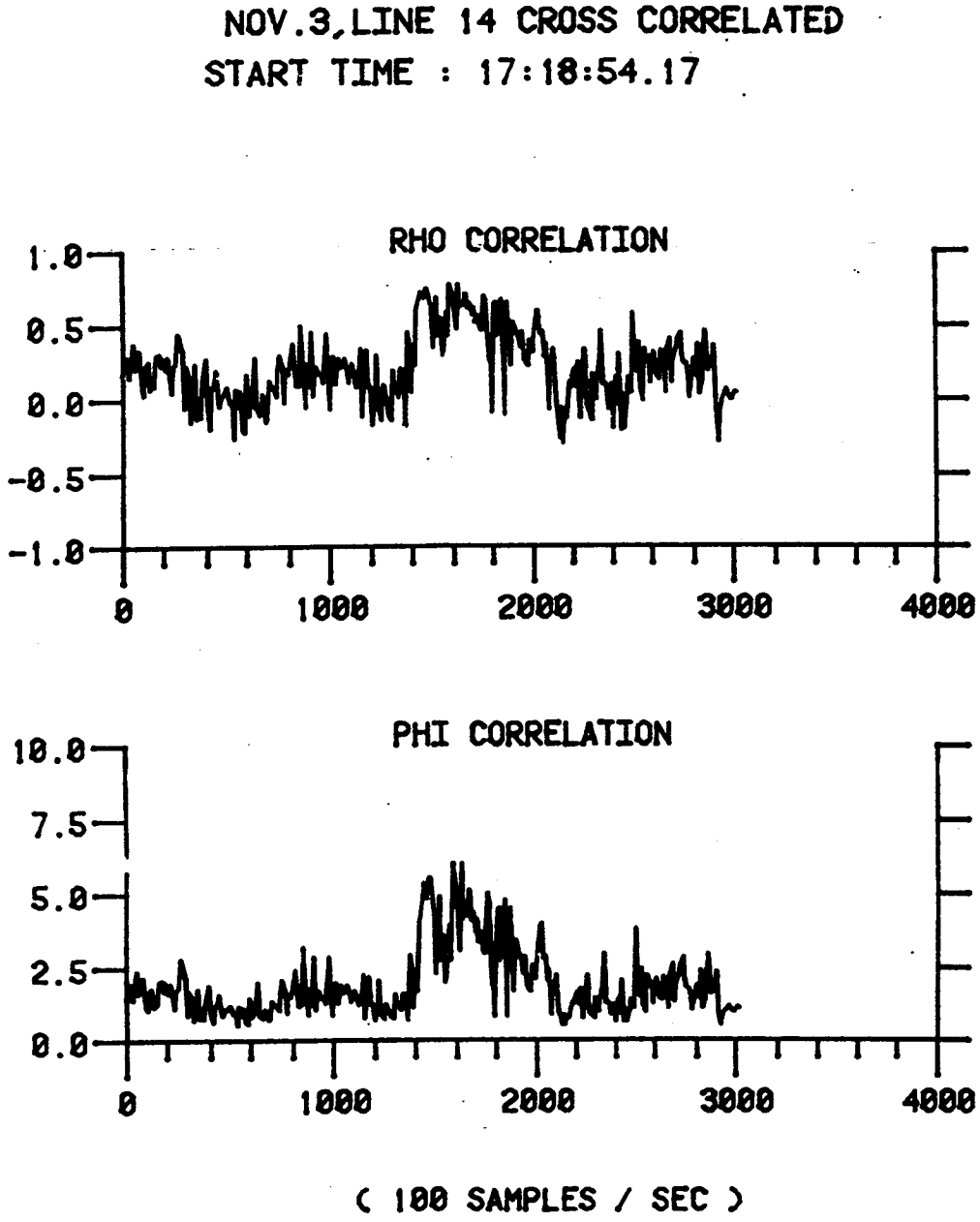

Figure 3.4.U. 16 channel correlation of airborne fluorescence spectrum of La Rosa crude oil with laboratory spectrum of Murban crude oil. RHO = log (PHI).

Figure 3.5.A.
November 2, line 03
Polarization VV
Time relative to 17:03:47.2 GMT

Normalized backscattering cross-section for six look angles of the microwave scatterometer fore beam, as a function of time. Joined arrows indicate coverage by Figure 4.5.A.

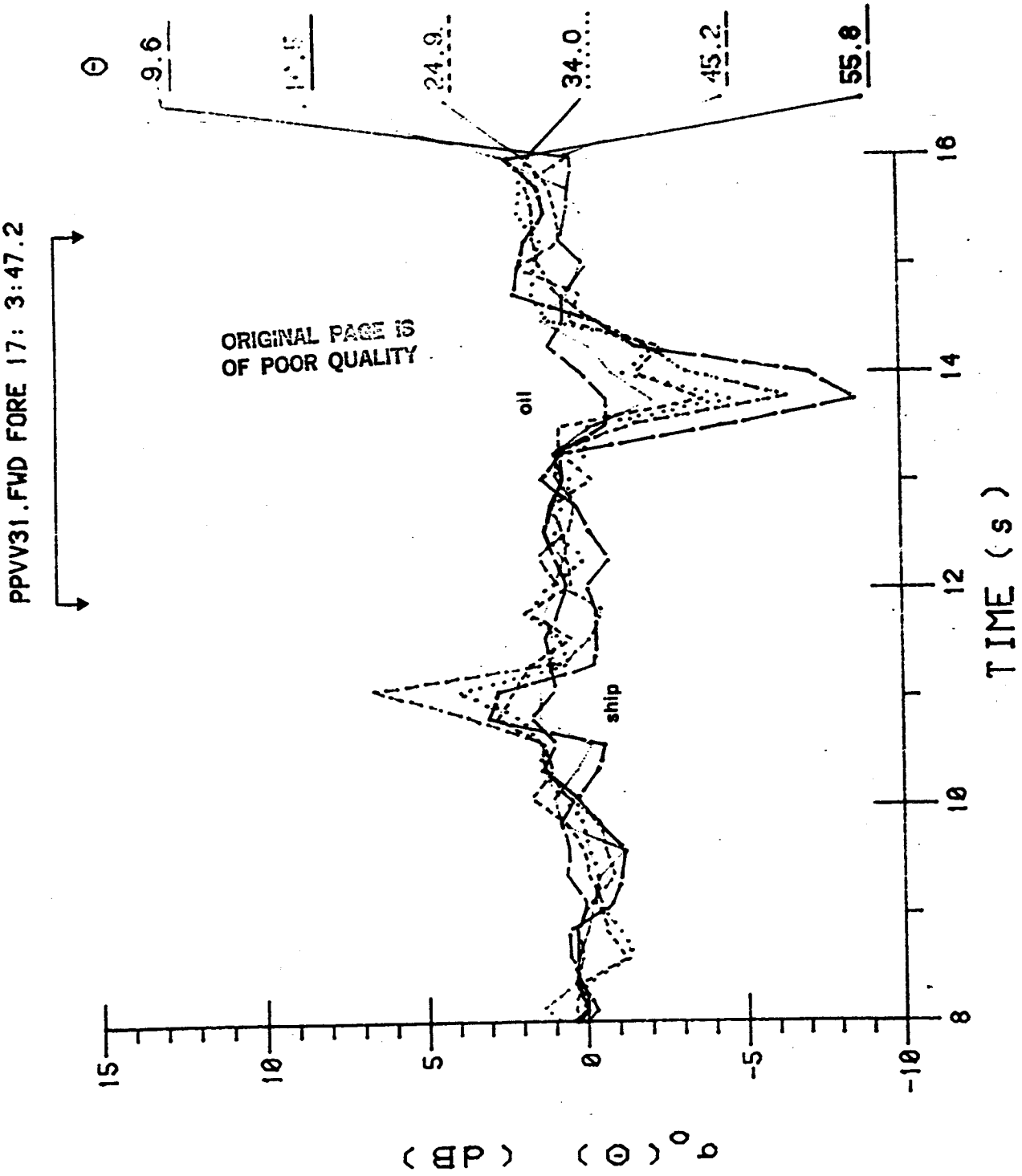

Figure 3.5.B.
November 2, line 03
Polarization VV
Time relative to 17:03:47.2 GMT

Normalized backscattering cross-section for six look angles of the microwave scatterometer aft beam, as a function of time. Joined arrows indicate coverage by Figure 4.5.A.

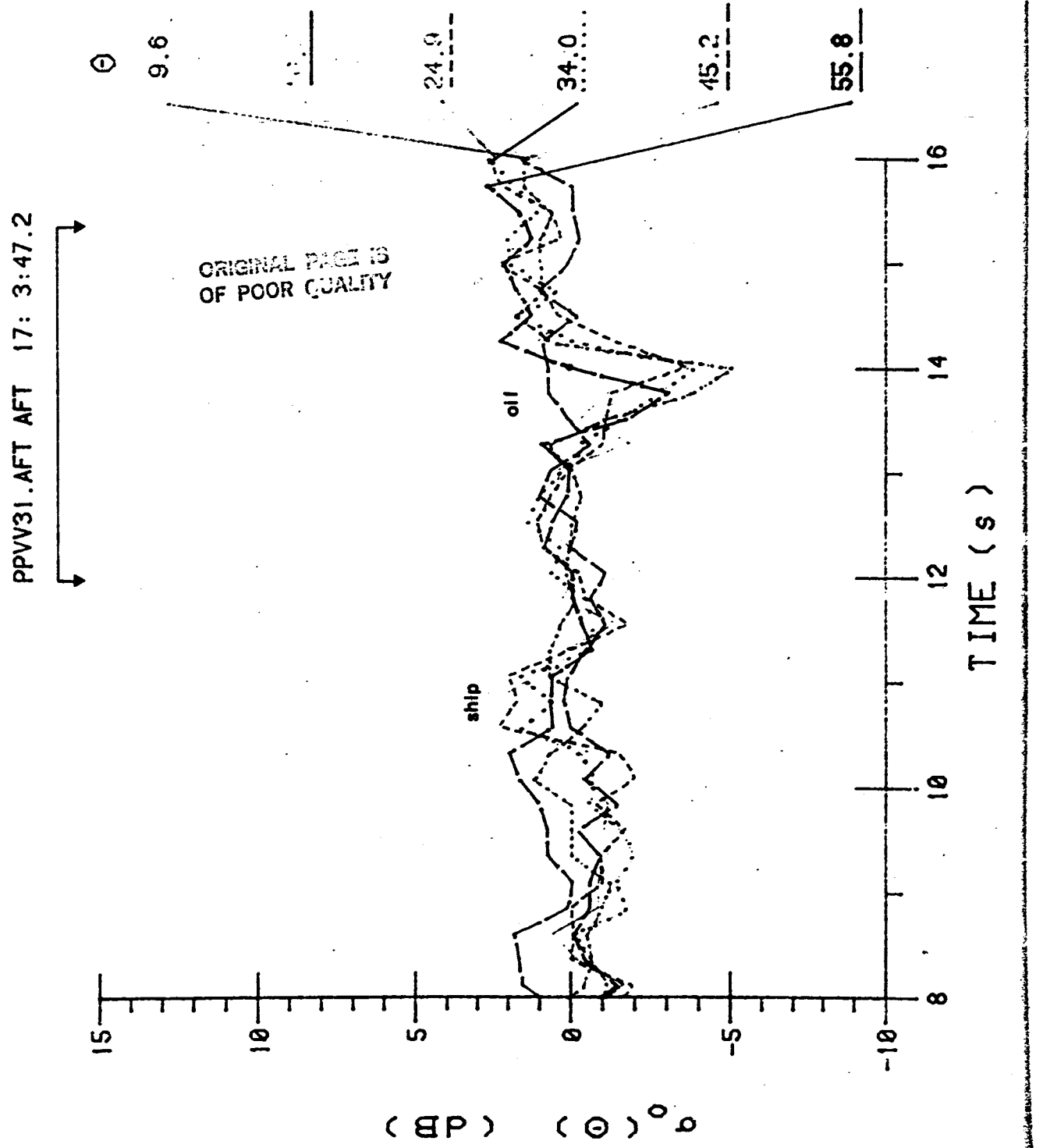

Figure 3.5.C.
November 2, line 03
Polarization VH
Time relative to 17:03:47.2 GMT

Normalized backscattering cross-section for six look angles of the microwave scatterometer fore beam, as a function of time. Joined arrows indicate coverage by Figure 4.5.B.

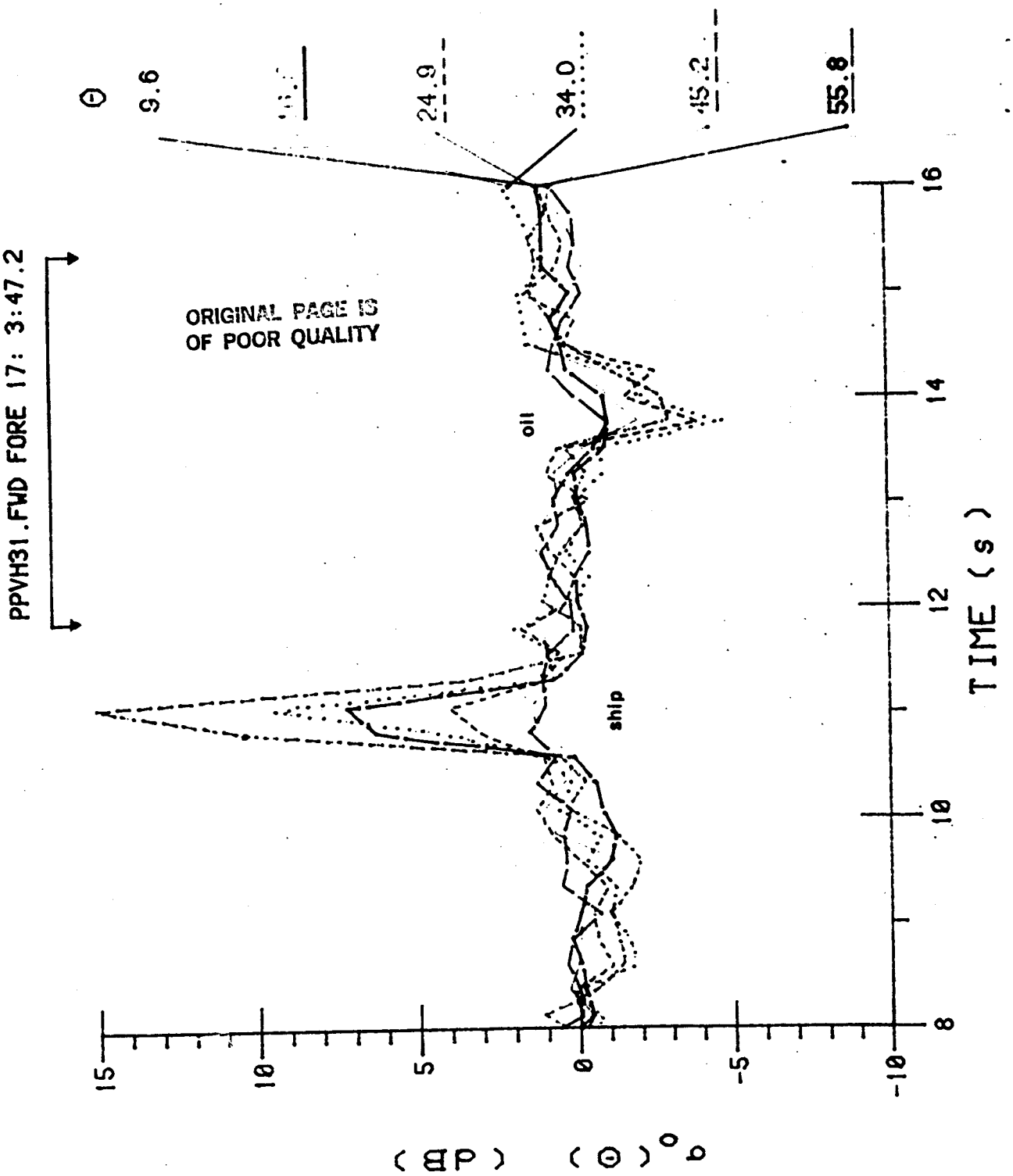

Figure 3.5.D.
November 2, line 03
Polarization VH
Time relative to 17:03:47.2 GMT

Normalized backscattering cross-section for six look angles of the microwave scatterometer aft beam, as a function of time. Joined arrows indicate coverage by Figure 4.5.B.

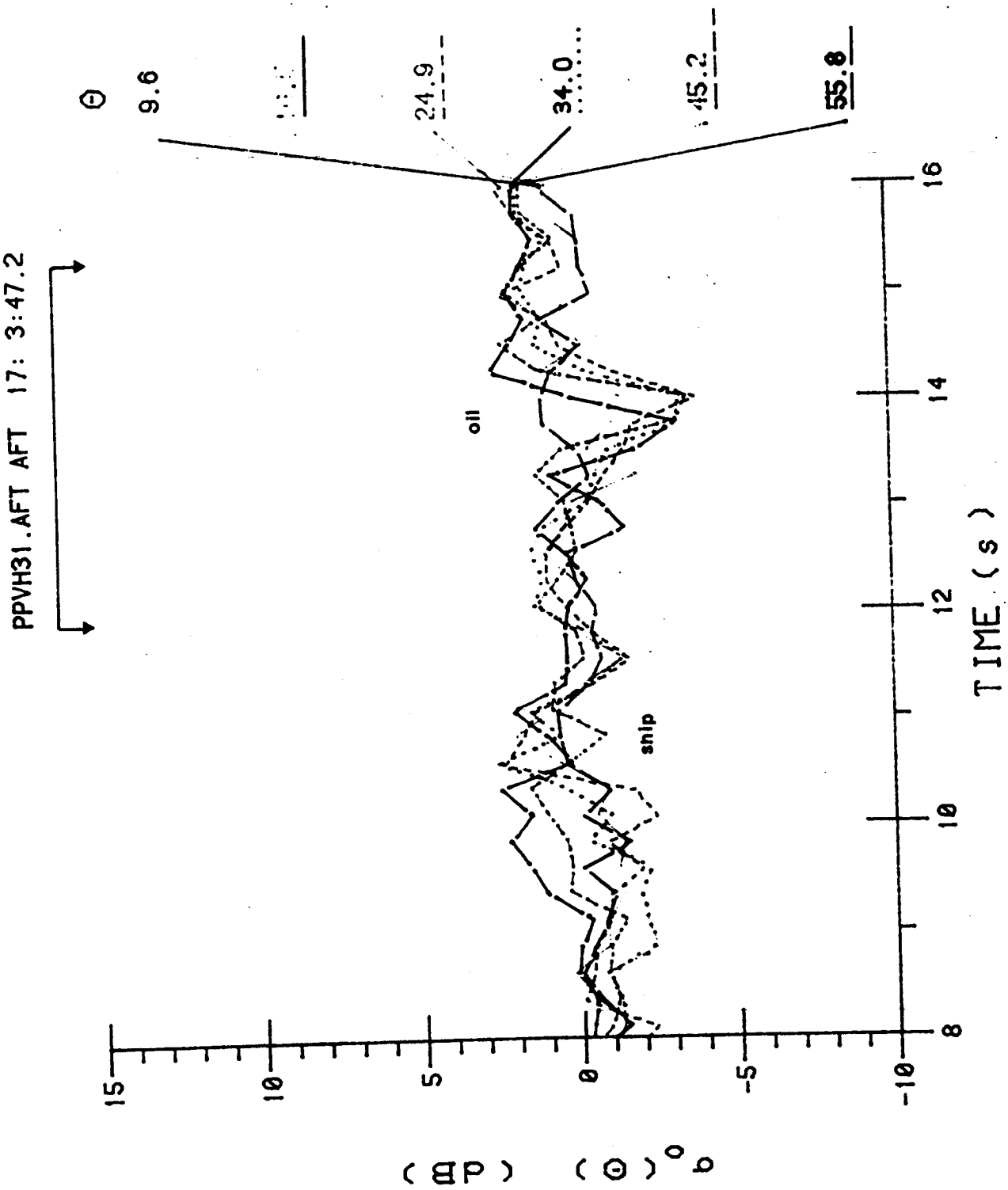

Figure 3.5.E.
November 2, line 06
Polarization HV
Time relative to 17:13:21.2

Normalized backscattering cross-section for six look angles of the microwave scatterometer fore beam, as a function of time. Joined arrows indicate coverage by Figure 4.5.C.

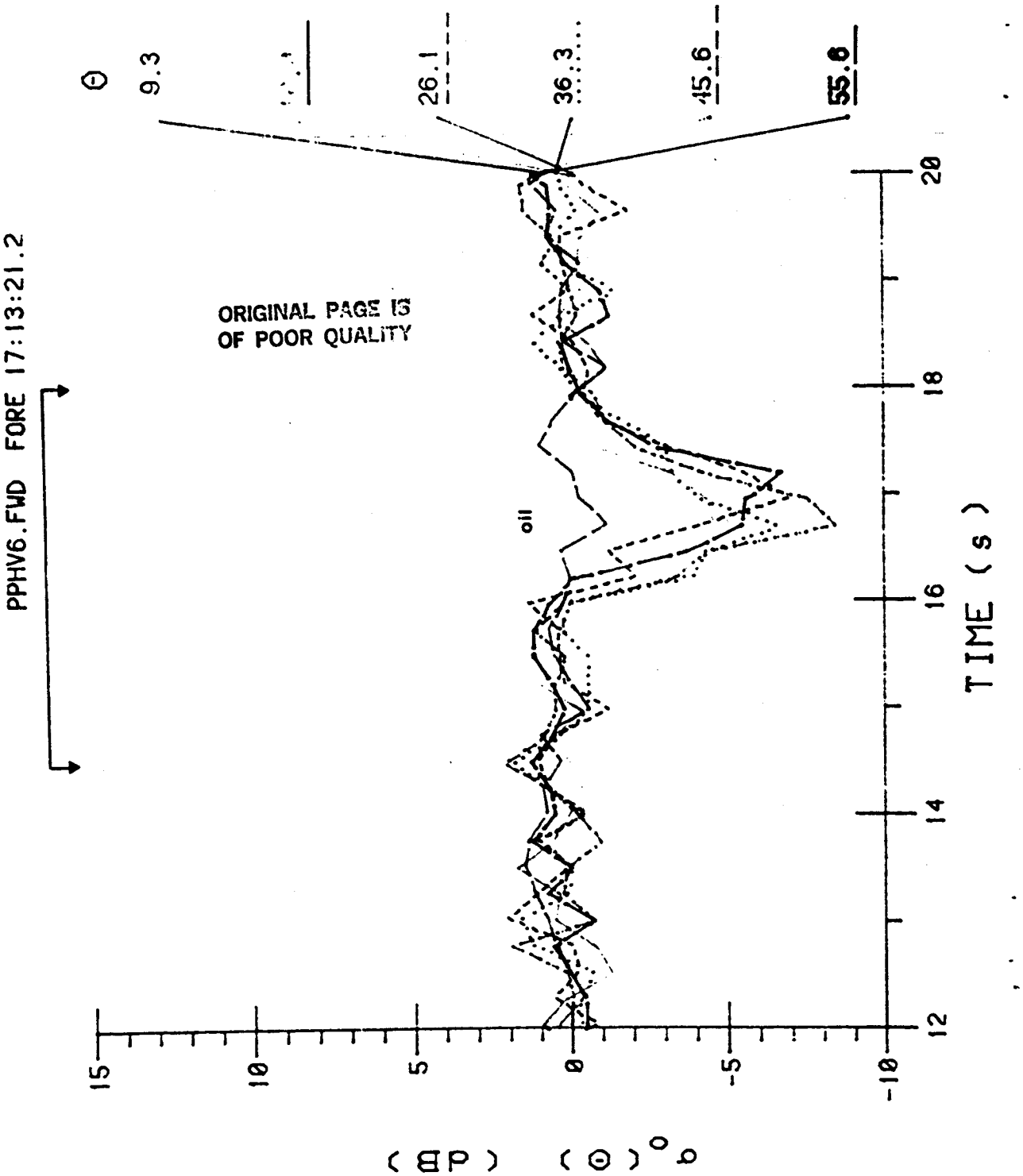

Figure 3.5.F.
November 2, line 06
Polarization HV
Time relative to 17:13:21.2 GMT

Normalized backscattering cross-section for six look angles of the microwave scatterometer aft beam, as a function of time. Joined arrows indicate coverage by Figure 4.5.C.

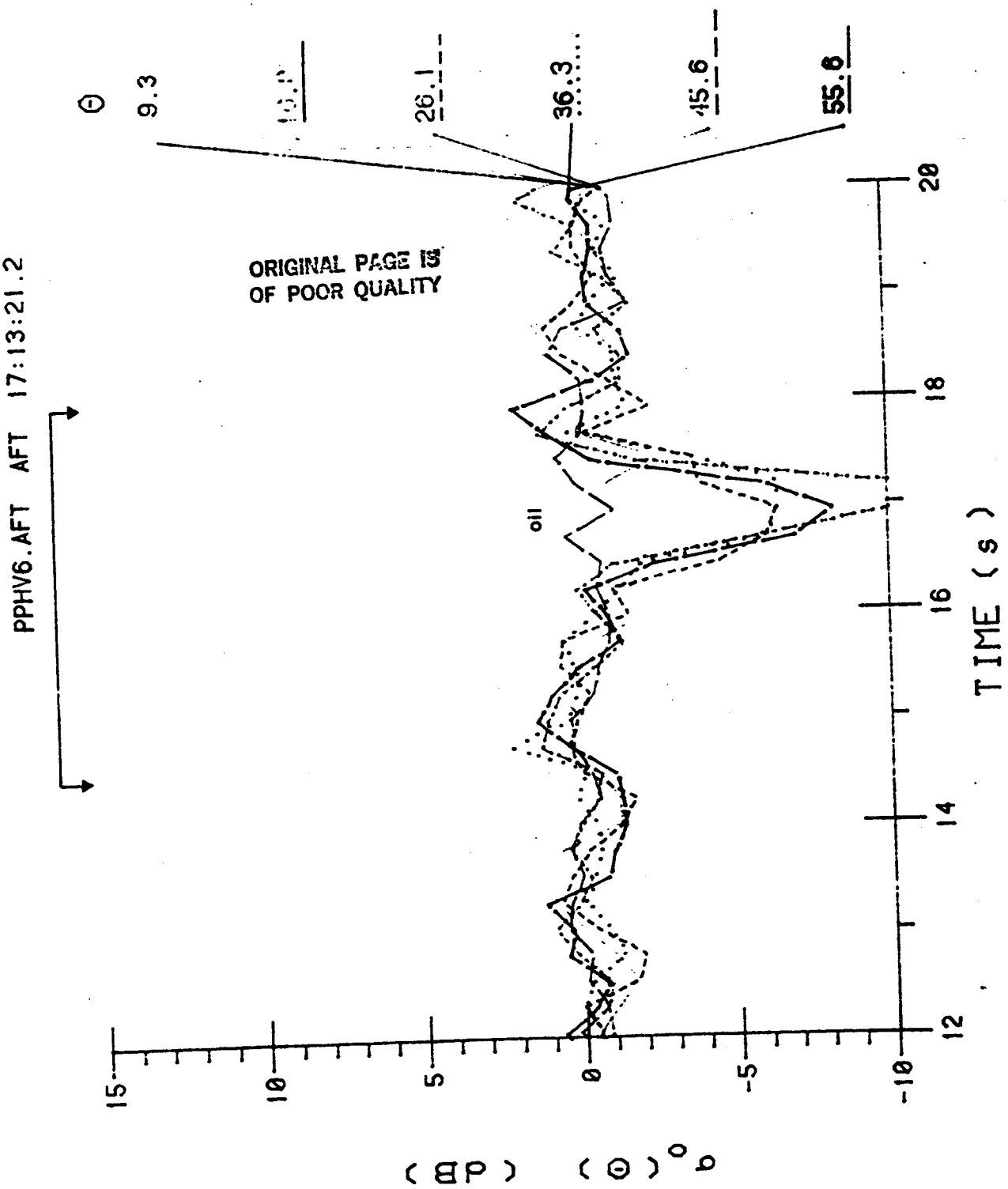

Figure 3.5.G.
November 2, line 06
Polarization HH
Time relative to 17:13:21.2 GMT

Normalized backscattering cross-section for six look angles of the microwave scatterometer fore beam, as a function of time. Joined arrows indicate coverage by Figure 4.5.D.

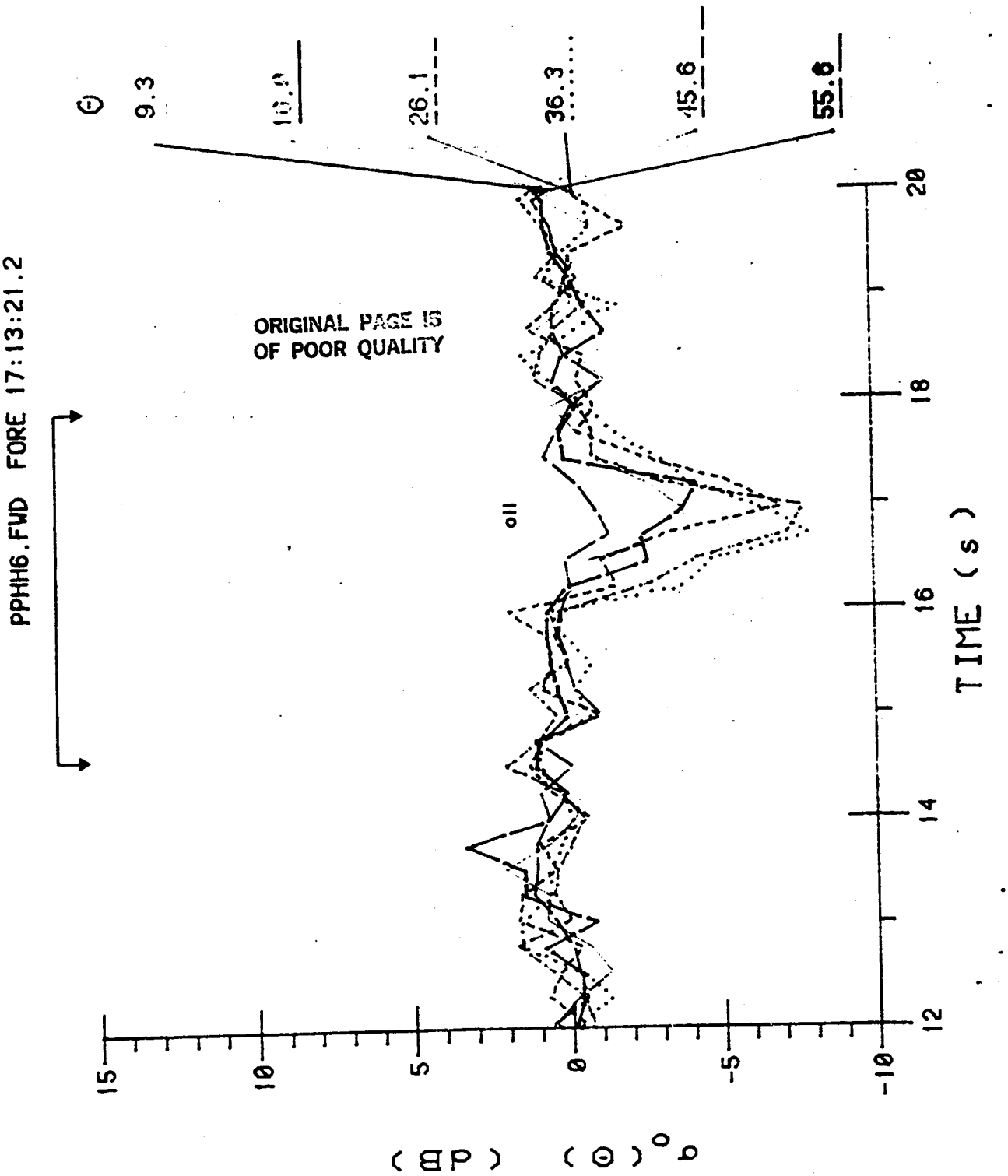

Figure 3.5.H.
November 2, line 06
Polarization HH
Time relative to 17:13:21.2

Normalized backscattering cross-section for six look angles of the microwave scatterometer aft beam, as a function of time. Joined arrows indicate coverage by Figure 4.5.D.

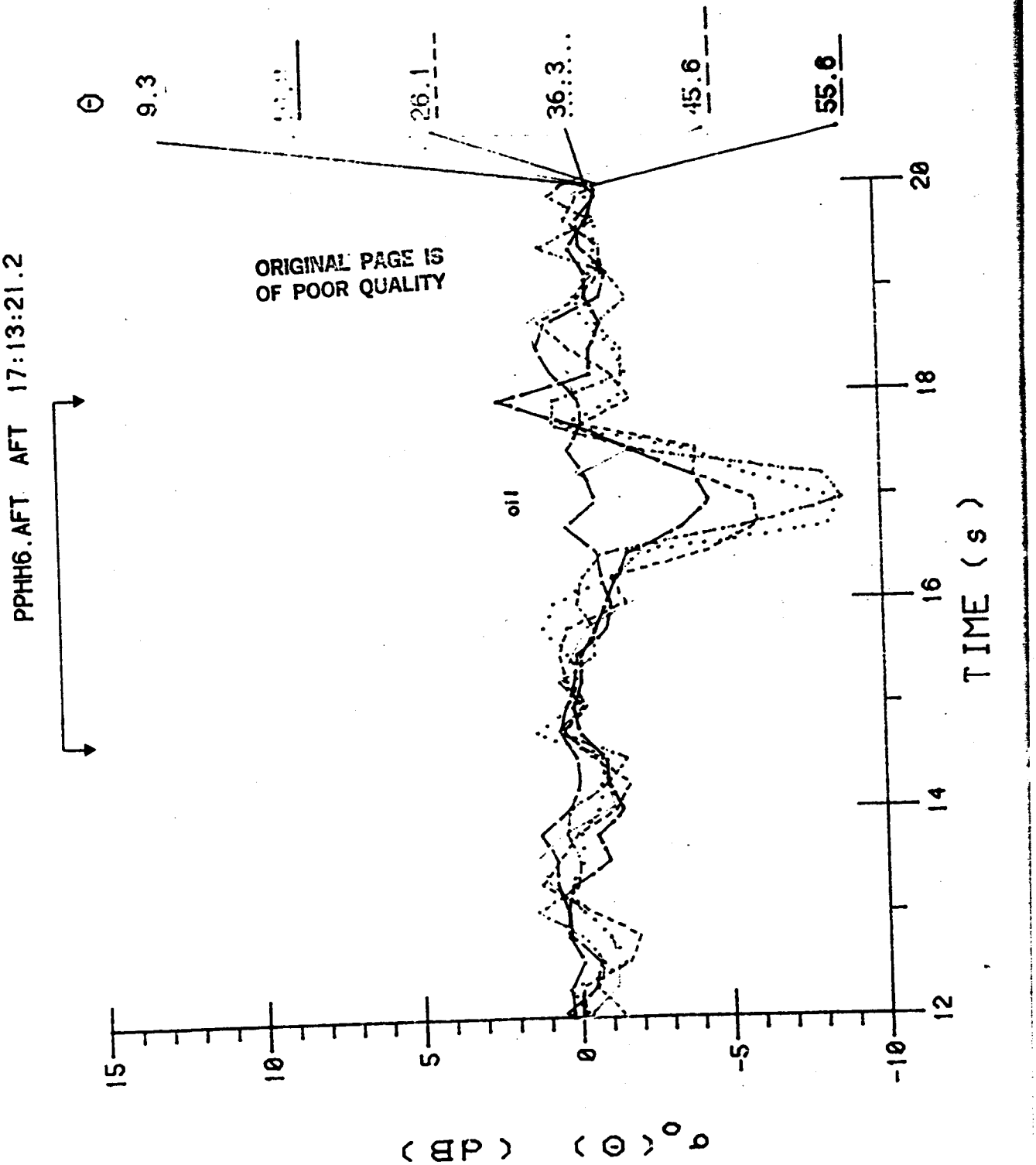

Figure 3.5.I.
November 3, line 4B
Polarization HV
Time relative to 15:30:10.2 GMT

Normalized backscattering cross-section for six look angles of the microwave scatterometer fore beam, as a function of time. Joined arrows indicate coverage by Figure 4.5.E.

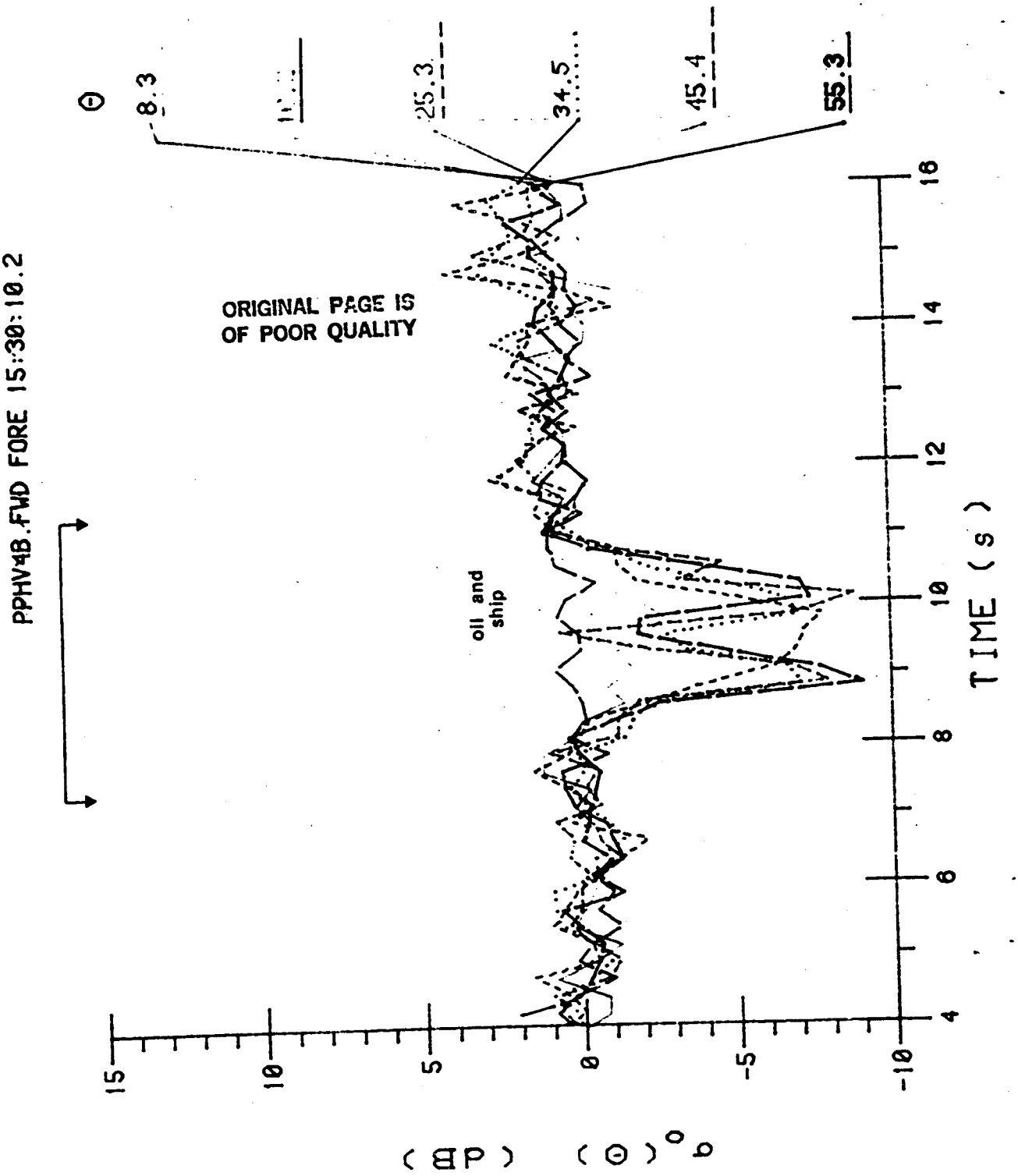

Figure 3.5.J.
November 3, line 4B
Polarization HV
Time relative to 15:30:10.2 GMT

Normalized backscattering cross-section for six look angles of the microwave scatterometer aft beam, as a function of time. Joined arrows indicate coverage by Figure 4.5.E.

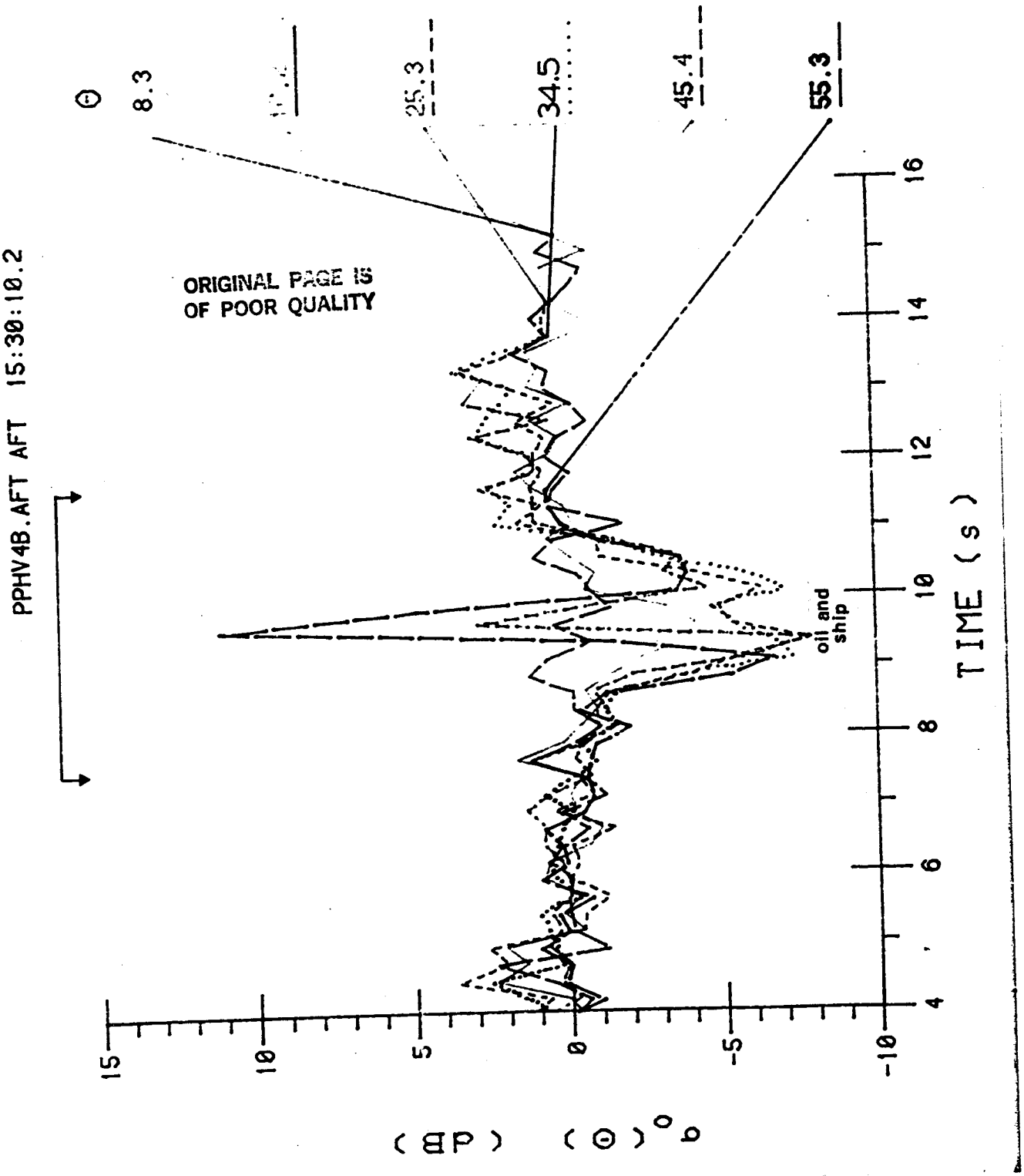

Figure 3.5.K.
November 3, line 4B
Polarization HH
Time relative to 15:30:10.2 GMT

Normalized backscattering cross-section for six look angles of the microwave scatterometer fore beam, as a function of time. Joined arrows indicate coverage by Figure 4.5.F.

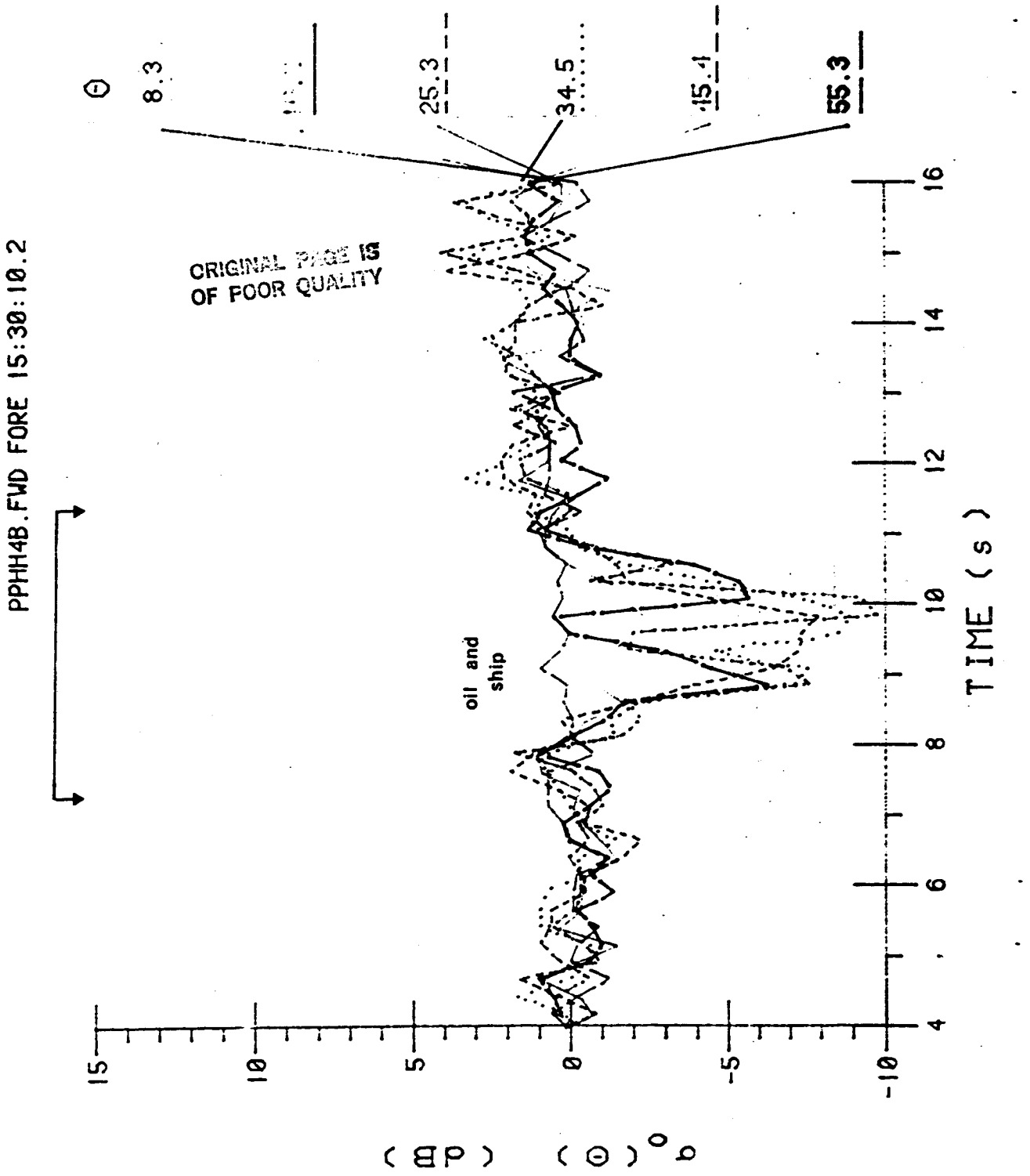

Figure 3.5.L.
November 3, line 4B
Polarization HH
Time relative to 15:30:10.2 GMT

Normalized backscattering cross-section for six look angles of the microwave scatterometer aft beam, as a function of time. Joined arrows indicate coverage by Figure 4.5.F.

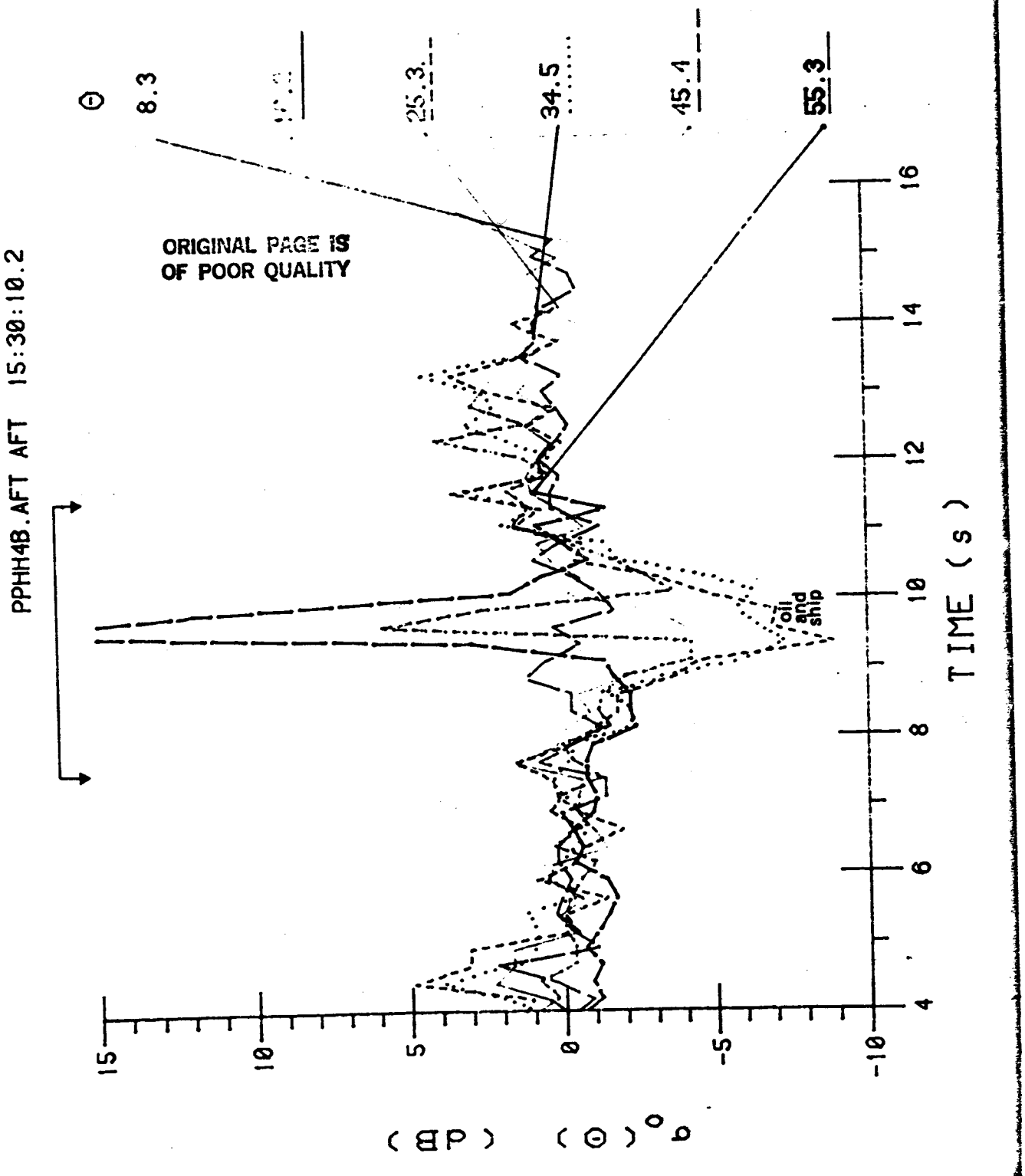

Figure 3.5.M. Time and look-angle history of MS backscatter for November 2, line 03; polarization VH.

FILE: WAVH31.AVE

STARTING TIME(HR:MIN:SEC): 17:03:56

ENDING TIME(HR:MIN:SEC): 17:04:03

GRAY LEVELS REPRODUCED ON NEXT LINE CORRESPONDING TO -10 DB TO 13 DB

EACH CHARACTER REPRESENTS 1 DEGREE INTERVAL FROM -60 TO 100
TIME CODE PRINTED IN REGION CLOSE TO NADIR FOR WHICH NO DATA IS AVAILABLE; ANGLE = - 5 TO + 5

-55 -45 -35 -25 -15 -5 0 5 15 25 35 45 55

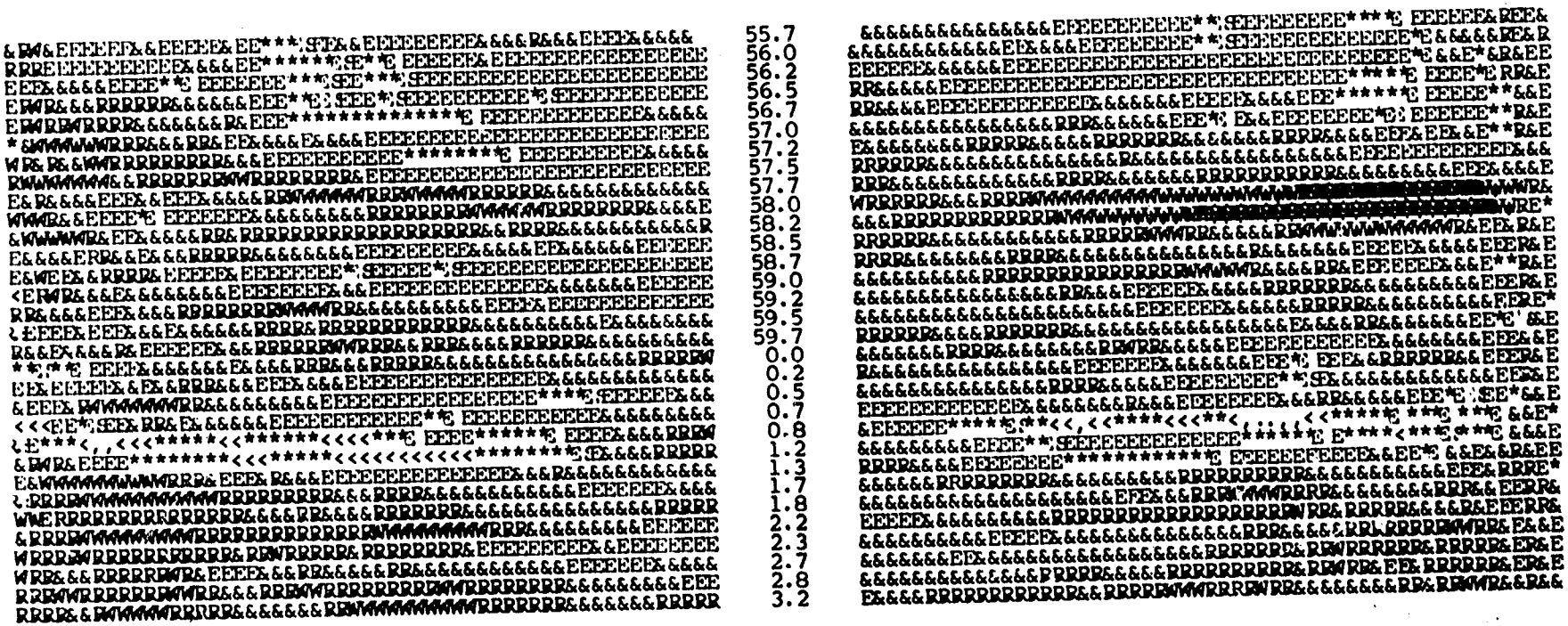

Figure 3.5.N. Time and look-angle history of MS backscatter for November 2, line 03; polarization VV.

FILE: WAVV31.AVE

STARTING TIME(HR:MIN:SEC) 17:03:56

ENDING TIME(HR:MIN:SEC) 17:04:03

GRAY LEVELS REPRODUCED ON NEXT LINE CORRESPONDING TO -10 DB TO 13 DB

EACH CHARACTER REPRESENTS 1 DEGREE INTERVAL FROM -60 TO +60
TIME CODE PRINTED IN REGION CLOSE TO NADIR FOR WHICH NO DATA IS AVAILABLE; ANGLE = - 5 TO + 5

-55 -45 -35 -25 -15 -5 0 5 15 25 35 45 55

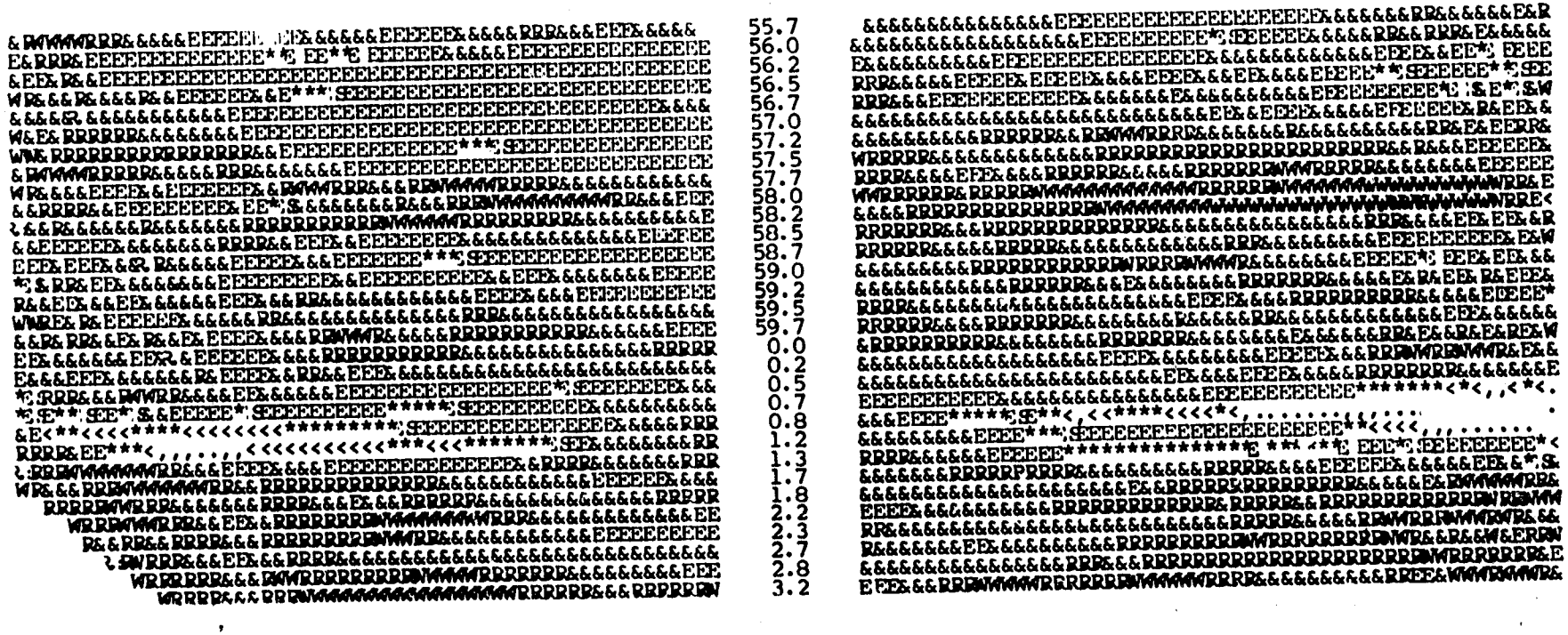

Figure 3.5.0. Time and look-angle history of MS backscatter for November 2, line 06; polarization HV.

FILE: WAHV6.AVE

STARTING TIME(HR:MIN:SEC) 17:13:34

ENDING TIME(HR:MIN:SEC) 17:13:41

GRAY LEVELS REPRODUCED ON NEXT LINE CORRESPONDING TO -10 DB TO 13 DB

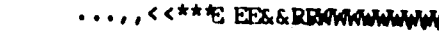

EACH CHARACTER REPRESENTS 1 DEGREE INTERVAL FROM -60 TO +60
TIME CODE PRINTED IN REGION CLOSE TO NADIR FOR WHICH NO DATA IS AVAILABLE; ANGLE = - 5 TO + 5

-55 -45 -35 -25 -15 -5 0 5 15 25 35 45 55

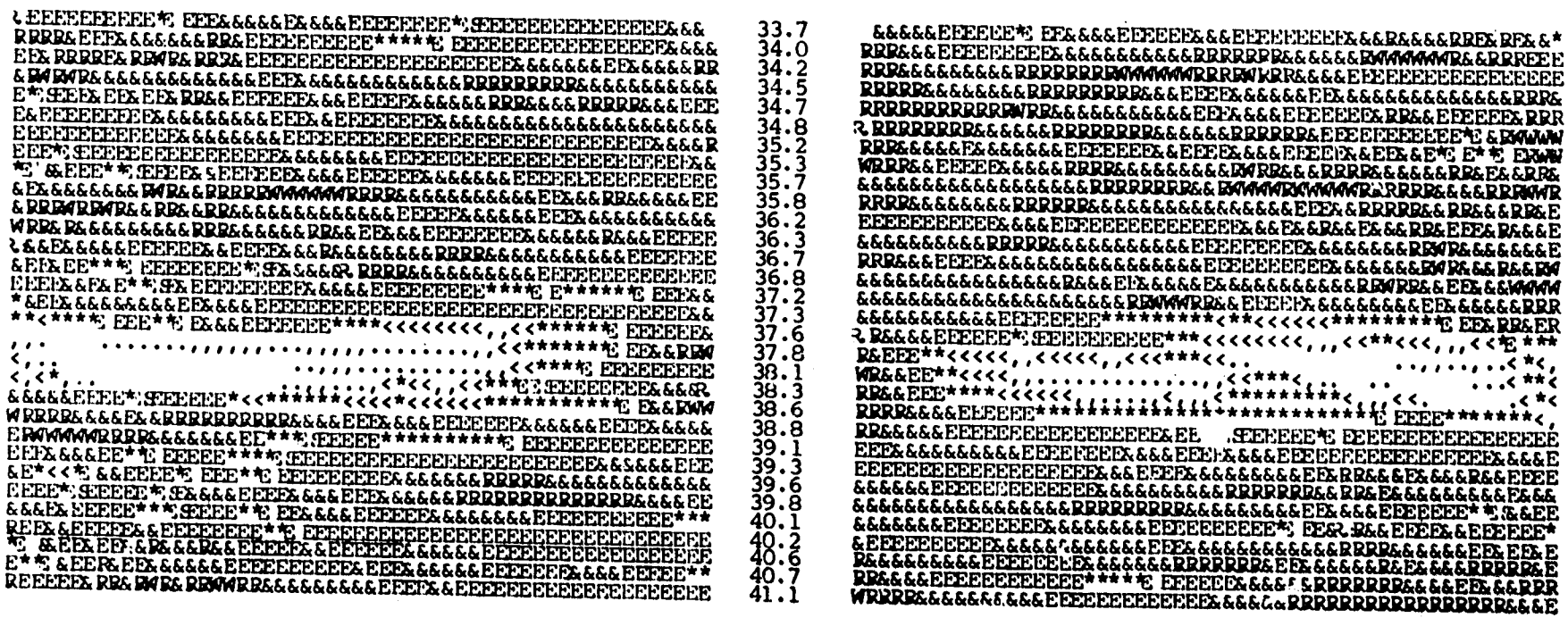

Figure 3.5.P. Time and look-angle history of MS backscatter for November 2, line 06; polarization HH.

FILE: WAHH6.AVE

STARTING TIME(HR:MIN:SEC 17:13:34

ENDING TIME(HR:MIN:SEC 17:13:41

GRAY LEVELS REPRODUCED ON NEXT LINE CORRESPONDING TO -10 DB TO 13 DB

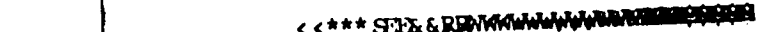

EACH CHARACTER REPRESENTS 1 DEGREE INTERVAL FROM -60 TO +60
TIME CODE PRINTED IN REGION CLOSE TO NADIR FOR WHICH NO DATA IS AVAILABLE; ANGLE = - 5 TO + 5

-55 -45 -35 -25 -15 -5 0 5 15 25 35 45 55

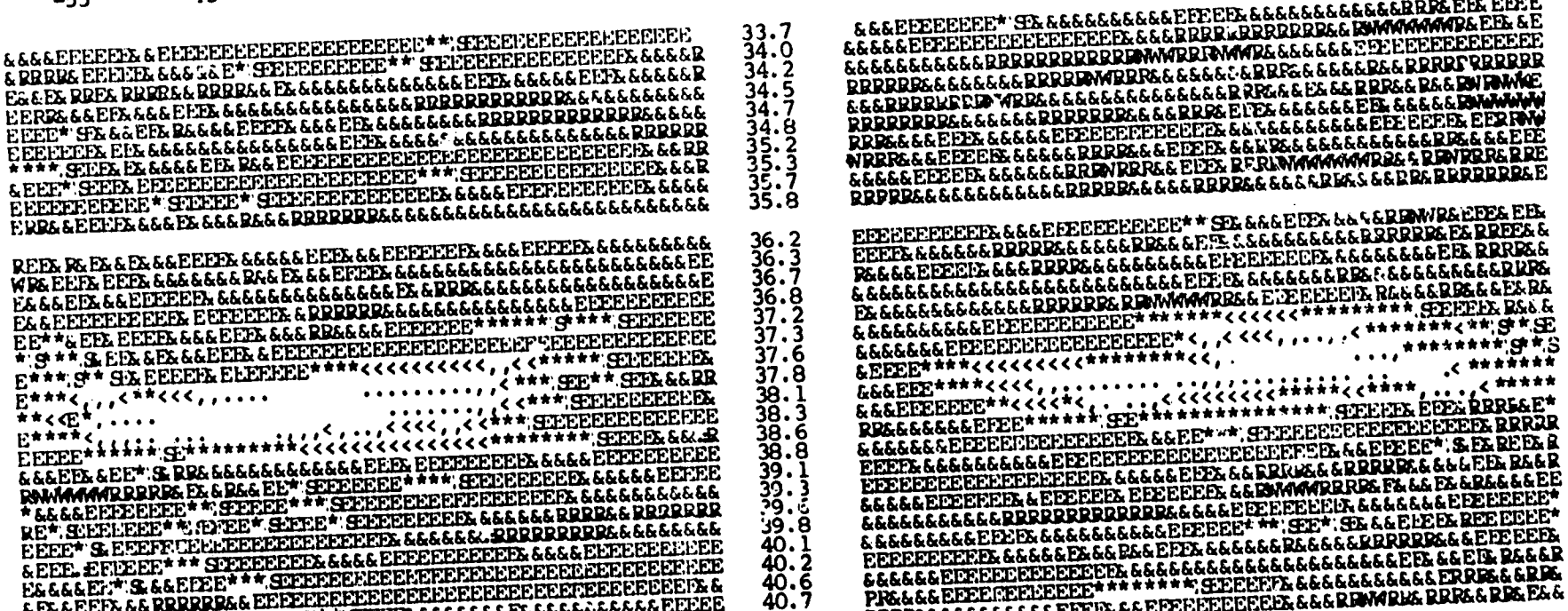

Figure 3.5.Q. Time and look-angle history of MS backscatter for November 3, line 4B; polarization HV.

FILE: WAHV4B.AVE

STARTING TIME(HR:MIN:SEC) 15:30:16

ENDING TIME(HR:MIN:SEC) 15:30:24

GRAY LEVELS REPRODUCED ON NEXT LINE CORRESPONDING TO -10 DB TO 13 DB

EACH CHARACTER REPRESENTS 1 DEGREE INTERVAL FROM -60 TO +60
TIME CODE PRINTED IN REGION CLOSE TO NADIR FOR WHICH NO DATA IS AVAILABLE; ANGLE = - 5 TO + 5

-55 -45 -35 -25 -15 -5 0 5 15 25 35 45 55

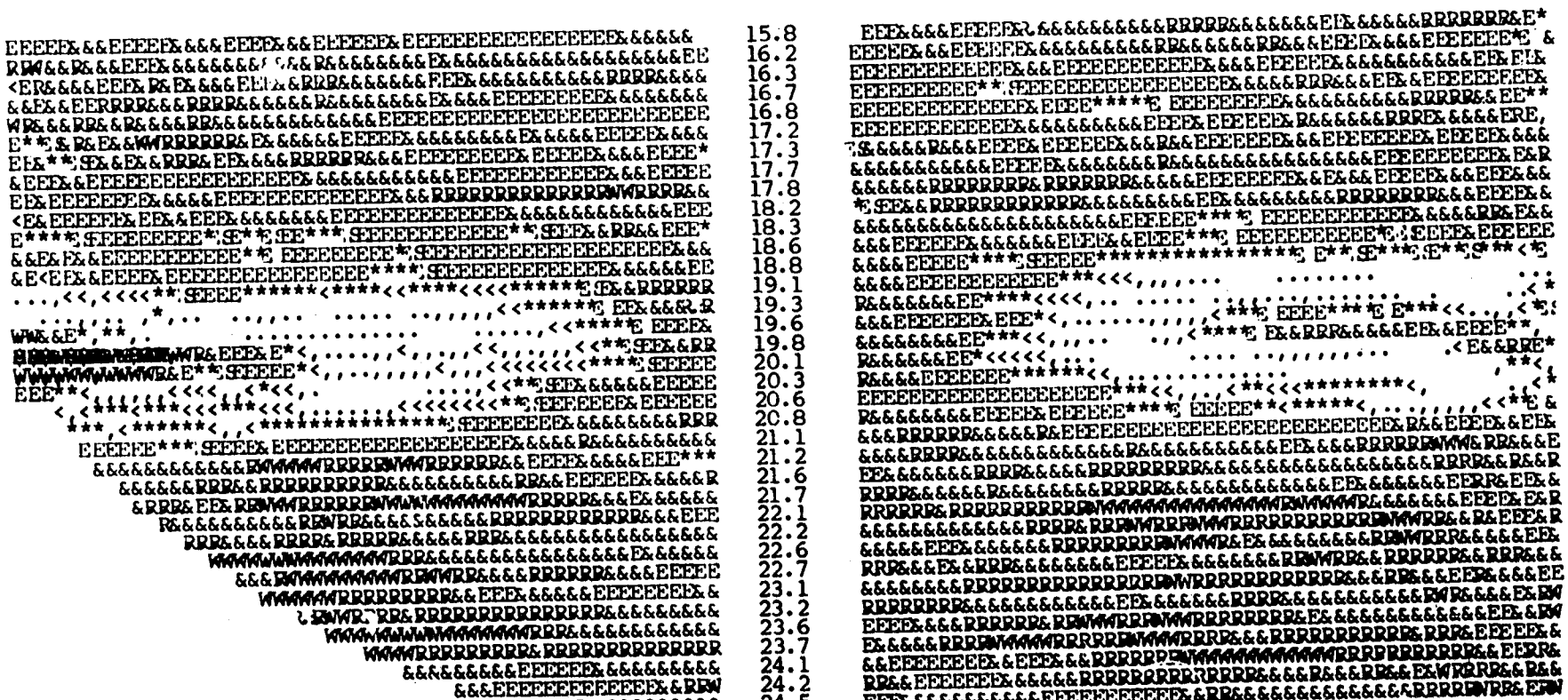

Figure 3.5.R. Time and look-angle history of HS backscatter for November 3, line 4B; polarization HH.

FILE: WAHH4B.AVE

STARTING TIME(HR:MIN:SEC) 15:30:16

ENDING TIME(HR:MIN:SEC) 15:30:24

GRAY LEVELS REPRODUCED ON NEXT LINE CORRESPONDING TO -10 DB TO 13 DB

EACH CHARACTER REPRESENTS 1 DEGREE INTERVAL FROM -60 TO +60
TIME CODE PRINTED IN REGION CLOSE TO NADIR FOR WHICH NO DATA IS AVAILABLE; ANGLE = - 5 TO + 5

-55 -45 -35 -25 -15 -5 0 5 15 25 35 45 55

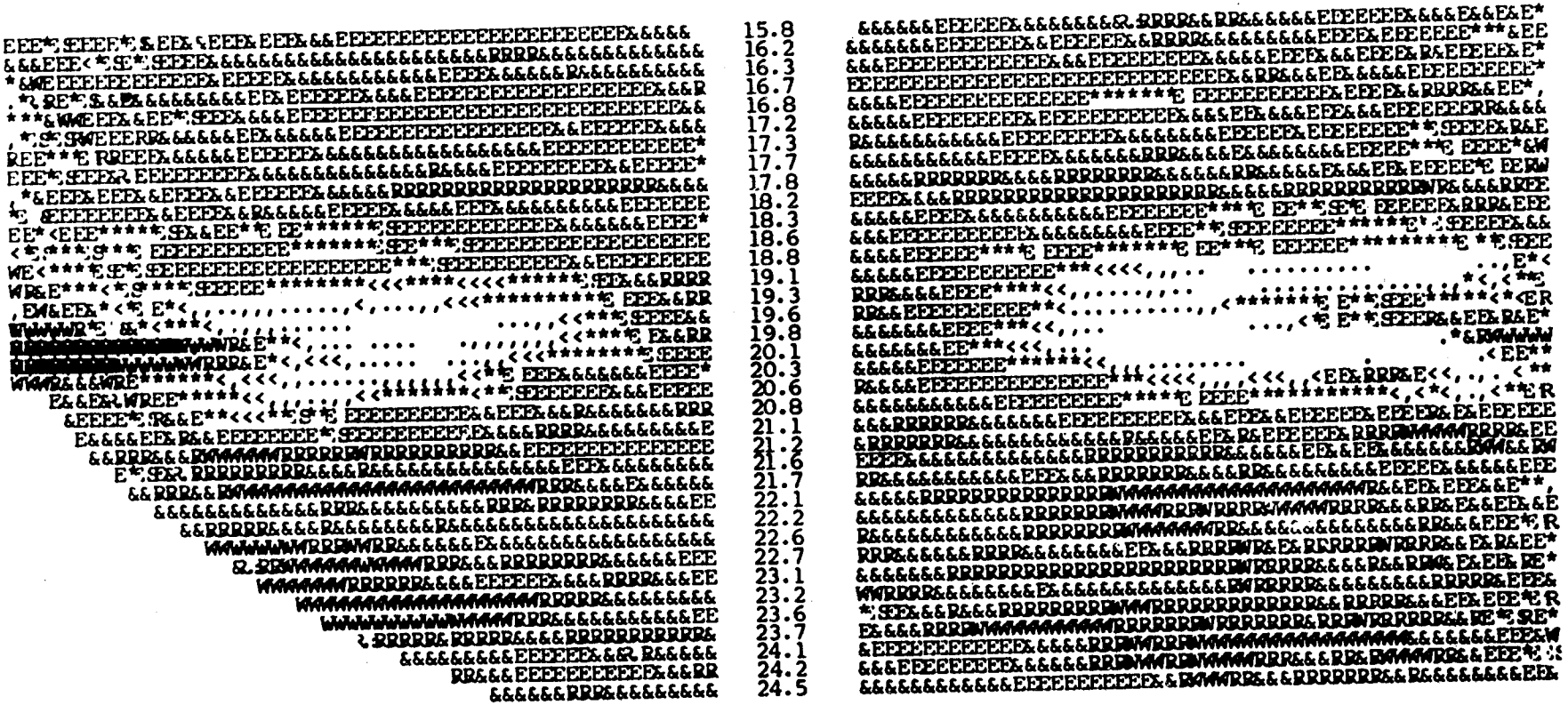

Figure 3.6.A SAR pass #2, November 2, 1978. Pixel size = 2.3m. Grey level themes represent four contiguous ranges of radar backscatter intensity.

Theme	dB Range
	24.1
1	20.7
2	18.2
3	15.7
4	12.6

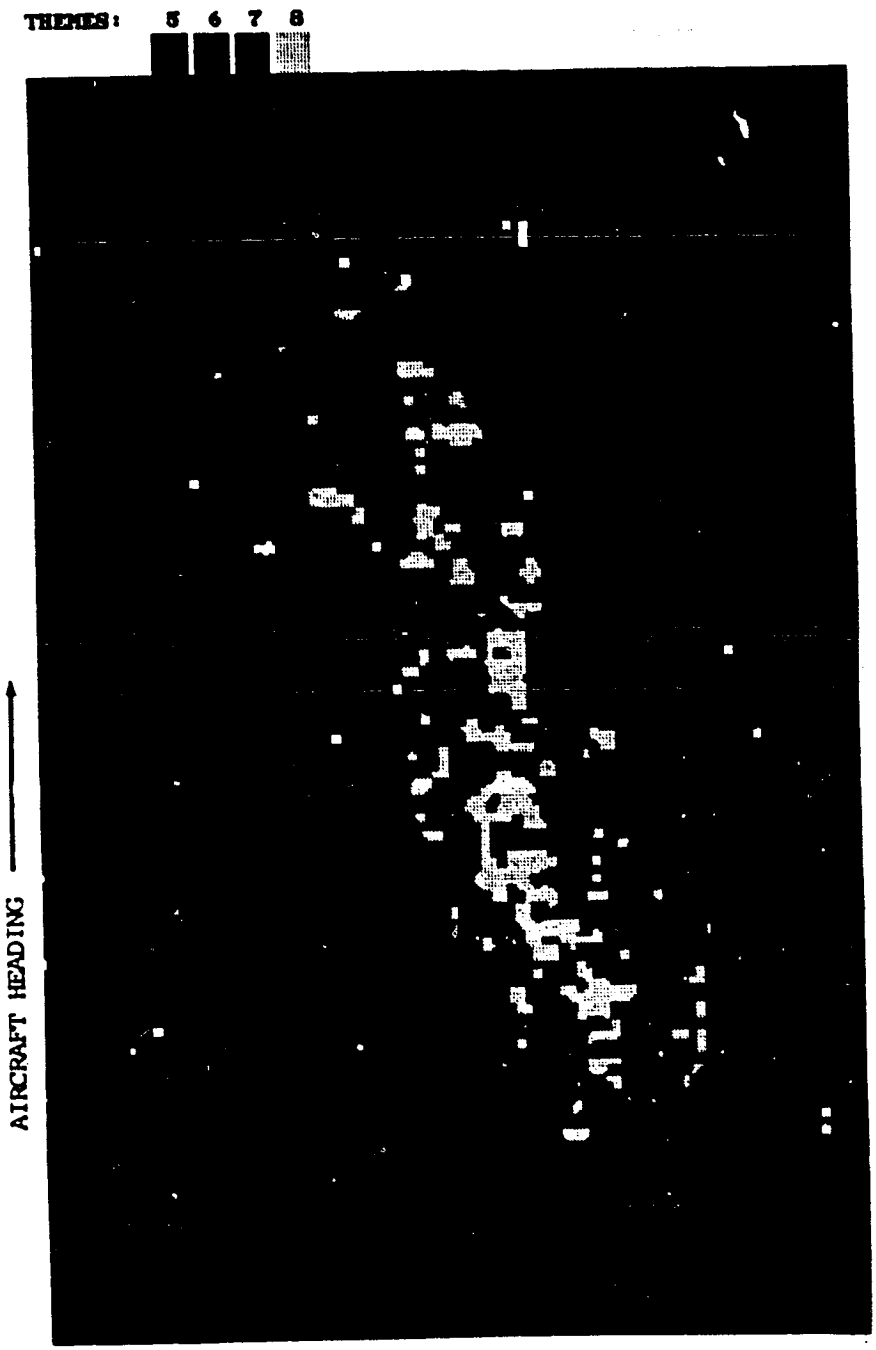

Figure 3.6.B. SAR pass #2, November 2, 1978. Pixel size = 2.3m. Grey level themes have been smoothed and represent four contiguous ranges of radar backscatter intensity.

Theme	dB Range
	24.1
5	20.7
6	18.2
7	15.7
8	12.6

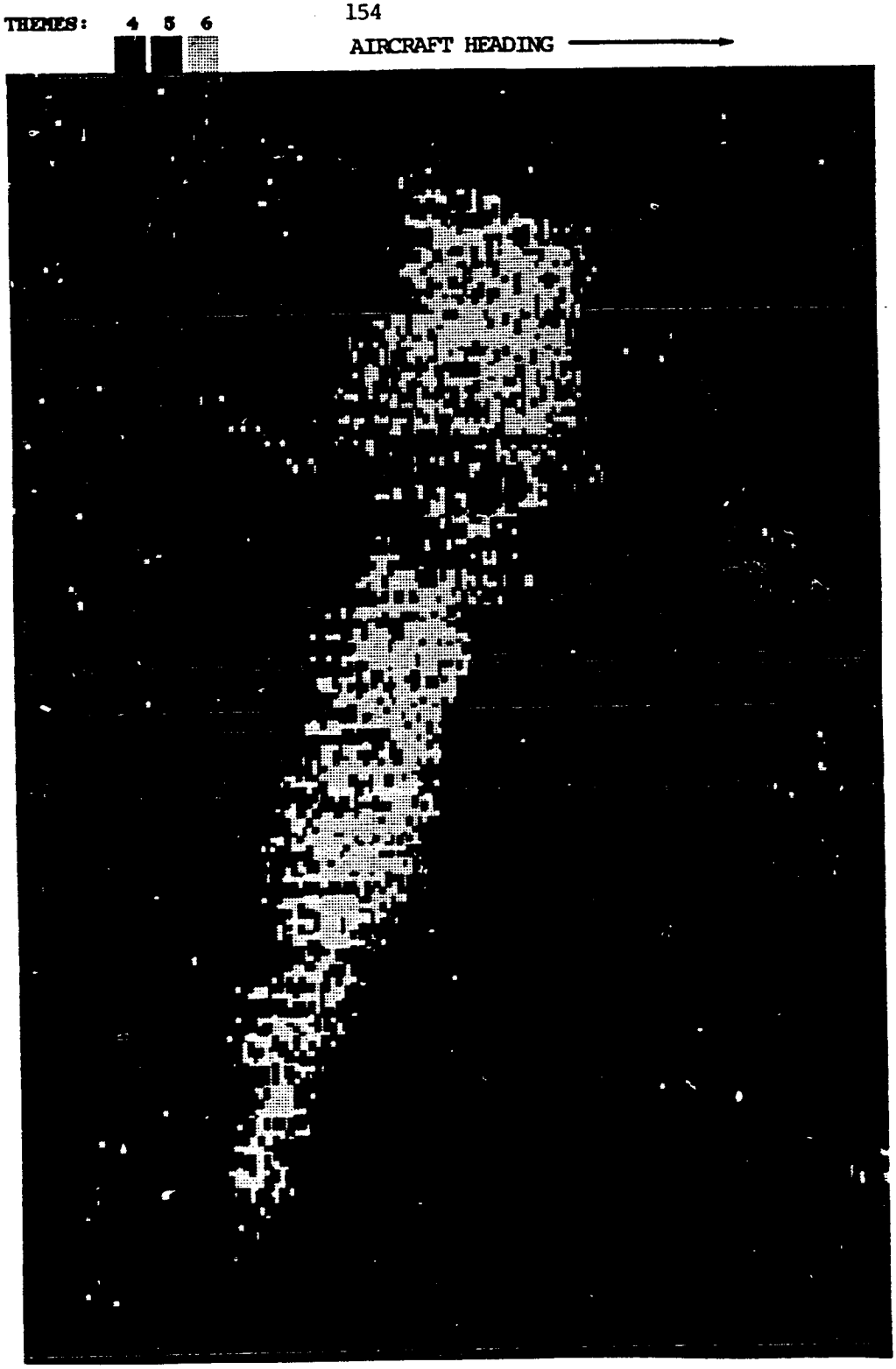

Figure 3.6.C. SAR pass #5, November 3, 1978. Pixel size = 3.5m. Grey level themes represent three contiguous ranges of radar backscatter intensity.

Theme	dB Range
	24.1
4	20.1
5	17.5
6	12.6

Figure 3.6.D. SAR pass #5, November 3, 1978 Pixel size = 3.5m. Grey level themes have been smoothed and represent three contiguous ranges of radar backscatter intensity.

Theme	dB Range
	24.1
1	20.1
2	17.5
3	12.6

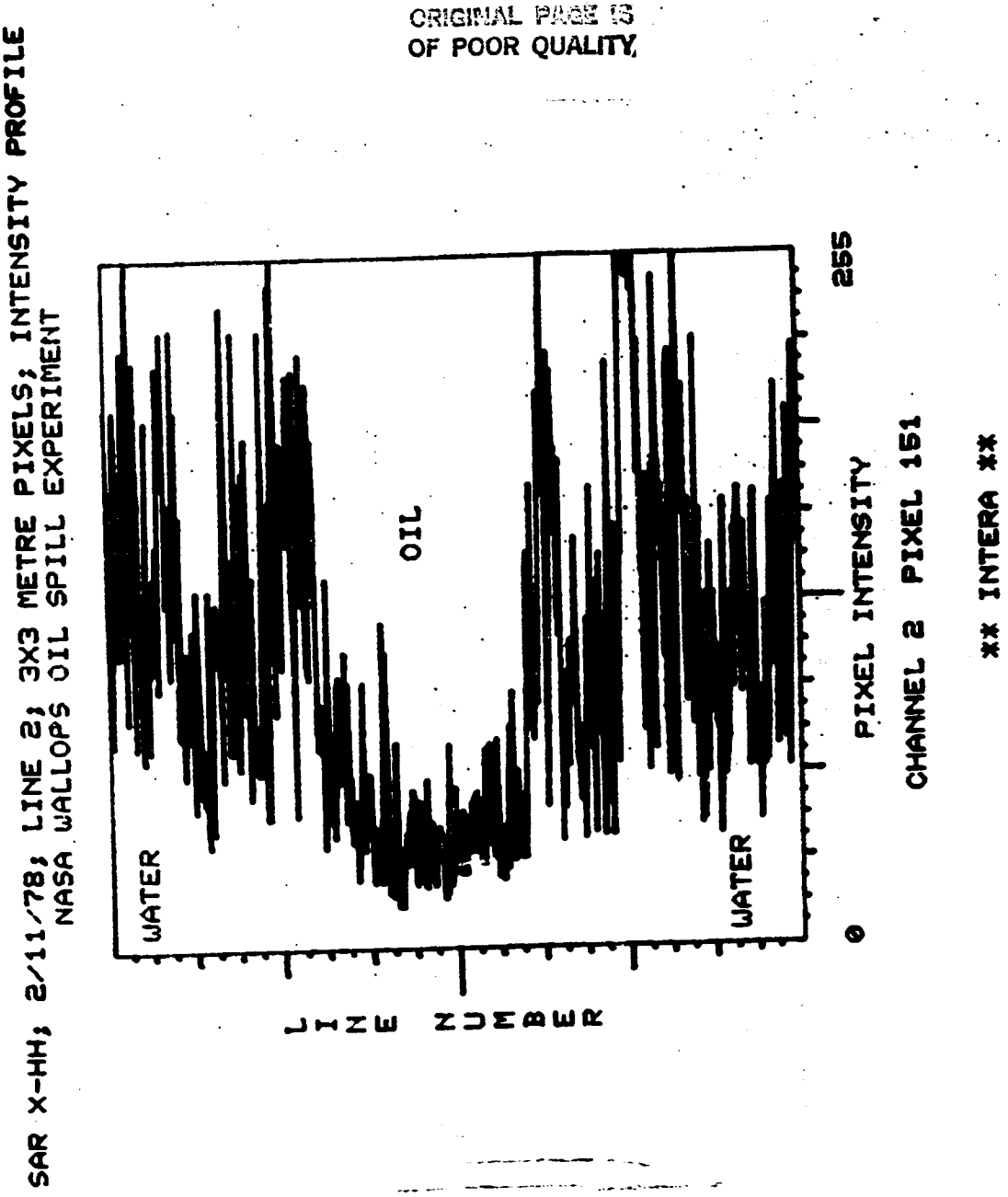

Figure 3.6.E. SAR profile transect of oil and water.

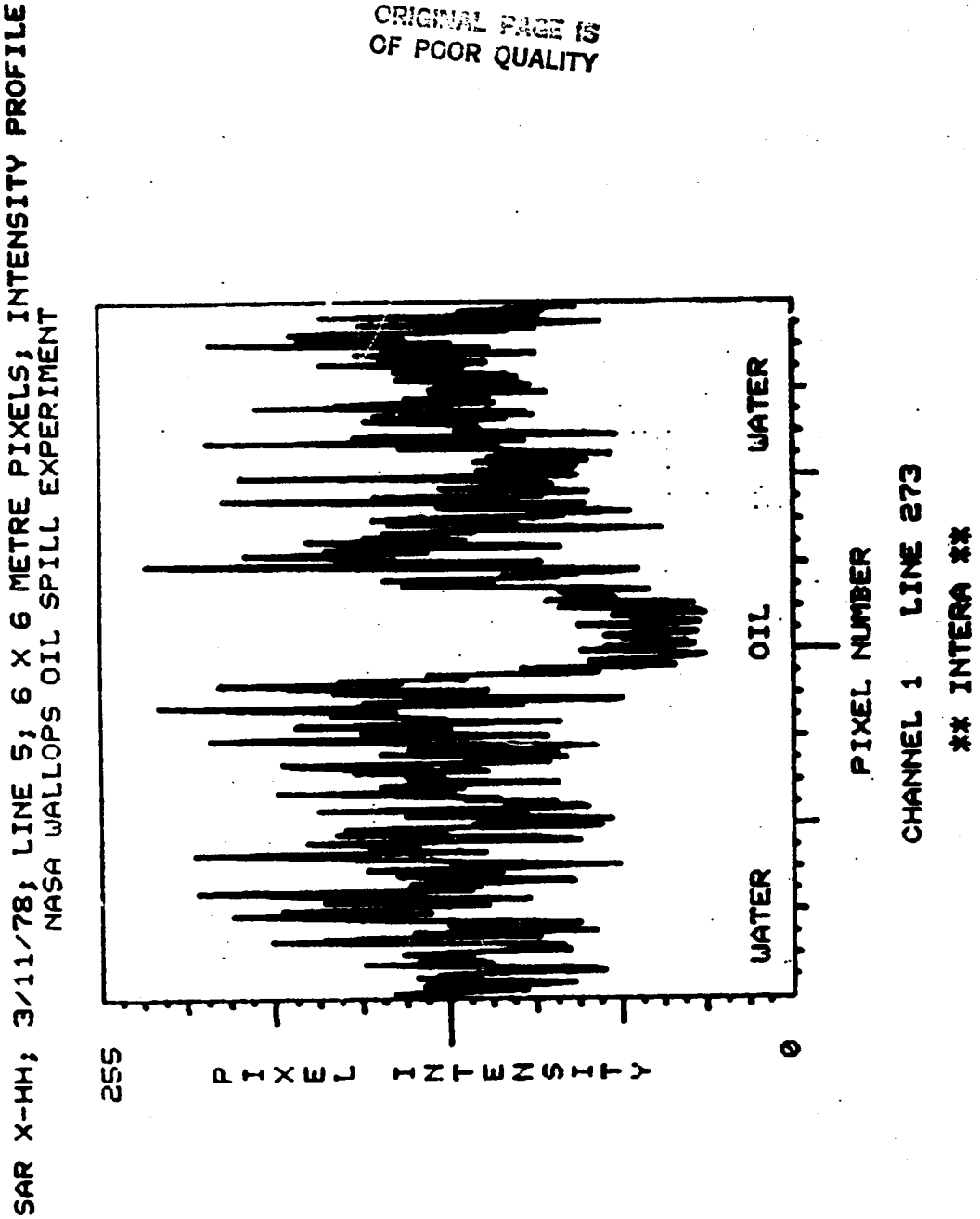

Figure 3.6.F. SAR profile transect of oil and water.

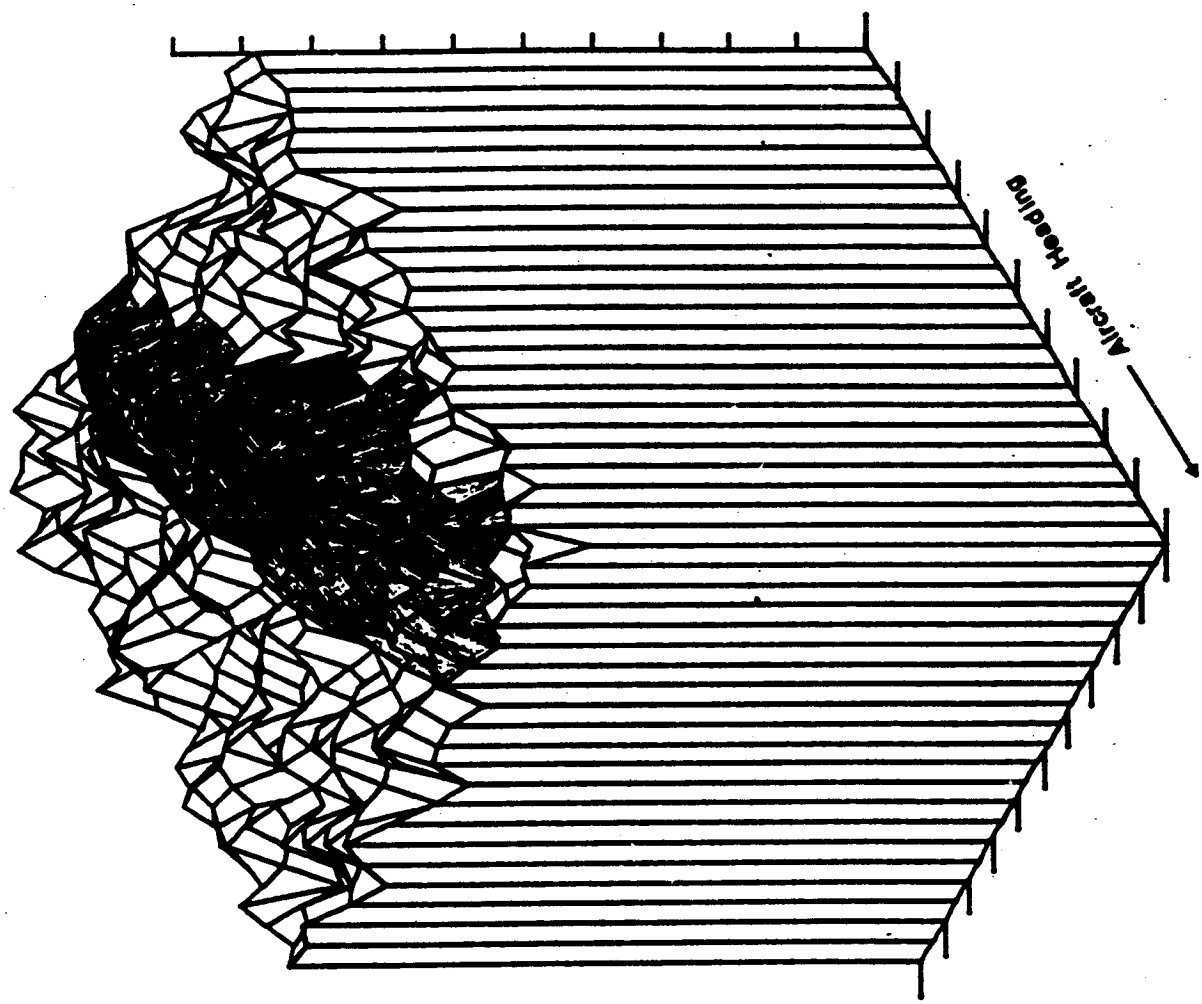

Figure 3.6.G. Pseudo three-dimensional view of oil slick target (shaded area) on SAR X-HH scene; November 2, 1978, pass #2. Vertical axis is inverted dB scale.

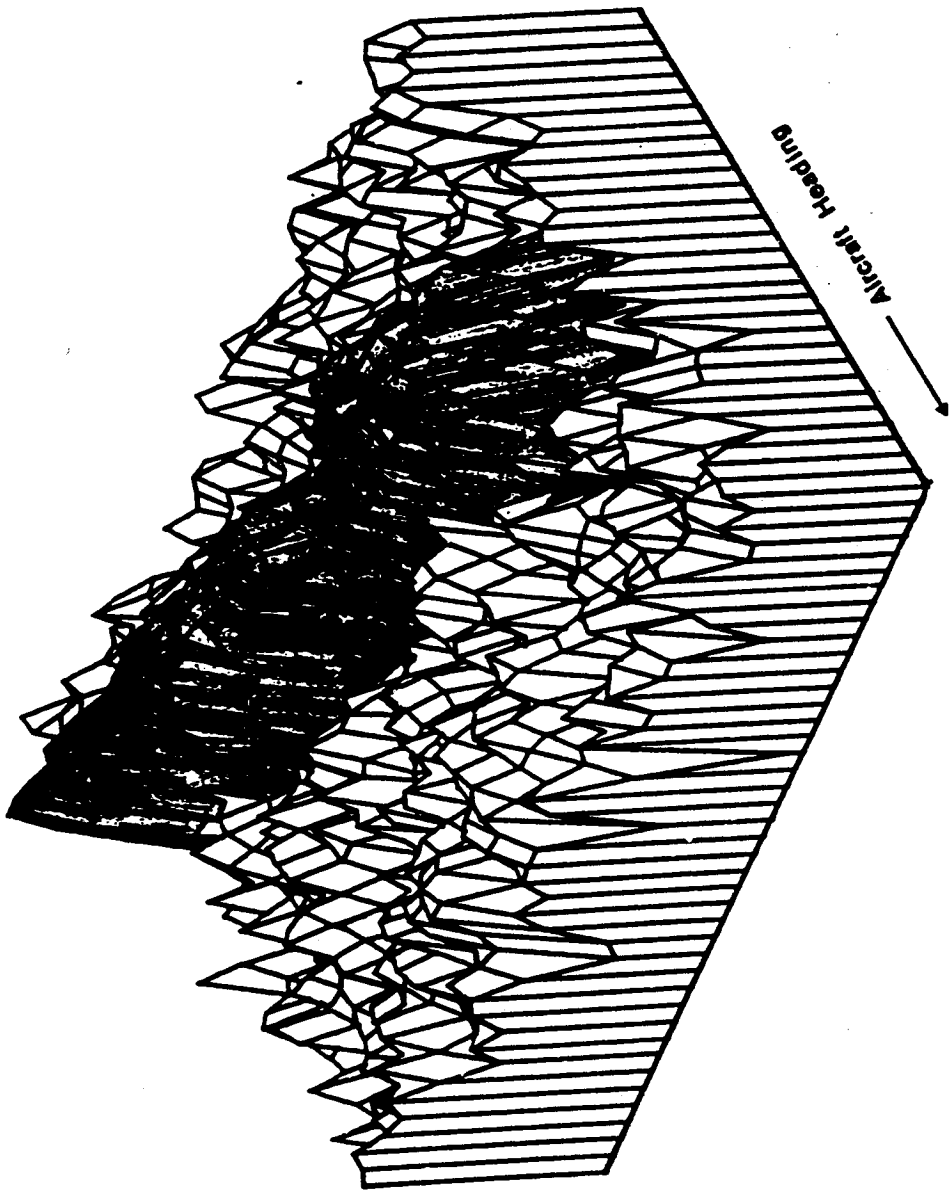

Figure 3.6.H. Pseudo three-dimensional view of oil slick target (shaded area) on SAR X-HH scene; November 3, 1978, pass #5. Vertical axis is inverted dB scale.

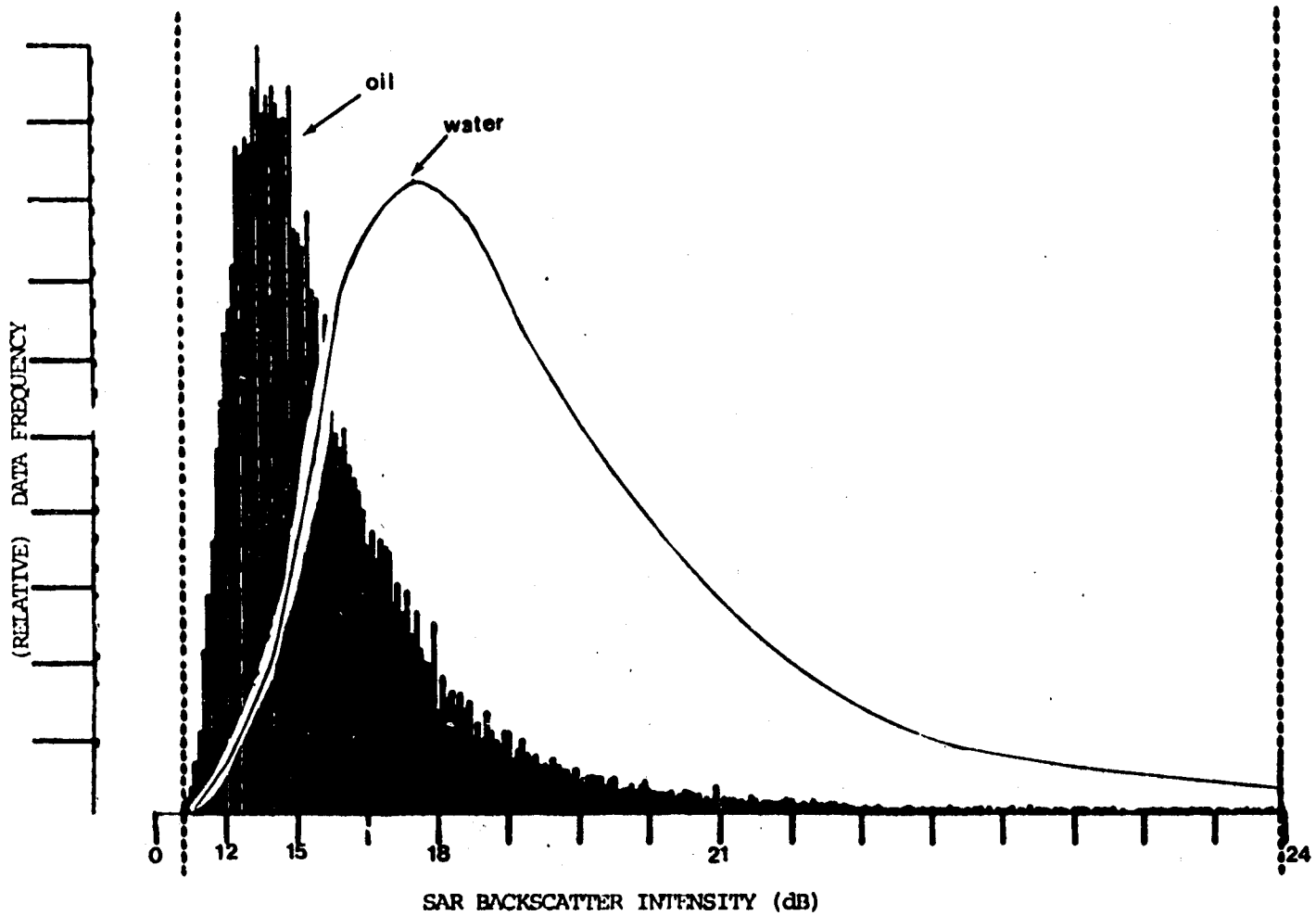

Figure 3.6.I. Backscatter histograms of SAR X-HH images of oil and water. Murban crude oil; 2 November 1978; pass #2.

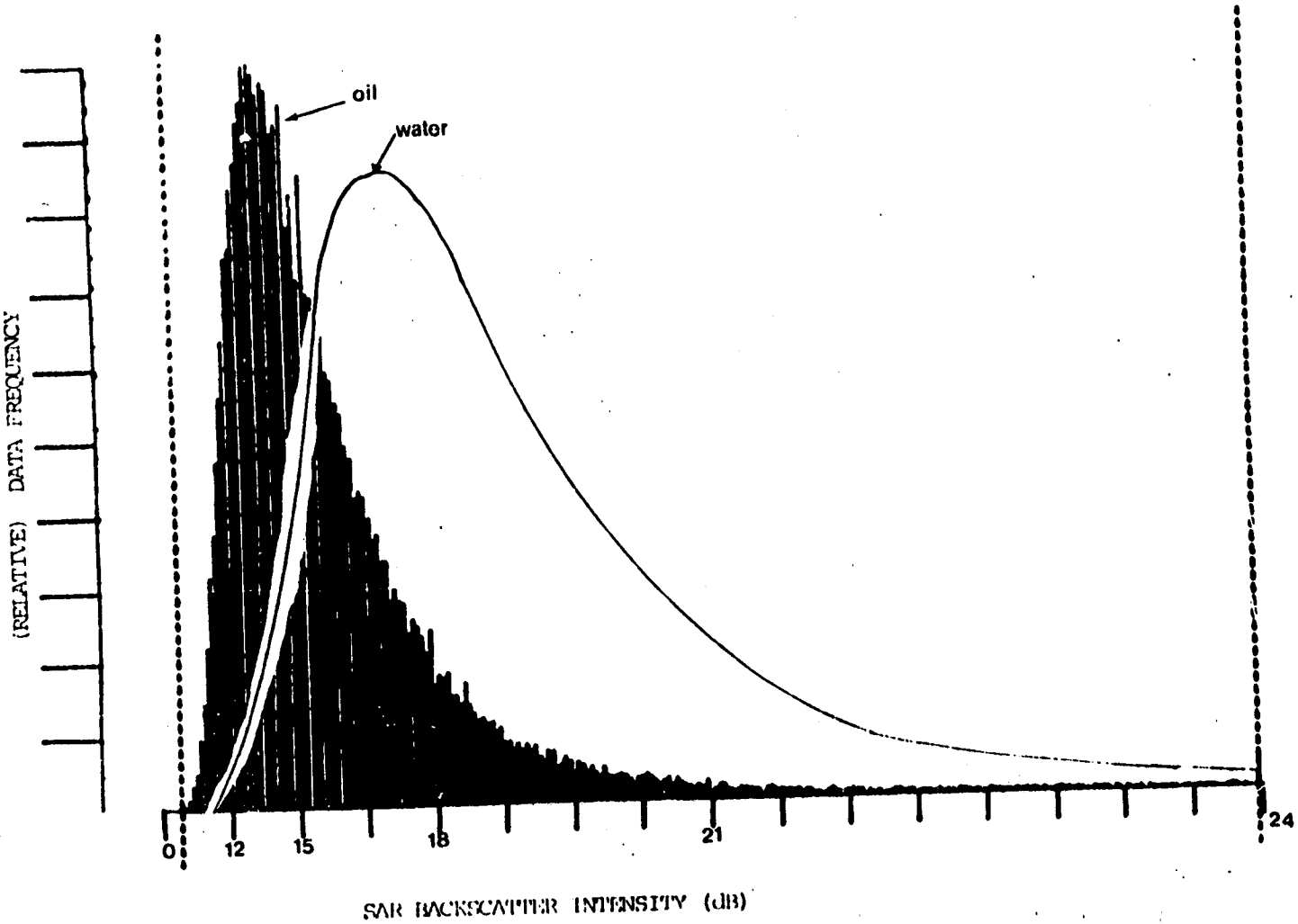

Figure 3.6.J. Backscatter histograms of SAR X-III images of oil and water. La Rosa crude oil; November 3, 1978; pass #5.

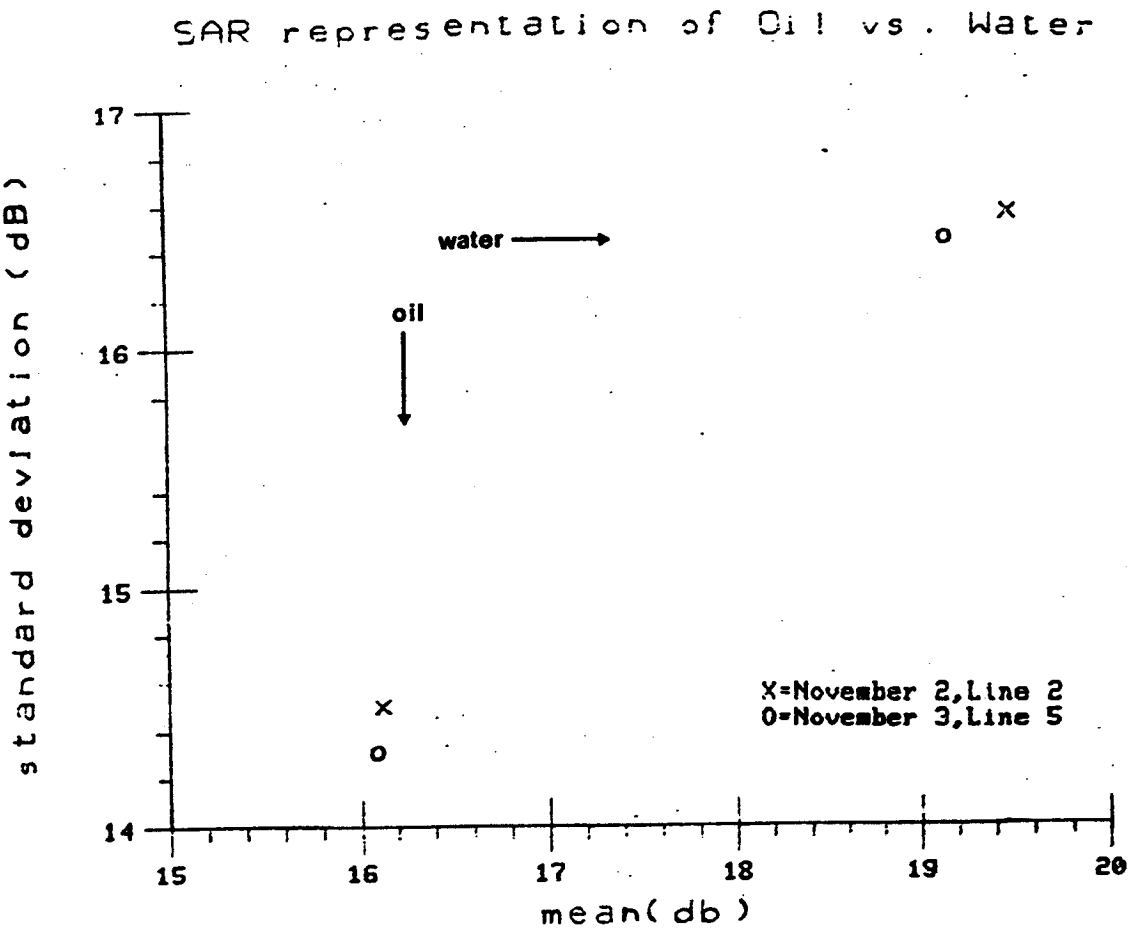

Figure 3.6.K. Relative radar cross-sections of oil and water; SAR X-HH.

Pages 163 - 173

are transparencies 4.1.A
through 4.1.k, to be
found in a packet
inside the back cover.

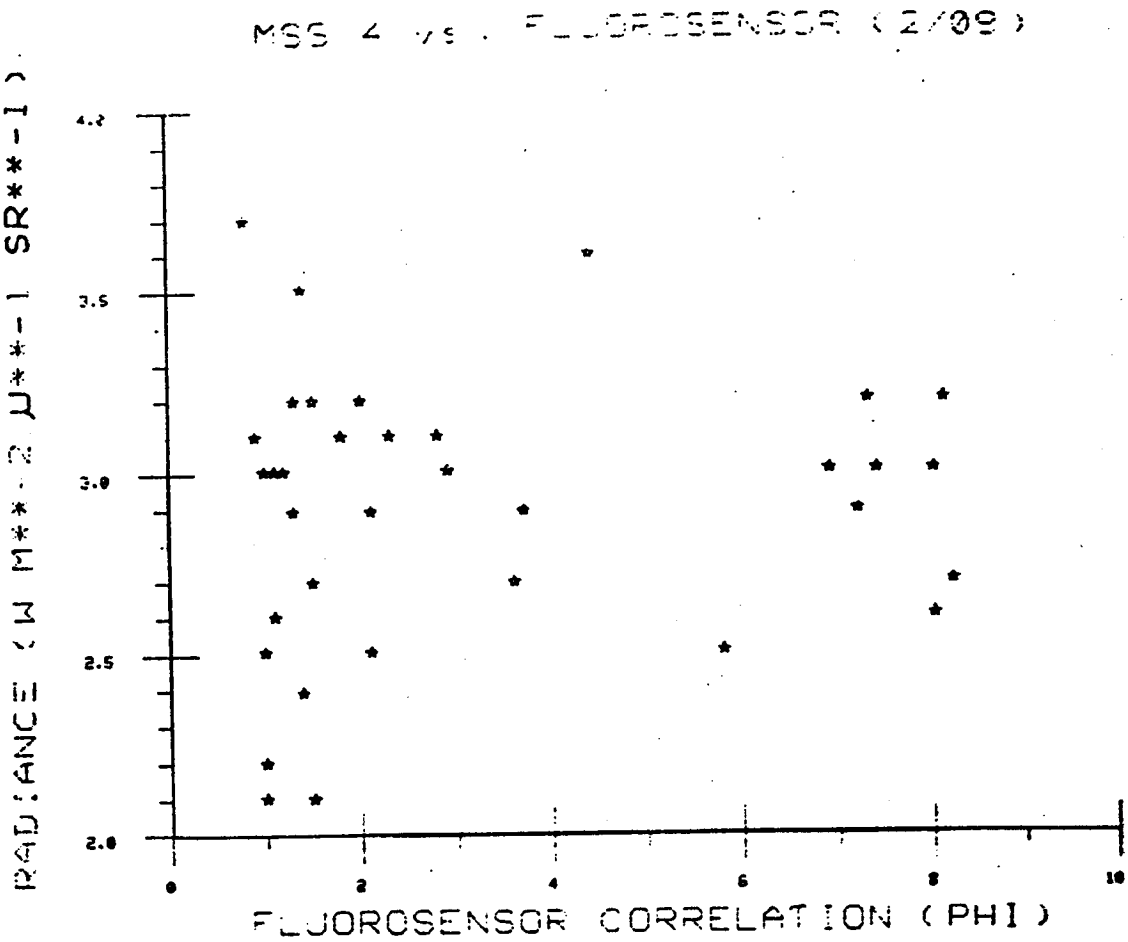

Figure 4.1.L. Scattergram showing relationship of MSS Band 4 radiance and fluorosensor (PHI) correlation; 2 November 1978, Line 09

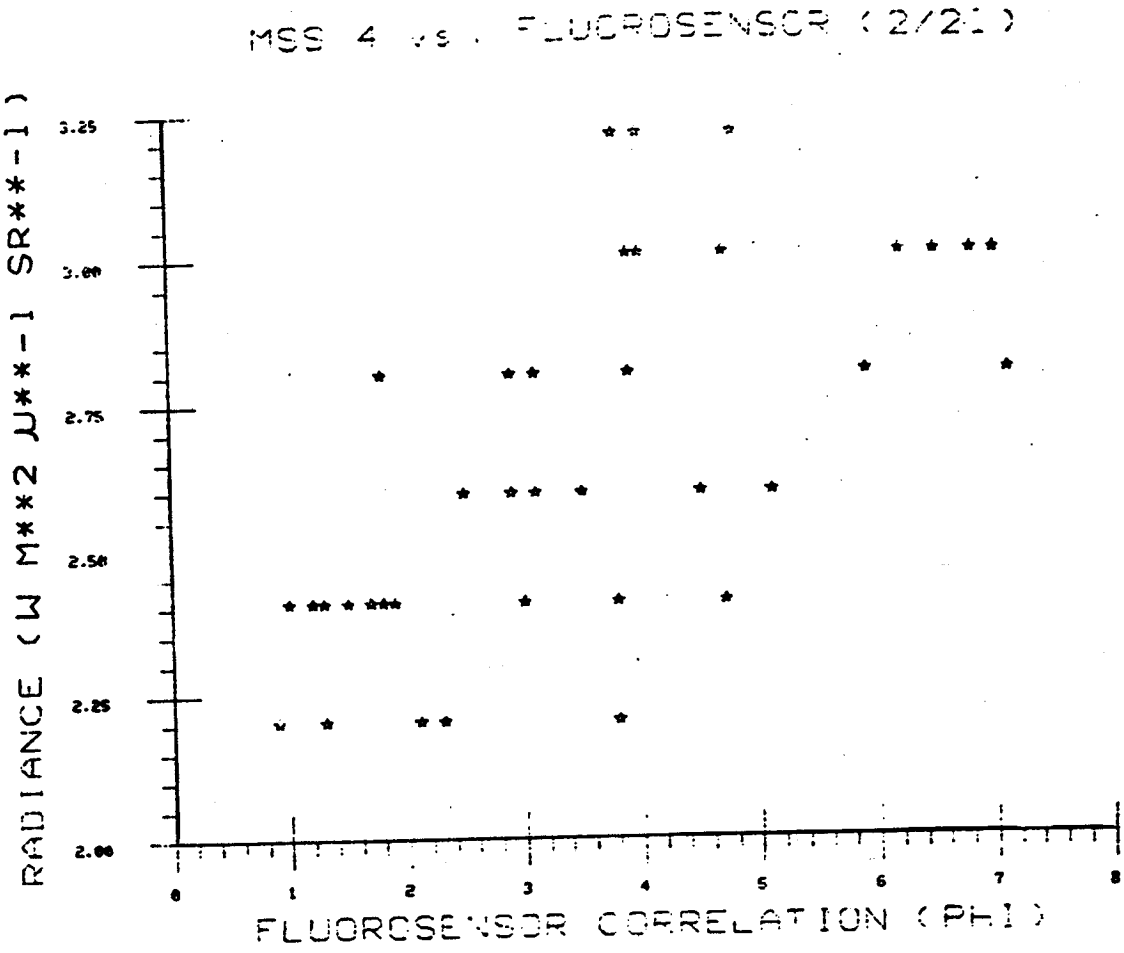

Figure 4.1.M. Scattergram showing relationship of MSS Band 4 radiance and fluorosensor (PHI) correlation; 2 November 1978, Line 21

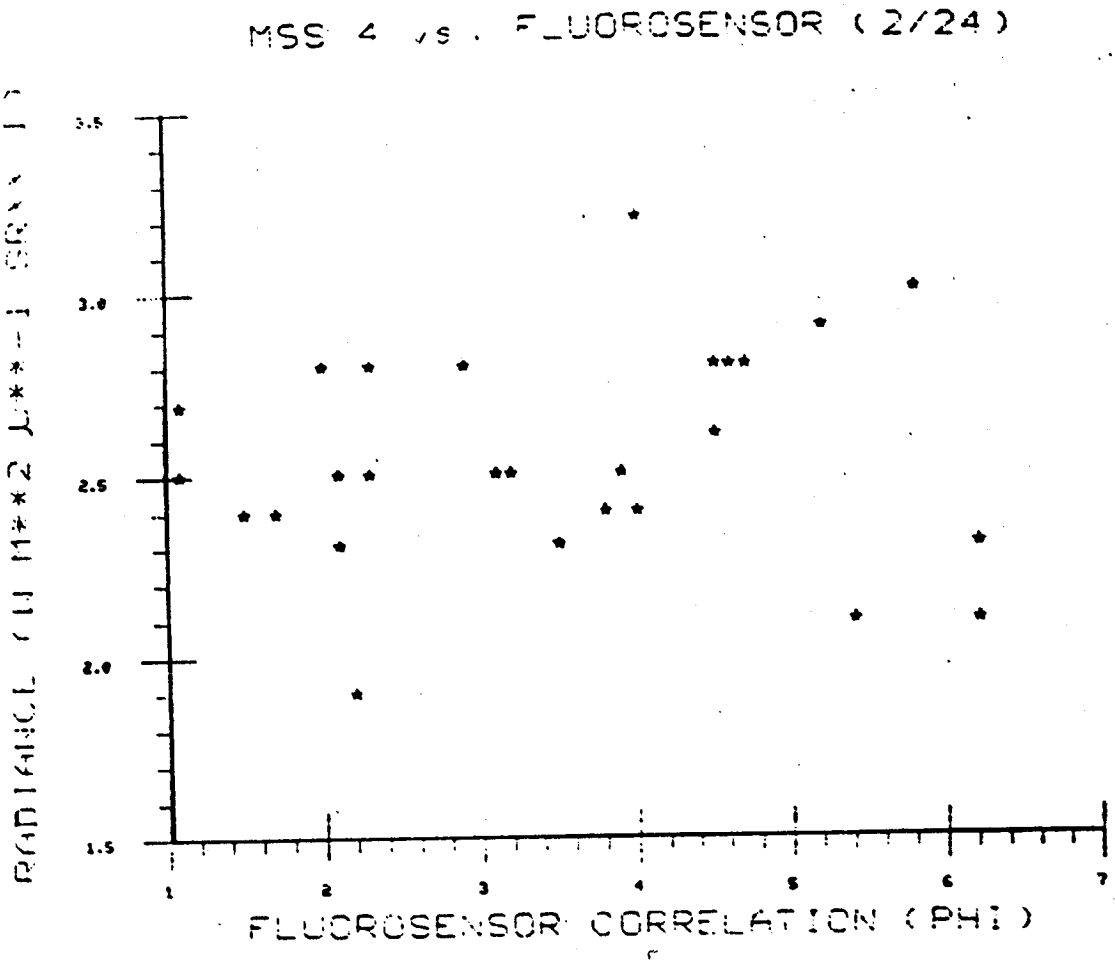

Figure 4.1.N. Scattergram showing relationship of MSS Band 4 radiance and fluorosensor (PHI) correlation; 2 November 1978, Line 24

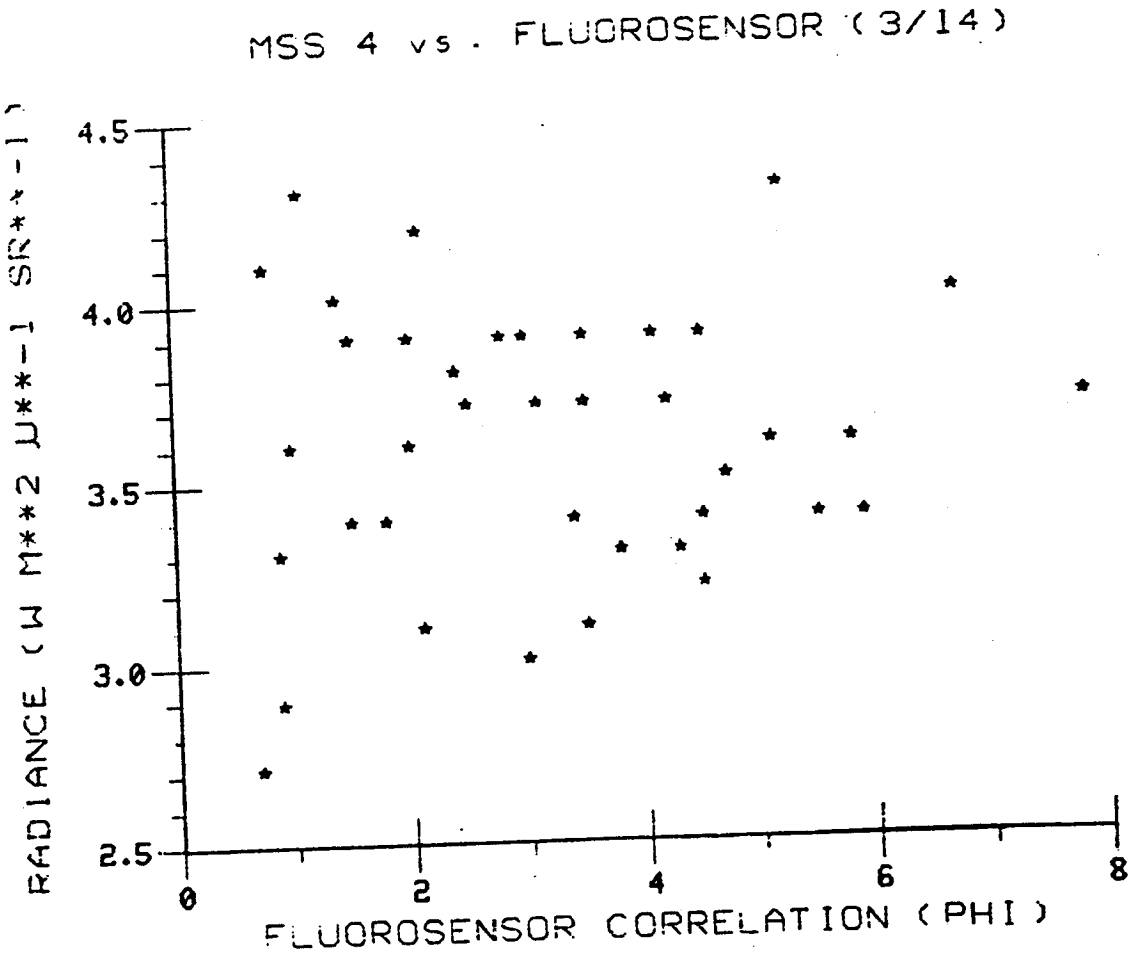

Figure 4.1.0. Scattergram showing relationship of MSS Band 4 radiance and fluorosensor (PHI) correlation; 3 November 1978, Line 14

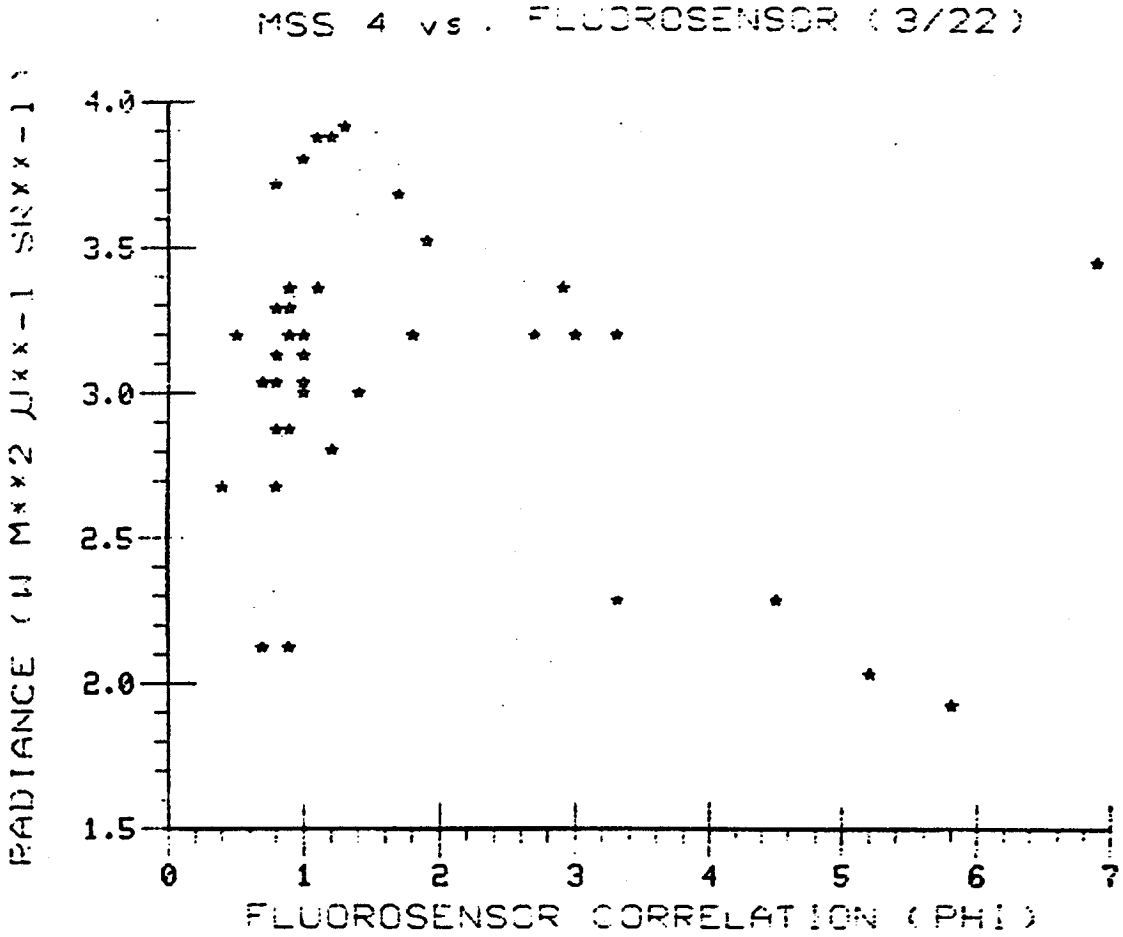

Figure 4.1.Q. Scattergram showing relationship of MSS Band 4 radiance and fluorosensor (PHI) correlation; 3 November 1978, Line 22

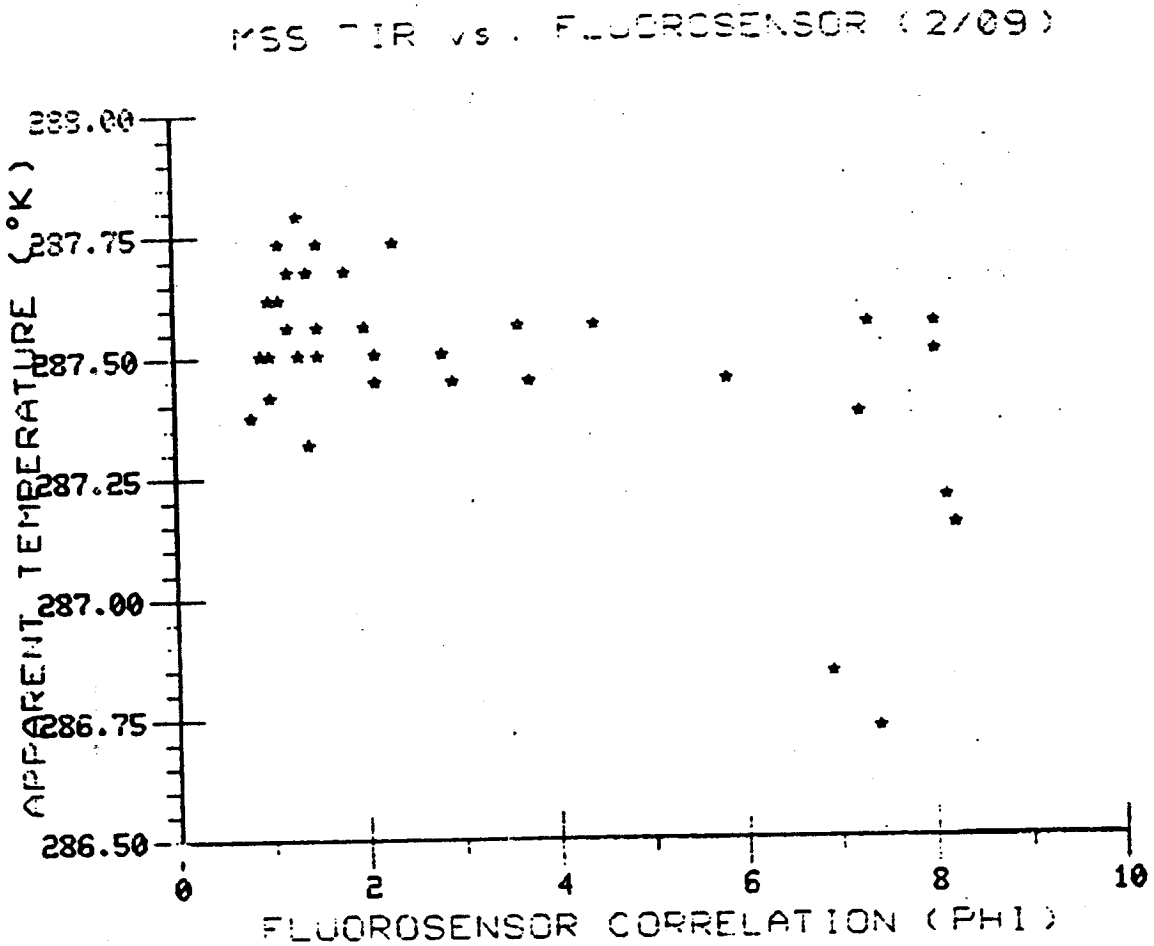

Figure 4.1.R. Scattergram showing relationship of MSS Band TIR radiance and fluorosensor (PHI) correlation; 2 November 1978, Line 09

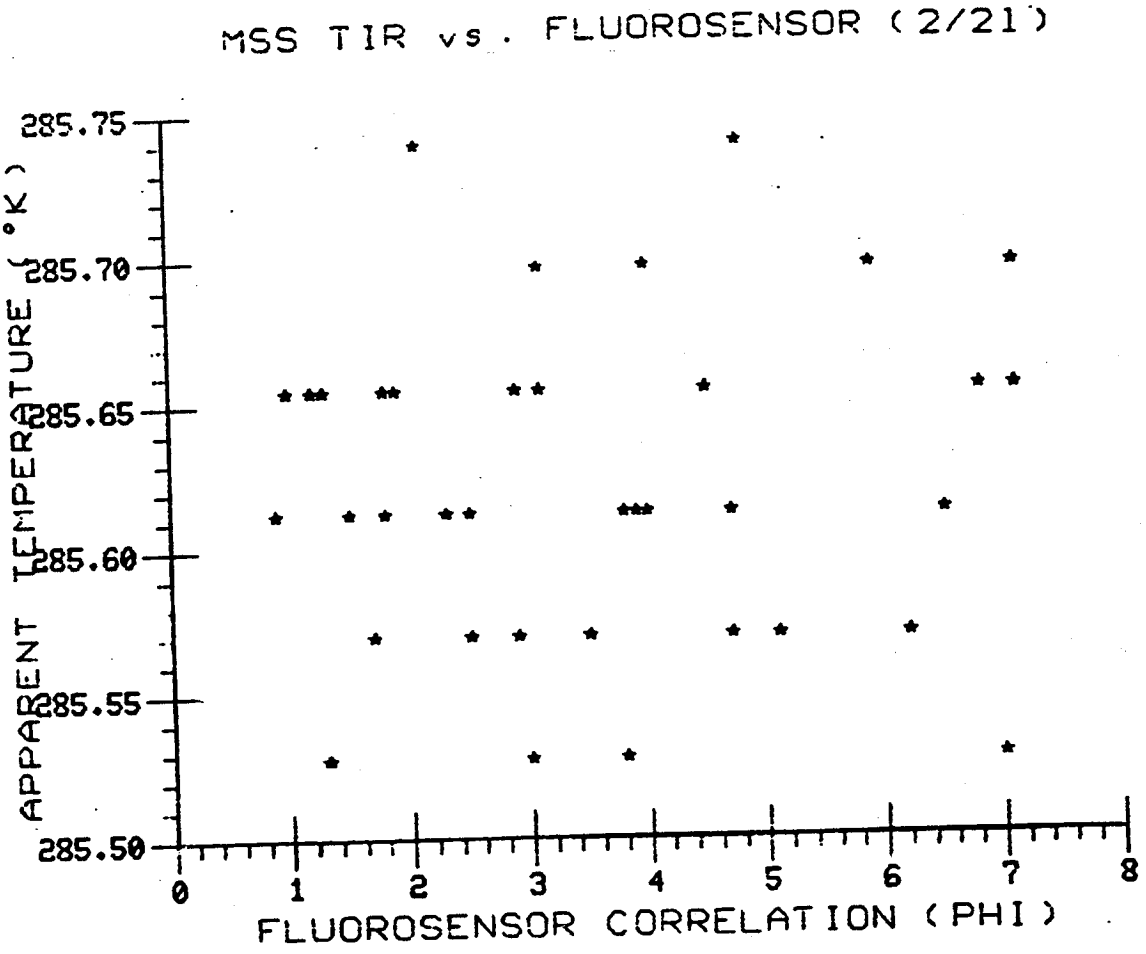

Figure 4.1.S. Scattergram showing relationship of MSS Band TIR radiance and fluorosensor (PHI) correlation; 2 November 1978, Line 21

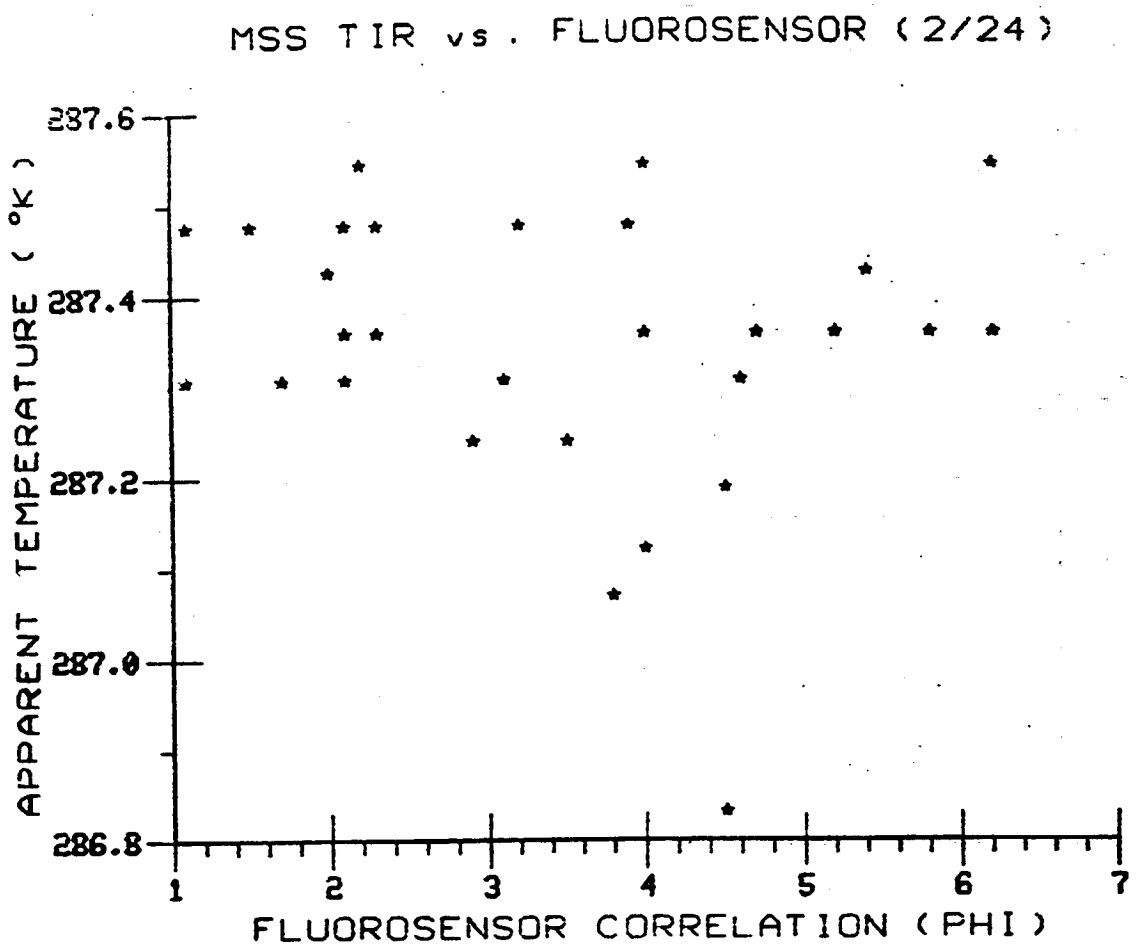

Figure 4.1.T. Scattergram showing relationship of MSS Band TIR radiance and fluorosensor (PHI) correlation; 2 November 1978, Line 24

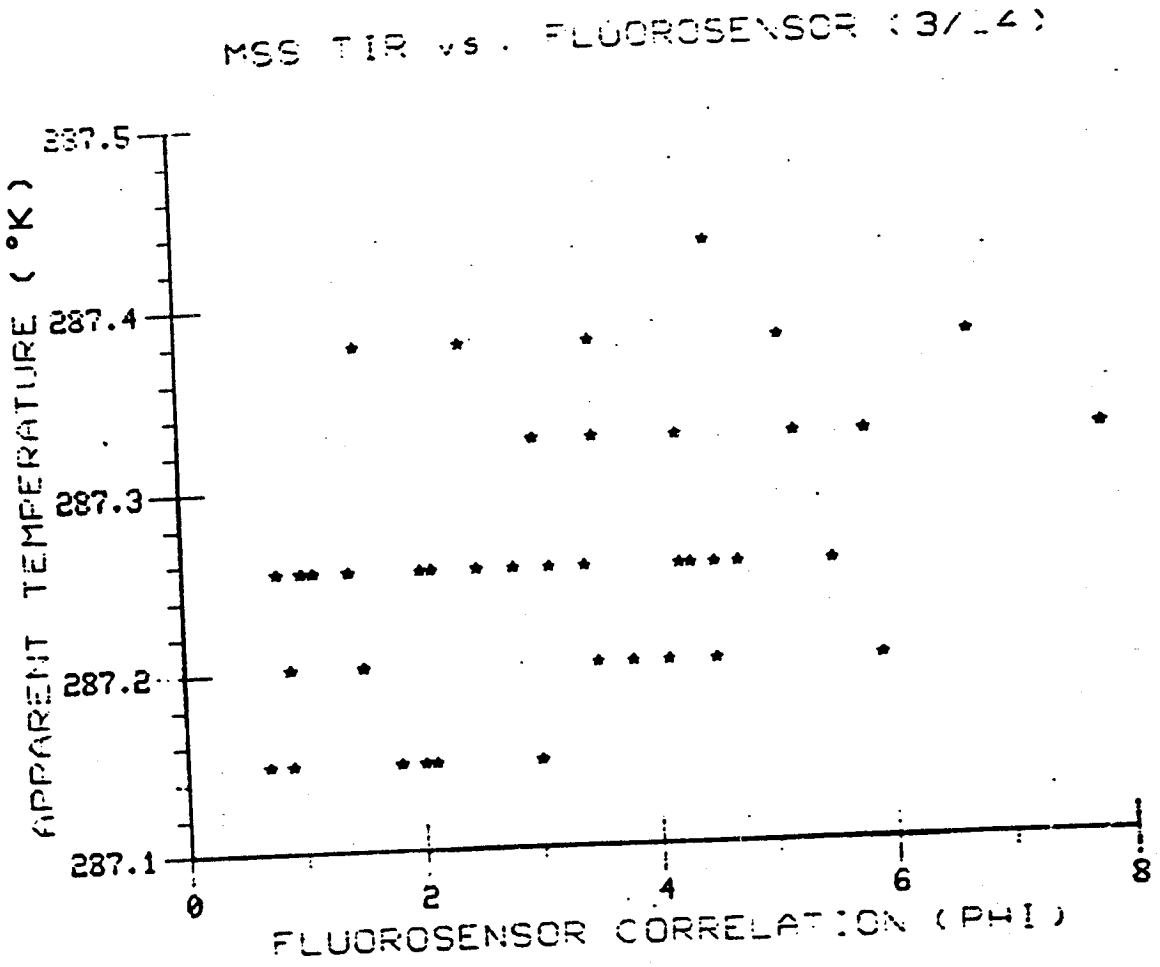

Figure 4.1.U. Scattergram showing relationship of MSS Band TIR radiance and fluorosensor (PHI) correlation; 3 November 1978. Line 14

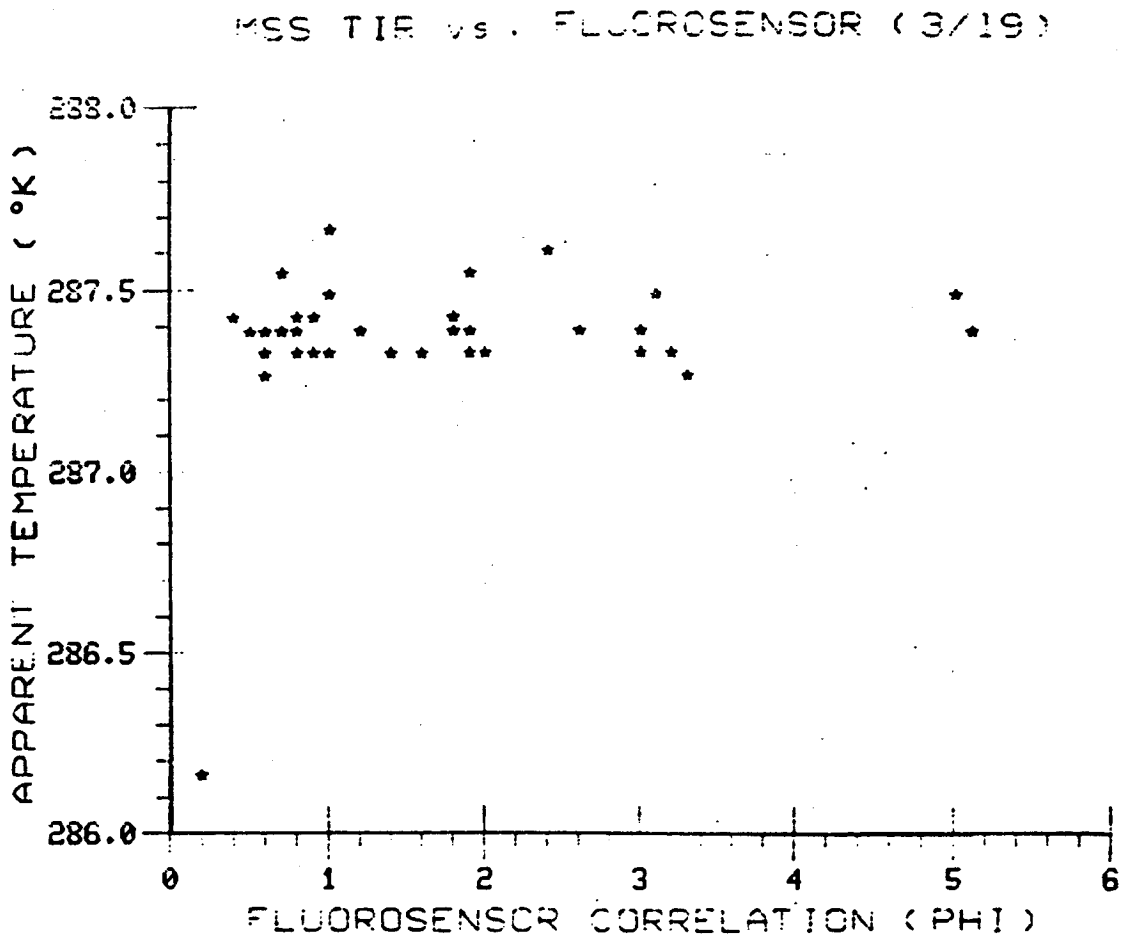

Figure 4.1.V. Scattergram showing relationship of MSS Band TIR radiance and fluorosensor (PHI) correlation; 3 November 1978, Line 19

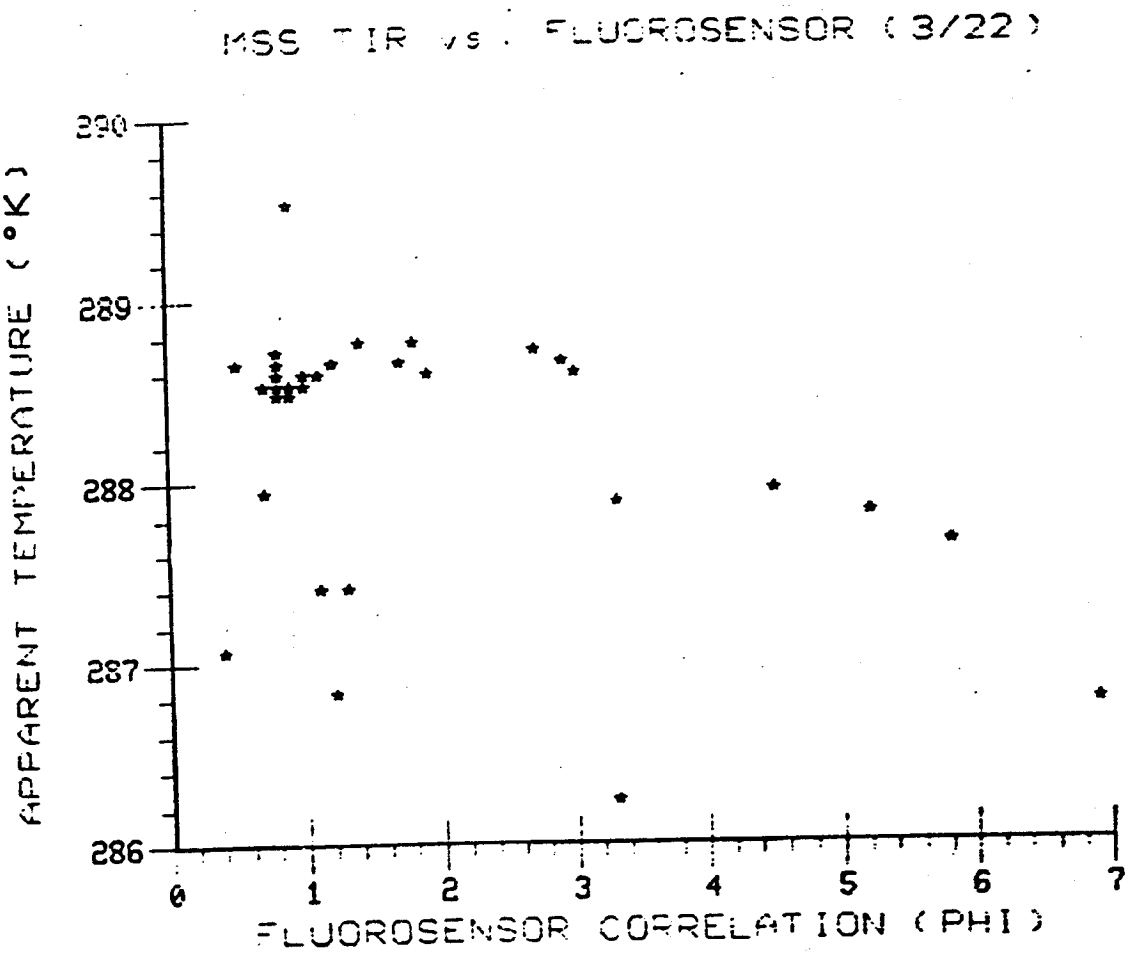

Figure 4.1.W. Scattergram showing relationship of MSS Band TIR radiance and fluorosensor (PHI) correlation; 3 November 1978, Line 22

Pages 186 - 188

are transparencies 4.2.A
through 4.2.C to be
found in a packet
inside the back cover.

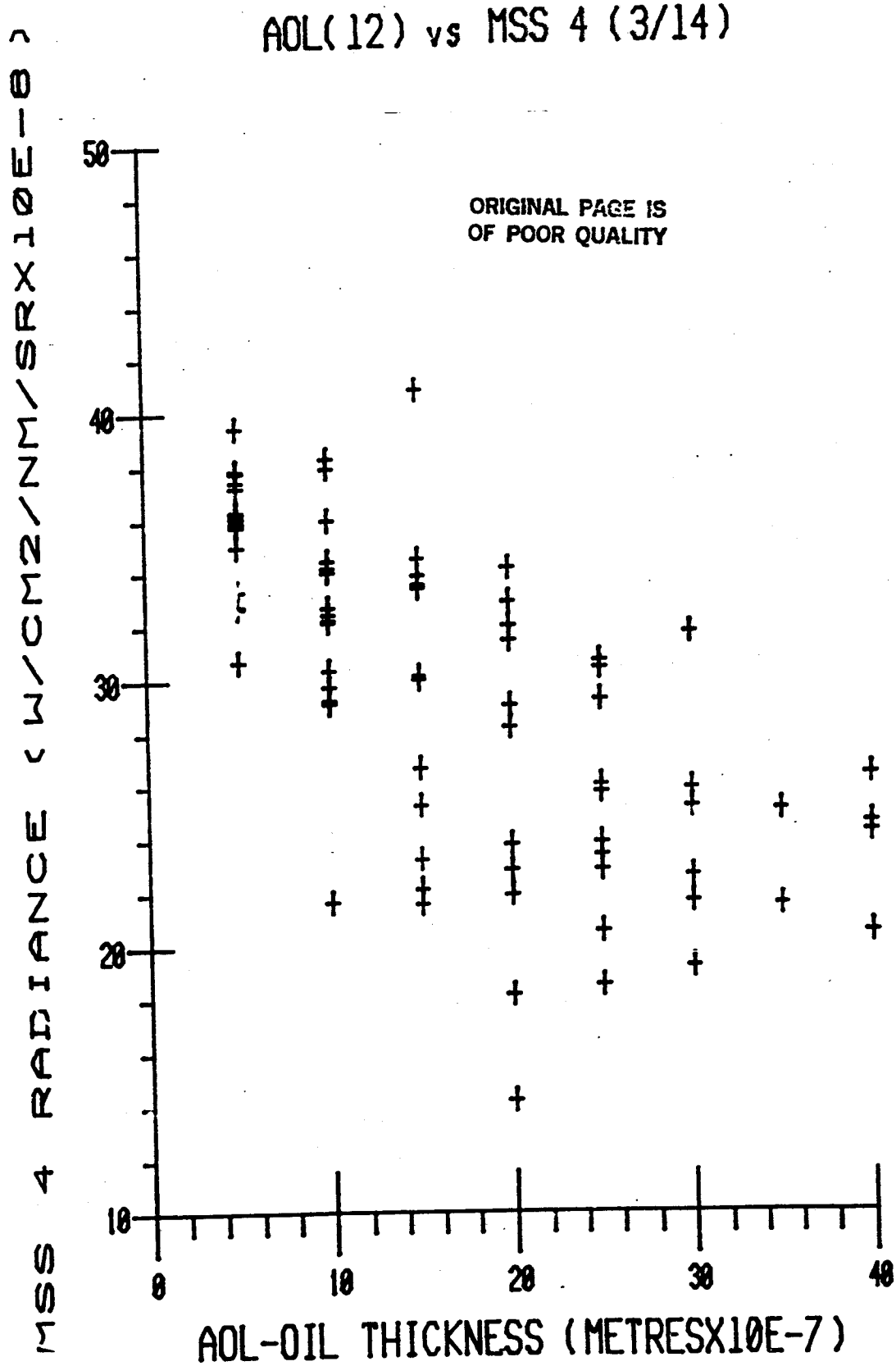

Figure 4.2.D. AOL pass #12 compared to MSS band 4, November 3, line 14.

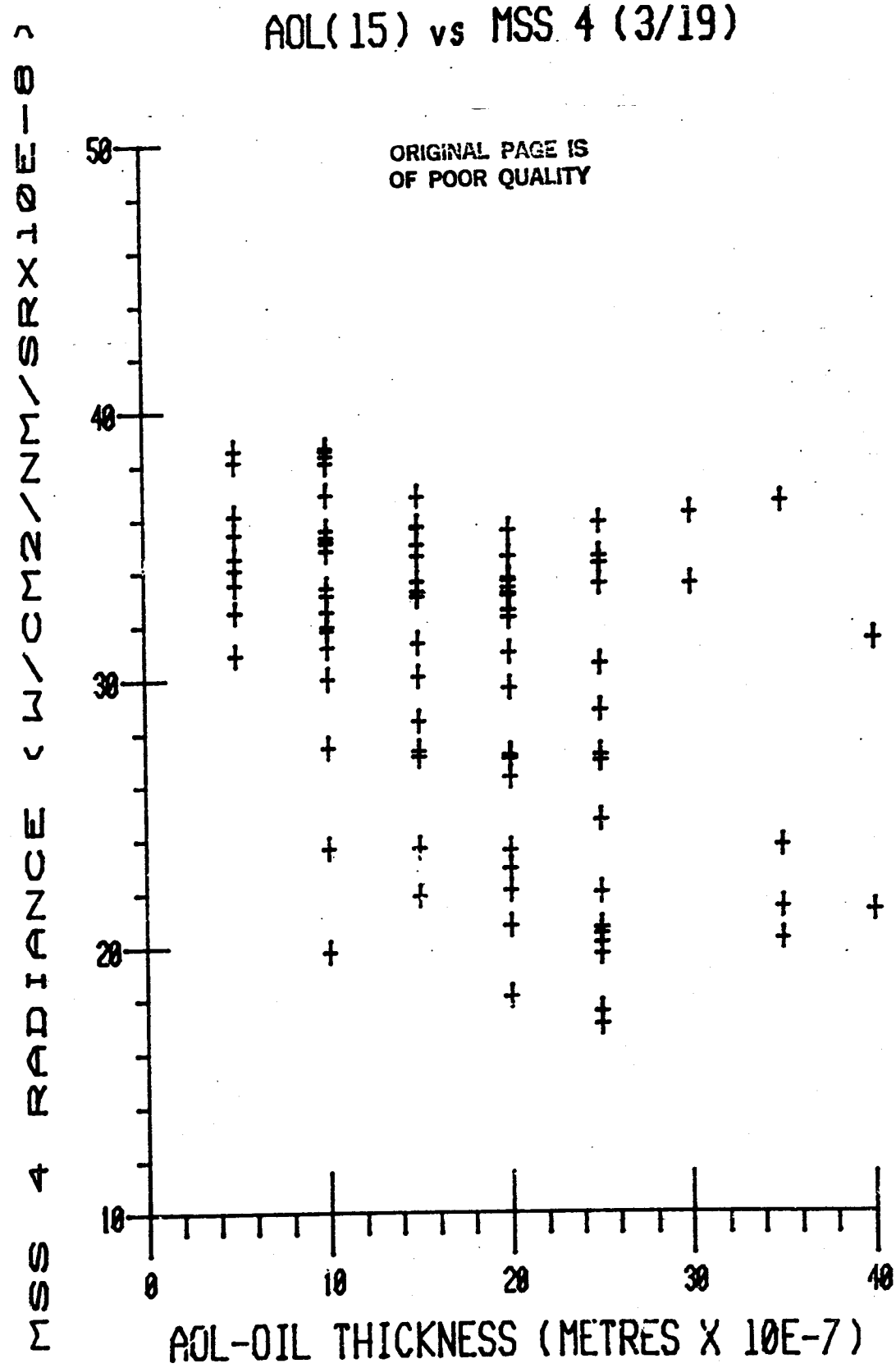

Figure 4.2.E. AOL pass #15 compared to MSS band 4, November 3, line 19.

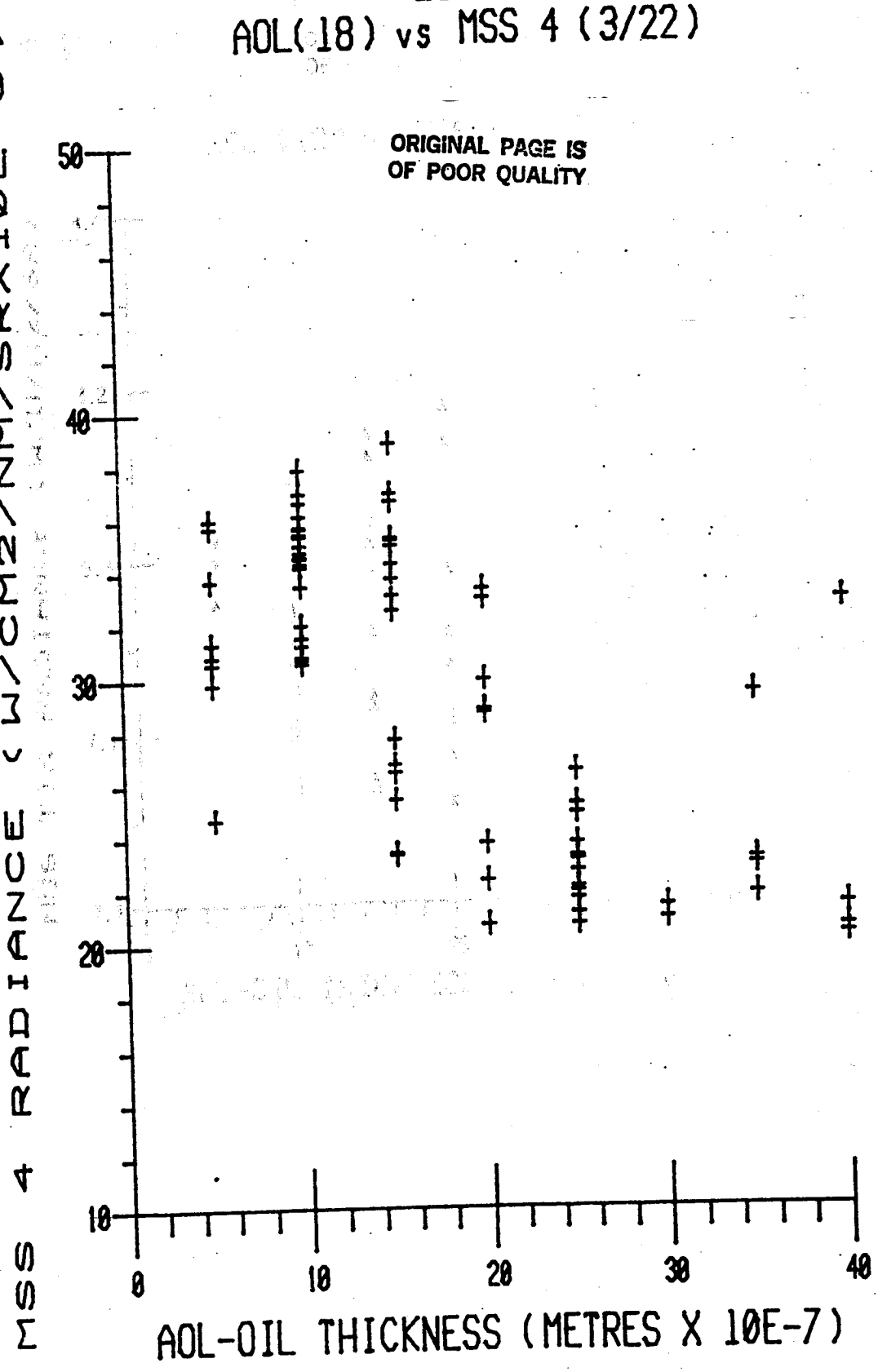

Figure 4.2.F. AOL pass #18 compared to MSS band 4, November 3, line 22.

C-3

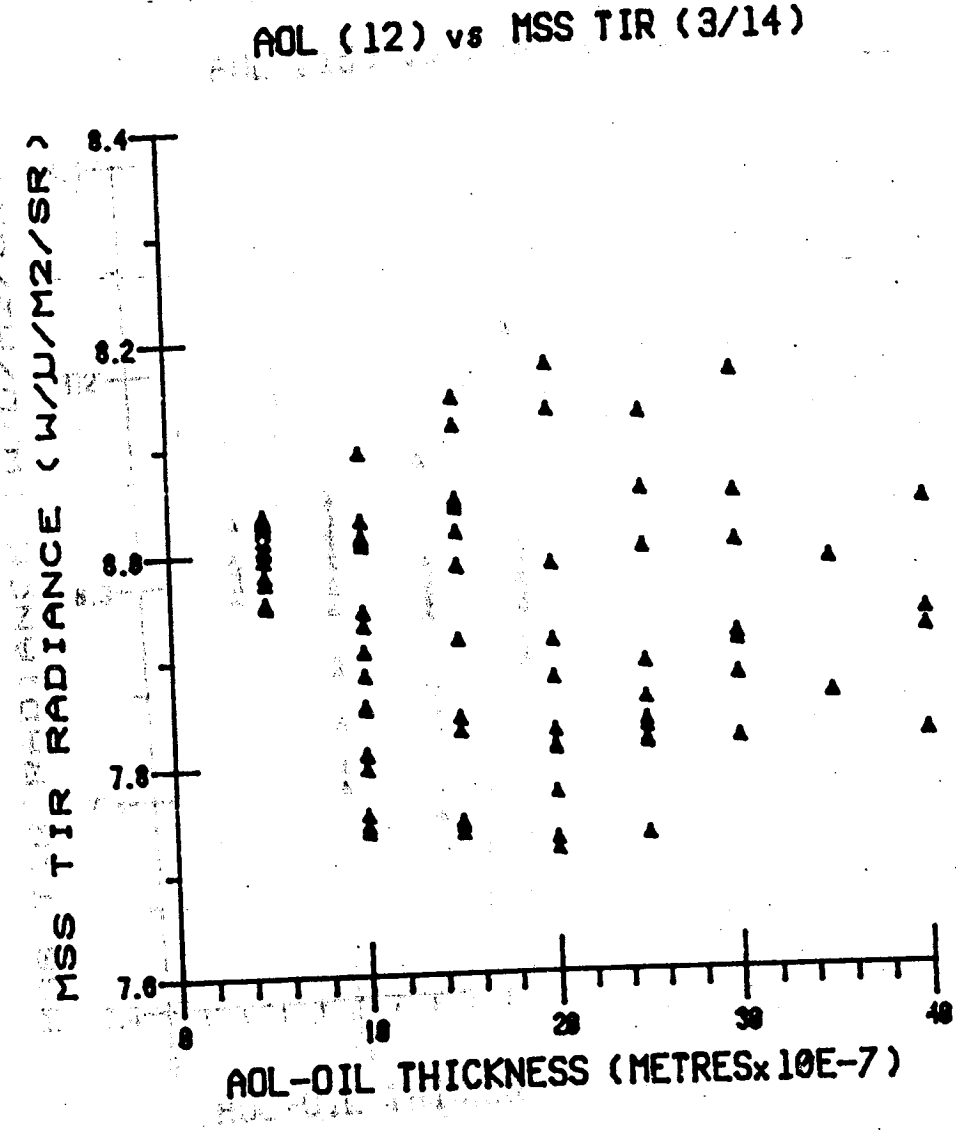

Figure 4.2.G. AOL pass #12 compared to MSS TIR, November 3, line 14.

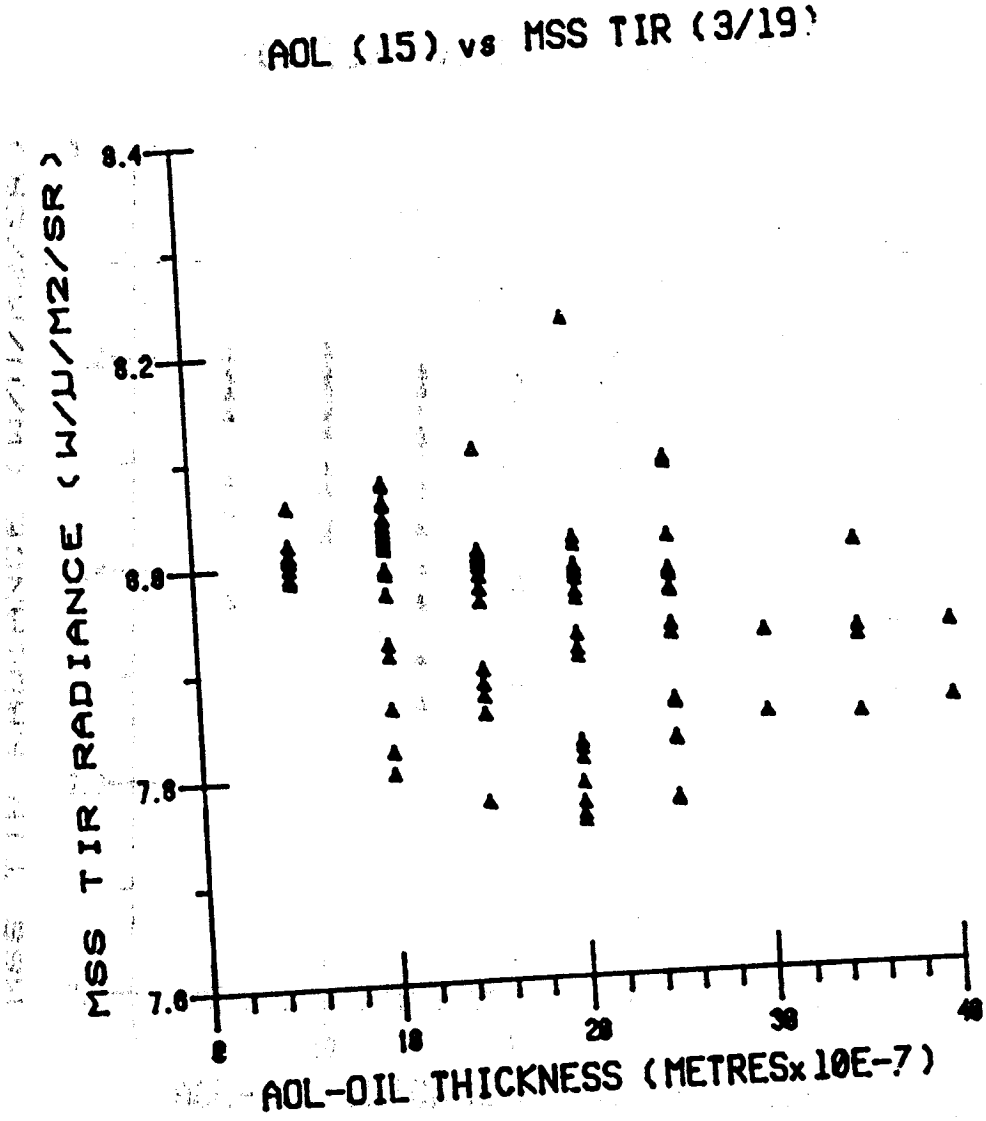

Figure 4.2.H. AOL pass #15 compared to MSS TIR, November 3, line 19.

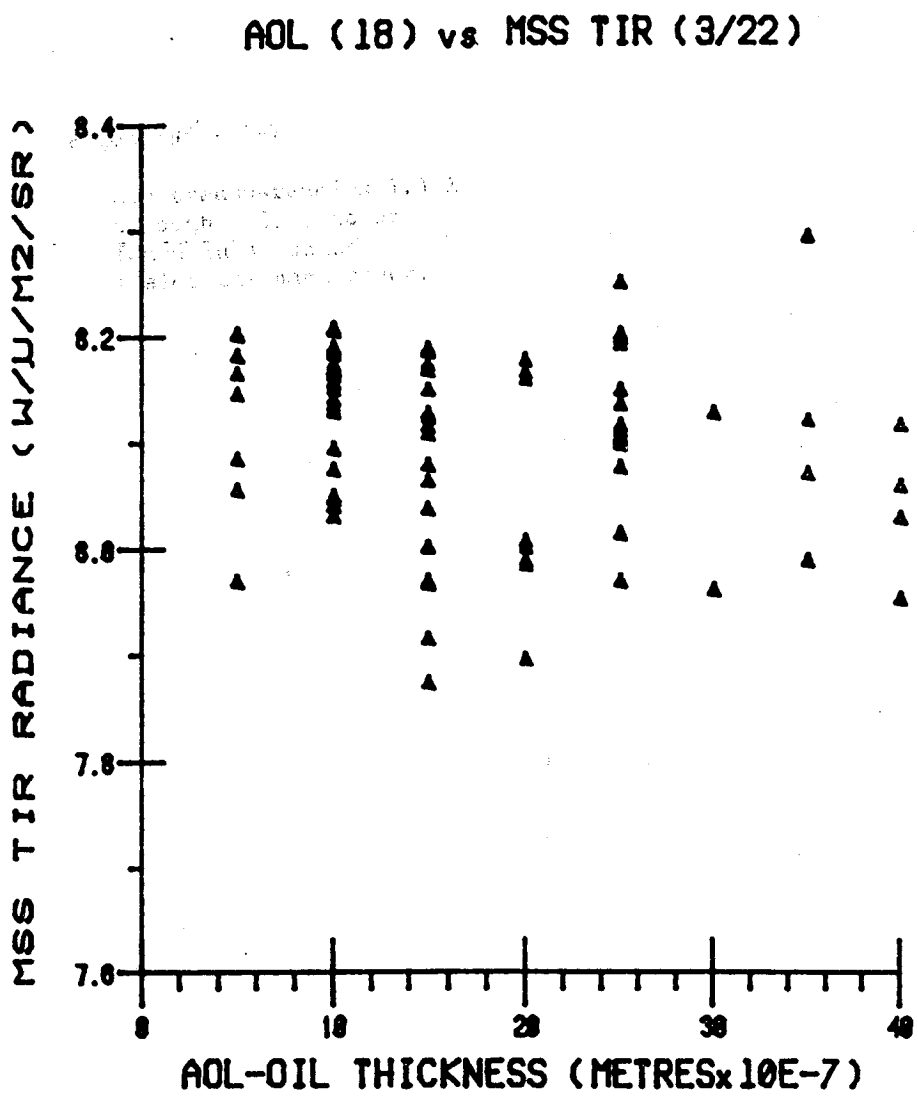

Figure 4.2.I. AOL pass #18 compared to MSS TIR, November 3, line 22.

Pages 195 - 197

are transparencies 4.3.A
through 4.3.C. to be
found in a packet
inside the back cover.

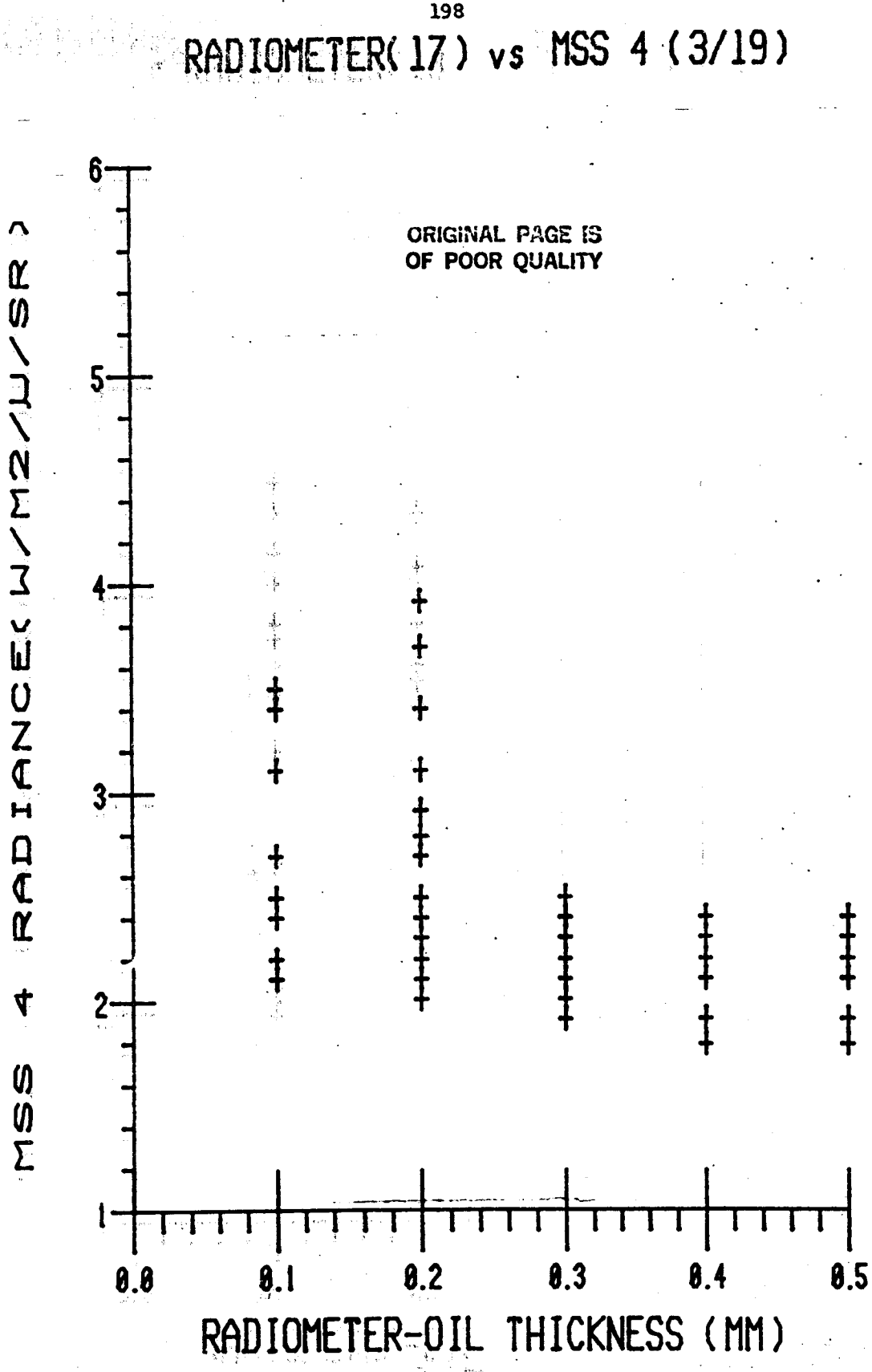

Figure 4.3.D. Microwave radiometer pass #17 compared to MSS band 4, November 3, line 19.

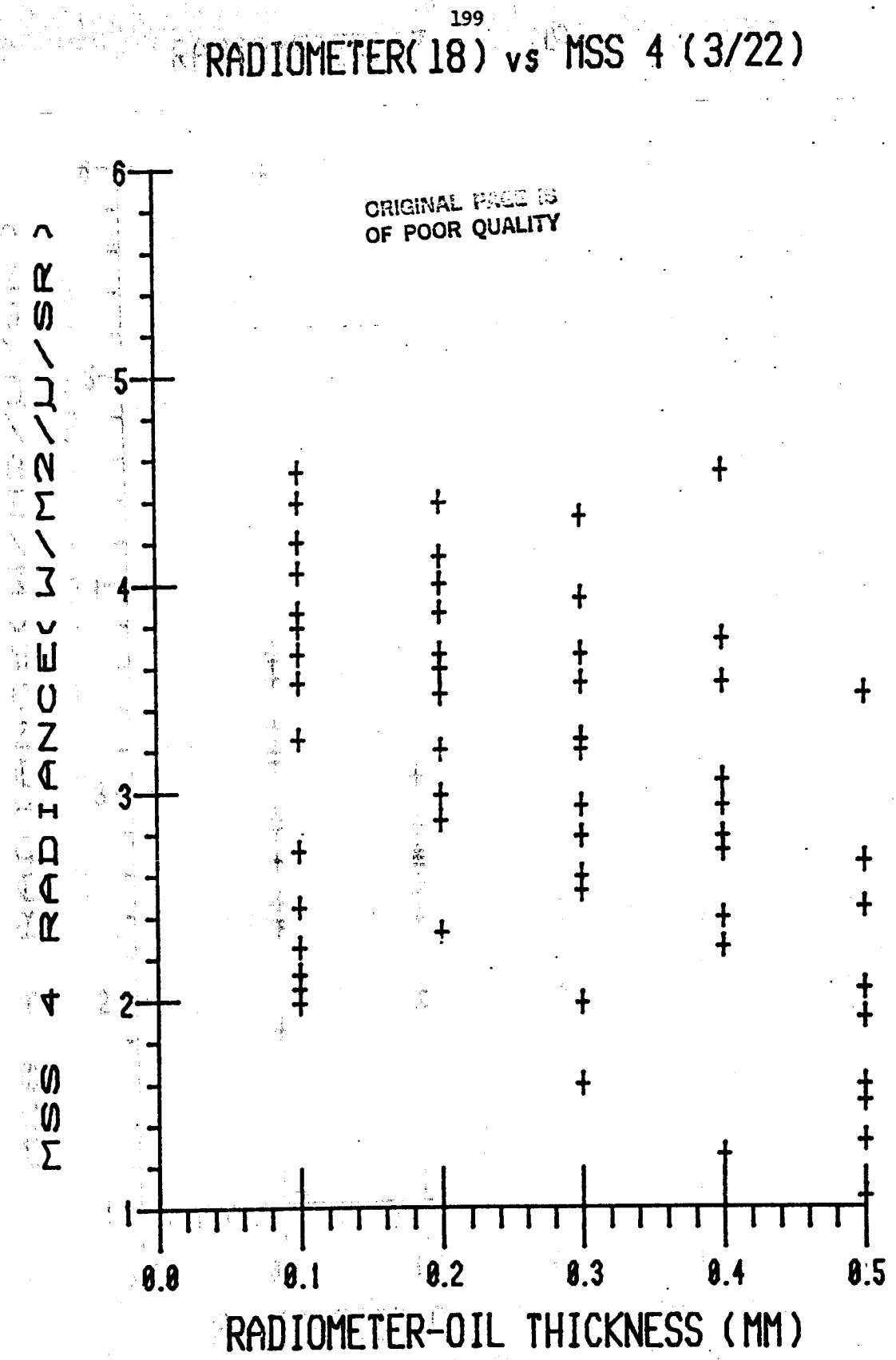

Figure 4.3.E. Microwave radiometer pass #18 compared to MSS band 4, November 3, line 22.

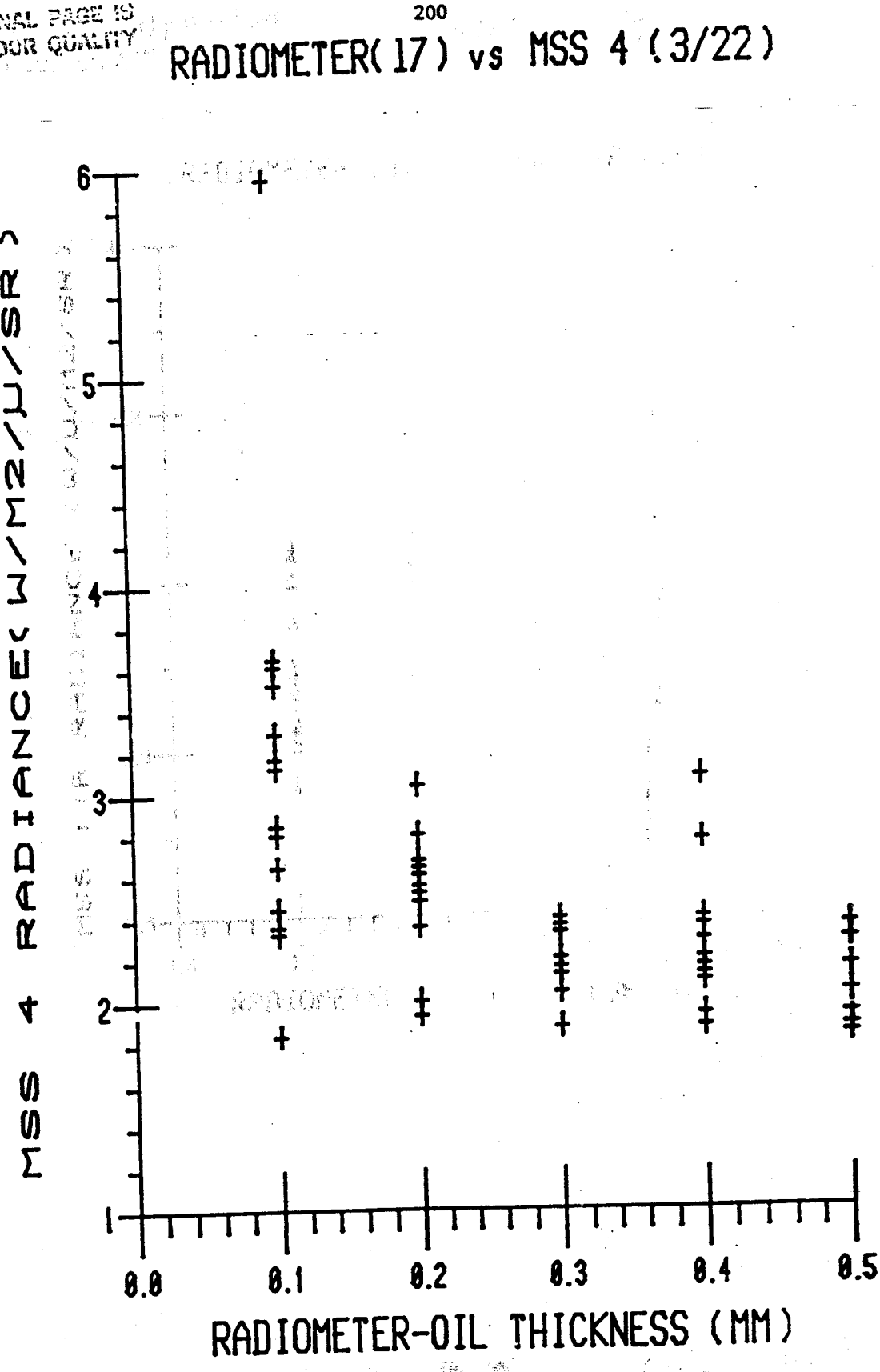

Figure 4.3.F. Microwave radiometer pass #17 compared to MSS band 4, November 3, line 22.

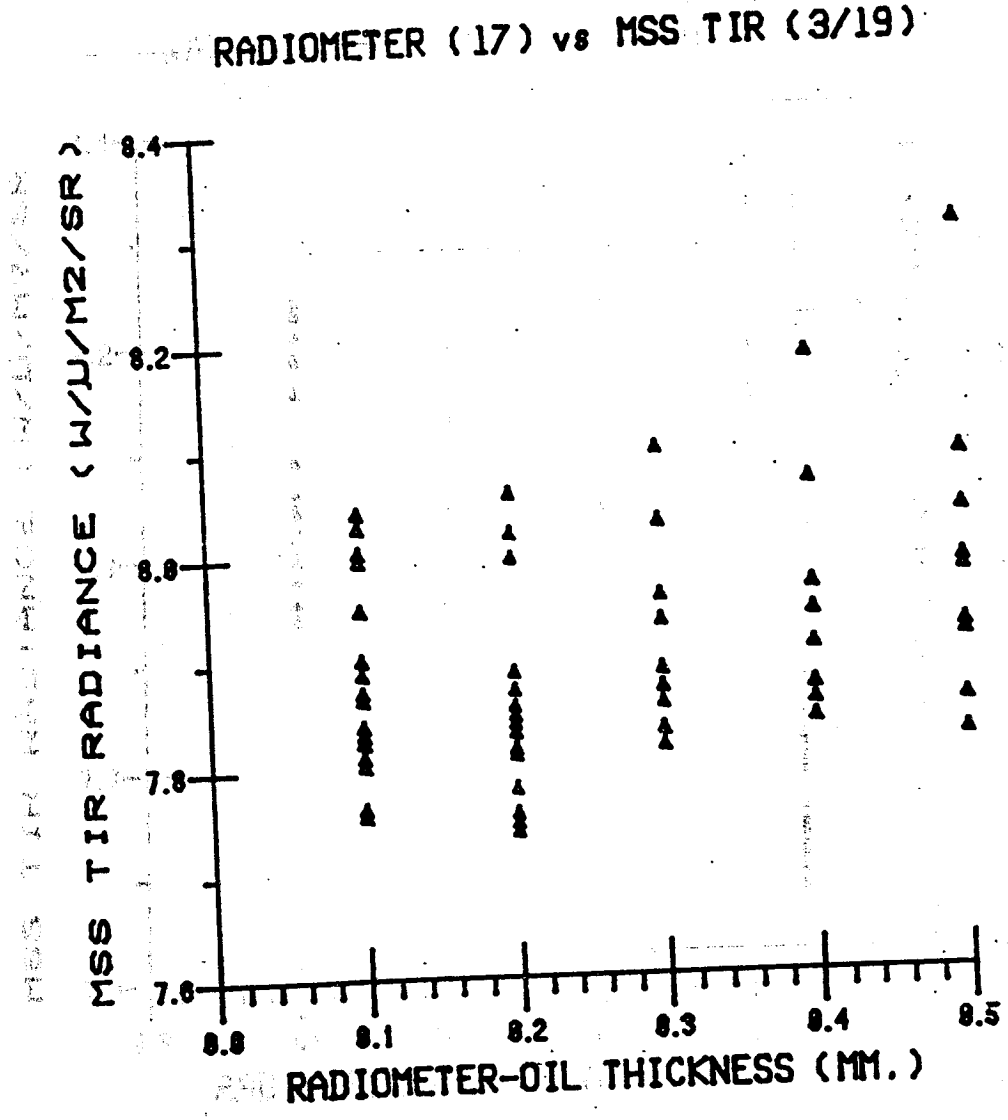

Figure 4.3.G. Microwave radiometer pass #17 compared to MSS TIR, November 3, line 19.

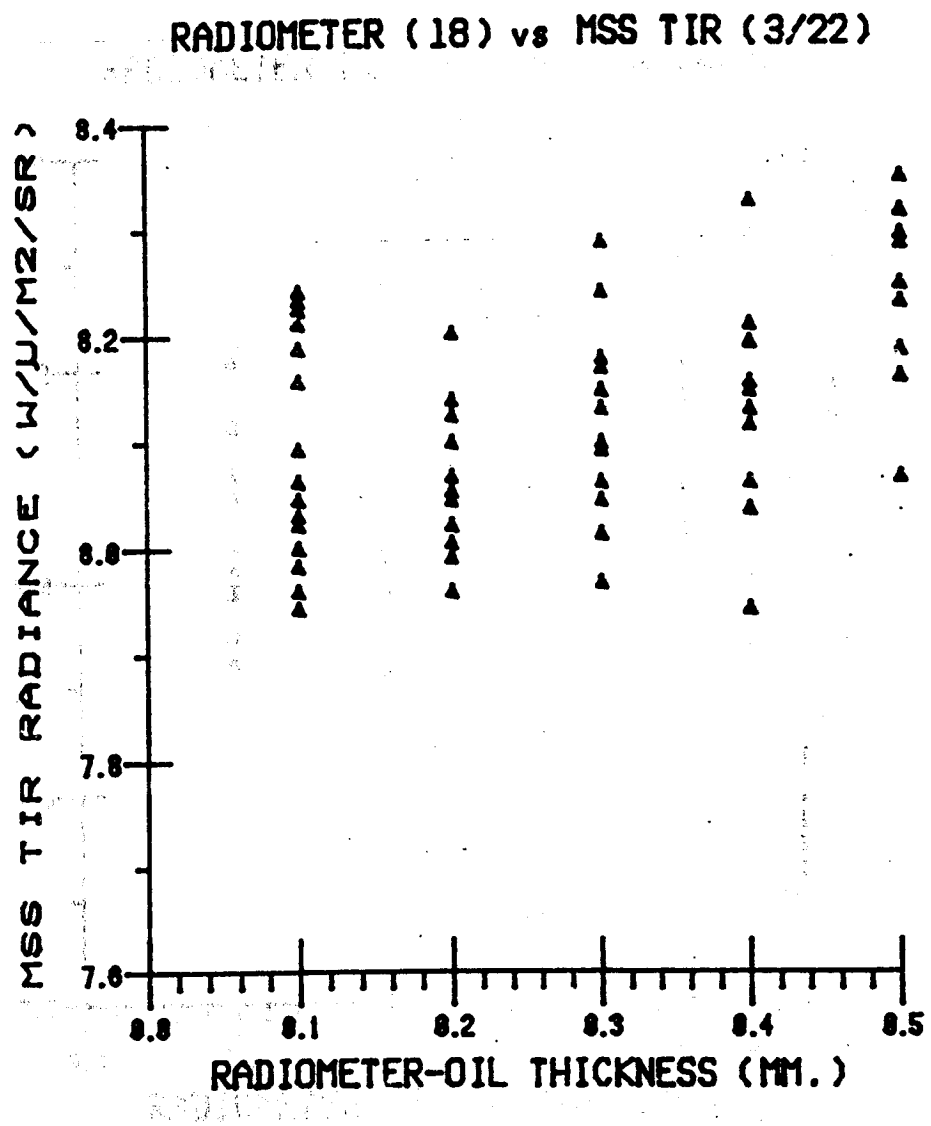

Figure 4.3.H. Microwave radiometer pass #18 compared to MSS TIR, November 3, line 22.

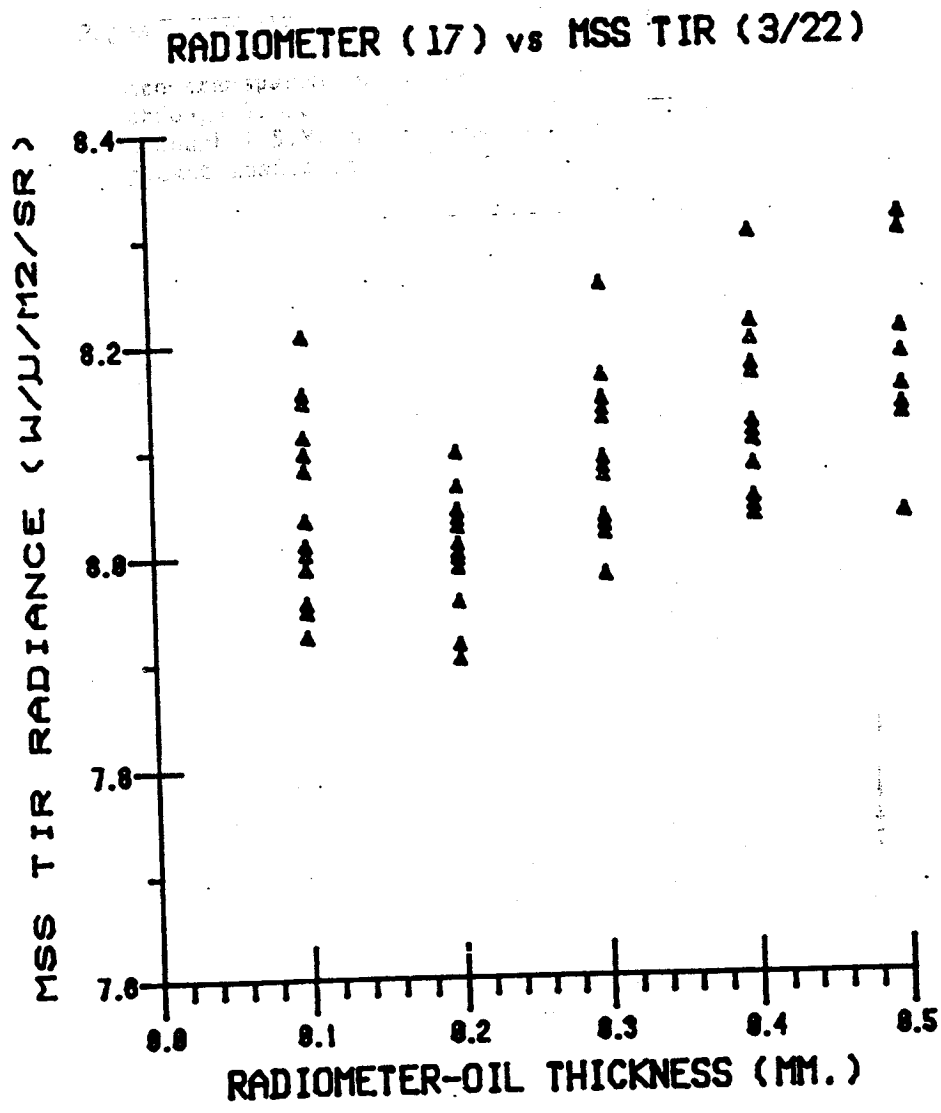

Figure 4.3.I. Microwave radiometer pass #17 compared to MSS TIR, November 3, line 22.

Pages 204 - 212

are transparencies 4.4.A
through 4.4.C and 4.5.A
through 4.5.F, to be found in a
packet inside the back cover.

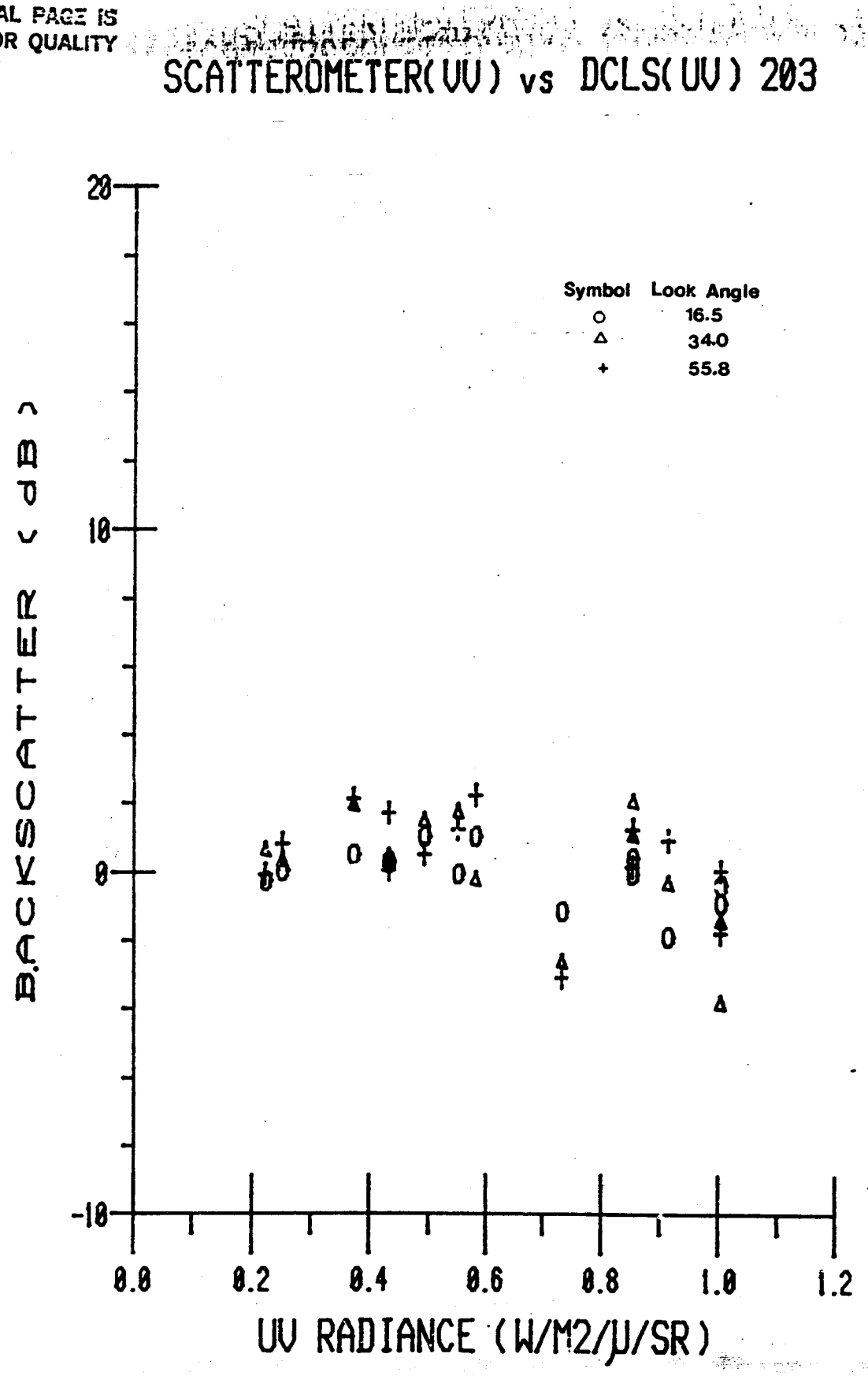

Figure 4.5.6. Microwave scatterometer (backscatter) versus UV (radiance) comparison. November 2, line 03; MS polarization W.

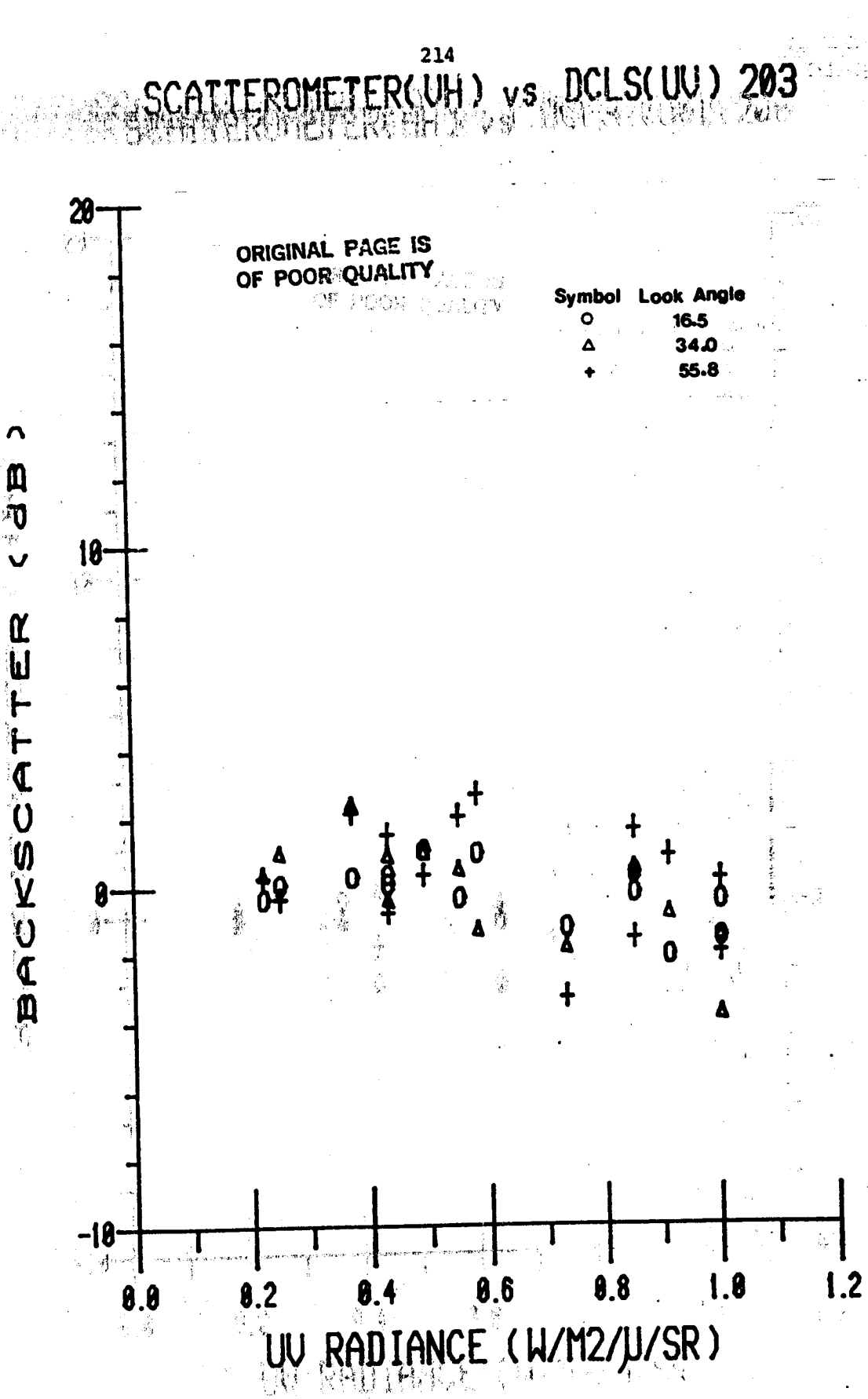

Figure 4.5.H. Microwave scatterometer (backscatter) versus UV (radiance) comparison. November 2, line 03; MS polarization VH.

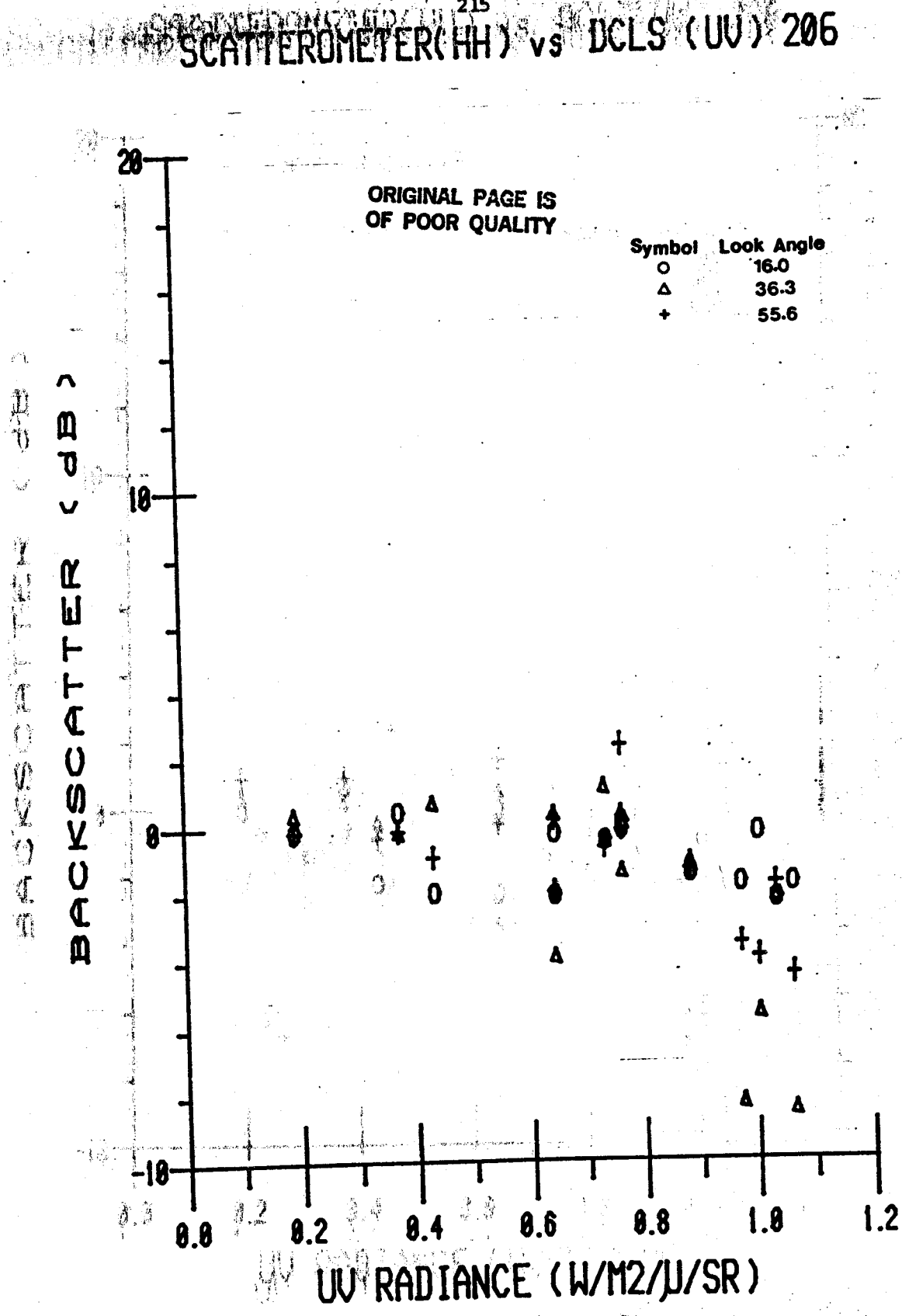

Figure 4.5.I. Microwave scatterometer (backscatter) versus UV (radiance) comparison. November 2, line 06; MS polarization HH.

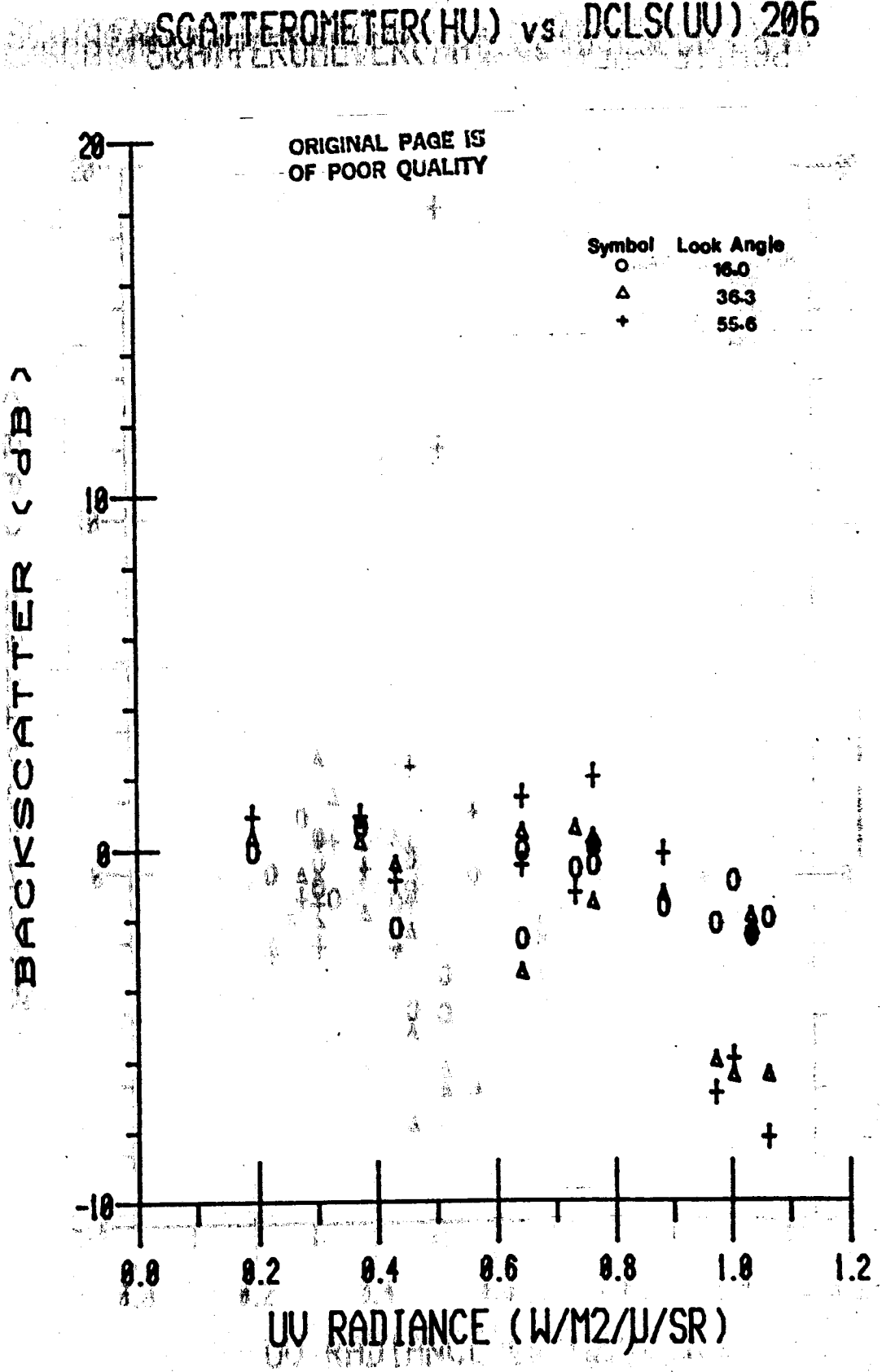

Figure 4.5.J. Microwave scatterometer (backscatter) versus UV (radiance) comparison. November 2, line 06; MS polarization HV.

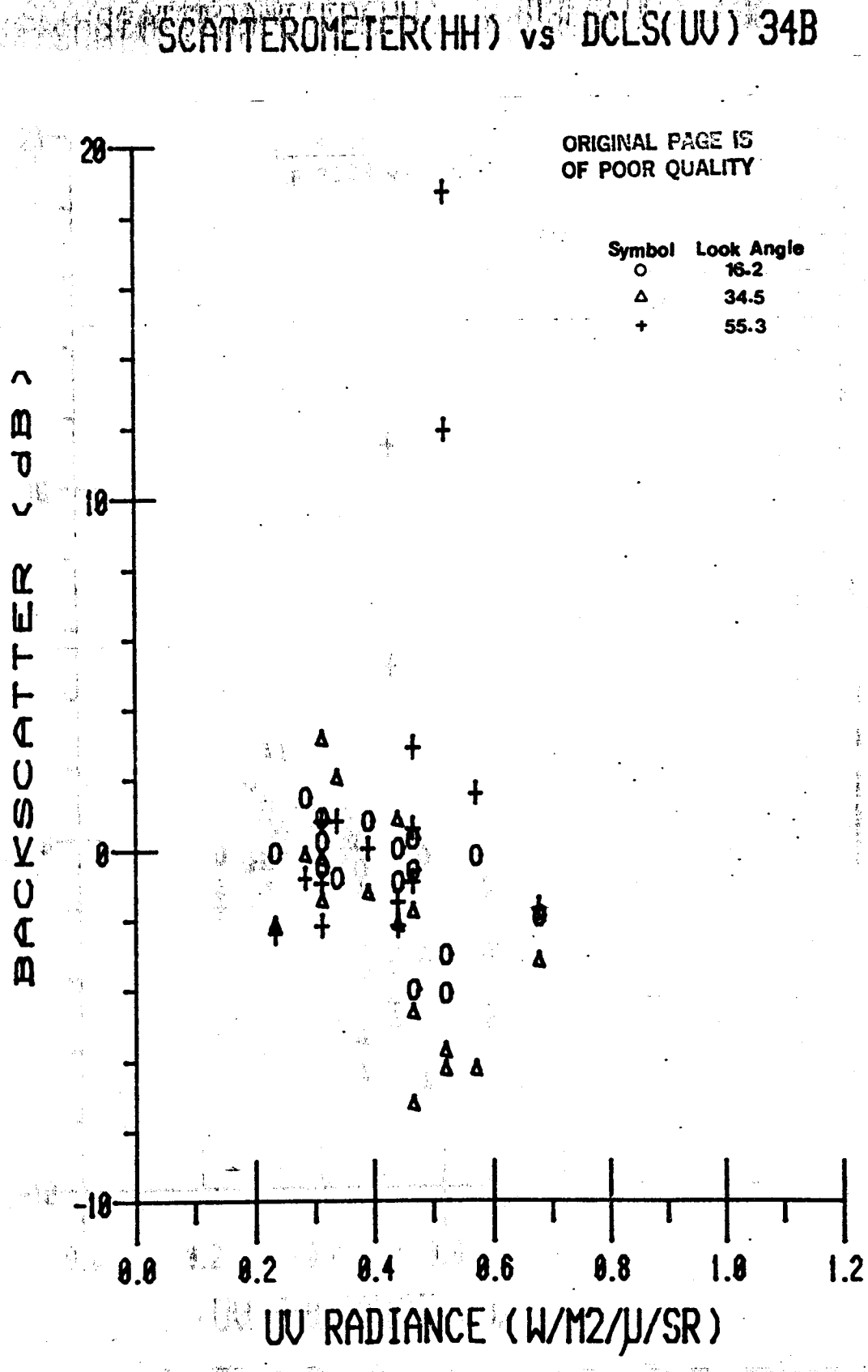

Figure 4.5.K. Microwave scatterometer (backscatter) versus UV (radiance) comparison. November 3, line 4B; MS polarization HH.

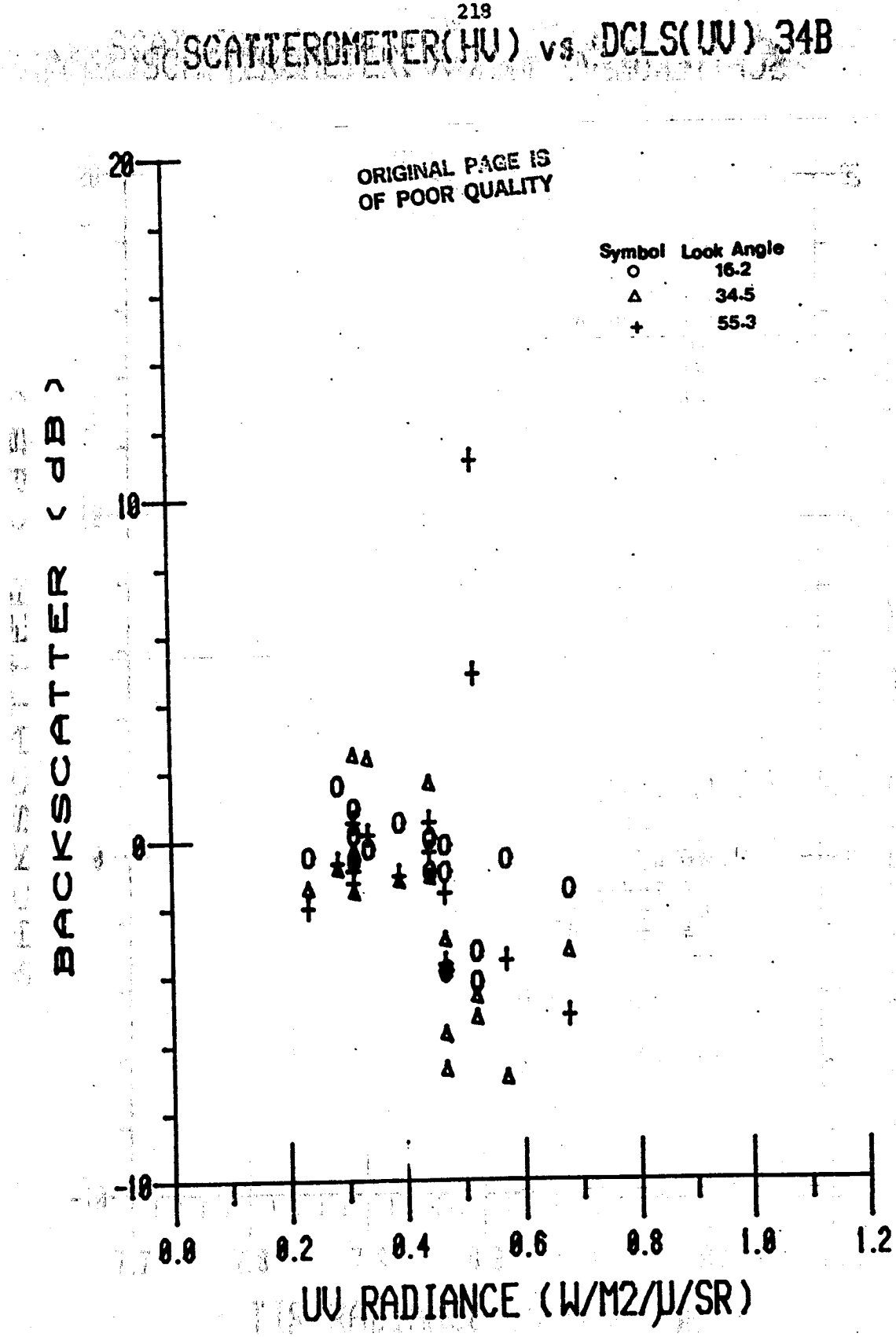

Figure 4.5.L. Microwave scatterometer (backscatter) versus UV (radiance) comparison. November 3, line 4B; MS polarization HV.

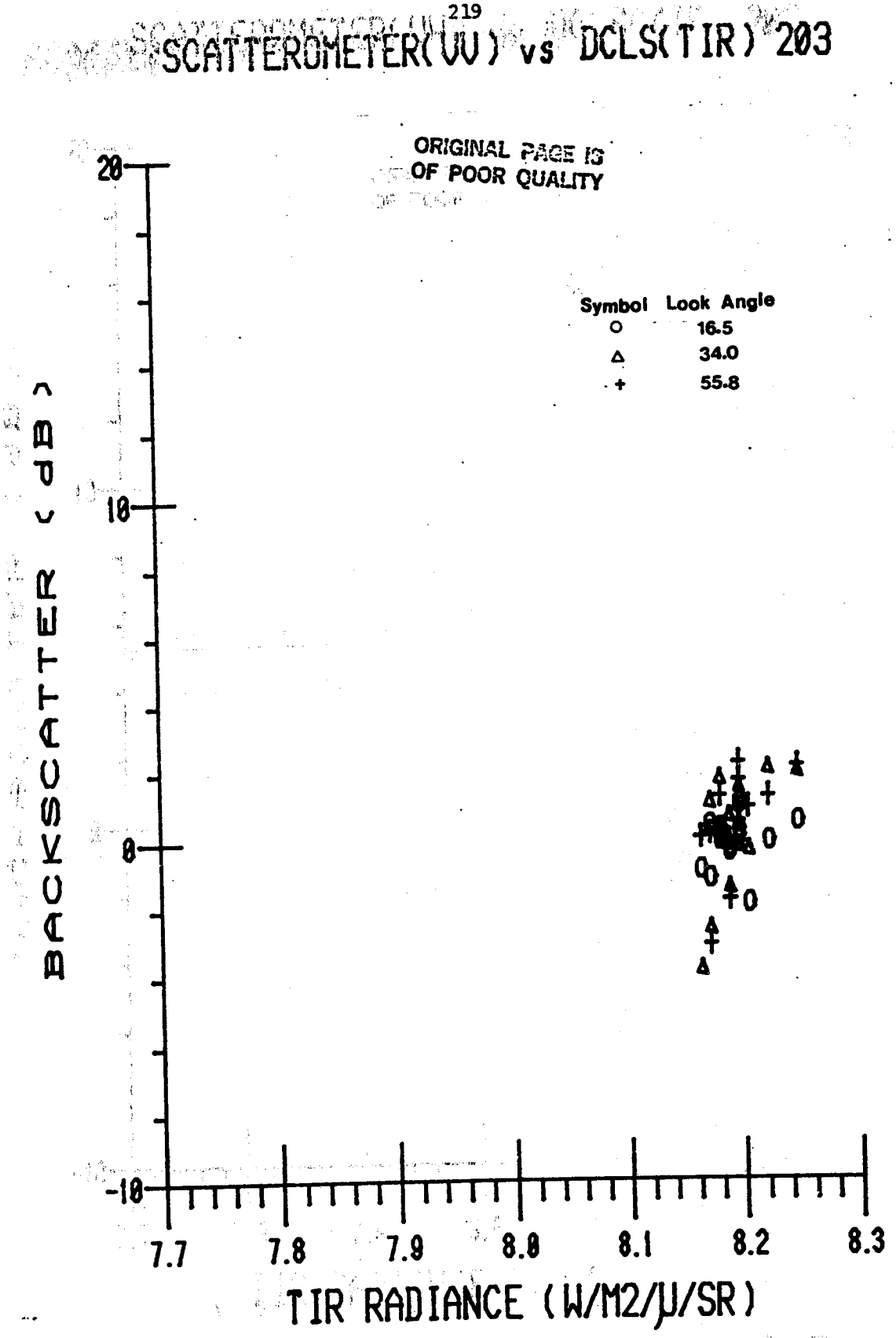

Figure 4.5.M. Microwave scatterometer (backscatter) versus TIR (radiance) comparison. November 2, line 03; MS polarization VV.

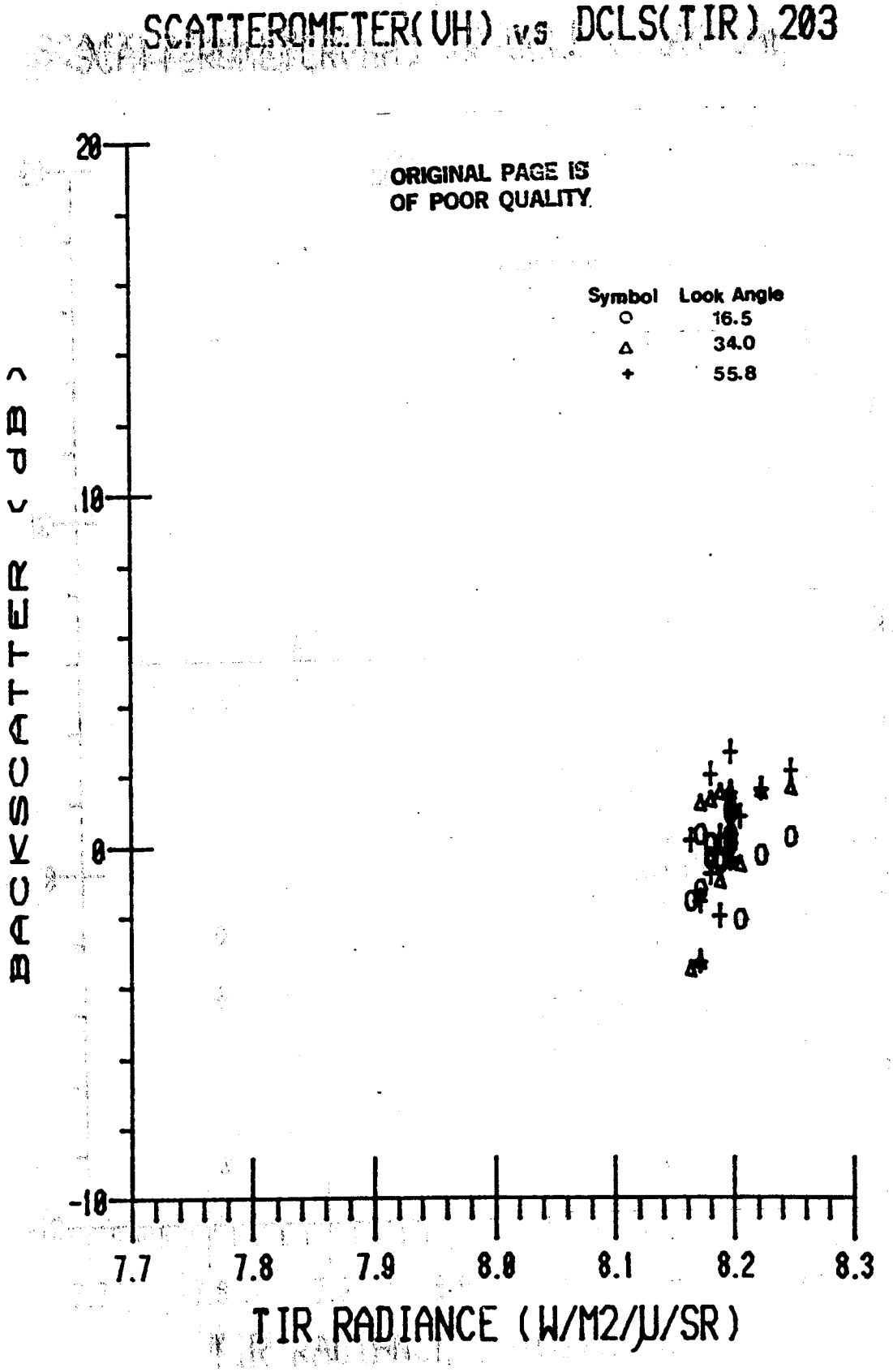

Figure 4.5.N. Microwave scatterometer (backscatter) versus TIR (radiance) comparison. November 2, line 03; MS polarization VH.

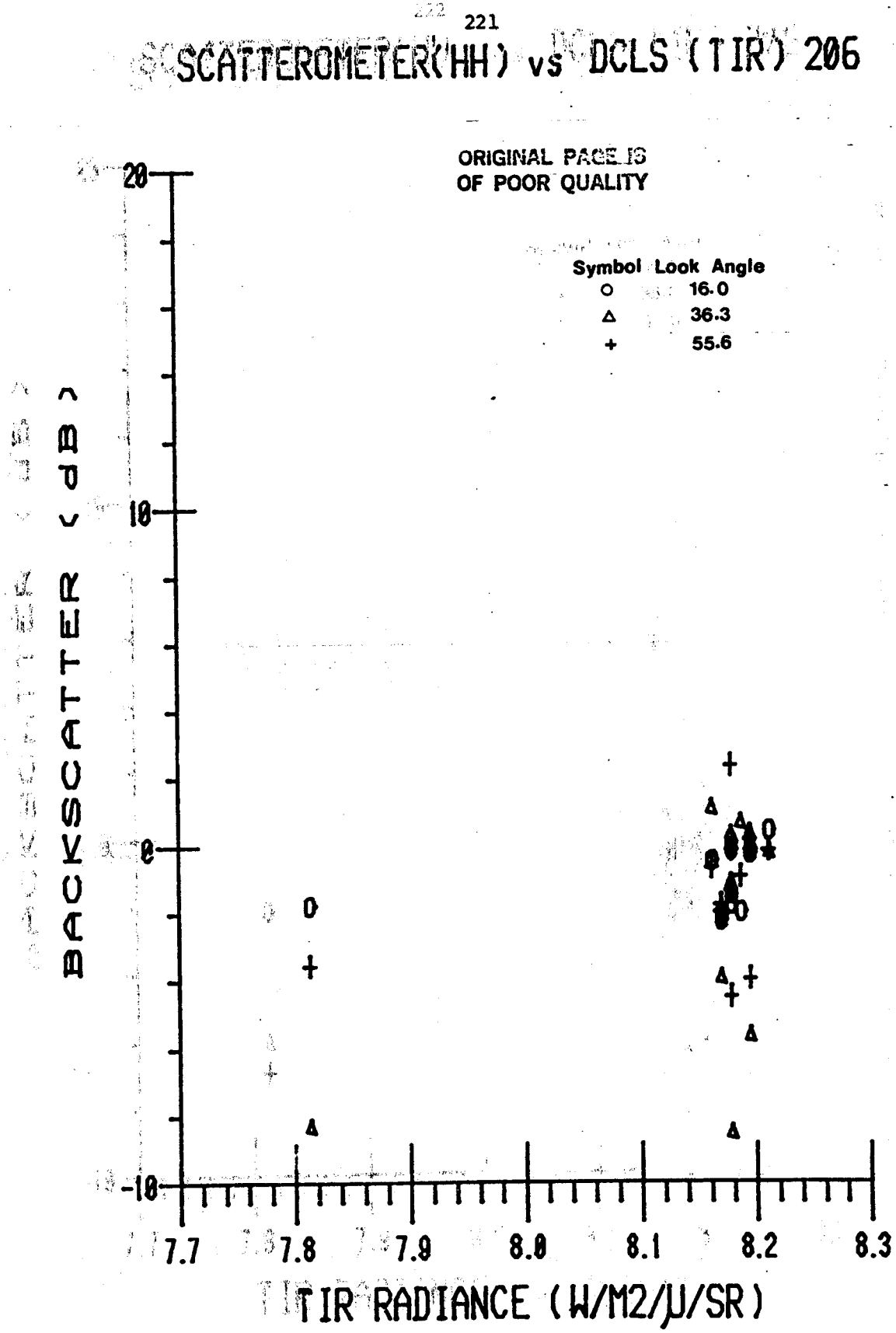

Figure 4.5.0. Microwave scatterometer (backscatter) versus TIR (radiance) comparison. November 2, line 06; MS polarization HH.

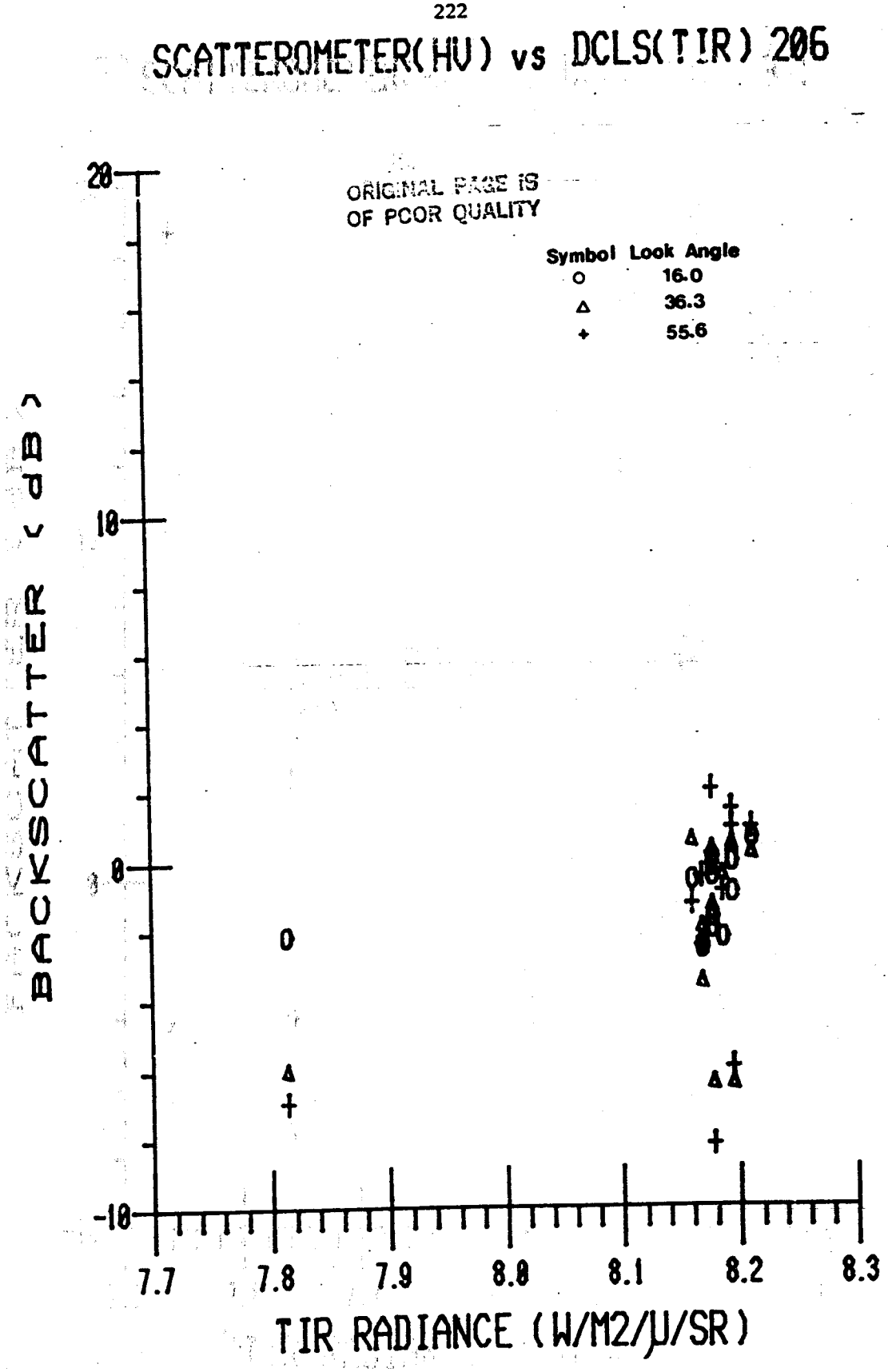

Figure 4.5.P. Microwave scatterometer (backscatter) versus TIR (radiance) comparison. November 2, line 06; MS polarization HV.

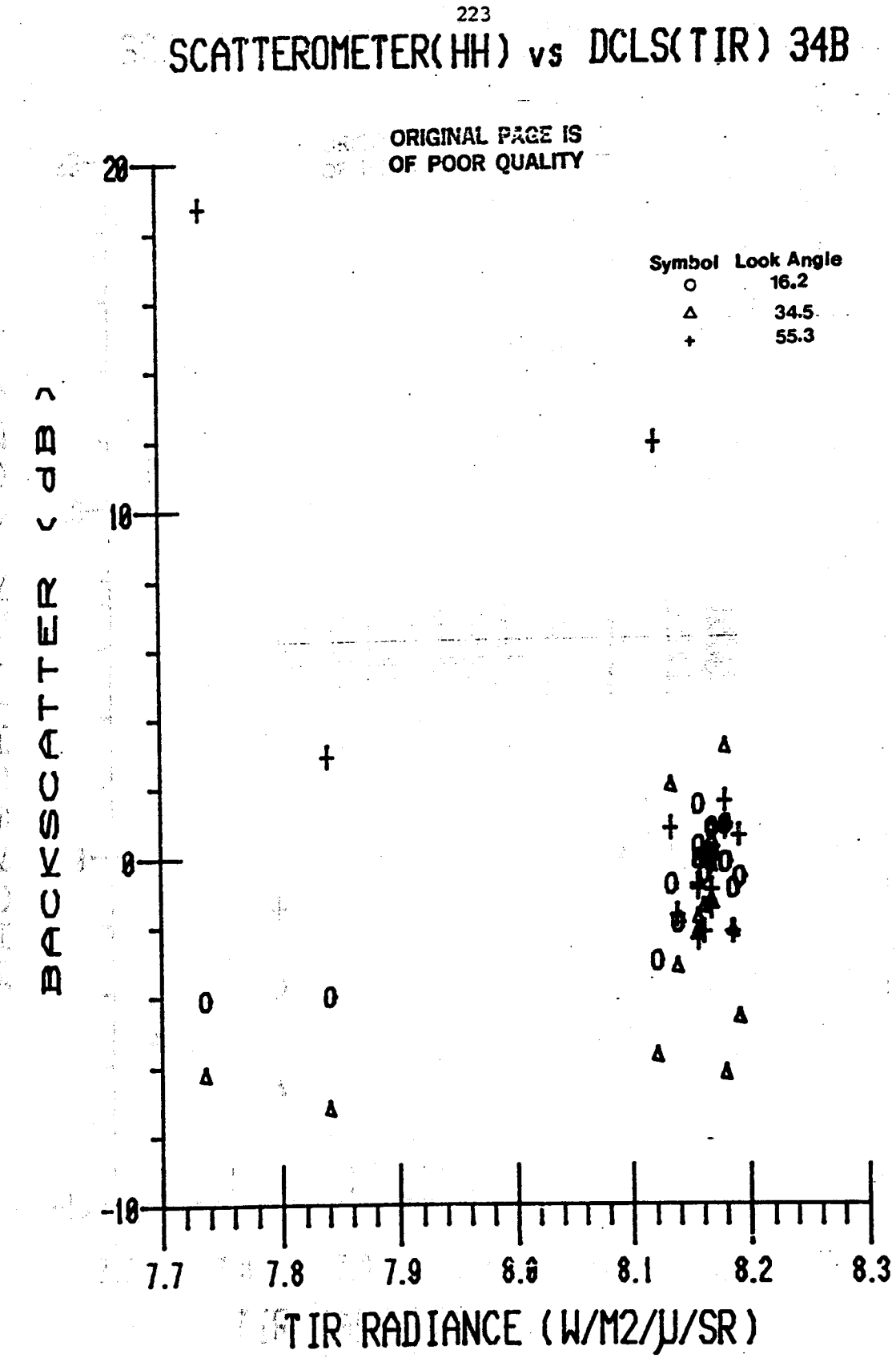

Figure 4.5.Q. Microwave scatterometer (backscatter) versus TIR (radiance) comparison. November 3, line 4B; MS polarization HH.

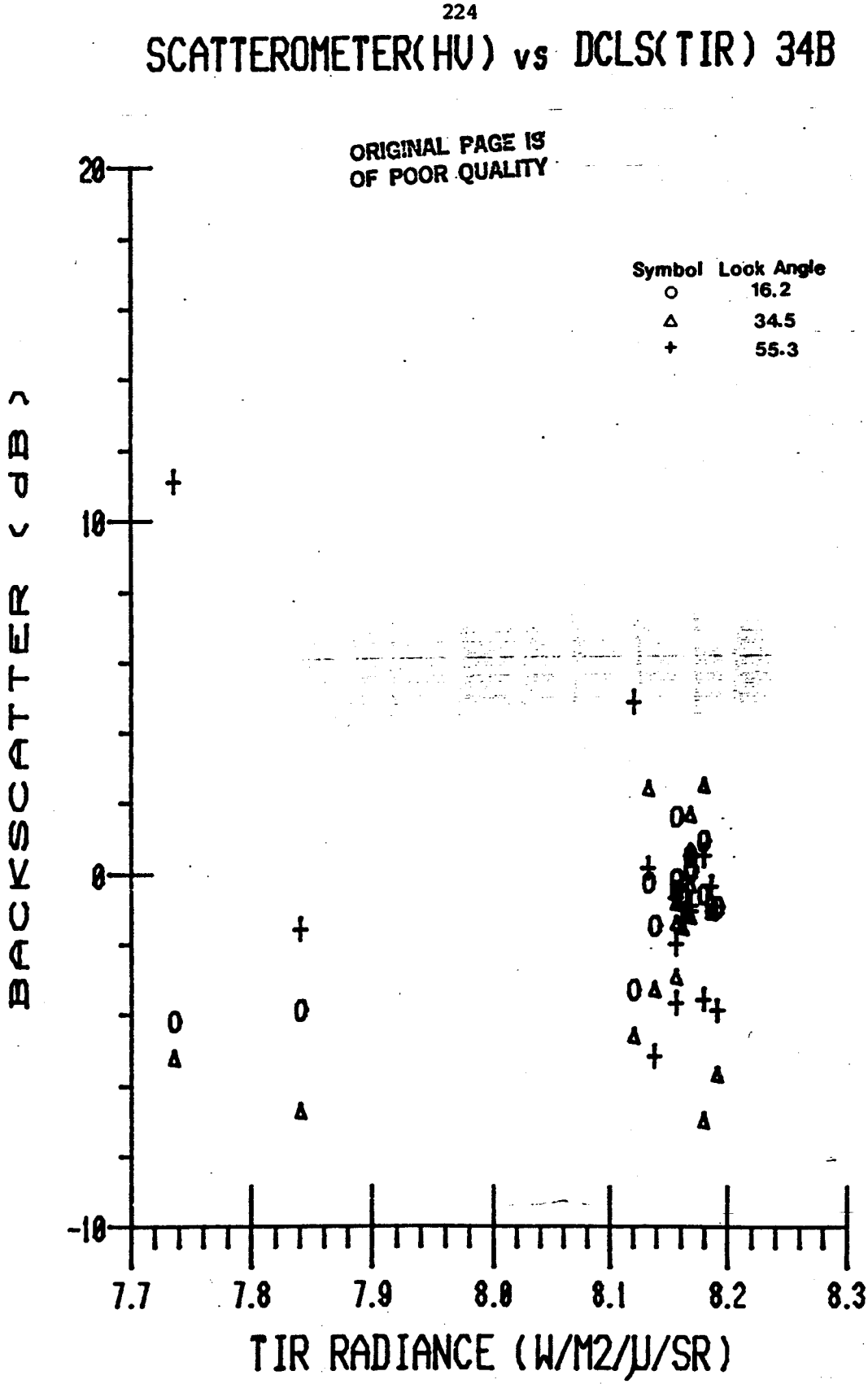

Figure 4.5.R. Microwave scatterometer (backscatter) versus TIR (radiance) comparison. November 3, line 4B; MS polarization HV.